STRUCTURES OF GASEOUS IONS BY INFRARED MULTIPLE PHOTON DISSOCIATION (IRMPD) SPECTROSCOPY

KHADIJEH RAJABI


CENTRE FOR NFLD. STUDIES
MEMORIAL UNIVERSITY
OF NEWFOUNDLAND

Structures of Gaseous Ions by Infrared Multiple Photon Dissociation (IRMPD) Spectroscopy

by

© Khadijeh Rajabi

A thesis submitted to the

School of Graduate Studies

in partial fulfillment of the

requirements for the degree of

Doctor of Philosophy

Department of Chemistry

Memorial University of Newfoundland

January 2010

St. John's Newfoundland

Abstract

The technique of infrared multiple photon dissociation (IRMPD) spectroscopy has shown its ability to determine the 3D (dimensional) structure of gaseous ions. Using this technique, the structures of small biologically relevant ions such as amino acids and nucleic acid bases bound with a proton or metal cations in the gas-phase were determined. The necessity of employing computational methods to analyze and interpret the experimental data has been demonstrated. However, the computational results must be analyzed with extreme caution to prevent any incorrect conclusions. Among the parameters one has to consider when dealing with the computational results is the experimental method used to obtain the data. For example, the simulated IR spectra for only two of the four lowest-energy protonated adenine dimer isomers were similar to the experimental IRMPD while, based on gas-phase calculations, the four lowest-energy structures were almost isoenergetic. Since the ions were produced by electrospray ionization (ESI) from the solution phase, the effect of water as a solvent was considered by applying two independent computational approaches to take solvation effects into account. Polarizable continuum model (PCM) calculations as well as microsolvation with five explicit water molecules calculations showed that water only preferentially stabilizes these two observed isomers, consistent with the interpretation of the IRMPD spectra. The results suggest great caution is required when using gas-phase calculations to predict the structures of gaseous ions borne in solution by ESI.

To investigate the influence of solvent on the structure of ions, an experimental method was developed to produce solvated ions in the gas-phase. These solvated ions then were investigated by IRMPD spectroscopy and blackbody infrared radiative dissociation (BIRD) to obtain kinetic and thermodynamic data. The solvation of electrosprayed ions occurs in the accumulation/collision hexapole of a hybrid quadrupole-Fourier transform mass spectrometer (Q-FTMS) by introducing the solvent into the collision cell. The most sensitive parameters based on our experience were the collision energy in the hexapole, the pressure of both collision gas and solvent in the hexapole, ion accumulation time, and the chemical nature of the species. This method was successfully applied to adenine and thymine cluster ions to produce multiply hydrated ions. The structures of singly hydrated ions were determined by IRMPD spectroscopy.

Due to the importance of m-DNA (metalated-DNA), an attempt to investigate the structure of singly hydrated thymine zinc ion-bound dimer was initiated. It was found that thymine loses one proton in the presence of zinc. Therefore, the $[(Thy_2\text{-}H)\text{-}Zn\text{-}(H_2O)]^+$ cluster was singly charged. Solely comparing the IRMPD spectrum in the 3100-3850 cm^{-1} and simulated IR spectra was not sufficient to assign only one structure to the observed spectrum. Based on thermochemical values, the two lowest energy structures were assigned as possible structures under the experimental conditions. In the most stable structure, the water is directly attached to the zinc in the zinc ion-bound dimer in which the Zn^{2+} is shared between the two thymines at N3O4 sites. Furthermore, computational data suggested that recording an IRMPD

spectrum in the 1800-2800 cm^{-1} region might be useful to distinguish between the two lowest energy structures. Therefore, recording the spectrum for the $[(Thy_2\text{-}H)\text{-}Zn\text{-}(H_2O)]^+$ cluster in this lower energy region is part of the future work.

Acknowledgements

I have greatly enjoyed the years I have spent at Memorial University of Newfoundland (MUN) and it will be hard to express my appreciation to the many people to whom I am indebted for such unforgettable experiences. This research project would not have been feasible without the support of many people.

First of all, I would like to express my deepest sense of gratitude to my wonderful supervisor, Professor Travis D. Fridgen, for his patient guidance and excellent advice throughout this study. I was very fortunate to have him as my supervisor. Travis has been abundantly helpful and offered invaluable assistance, support and encouragement in terms of both academic and non-academic matters and became more of a friend than a supervisor. I appreciate his vast knowledge and skill in many areas and his assistance in writing papers. Also, I would like to thank Lisa, Travis's wife (boss) and a super-mom, for her unrestricted hospitality and all the fun we had at their place.

Deepest gratitude is also due to the members of the supervisory committee, Prof. Christopher Flinn and Prof. Robert W. Davis without whose knowledge and assistance this study would not have been successful. I would like to thank Dr. Flinn for also being a teaching supervisor for the graduate program in teaching (GPT) program and trusting me to take charge of three sessions of his course. A very special thanks goes to Dr. Davis who has been the head of the department during most of my graduate studies. He is probably one of the most philanthropist I have ever met.

I doubt that I will ever be able to fully convey to him my appreciation.

Also, I would like to thank my internal and external examiners, Prof. Raymond Poirier, Prof. Robert Helleur, and Prof. John Klassen for carefully reading this thesis as well as providing me with the constructive comments.

Special thanks also to all my friends, especially our research group members: Osama, Mike, Julie, Elizabeth, Chad and Amench for sharing the literature and invaluable assistance. I am not forgetting all my best friends who always been there for me.

I would also like to convey thanks to the warm and lovely staff at the chemistry department who welcomed me as a friend during the different stages of my life as a graduate student. Just to name a few, I would like to thank Professor Peter Pickup, Rosalind, Viola, Teresa, Mary, Gerry, and Marlene for their administrative information. In addition, I would like to thank them for always positive compliments, funny little stories, condolences when I needed them, teaching me Newfie (since I lived in Newfoundland for four years, I guess I can authorize myself to use this word) expressions b'y, as well as suggesting inventive methods to survive in the cold such as putting hot water bottles under the coat.

I wish to express my love and gratitude to Saeid, my beloved husband. He has been always there for me with his endless love, encouragement, patience and support. Of course, I can never express my great appreciation for his sacrifice for giving up his settled life in Iran and immigrating to another continent for me. He has been

very sensitive to the quality of my academic work as well and supported me in every aspects. He patiently listened to my presentations before I gave them, providing me with excellent comments and feedback. I feel incredibly privileged to have him as my husband.

Although Newfoundland weather was not completely in-line with my predictions, I feel very lucky to have become acquainted with this part of world. The fact that St. John's, the provincial capital of Newfoundland, has the third mildest winter in Canada because of its humid weather is in agreement with my geographical expectations but it also has the most snowy, windy and cloudy days in Canada. St. John's, as the oldest (~1500s) English-founded city in North America, has an exceptionally warm and friendly population. I take this opportunity to pass my special thanks to the Mouland family. In particular, my landlady Wilma, who sadly passed away from cancer almost a year ago, was a very pleasant and loving person and treated me as one of her family members.

Of course, none of this would have happened if not for my parents, Aghdas and Ali, especially my mom. They always provided me with the freedom of choice and supported my interest in science, even when that interest led me to distant shores.

- To Saeid, The love of my life -

"A scientific truth does not triumph by convincing its opponents and making them see the light, but rather because its opponents eventually die and a new generation grows up that is familiar with it."

- Max Planck -

Contents

List of Tables

List of Figures

Abbreviations

BIRD	blackbody infrared dissociation
CID	collision-induced dissociation
CLIO FEL	centre laser infrarouge d'Orsay free electron laser
DFT	density functional theory
ECP	effective core potential
ESI	electrospray ionization
FELIX	FEL (free electron laser) for infrared eXperiments
FT-ICR MS	Fourier transform ion cyclotron resonance mass spectrometry
IRMPD	infrared multiple photon dissociation
IVR	intramolecular vibrational energy redistribution
KTP	potassium titanyl phosphate, KTiOPO4
MALDI	matrix-assisted laser desorption/ionization
m-DNA	metalated-DNA
MS-MI	mass spectrometry-matrix isolation
OPO/A	optical parametric oscillator/amplifier
QIT	quadrupole ion trap
RF	radio frequency
TCID	threshold collision-induced dissociation
YAG	yttrium aluminum garnet

Co-authorship Statement

Most of the experiments were performed at Universite de Paris Sud 11 where there are facilities for IRMPD spectroscopy studies. Recently at Memorial University of Newfoundland (MUN) we have built a laboratory to study the structures and energetics of gaseous ions in an FTICR mated to a tunable IR laser. All experiments are conducted by the principal author and co-authors. The experimental and computational data was analysed by the principal author and the first draft of papers was written by the principal author. The final versions of the papers were written with the help of Dr. T. Fridgen. In Chapter 4, the micro-solvated model calculations at the double-hybrid B2P3LYP density functional were performed by Ms. K. Theel and Dr. G. Beran at the University of California, Riverside. Most part of experiments in Chapter 5 were conducted at Bruker (at Billerica) where the principal author was trained by Dr. C. Berg and Dr. M. Easterling to perform BIRD experiments.

Chapter 1

Introduction

1.1 Structural Determination of Gas-phase Ions by Mass Spectrometry

Determining three dimensional (3D) structures can lead to a full understanding of a molecule's chemical properties as in chemistry it is believed that "structure controls function". One or two dimensional information gained from chemical formula and molecular drawing, respectively, may not provide all the necessary information to be able to characterize chemical behaviours whereas by obtaining 3D structures one can fully describe a molecule in terms of its atoms connectivity and their orientation in space as well as its bond length and dihedral angles. Once the structure is known, the chemical behavior of the species can be understood. Protein secondary (2° regularly repeating local structures stabilized by hydrogen bonds) and tertiary (3° the spatial

relationship of the secondary structures to one another) structure has an impact on nutritional quality, fermentation and degradation behavior in both human and mammals.[1] For example, a high percentage of β-sheets usually reduces the access of digestive enzymes to the protein, causing poor digestibility and, as a result, low protein value. Such information is only available from a precise description of the structure.

Mass spectrometry is the leading technique for determining gaseous ion structures. Mass spectrometry has significantly contributed to determining "primary" and "secondary" structures for molecular ions - primary refers to the connectivity of the atoms within the different building blocks of a biological molecule, and secondary refers to the position of the different components in a complex in the general 3D form, respectively.

The development of electrospray ionization (ESI)[2] and matrix-assisted laser desorption/ionization (MALDI)[3] has led to an extensive investigation of biomolecular ions. Noncovalently bound biological complexes such as protein-receptor, enzyme-substrate and multiprotein complexes can be transferred from aqueous solutions to the gas phase by ESI.[4] Noncovalent interactions are generally much weaker than covalent bonds and control the biochemical function of biopolymers by providing them more flexibility to vary their structure. The study of these systems in the gas phase is a promising experimental approach to investigate directly key intermolecular interactions in the absence of solvent perturbation. This is in contrast to the condensed

phase where solvent effects can affect the interactions within a system. Furthermore, the interactions of the ion with solvent in the gas-phase provide information about the preferred coordination of ions by solvent molecules and their conformational changes of geometry upon solvation.[5] In contrast to the solution phase, numerous conformers and isomers can be present in the gas phase.[6] These solvent effects can also be studied through mass spectrometric (MS)-based methods by adding solvent molecules in a selective and stepwise manner (see Chapter 5). The ultimate purpose and challenge for studying the physical properties of sequentially solvated ions is to extrapolate to or contrast these properties with those in the solution phase, especially for biologically relevant molecular systems.

Different mass spectrometric-based methods have been developed for selectively cleaving linkages in biopolymers for sequence information as well as for structural and for thermodynamic determinations. These methods are based on collisional and photochemical activation methods, as well as the employment of neutral reagents to effect chemical transformations in low-energy collisions.[7]

This dissertation is focussed on three goals. The first is elucidation of the structures of small biologically relevant ions such as proton-bound aliphatic amino acid complexes and metal ion-bound/proton-bound DNA nucleic acid base complexes in the gas phase using infrared multiple photon dissociation spectroscopy (IRMPD) and density functional theory (DFT) calculations (Chapters 3 and 4). A second important goal (Chapter 5) is the development of a MS-based technique to produce solvated gas-

phase ions. Finally, in Chapter 6 and 7 this method of solvating ions was successfully applied to produce singly solvated metal ion-bound adenine and [Zn (Thymine-H)]$^+$ systems. IRMPD spectroscopy was used to study the structure of these solvated ions. The conclusions and proposals for future work will be summarized in Chapter 8.

In the following sections of this chapter, different MS-based techniques for structural studies of gaseous ions including collision-induced dissociation (CID), thermochemical methods, and spectroscopic methods will be introduced. IRMPD spectroscopy is the technique used extensively in this research. Experimental and theoretical details of IRMPD will be discussed in more detail in Chapter 2 as well as the computational methods used to assist in analyzing the experimental data.

1.2 Mass Spectrometric-based Techniques for Structural Studies of Gaseous Ions

1.2.1 Collision-Induced/Activated Dissociation (CID/CAD) Methods

Collision-induced dissociation (CID) is a common method used to obtain structural connectivity information by dissociation of the analyte and investigating the resulting ionic fragments.[8–10] In general, mass-selected ions, which are accelerated,

undergo collisions with a noble gas (typically argon) at low pressure. In this method, each ion collides with an inert collision gas atom and, in the case of very low pressures, the collision happens only once, i.e. single-collision conditions. During a collision, a portion of the ion's kinetic energy can be converted into internal energy which causes dissociation. According to the law of conservation of momentum, the kinetic energy of a rapidly moving particle (analyte ions) colliding with a static target (inert collision gas) cannot be entirely converted into internal energy. The maximum kinetic energy converted to internal energy of the ion during a collision with a background gas molecules is given by Equation 1.1,

$$E_{com} = E_{lab}\frac{M_g}{M_g + M_p} \tag{1.1}$$

where E_{com} is the maximum energy fraction converted into internal energy (center of mass collision energy), E_{lab} is the laboratory-frame kinetic energy, M_g and M_p are the mass of the neutral collision gas and the parent ion respectively.[11]

CID is highly dependent on the conditions of the experiment such as instrument configuration, the nature of the inert collision gas and the parent ion, the ion kinetic energy, and the number of collisions occurring during the activation period.[12] In practice, two commonly used regiments for CID of gas-phase ions are based on the ion kinetic energy. These two regiments are low-energy CID with a collision energy of up to 100 eV (1-100 eV) and high-energy CID in the range of several thousand electron volts (keV) of collision energy.

1.2.1.1 Low-energy CID

Low-energy CID is typically conducted in quadrupole/multipole collision cells, ion traps, or ion cyclotron resonance (ICR) mass spectrometers. The collision energy in these instruments is low (under 100 eV) in order to be able to trap and detect the mass-selected ions inside these traps. Due to the low collision energy, the excitation usually occurs in the vibrational levels and leads to the weakest bond cleavage pathways. For instance, in the low-energy CID of bradykinin,[13] side-chain cleavage peaks are absent but they were observed at the keV dissociation CID.[14] One of the advantages of low-energy CID is its high collision yields. i.e. the number of effective collisions leading to dissociation of an ion. This is partly because the selected collision gas pressure allows multiple collisions (tens to hundreds) to occur.

CID can be performed inside the ICR cell by introducing the collision gas into the cell through a pulse valve and at a pressure on the order of 10^{-8} mbar. Traditionaly, fragmentation of ions in the ICR cell was achieved by exciting the ions with a short radio frequency (RF) pulse ($\prec$500 μs) in which the frequency of the RF pulse is on-resonance with the cyclotron frequency of ions(see Chapter 2). Ions are accelerated to the desired kinetic energy and activated by collisions with neutral gas. Since ions collide with the neutral target gas, they lose kinetic energy. Therefore, multiple-collision activation with on-resonance excitationis relatively inefficient. Several alter-

native methods of excitation such as sustained off-resonance irradiation collisionally induced dissociation (SORI- CID)have been developed.[15,16] In this technique, the RF pulse is off-resonance, slightly above or below, with the resonant frequency of the precursor ion, causing ion kinetic energy to oscillate with time. Fragments are produced by increasing the kinetic energy of ions at the same time as the collision gas is pulsed into the ICR cell. Freiser *et al.*[17] first conducted CID of small molecules in a Fourier transform ion cyclotron resonance (FT-ICR) spectrometer. A valuable review on the CID in FT-ICR mass spectrometry has been published by Lifshitz.[18]

CID has been widely used for structural determination and to distinguish between isomers. For example, two isomers of intertwined rotaxane and the non-intertwined (axle-wheel) complex shown in Figure 1.1, are distinguished using CID by their different fragmentation patterns.[19,20] In the CID spectrum of the complex, the major fragmentation pathway is loss of the axle which is not observed in the rotaxane CID spectrum. This can be explained based on their topologies. In rotaxane, the axle is mechanically bonded to the wheel and cleavage of this covalent bond is a high energy pathway. However, in the complex, the axle is connected to the wheel through four hydrogen bonds which can be easily cleaved. Therefore, the intact axle can be released and the evidence is provided by the CID spectrum. These types of experiments are highly interesting from both a fundamental point of view and that of synthetic chemists dealing with these species.

CID is a fast and reliable method for structure elucidation in multi-component

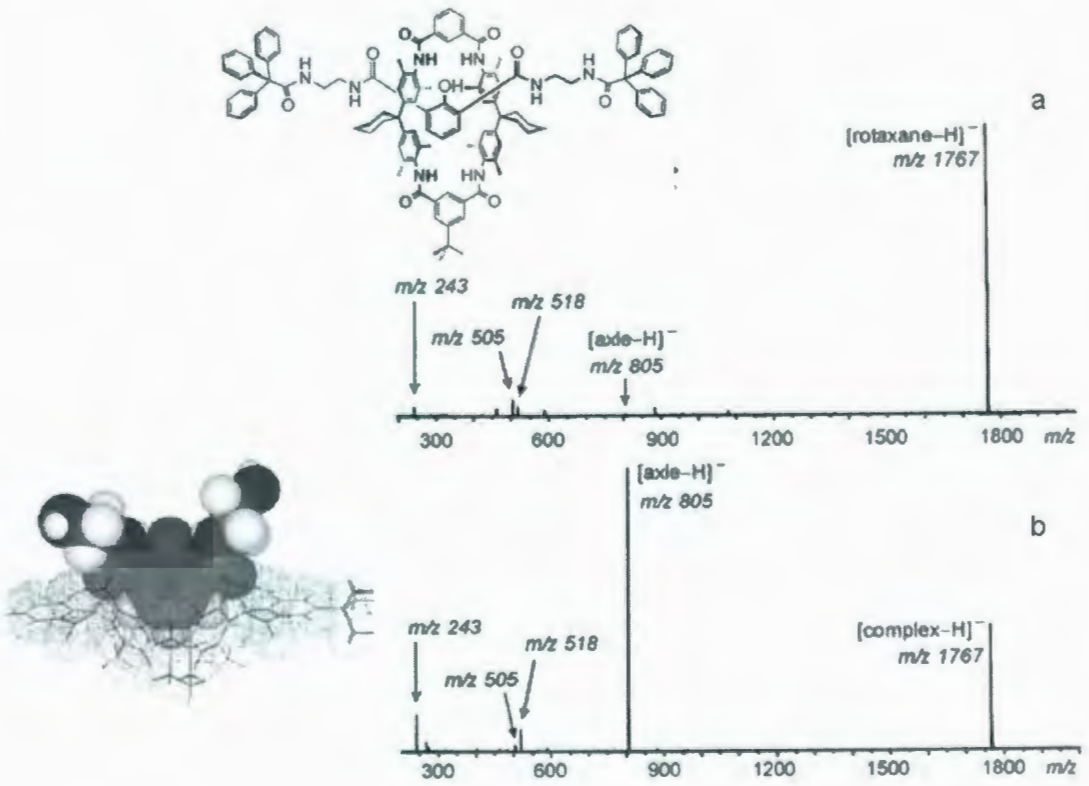

Figure 1.1: CID spectra of a) rotaxane and b) axle-wheel complex when collided with argon. Note that no signal is observed for the deprotonated axle in the rotaxane spectrum while it is prominent among the products generated from the axle-wheel complex. Figure reproduced from Int. J. Mass Spectrom. 2004, 232, 249 with permission from Elsevier.

mixtures without an extensive sample cleanup or separation process. The CID behavior of tetra(aryl)benzidine derivatives is interesting because they contradict the "even electron rule".[21–23] Based on this rule, CID of closed-shell even-electron (EE)

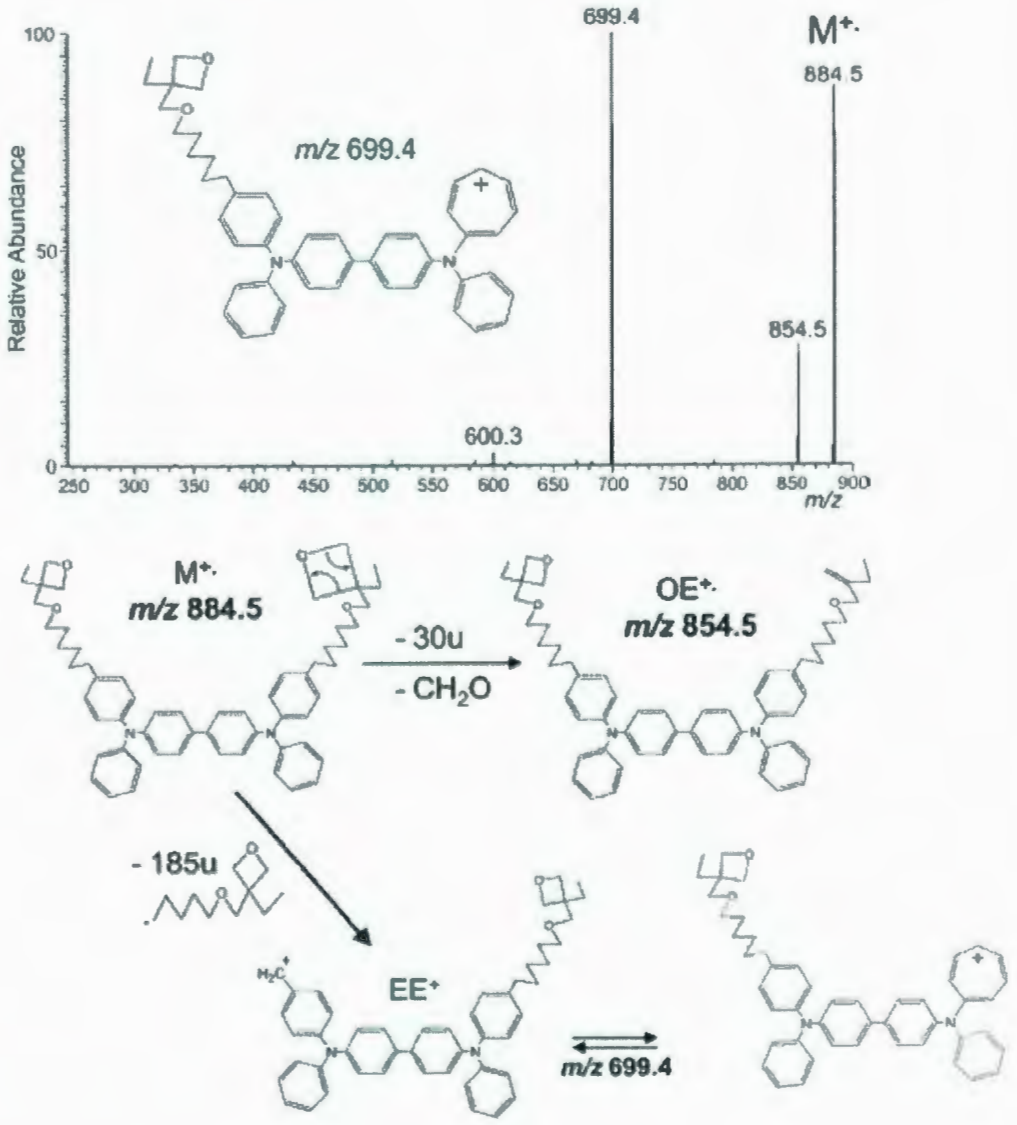

Figure 1.2: ESI-MS^2 of a tetra(aryl)benzidine derivative along with fragmentation reactions of the precursor ion $[M]^{+\bullet}$ at m/z 884.5. Figure reproduced from Eur. J. Org. Chem. 2007, 5162 with permission from John Wiley and Sons Inc.

cations preferentially produce closed-shell product ions and neutral fragments. These compounds are easily oxidizable with $E_{1/2(ox)}$ values distinctively below 1 V (vs. ferrocene). However, in Schafer *et al.*[24] CID experiments, transient odd-electron reaction intermediates were detected which were explained based on the strong ability of compounds with low oxidation potentials to stabilize the corresponding open-shell cations. The ESI-MS/MS (MS^2) spectrum of the radical precursor of one of the derivatives is shown in Figure 1.2. In this Figure, OE represents the odd-electron-number intermediates while EE represents ions with even numbers of electrons.

1.2.1.2 High-energy CID

In high-energy CID, the precursor ion kinetic energies are on the order of several thousand electron volts (keV). Only sector instruments, time-of-flight. or hybrid instruments are practical for such high-energy studies. In this technique, the ions are directed through a higher pressure region of the mass spectrometer called the collision cell. A schematic of a typical three sector instrument of BEE geometry in which B and E refer to magnetic and electrostatic sectors respectively, is shown in Figure 1.3. The desired ion can be separated from all other ions by the magnetic field (B) and directed into the collision cells which are located in the field-free regions to perform CID. The analysis of all ionic dissociation products of the experiment is performed in the electrostatic sector.

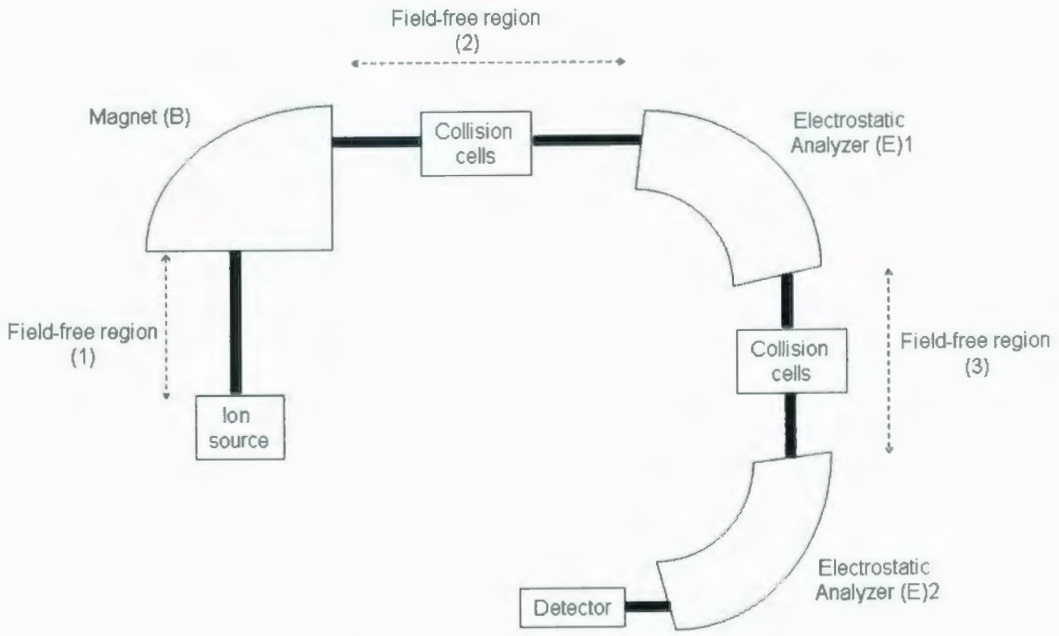

Figure 1.3: Schematic of a typical three sector instrument of BEE geometry.

Wang and Holmes[25] used CID with an ion accelerating voltage of 8keV and helium collision gas to investigate an unexpected composite metastable ion (MI) peak, resulting from the isobaric losses of CO and C_2H_4 ($M^{+\bullet}$-28) from 2,3-pentanedione radical cation. Metastable ions are formed with sufficient excitation to dissociate spontaneously and without collision during its flight from the ion source to the detector. In the MI time frame (10^{-4} to 10^{-6} s), a McLafferty rearrangement[26–28] (see Scheme 1.1) leads to an ethene loss in the 2,3-pentanedione radical cation. However, the presence of a composite peak at ($M^{+\bullet}$-28) shows that there must also be another fragmentation channel (Fig. 1.4). Since this peak consists of a large kinetic energy

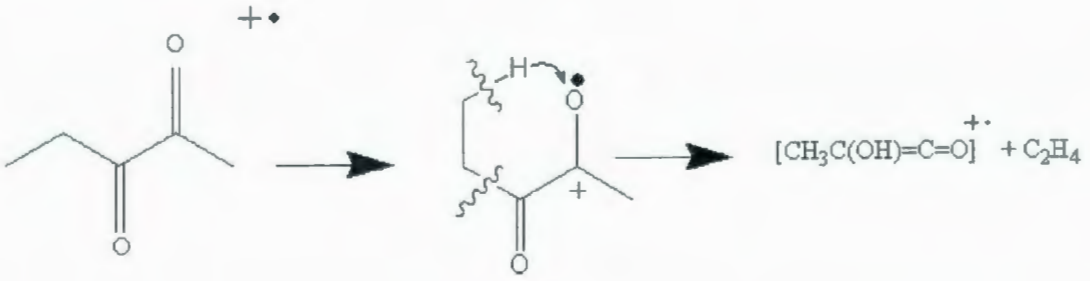

Scheme 1.1

release (KER) (the broad base) section and a small KER section (at the center), the possibility of two competing dissociation pathways was investigated by identifying the structure of each component of the composite peak using a modified VG-ZAB tandem mass spectrometer (Fig. 1.3).[29] Metastable ion and CID mass spectra of the ionized diketone molecules were performed in the second field-free region (FFR) of the mass spectrometer. Using the electrostatic analyzer, each component of the peak was transmitted into the third FFR where a CID spectrum of the fragment ions generated in the second FFR was recorded. In the CID spectrum of the large KER component (Fig. 1.5b). two major products were observed at m/z 13 and 57 which is similar to that of the ionized 2-butanone (Fig. 1.5c). This similarity in the fragmentation spectrum proves that the large KER component arises from the loss of CO from a rearranged, ionized 2,3-pentanedione. The CID spectrum of the small KER component (Fig 1.5a) shows another major fragment at m/z 44 which is absent in the CID spectrum of the 2-butanone ion. This fragmentation was explained based on the McLafferty rearrangement. The carbonyl group at atom 2 of 2,3-pentanedione abstracts a γ-hydrogen from the ethyl group and produces a hydroxyl-substituted

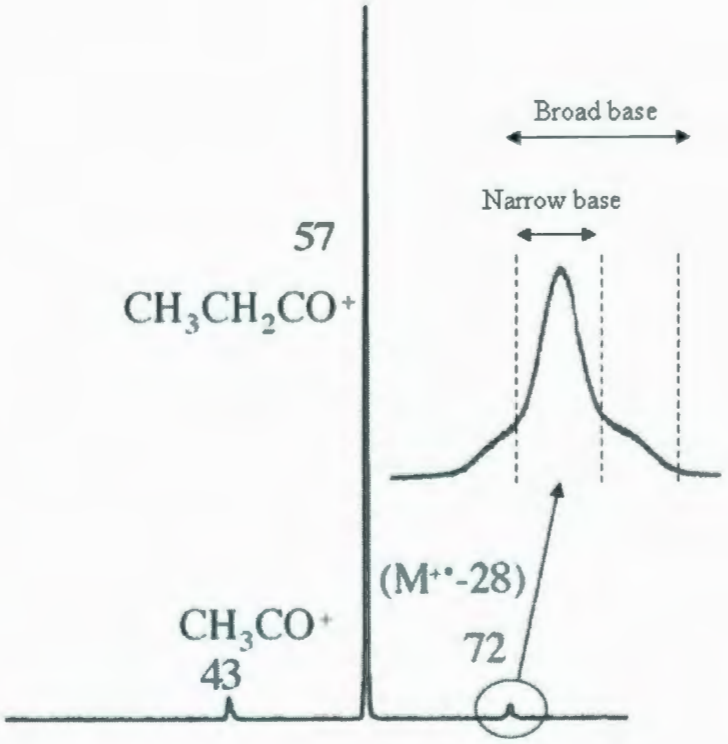

Figure 1.4: Metastable ion (MI) mass spectrum of ionized 2,3-pentanedione. Figure reproduced from Int. J. Mass Spectrom. 2006, 249-250, 222 with permission from Elsevier.

methylketene ion with an m/z of 72 from the intermediate shown in Scheme 1.1. Based on computational data, a small barrier for the cleavage of the α-β bond in the intermediate ion which leads to the formation of ethene is predicted. Therefore, based on the CID spectra, it was concluded that the CO loss results in the large KER part while the small KER slice arises from the loss of C_2H_4.

CID can provide the connectivity of atoms in an ion, but it is not obvious how

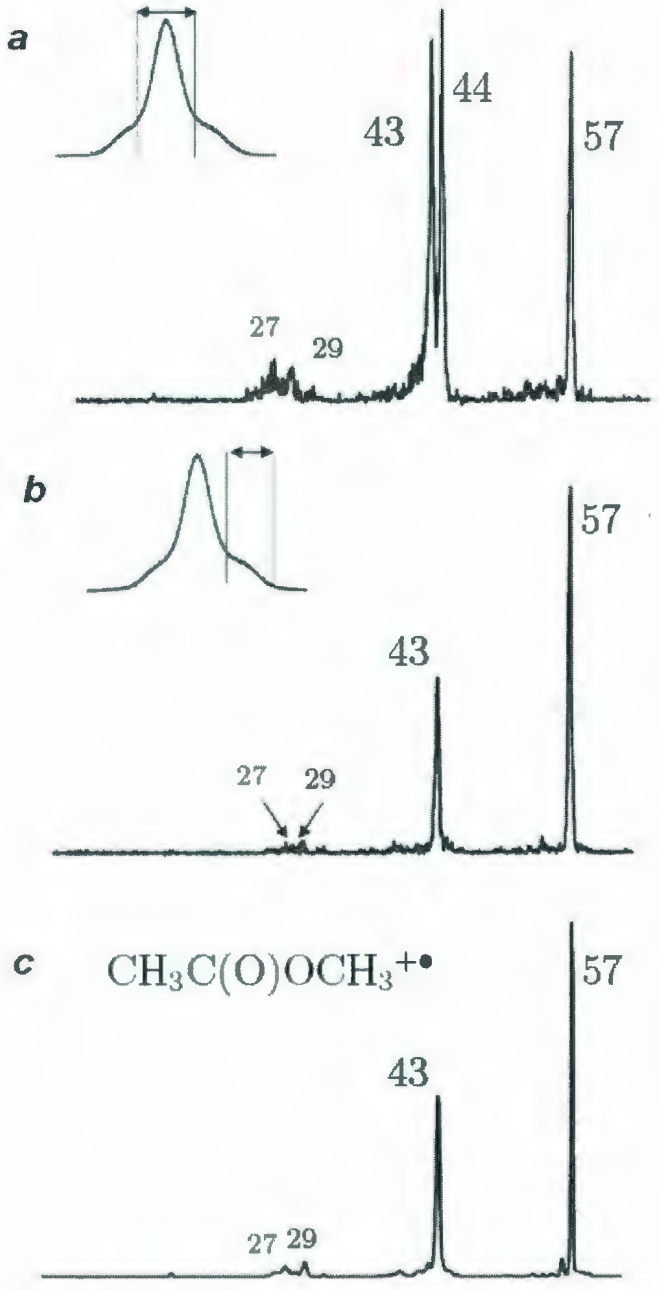

Figure 1.5: CID mass spectra of: (a) the middle, (b) the edge component of the composite $(M-28)^{+\bullet}$ peak and (c) ionized 2-butanone. Figure reproduced from Int. J. Mass Spectrom. 2006, 249-250, 222 with permission from Elsevier.

one would obtain higher order structure information directly from CID data. One of the main limitations of CID is that the energy cannot be completely transferred to the ion. This limits the degree of fragmentation. As well, for large ions with large numbers of degree of freedom, the energy is distributed over the higher number of bonds which slows fragmentation rates. CID of proteins provides information about the primary structures to some extent but it does not necessarily contain information about 2° and 3° structures. In practice, the CID fragmentation technique seems to be insufficient in proteomics.[30] The main reason is that this technique does not necessarily lead to the cleavage of all required bonds to provide full information on the primary structure of a polypeptide.[31] For instance, a variety of factors such as the differences in the proton affinities of backbone amides, steric effects, and interactions between certain amino acid side chains and the backbone amide causes a large preference for cleavage of certain sites while cleavages at other sites are suppressed.[32] Even in cases where all bonds are cleaved, identifying the sequence and its modifications is difficult based on information obtained on the fragment masses.[33] An overlap of the masses of N-terminal and C-terminal fragments in sequencing of polypeptides can cause ambiguity in mass spectral interpretation and peak assignment. Furthermore, possible isomerization and/or rearrangement of molecular ions during CID is another problem that one has to take into consideration when determining ion structure.[10] One example that CID experiments could not address properly is the keto-enol isomerization of methyl acetate ion. Based on the early experiments, both keto $CH_3C(O)OCH_3^{+\bullet}$

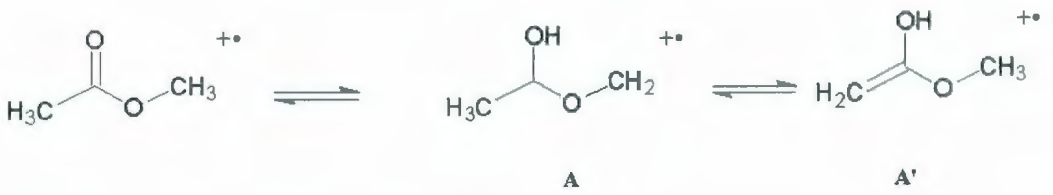

A A'

Scheme 1.2

and enol $CH_2{=}C(OH)OCH_3^{+\bullet}$ isomers fragment by loss of a $[C,H_3,O]^\bullet$ (methoxy radical) exclusively to produce CH_3CO^+. The kinetic energy release for these dissociations were found to be identical for the two isomers, suggesting that the two isomers can interchange without a significant energy barrier.[34] A 1,3-hydrogen shift was then believed to take place in the tautomerization. However, further methoxy deuterium-labeled (CH_3COOCD_3) experiments revealed H/D scrambling since loss of $[C,D_3,O]^\bullet$ was not the only fragmentation channel. Instead a 1,4-hydrogen shift was proposed in which an intermediate results in enol-isomer formation, followed by an H-atom abstraction from the methyl group of the enol-intermediate (A) as shown in Scheme 1.2.[34,35] With this mechanism the H/D scrambling was explained. The case was not closed as more investigations through collisionally induced dissociative ionization (CIDI) showed loss of $^\bullet CH_2OH$ radicals in addition to $CH_3O^\bullet$ occurs during the ionization of methyl acetate.[36–39] In CIDI method, the structure of neutral products from the unimolecular dissociative ionizations of mass selected ions are studied by means of the collisionally induced dissociative ionization of the neutral species themselves. The neutral species, with kilovolt translational energies, enter a posi-

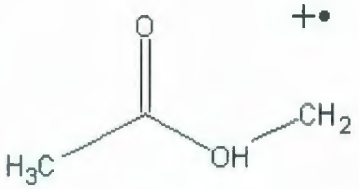

B

Scheme 1.3

tively charged collision cell located in the second field free region of a standard ZAB mass spectrometer. Dissociative ionization of the neutrals results therein from their collisions with He target gas. The resulting ions are analysed by means of the electric sector and the relative ion abundances are shown to be structure characteristic. Burgers *et al.*[40] proposed another intermediate, shown in Scheme 1.3, to be involved in $^{\bullet}CH_2OH$ production. The problem with this new intermediate was that it is difficult to produce this distonic ion independently. Therefore, the ion chemistry experiments could not comprehensively clarify the tautomerization mechanism. Finally, computational chemistry techniques were used to fully understand the mechanism and these will be explained in section 1.3.[41,42]

1.2.2 Thermochemical Methods

1.2.2.1 Threshold Collision Induced Dissociation (TCID)

Threshold collision induced dissociation (TCID) is a modified CID technique. A schematic overview of a guided ion beam tandem mass spectrometer used for TCID experiments is shown in Figure 1.6.[43] Sample vapours are introduced into the ion source at pressures between 0.5-0.8 Torr of helium and are ionized by electron ionization. Ions are mass selected by a magnetic sector and focussed into the octopole ion guide region. CID occurs with an inert gas (usually Xe because of its large M_g in Eq. 1.1) in a collision cell at pressures ranging from 0.05 to 0.2 mTorr surrounded

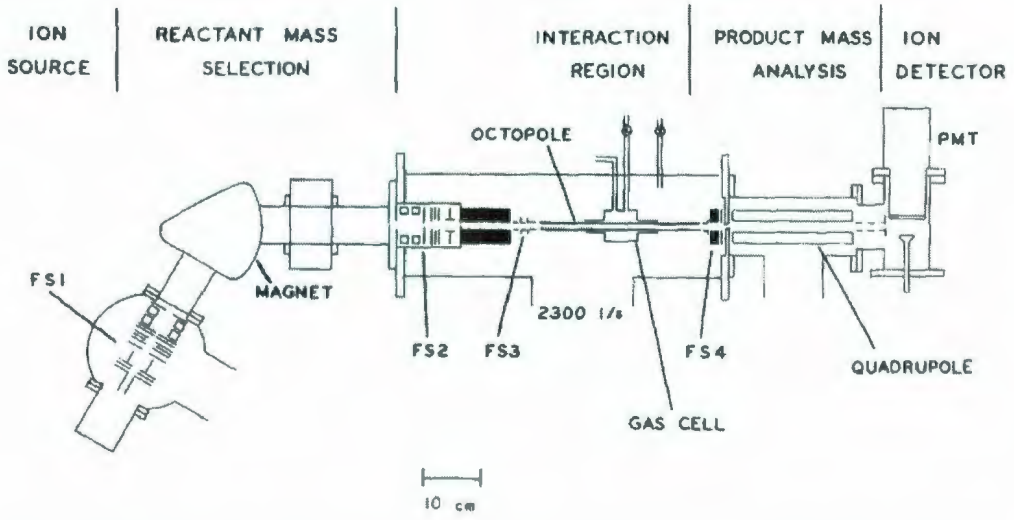

Figure 1.6: Schematic overview of the guided ion beam tandem mass spectrometer. FS represents focusing stages. Figure reproduced from J. Chem. Phys. 1985, 83, 166 with permission from American Institute of Physics.

by an octopole ion guide. All products and unreacted sample ions are guided to a quadrupole mass filter for mass analysis. Reactant and product ion intensities are measured vs the interaction energy and collision gas pressure in the collision cell which can be converted to cross sections. Thermodynamic information from the low-energy TCID can be extracted from the energy dependence of the integral cross sections in the threshold region. Armentrout *et al.*[44] as well as Rodgers *et al.*[45] have focussed their studies on improving the accuracy of thermochemical measurements by TCID.

1.2.2.2 Ion-Molecule (I-M) Reactions

In 1913, Thomson first introduced the idea of gas-phase ion reactions in which ion-neutral interactions are not affected by environment factors such as ion pairing, solvation, and inter-molecular interactions.[46] In ion-molecule (I-M) reactions, a bi-molecular reaction occurs between the reacting ion with minimized internal energy and a neutral molecule. Since the ion's kinetic energy is controlled and kept under the dissociation threshold, the efficiency of the reaction is high with minimal or no ion dissociation. Also, reaction conditions such as pressure, temperature and time can be easily controlled.[47] In a typical I-M reaction, a reactant gas is introduced into the reaction cell and a gas-phase reaction can occur due to the collisions between the ion and the molecule in which the intrinsic properties of charged species along with their chemical reactions can be studied.[48,49] I-M reactions are highly selective and efficient.

Also, I-M reactions are relatively simple with a flexibility to perform the experiments on a variety of ions and neutrals.[50]

I-M reactions can be used to study the structures of proteins and peptides. Two valuable types of I-M reactions are H/D exchange and proton transfer reactions. In H/D exchange, a protonated ion reacts with a deuterated reactant such as D_2O. Upon exchange between the active hydrogens of the ion with deuterium, an increase in the mass-to-charge ratio (m/q or m/z) of the ion occurs. Therefore, some information about the structure of the ion can be concluded based on the mass difference due to deuterium exchange. One application of H/D exchange is to distinguish between folded and unfolded proteins/peptides. In the folded conformer the degree of exchange would be lower since some of the active protons are buried inside the protein. The degree of H/D exchange is higher for the unfolded structure and the rate of H/D exchange is faster because more exchangeable hydrogens are uncovered.[51]

Another key I-M reaction is the gas-phase proton transfer reaction,[52,53] Equation 1.2,

$$AH^+ + B \rightleftharpoons A + BH^+ \tag{1.2}$$

The negative of the free energy (-ΔG) and the enthalpy (-ΔH) are called the gas-phase basicity (GB) and the proton affinity (PA), respectively. "Equilibrium" methods are used to determine relative GB and PA values.

Gross and Williams[54] probed the structure of $(M+H+X)^{+2}$ of gramicidin S (cyclo[-

Pro-Val-Orn-Leu- D-Phe-]$_2$) ions where X=Li, Na, and K using I-M reactions. Ions of gramicidin S were produced by ESI and isolated in the ICR cell where they were reacted with neutral reference bases. Data were fitted to pseudo-first-order kinetics to calculate the rate constants. The apparent gas-phase basicity (GB^{app}) of these ions was assigned a value half-way between the GB of the two bases which bracket the absolute rate constant of 1×10^{-11} cm^3/(mol.s). This assignment is somewhat arbitrary; for example, in this case, a reaction with a rate constant lower than 1×10^{-11} cm^3/(mol.s) was assumed to be "slow" and the GB of the two reference bases with the rate constants on either side of this value (lower and upper) were averaged to find the apparent basicity of the unknown ion. It is possible to obtain the GB^{app} based on the proton transfer rate measurements and according to the simple charge model for multiply protonated ions in which charges are separated by$\geq$10 Å, Equation 1.3,

$$Coulomb\ energy = \sum \frac{q^2}{(4\pi\epsilon_0)\epsilon_r r_{i,t}} \approx GB_{intrinsic}(M) - GB^{app}(M+nH)^{(n-1)+} \quad (1.3)$$

In Equation 1.3, $GB_{intrinsic}$(M) is the gas-phase basicity of a neutral molecule protonated at site t, GB^{app}(M+nH)$^{n+}$ is the apparent gas-phase basicity of the (M+nH)$^{n+}$ ion, ϵ_r (dielectric constant) reflects both the shielding between charges and the potential energy surface of the proton transfer reaction,[55] and $r_{i,t}$ is, the distance between charge centers in (M+H+X)$^{2+}$. Using this method, the distance between charge centers in (M+H+X)$^{2+}$ was determined to be ~11.5 Å. Therefore, information about the ion structure and alkali metal binding sites was obtained in which the alkali metal ion was found at the exterior surface of the peptide. Using molecular mechanics, a

Figure 1.7: Proposed structure of $(M+H+Na)^{2+}$ of gramicidin S (cyclo[-Pro-Val-Orn-Leu- D-Phe-]$_2$) using molecular mechanics in which the Na^+ is attached to the exterior surface of the peptide. Figure reproduced from J. Am. Chem. Soc. 1996, 118, 202 with permission from the American Chemical Society.

structure was proposed for $(M+H+Na)^{2+}$ ion and is shown in Figure 1.7.

1.2.2.3 Pulsed-Electron High Pressure Mass Spectrometry (PHPMS)

Pulsed-electron high pressure mass spectrometry PHPMS (also known as HPMS) is one of the most reliable methods to determine thermochemical values for I-M reactions. In a typical PHPMS experiment, the ion source-reaction chamber contains about 5 Torr of a bath gas (M) such as CH_4 and trace amounts of neutral reactant and precursor to the desired ion. Using a 2keV energy primary electron pulse for a few

μs, the bath gas is ionized by the primary beam producing slow secondary electrons (Equation 1.4).

$$M + e^{-}(1^{\circ}, fast) \longrightarrow M^{+\bullet} + e^{-}(1^{\circ}, fast) + e^{-}(2^{\circ}, slow) \tag{1.4}$$

Some of the slow secondary electrons are captured by the sample, leading to ion formation. At these pressures, ions collide approximately 10^8 times before diffusing out of a small ion exit slit in the wall of the ion source and reaching the detector. This ensures not only thermal equilibrium at the known temperature in the ion source but also chemical equilibrium prior to the ion exiting the source. The ions are captured by electric fields, accelerated, and transferred to the mass analyzer. Measurements of reactant and product ion intensities are taken at various temperatures. The thermodynamic equilibrium constant at a given temperature can also be calculated by taking the ratio of the product to reactant ion intensities, $I_{(P-)}$ and $I_{(R-)}$ respectively, during the period in which the two ions were in equilibrium and dividing by the neutral partial pressures. For example, for ion-solvent molecule equilibria, Equation 1.5,

$$R^{-} + solvent \rightleftharpoons P^{-} \tag{1.5}$$

the thermodynamic equilibrium constant is given by Equation 1.6, where P_0=1 bar and $P_{(solvent)}$ is the partial pressure of the neutral solvent gas,

$$K_{eq} = \frac{I(P^{-})}{I(R^{-}) \times P_{(solvent)}} \times P_0 \tag{1.6}$$

Furthermore, once K_{eq} at various temperatures is measured, the enthalpy and entropy changes for a given equilibrium can be obtained based on the van't Hoff equation,

Equation 1.7,

$$\ln(K_{eq}) = -\frac{\Delta H^{\circ}_{rxn}}{RT} + \frac{\Delta S^{\circ}_{rxn}}{R} \tag{1.7}$$

Based on a comparison of the measured HPMS values with the calculated energetics for a variety of structures, structural information can be obtained. For instance, Nieckarz *et al.*[56] very recently determined the structures of solvated $(ROH)_n...FHF^-$ (n=1,2 and R=H, CH_3, C_2H_5) clusters via HPMS measurements. In these experiments, a mixture of 1 percent NF_3 in CH_4 and the protic solvent (ROH) entered the ion source in the 40-140 °C temperature range. The reactant gas was bombarded with 2keV pulsed electrons to produce the desired anionic product according to equations 1.8 to 1.12,

$$CH_4 + e^-(1^\circ) \longrightarrow CH_3^+ + H^\bullet + e^-(1^\circ) + e^-(2^\circ) \tag{1.8}$$

$$NF_3 + e^-(2^\circ) \longrightarrow F^- + NF_2^\bullet \tag{1.9}$$

$$F_2NF + H^\bullet \longrightarrow HF + NF_2^\bullet \tag{1.10}$$

$$F^- + HF \longrightarrow FHF^- \tag{1.11}$$

$$(ROH)_{n-1}...FHF^- + ROH \Longleftrightarrow (ROH)_n...FHF^- \tag{1.12}$$

The low-energy secondary electrons from Eq. 1.8 combine with NF_3 to produce F^- and finally lead to solvated anions based on the above mechanism. K_{eq} for reaction 1.12 was determined at various temperatures. From the slope and the intercept of a plot of $\ln(K_{eq})$ vs T^{-1} (Eq 1.7) the enthalpy and entropy, respectively, of the clustering reaction Eq. 1.12 can be found. The anion-solvent structures were elucidated

Figure 1.8: Structures and geometric properties of $FHF^{-}...(H_2O)_2$ cluster. Oxygen in red, F in Blue and H in gray color.

by comparing the experimentally measured and calculated thermochemical data for numerous structures. For example, for the doubly hydrated FHF^{-} structure B in Figure 1.8 is the less favoured structure by enthalpy because of forming one less bond compared to structure A but the most favoured entropically. A better agreement between the HPMS measured and calculated ΔG for structure 1.8B shows structure B to be the most thermodynamically favoured isomer even though it is not the lowest energy isomer. In fact in structure 1.8A, more bonds are formed between ion and solvents but it is tighter than B, causing it to be less favoured entropically. This is one example that clarifies the ability of HPMS experiments to distinguish between isomers based on the thermochemical properties.

1.2.2.4 Blackbody Infrared Dissociation (BIRD)

In 1919, Perrin[57] proposed that unimolecular dissociations were activated by absorption of ambient blackbody radiation in the gas phase. Langmuir[58] and Lewis[59] rejected Perrin's hypothesis. The argument was that visible radiation is required for bond dissociation, but some molecules were colorless and could not absorb visible light. Also, there was insufficient energy density of blackbody radiation at visible wavelengths to account for the observed rate of dissociation. At the time, the problem was solved by accepting the Lindemann-Hinshelwood (L-H) mechanism[60] in which non reactive collisions are responsible for exciting molecules as well as de-exciting them in unimolecular dissociation reactions over a wide range of pressure. The L-H mechanism could be represented by a two-step reaction sequence (Equations 1.13 and 1.14). In the first step, A is excited through collisions with surrounding molecules M, and then the excited molecule, A*, dissociates to give products in step two.

$$A + M \underset{k_{-1}}{\overset{k_1}{\rightleftharpoons}} A^* + M \tag{1.13}$$

$$A^* \xrightarrow{k_d} B + C \tag{1.14}$$

According to this mechanism, a rate constant of zero is calculated from extrapolation of thermal reaction rates to zero pressure.[61] However, in 1994 after over 70 years from the acceptance of the L-H mechanism for unimolecular reactions, the first experimental evidence by McMahon *et al.*[62] proved that at pressures below $\sim 10^{-8}$ Torr,

dissociation rates of weakly bound cluster ions, stored in a FT-ICR, were independent of pressure. Furthermore, the rate constants could not be accounted for by the collision mechanism as the pressure was too low. Because of such low pressures, the method was termed zero-pressure thermal radiatively induced dissociation (ZTRID). At low pressures, dissociation of ions occur by absorbing the blackbody radiation from the instrument walls. The new mechanism, at very low pressure, is shown by Equations 1.15 and 1.16,

$$A + h\nu \underset{k_{em}}{\overset{k_{abs}}{\rightleftharpoons}} A^* \tag{1.15}$$

$$A^* \xrightarrow{k_d} B + C \tag{1.16}$$

where hν is a photon. This mechanism was previously proposed by Dunbar[63] for infrared photodissociation of ions by low intensity continuous wave (CW) CO_2 laser radiation.

Using BIRD experiments and by varying the wall temperature, the activation energy and the pre exponential factor can be determined based on an Arrhenius plot of ln (k_{diss}) vs (1/T). The slope of this plot is -E_a/R where R is the gas constant and E_a is the activation energy for dissociation. Williams[61,64] and Klassen[65] have dedicated a significant amount of work to BIRD experiments. Klassen and his group have developed and become experts in a combinatory approach using both BIRD thermal dissociation and functional group replacement (BIRD/FGR) to probe the interactions within gaseous biological complexes.[66]

Wong and Williams[67] studied the dissociation pathways of $SO_4^{2-}(H_2O)_n$ clusters for n=3-17 by ESI FT-ICR at room temperature (~21 °C) and at a base pressure in the ion cell of 5×10^{-10} Torr, using BIRD experiments. Solutions of 1×10^{-4} M $MgSO_4$ in water/methanol solvent were introduced to the mass spectrometer by nanoelectrospray under gentle source and ion introduction conditions to promote transmission of the solvated ions. Hydrated anions with 3-17 water molecules were selected and thermalised in the accumulation process by introducing N_2 gas. $SO_4^{2-}(H_2O)_n$ clus-

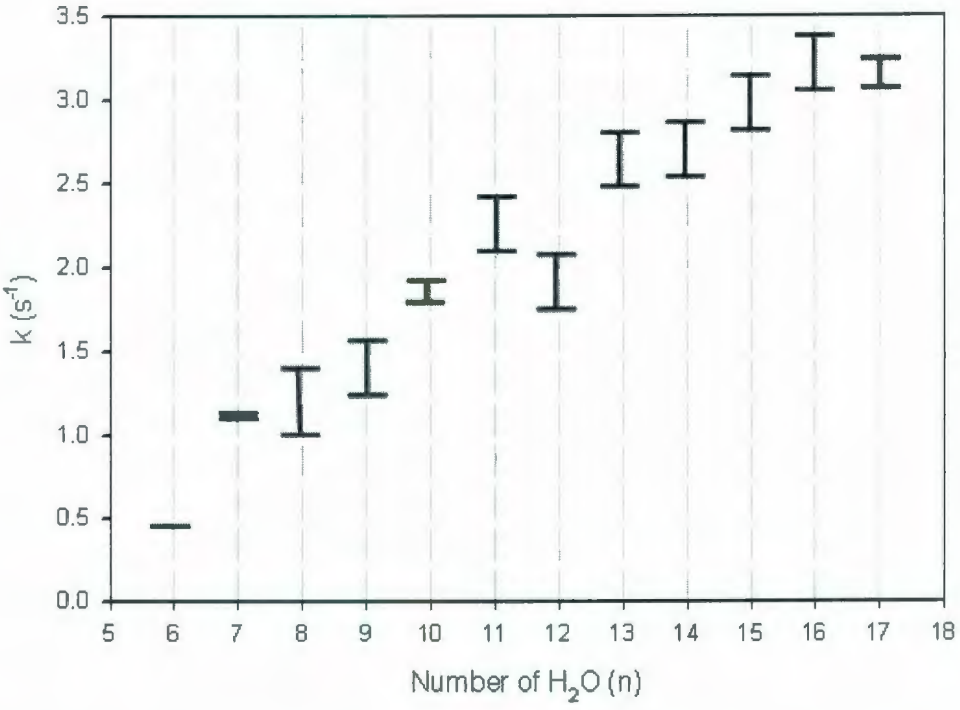

Figure 1.9: Rate constant for loss of a water molecule from $SO_4^{2-}(H_2O)_n$, n=6-17, with BIRD at 21 °C as a function of n. The error bars represent 1 standard deviation of the measured rate constant.

ters with n=6-17 were individually isolated in the ICR and dissociation pathways for loss of a water molecule from the isolated cluster by BIRD were obtained. From the relative intensity vs time plots, rate constants were measured. Dehydration rate constants for $n \leq 5$ could not be obtained since charge separation was the dominant dissociation pathway. As shown in Figure 1.9, an overall increase in the rate of dehydration with increasing number of water molecules in the clusters was observed which is consistent with the lower binding energy and larger IR absorption cross section with increasing cluster size. However, a smaller rate constant at n=12 compared to either n=11 or n=13 was observed which could be because of a stronger water binding interaction for this ion. Based on the experimental observations at n=7 and n=12 and molecular mechanics two water molecules were found in the second solvation shell for the lowest energy structure of this cluster (Fig. 1.10a). In addition, a sudden rate constant increase for n=7 shows a weaker bond between the seventh water molecule and the n=6 hydrated cluster ion. This shows a disruption in the stable arrangement of water molecules at n=6 which could be because the seventh water molecule enters in the second solvation shell in which it could not form a direct hydrogen bond with SO_4^{2-}. For $SO_4^{2-}(H_2O)_6$, a structure was proposed (Figure 1.10b) in which the first solvation shell is filled with six water molecules and each water bonds to the sulphate through two hydrogen bonds.

The thermal equilibrium time of the ICR cell can be significantly long. To change the temperature, the region of the vacuum chamber surrounding the ions has to be

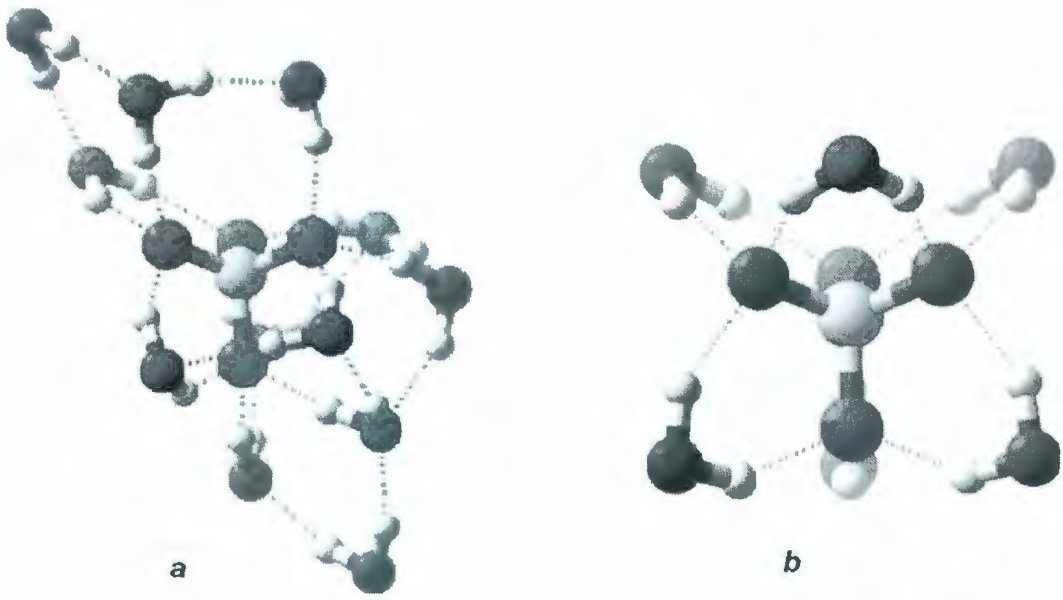

Figure 1.10: Molecular mechanics lowest energy structures of (a) $SO_4^{2-}(H_2O)_{12}$ and (b) $SO_4^{2-}(H_2O)_6$. Figure reproduced from J. Phys. Chem. A 2003, 107, 10976 with permission from American Chemical Society.

changed since the source of blackbody is the vacuum chamber of the FT-ICR mass spectrometer. To set the temperature can take as long as 10 hours. Also, the desired temperature has to be maintained during the experiments.[68,69] One of the disadvantages of BIRD experiments is that the useful temperature range of the experiment is limited because vacuum chamber temperatures above 200 °C could result in increased superconducting magnet dewar cryogen boil-off as well as increased base pressure. Therefore, only weak bonds such as noncovalent interactions can be investigated using BIRD experiments.

1.2.3 Spectroscopic Methods

CID and thermochemical methods are very useful in determining ion structures although they can be less direct than spectroscopic methods, in particular IR spectroscopy. In spectroscopy the interaction of chemical species with light is investigated. Since atoms and molecules only exist in discrete energy states, the amount of energy required to change a state is exactly equal to the difference in energy between the states.[70] IR spectroscopy is able to reveal a great deal of structural information. As well, it is very sensitive such that even the smallest changes in chemical environment will be reflected in the vibrational modes of the ion or molecule.[71] One way to investigate the species is to directly measure the light absorption or emission at different wavelengths. One alternative approach is to measure another property which is a consequence of light absorption. Three IR spectroscopic methods used to obtain ion vibrational spectra based on these two approaches will now be discussed: matrix isolation, vibrational pre-dissociation, and infrared multiple photon dissociation spectroscopy.

1.2.3.1 Matrix Isolation (MI) Spectroscopy

Matrix isolation spectroscopy has been well reviewed[72–74] and has been the topic of books[75–77]. Matrix isolation includes a range of experimental techniques in which trapped guest molecules in rigid host materials are investigated (Figure 1.11). Crystalline solids, polymers, or glasses formed by freezing liquids or gases are common

materials used as hosts. George Pimentel *et al.*[78] introduced solidified noble gases as trapping media for non-stable species because of their chemical inertness, transparency in the IR, visible, and ultraviolet regions of the electromagnetic spectrum, and their tendency to form transparent glasses. They also indicated that the ratio M/A (the mole ratio of the matrix to active substance) should be 100 or greater for successful isolation (e.g. for a xenon matrix at 66K). Although there were some restrictions in the Pimentel *et al.*[78] experiment, the inventive idea and its application resulted in significant advances in the matrix isolation technique and 1954 was considered as the "Anno Domini"[75] of matrix isolation.

Matrices are formed by deposition from the gas phase onto a cold window. As a result, the analyte must be volatile at a temperature below its decomposition point, at least to a small extent, to conduct matrix isolation experiments. Matrix isolation can also be used for guests of low volatility using a side-arm attached to the vac-

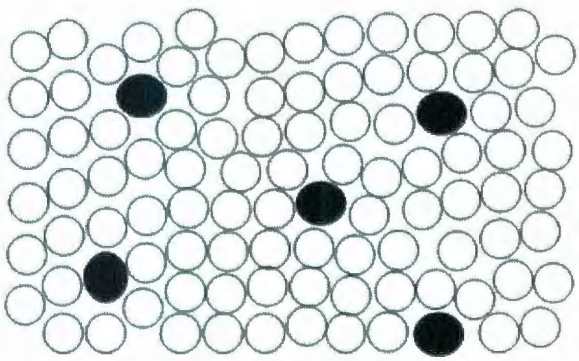

Figure 1.11: Isolation of molecules of a reactive species (black circles) by a rigid host lattice (shown as open circles).

uum chamber of the cold cell while the host gas is deposited simultaneously. After preparing a nice crystalline solid on a cold window, the guest can be investigated with spectroscopic methods such as IR, NMR, UV-Vis, or ESR.

If the spectroscopic method is IR, matrix isolation vibrational bands are very sharp since the rigid matrix does not allow for rotations at cryogenic temperatures. Also, a basic rule of thumb in matrix isolation is that bands which grow together at the same rate and diminish together at the same rate belong to the same species. This is very useful for assigning IR bands to a specific chemical species. Another common technique in IR spectroscopy of cryogenic ions is annealing the matrix i.e. warming the matrix to a softening point. This allows the guest species to diffuse to a certain extent and rearrange within the matrix host.

Ma and coworkers[79] recorded the IR spectrum of nitrobenzene anion in solid argon from 400 to 4000 cm^{-1}. The nitrobenzene anion was produced by high-frequency discharge combined with matrix isolation. A high-frequency generator (Tesla coil with a voltage alteration of 0 to 9 kV and frequency of 10 to 15 kHz) was used to discharge a pure argon gas stream. The resulting beam was mixed with the nitrobenzene/Ar (0.05-0.1 percent of sample in Ar) and the mixture was co-deposited on the surface of a cryogenic (4K) CsI window for 1h at a rate of ~5mmol/h. This window was cooled by a helium refrigerator. The IR spectra for isotopically substituted nitrobenzene anions such as $C_6H_5{}^{15}NO_2{}^-$ and $C_5D_5NO_2{}^-$ isolated in solid Ar were also measured using the same method. Based on deuterium and ^{15}N shifts and theoretical frequency

calculations, observed absorption bands were assigned to different vibrational modes and a planar C_{2v} structure was proposed for $C_5H_5NO_2^-$. A longer N-O bond compared to the neutral nitrobenzene was found in this structure which is in agreement with the observed red shift of the N-O stretch vibration.

One of the limitations of matrix isolation spectroscopy is that the environment can perturb the ion thorough noncovalanet interactions and result in large shifts in the IR spectra of the measured ions. Also, another common problem in matrix isolation is the generation of several reactive species rather than just one. The latter problem has been solved to some extent with the development of mass spectrometry-matrix isolation (MS-MI) technique.[80] This technique benefits from mass spectrometry's ability to select the desired ions and then applies matrix isolation spectroscopy to record the spectrum. The schematic of the instrument is shown in Figure 1.12. The ions are generated in the ion source with one of the common mass spectrometric ionization methods such as electron impact (EI). The ions of interest are mass selected by a quadrupole mass spectrometer. Subsequently, a mixture of the ions and the host gas (i.e. Ne) are prepared and are deposited onto a cold window at cryogenic temperatures ($\sim$5K) for a couple of hours to produce a thick matrix. This matrix is then subjected to spectroscopic methods such as IR to record the spectrum.

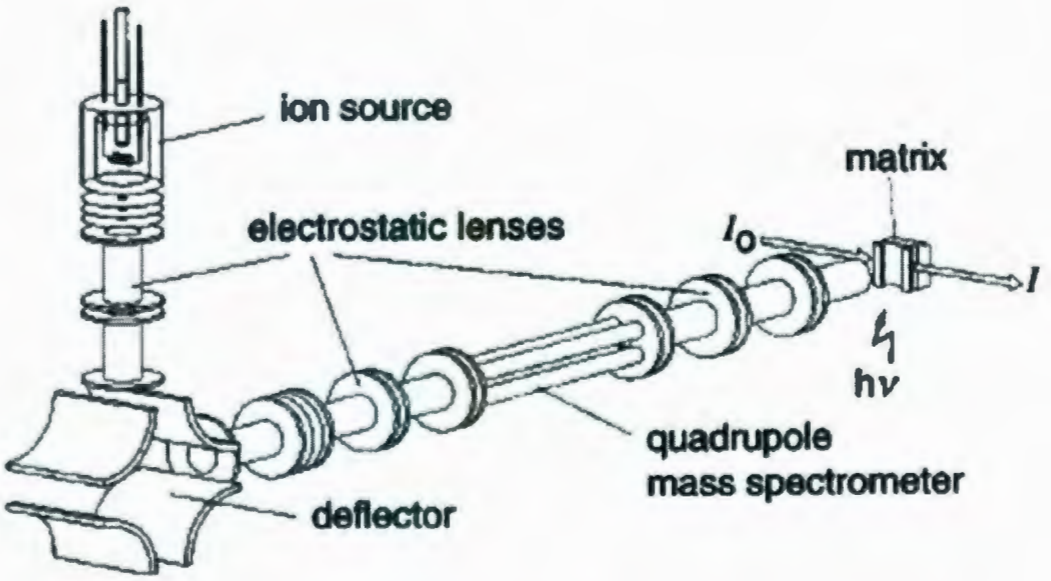

Figure 1.12: Schematic layout of MS-MI instrument. Figure reproduced from J. Phys. Chem. A 1998, 102, 3462 with permission from American Chemical Society.

1.2.3.2 Vibrational Pre-Dissociation (VPD)

IR spectroscopy of gaseous ions is difficult because of the difficulty of obtaining a high enough density of ions of a known mass in a small volume to yield a measurable absorbance and record reliable spectra. Therefore, an indirect method, such as photodissociation of the ion using a high-intensity tunable laser, known as consequence spectroscopy, is required to record the spectra and obtain structural information for gaseous ions. Lee and coworkers played a crucial role in the development of gas-phase ion spectroscopy[81] using a technique called vibrational pre-dissociation spectroscopy. The elegant concept behind the idea was that the consequence of infrared photon ab-

sorption was detected rather than the absorption of the infrared photon itself. Based on this concept, a "messenger" technique was developed in which the molecular ion is tagged with a rare gas atom (or a small molecule) and the detachment of the weakly bound atom/molecule from the molecular ion is detected as a sign of photon absorption. In this technique, a single photon is usually enough to cause dissociation as a weakly bound van der Waals atom is removed from the complex. This method was used[82] to record the IR spectrum for weakly bound naphthalene-Ar van der Waals cluster cations in the 400-1600 cm^{-1} range.

One of the limitations of this technique, similar to the matrix isolation technique, is that the messenger atom/molecule can perturb the vibrational modes. It was found that the lower the binding energy of the messenger atom, the less the structure of the ion is affected by it.[83] However, due to the perturbation of the symmetry of the system, the spectroscopic selection rules are affected. Therefore, the spectrum changes regardless of the nature of the messenger atom.[84] For example, the effect of different messenger atoms, Ar and Ne, on the VPD spectra of water proton-bound dimer is depicted in Figure 1.13. The symmetric (ν_s) and asymmetric (ν_a) absorption bands for Ne-tagged water proton-bound dimer (Figure 1.13b) are marginally shifted compared to the proton-bound dimer water. However, in the Ar-tagged spectrum, not only are the shifts higher but also the bands split as shown in Figure 1.13a with ${\nu_s}^{Ar}$ and ${\nu_a}^{Ar}$ labels. The band splitting reflects the strong interaction of Ar atom with one of the OH groups in the water proton-bound dimer system. Therefore, in

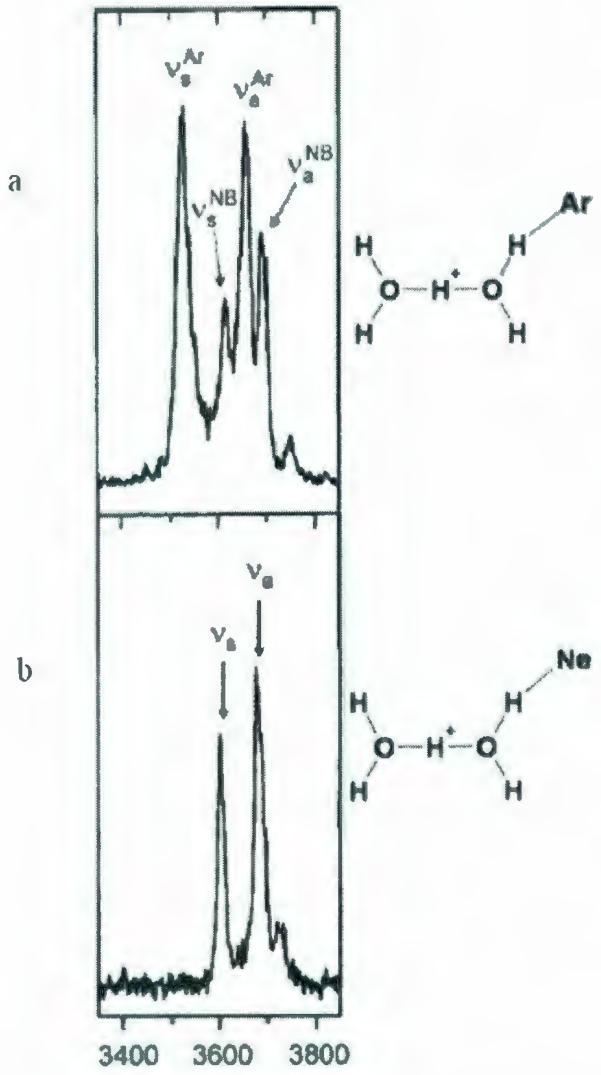

Figure 1.13: Vibrational predissociation spectra of water proton-bound dimer tagged with Ar (a) and Ne (b) messenger atoms. NB corresponds to non-bonded. Figure is reproduced from Science 2005, 308, 1765 with permission from The American Association for the Advancement of Science and J. Chem. Phys. 2005, 122, 244301 with permission from American Institute of Physics.

the spectrum of water proton-bound dimer, four bands were observed including the symmetric($\nu_s{}^{NB}$) and asymmetric ($\nu_a{}^{NB}$) free water absorptions as well as bonded symmetric Ar...O-H ($\nu_s{}^{Ar}$) and asymmetric Ar...O-H ($\nu_a{}^{Ar}$) vibrations.

1.2.3.3 Infrared Multiple Photon Dissociation (IRMPD)

To eliminate the need for tagging, a higher intensity laser system has been used to obtain structural information for gaseous ions. Gaseous ions can be trapped inside an ion trap and irradiated with an infrared laser through a window. If the incoming radiation is in resonance with the vibrational levels of the precursor ion, many photons will be absorbed and eventually cause fragmentation of the precursor ion. Since usually more than one IR photon is required to break a bond in a typical ion, this technique is called infrared multiple photon dissociation (IRMPD). The intensities of precursor and fragment ion as a function of wavelength is measured to obtain a vibrational spectrum. The amount of the internal energy deposited into the ion depends on the absorption cross section of the ion at a particular wavelength.[85] Since this technique was used in my research for structural determination of gaseous ions, more details on theory and instrumentation of IRMPD will be given in Chapter 2.

It is also important to mention about another practical technique which has been used for ion structure characterization, ion mobility mass spectrometry.[86,87] The mobility of a gas-phase ion is a measure of how rapidly it moves through a buffer gas

under the influence of an electric field. The mobility depends on the average collision cross section, which is related to the geometry. The general procedure for ion mobility mass spectroscopy with a time-of-flight analyser is to vaporize a sample and introduce it into the ion source. Ions are injected into the drift tube filled with an inert gas such as helium by low voltage where they thermalize through collisions with the inert gas(see Figure 1.14). By applying an electric field. ions are made to drift through an elevated pressure region. The drift velocities of the bunches of ions which are feeling the electric field of the drift region are determined. Finally, the ions are detected through displaying of the electrical signal. The low-energy collision between sample ions and inert gas decelerate larger ions more than smaller ions. The distributions of arrival time at the end of the drift tube can be related to the collision cross-section which provides information about an ion size, shape and gas-phase conformations. The experimentally measured cross sections are compared with calculated ones for low-energy structures to find the best match to the experimental values.

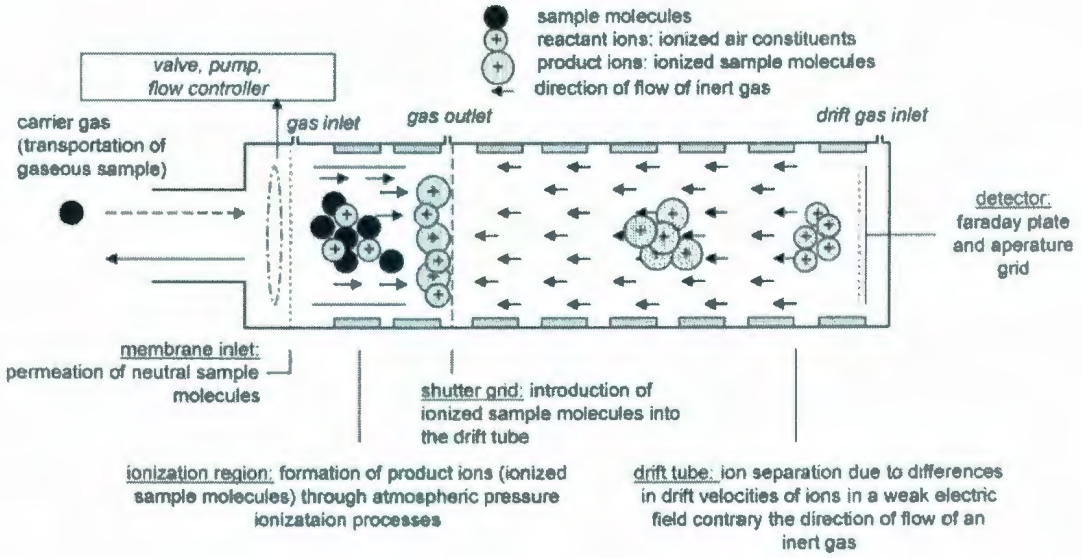

Figure 1.14: An ion mobility spectrometer with a traditional time-of-flight. Figure is reproduced from Appl. Spectrosc. Rev. 2006, 41, 323 with permission from Taylor and Francis.

1.3 Computational Chemistry to Determine Ion Structure

Computational chemistry is complementary to experimental methods in ion structure determination. A complete potential energy surface of an ion's reactions can be obtained by using computational techniques. The three main outputs of computational chemistry include geometry optimization, vibrational frequency calculations and ion thermochemistry.

Computational methods have been used to explain and understand some unconventional ion structures such as distonic ions whose existence were first considered by Morton and Beauchamp.[88] In distonic ions, the radical and ionic sites are located at different atoms of the species. For example, for many years, a fragmentation peak at mass-to-charge ratio of 32 had been assigned to the connectivity pattern of the methanol radical cation, i.e. $CH_3OH^{+\bullet}$. However, Holmes and Lossing[89] experimentally observed $[CH_2OH_2]^{+\bullet}$ and related stable gas-phase ion-dipole complexes. Radom's group[90–92] showed that methyleneoxonium radial cation isomer, $^{\bullet}CH_2{}^{+}OH_2$ with separated radical and charged centers, is in fact 28.6 kJ mol^{-1} lower in energy relative to the conventional ionized methanol radical (Figure 1.15) at 0 K. A barrier of 108 kJ mol^{-1} is calculated for the interconversion of $CH_3OH^{+\bullet}$ and the thermodynamically more stable distonic ion isomer.

Computational chemistry shed some light on another mysterious case, the keto-

enol isomerization of ionized methyl acetate which was discussed in Section 1.2.1. As explained before, in addition to methoxy radicals, $^{\bullet}CH_2OH$ radicals were also lost in the experiment. Intermediate B in Scheme 1.3 was first believed to be responsible for formation of $^{\bullet}CH_2OH$. However, later it was found that intermediate B cannot be formed independently and, consequently, formation of $^{\bullet}CH_2OH$ from this intermediate could not be concluded. This issue could not be resolved with the experimental

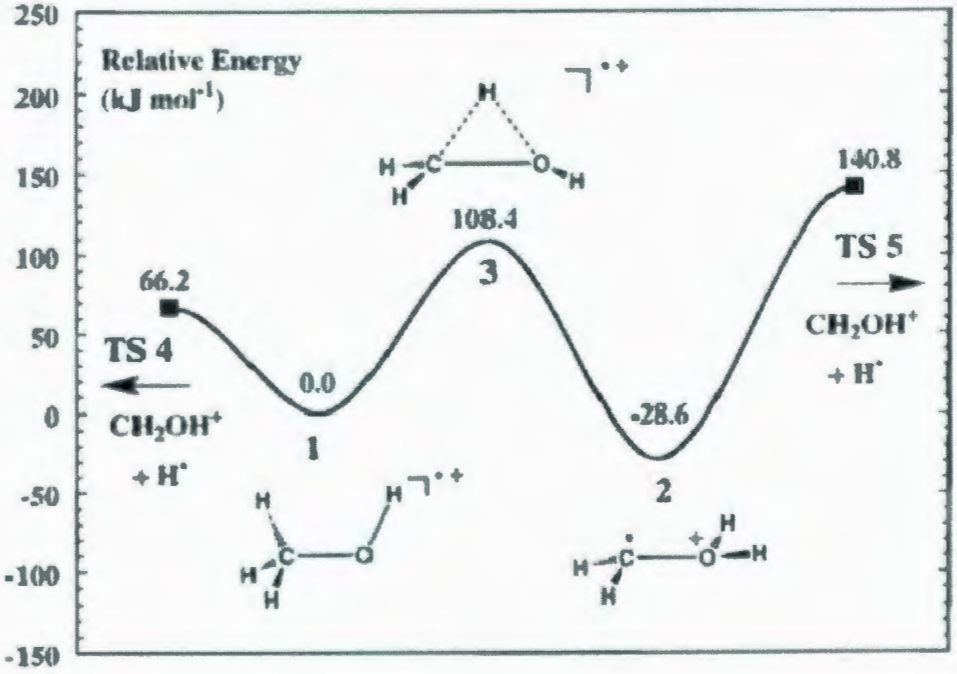

Figure 1.15: Energy profile for interconversion of the $CH_3OH^{+\bullet}$(1) and $^{\bullet}CH_2{}^{+}OH_2$(2) showing their relative stabilities (0K, modified G2). Figure is reproduced from J. Am. Chem. Soc. 1996, 118, 6299 with permission from American Chemical Society.

techniques. Finally, with the use of computational chemistry at the HF/3-21G(d) the two intermediates in Scheme 1.2 were found to be connected and the interconversion between the two was calculated to take only microseconds. However, the potential energy surface did not provide any evidence for the formation of $^{\bullet}CH_2OH$ from $H_2C{=}C(OH)O\text{-}CH_3^{+\bullet}$. With further effort, ion-molecule complex C shown in Scheme 1.4, was found. This intermediate is calculated to be 3 kJ mol^{-1} lower in energy than

$$[H_3CCO...H...OCH_2]^{+\bullet}$$

Scheme 1.4

the methyl acetate ion and interestingly it is connected to intermediate A. Intermediate C leads to the formation of more favoured $^{\bullet}CH_2OH$ and CH_3CO^+ which is a thermodynamically 35 kJ mol^{-1} lower energy pathway compared to CH_3CO^+ and $CH_3O^{\bullet}$ production. The potential energy diagram for the dissociation is shown in Scheme 1.5 illustrates the mechanism. Intermediate $H_2C{=}C(OH)O\text{-}CH_3^{+\bullet}$ (A' in Scheme 1.2) is also shown in the potential energy pathway, is 84 kJ mol^{-1} lower than methyl acetate ion. However, this intermediate does not lead to neither $^{\bullet}CH_2OH$ nor CH_3CO^+ production because it is connected to the product through the intermediate A. Producing $^{\bullet}CH_2OH$ from A' requires a 1,3-H shift which needs a 102 kJ mol^{-1} energy barrier. A hydrogen shift from the hydroxyl group is entropy unfavoured since a tight transition state has to be formed. This energy barrier is too high and therefore formation of $^{\bullet}CH_2OH$ is very unlikely. Formation of C from A is the most favoured

path, resulting in production of $^{\bullet}CH_2OH$.

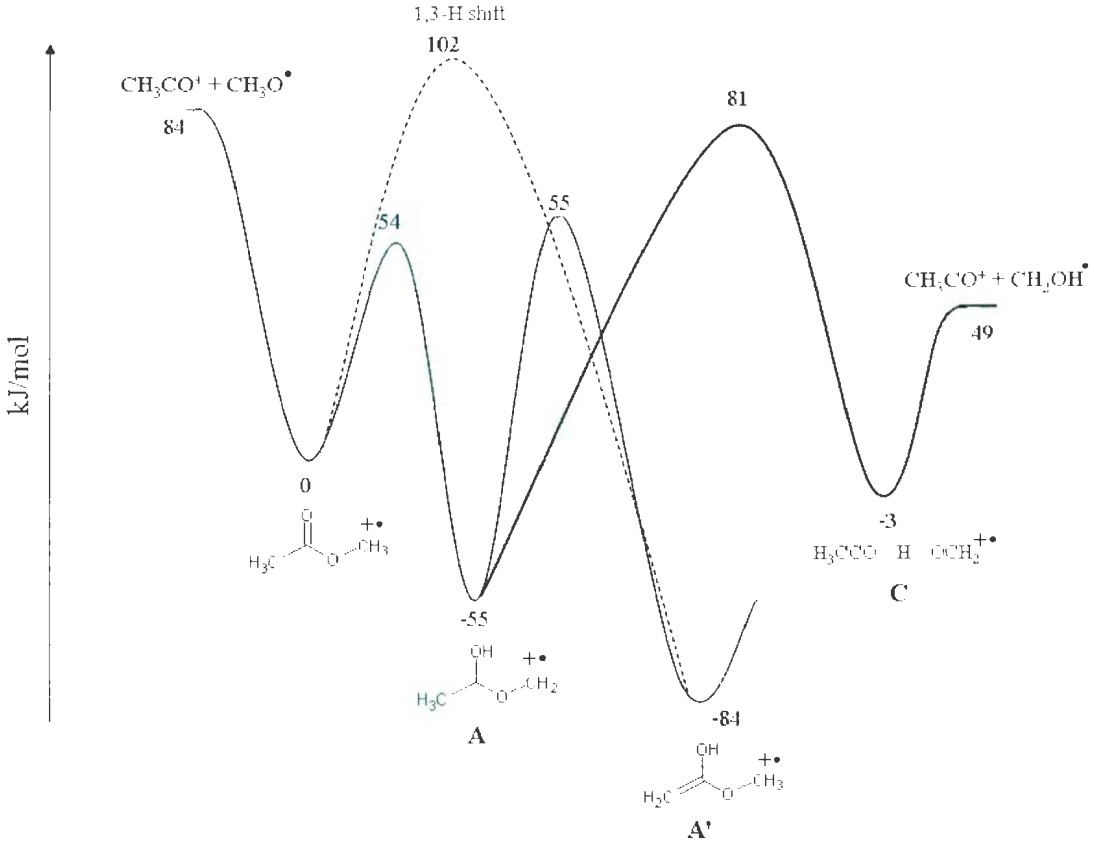

Scheme 1.5

Bibliography

1. Yu, P.; Jonker, A.; Gruberb, M. *Spectrochimica Acta Part A* **2009**, *73*, 846.
2. Fenn, J. B.; Mann, M.; Meng, C. K.; Wong, S. F.; and Whitehouse, C. M. Science **1989**, *246 (4926)*, 67.
3. Karas, M.; Hillenkamp, F. *Anal. Chem.* **1988**, *60*, 2299.
4. Wang, W.; Kitova, E. N.; Sun, J.; Klassen, J. S. *J. Am. Soc. Mass. Spectrom.* **2005**, *16*, 1583.
5. Desfrancois, C.; Carles, S.; Schermann, J. P. *Chem. Rev.* **2000**, *100*, 3943.
6. Ruotolo, B. T.; Giles, K.; Campuzano, I.; Sandercock, A. M.; Bateman, R. H.; Robinson, C. V. *Science* **2005**, *310*, 1658.
7. Rodgers, M. T.; Campbell, S.; Marzluff, E. M.; Beauchamp, J. L. *Int. J. Mass Spectrom. Ion Processes* **1995**, *148*, 1.
8. Douglas, D. J. *J. Phys. Chem.* **1982**, *86*, 185.
9. McLuckey, S. A. *J. Am. Soc. Mass Spectrom.* **1992**, *3*, 599.
10. Shukla, A. K.; Futrell, J. H. *J. Mass Spectrom.* **2000**, *35*, 1069.
11. de Hoffmann, E.; Stroobant, V. *Mass pectrometry, Principles and applications*, 3rd edition, **2007**, John Wily & Sons, Ltd, Chapter 4.
12. Wells, J. M.; McLuckey, S. A. *Methods Enzymol.* **2005**, *402*, 148.
13. Tang, X.; Thibault, P.; Boyd, R. K. *Anal. Chem.* **1993**, *65*, 2824.
14. Downard, K. M.; Biemann, K. *J. Am. Soc. Mass Spectrom.* **1994**, *5*, 966.
15. Heck, A. J. R.; de Koning, L. J.; Pinkse, F. A.; Nibbering, N. M. M. *Rapid Commun.*

Mass Spectrom. **1991**, *5*, 406.

16. Gauthier, J. W.; Trautman, T. R.; Jacobson, D. B. *Anal. Chim. Acta* **1991**, *246*, 211.
17. Cody, R. B.; Freiser, B. S. *Int. J. Mass Spectrom. Ion Phys.* **1982**, *41*, 199.
18. Lifshitz, C. *Mass Spectrom. Rev.* **2003**, *22*, 158.
19. Schalley, C. A.; Ghosh, P.; Engeser, M. *Int. J. Mass. Spectrom.* **2004**, *232*, 249.
20. Baytekin, B.; Baytekin, H. T.; and Schalley, C. A. *Org. Biomol. Chem.* **2006**, *4*, 2825.
21. Levsen, K. *Progress in Mass Spectrometry*, vol. *4* (Ed.: H. Budzikiewicz), Verlag Chemie, Weinheim, New York, **1978**, 152.
22. M. Karni, A. Mandelbaum, *Org. Mass. Spectrom.* **1980**, *15*, 53.
23. W. Wagner, H. Heimbach, K. Levsen, *Int. J. Mass. Spectrom. Ion Phys.* **1980**, *36*, 125.
24. Schäfer, M.; Drayß, M.; Springer, A.; Zacharias, P.; Meerholz, K. *Eur. J. Org. Chem.* **2007**, 5162.
25. Wang, X.; Holmes, J. L. *Int. J. Mass Spectrom.* **2006**, *249-250*, 222.
26. Nicholson, A. J. C. *Trans. Faraday Soc.* **1954**, *50*, 1067.
27. McLafferty, F. W. *Anal. Chem.* **1956**, *28*, 306.
28. McLafferty, F. W.; Hamming, M. C. *Chem. Ind. (Lond.)* **1958**, 1366.
29. Holmes, J. L.; Mayer, P. M. *J. Phys. Chem.* **1995**, *99*, 1366.
30. Zubarev, R. A. *Expert Rev. Proteomics* **2006**, *3*, 251.
31. Savitski, M. M.; Nielsen, M. L.; Kjeldsen, F.; Zubarev, R. A. *J. Proteome Res.* **2005**, *4*, 2348.

32. Huang, Y.; Triscari, J. M.; Pasa-Tolic, L.; Anderson, G. A.; Lipton, M. S.; Smith, R. D.; Wysocki, V. H. *J. Am. Chem. Soc.* **2004,** *126*, 3034.

33. Zubarev, R. A.; Zubarev, A. R.; Savitski, M. M. *J. Am. Soc. Mass Spectrom.* **2008,** *19*, 753.

34. Vajda, J. H.; Harrison, A. G.; Hirota, A.; McLafferty, F. W. *J. Am. Chem. Soc.* **1981**, *103*, 36.

35. Wesdemiotis, C.; Csencsits, R.; McLafferty, F. W. *Org. Mass Spectrom.* **1985**, *20*, 98.

36. Burgers, P. C.; Holmes, J. L.; Mommers, A. A.; Szulejko, J. E.; Terlouw, J. K. *Org. Mass Spectrom.* **1984**, *19*, 492.

37. Wesdemiotis, C.; Feng, R.; Williams, E. R.; McLafferty, F. W. *Org. Mass Spectrom.* **1986**, *21*, 689.

38. Holmes, J. L.; Hop, C. E. C. A.; Terlouw, J. K. *Org. Mass Spectrom.* **1986**, *21*, 776.

39. Mazyar, O. A.; Mayer, P. M.; Baer, T. *Int. J. Mass Spectrom. Ion Processes* **1997**, *167/168*, 389.

40. Burgers, P. C.; Holmes, J. L.; Hop, C. E. C. A.; Terlouw, J. K. *Org. Mass Spectrom.* **1986,** *21*, 549.

41. Heinrich, N.; Schmidt, J.; Schwartz, H.; Apeloig, Y. *J. Am. Chem. Soc.* **1987**, *109*, 1317.

42. Holmes, J. L.; Aubry, C.; Mayer, P. M. *Assigning Structures to Ions in Mass Spectrometry*, CRC Press, Taylor & Francis Group, **2007**.

43. Ervin, K. M.; Armentrout, P. B. *J. Chem. Phys.* **1985**, *83*, 166.

44. Muntean, F.; Armentrout, P. B. *J. Phys. Chem. A* **2003**, *107*, 7413.

45. Amunugama, R.; Rodgers, M. T. *Int. J. Mass. Spectrom.* **2000**, *195/196*, 439.

46. Thomson, J. J. *Rays of Positive Electricity and their Application to Chemical Analyses*, Longmans, Green and Co.; London, **1913**.

47. Eberlin, M. N. *J. Mass Spectrom.* **2006**, *41*, 141.

48. Armentrout, P. B.; Baer, T. *J. Phys. Chem.* **1996**, *100*, 12866.

49. Combariza, M. Y.; Fahey, A. M.; Milshteyn, A.; Vachet, R. W. *Int. J. Mass Spectrom.* **2005**, *244*, 109.

50. Combariza, M. Y.; Vachet, R. W. *J. Am. Soc. Mass Spectrom* **2002**, *13*, 813.

51. Payne, A. H.; Glish, G. L. *Methods Enzymol.* **2005**, *402*, 109.

52. Brodbelt, J. S. *Mass Spectrom. Rev.* **1997**, *16*, 91.

53. Green, M. K.; Lebrilla, C. B. *Mass Spectrom. Rev.* **1997**, *16*, 53.

54. Gross, D. S.; Williams, E. R. *J. Am. Chem. Soc.* **1996**, *118*, 202.

55. Schnier, P. D.; Gross, D. S.; Williams, E. R. *J. Am. Chem. Soc.* **1995**, *117*, 6747.

56. Nieckarz, R. J.; Oldridge, N.; Fridgen, T. D.; Li, G. P.; Hamilton, I. P.; McMahon, T. B. *J. Phys. Chem. A* **2009**, *113*, 644.

57. Perrin, J. *Ann. Phys.* **1919**, *11*, 1.

58. Langmuir, I. *J. Am. Chem. Soc.* **1920**, *42*, 2190.

59. Lewis, G. N.; Mayer, J. E. *Proc. Natl. Acad. Sci. USA* **1927**, *13*, 623.

60. Lindemann, F. A. *Trans. Faraday Soc.* **1922**, 17, 598; Hinshelwood, C. N. *Proc. Roy.*

Soc. London, A **1927**, *113*, 230.

61. Price, W. D.; Schnier, P. D.; Jockusch, R. A.; Strittmatter, E. F.; and Williams, E. R. *J. Am. Chem. Soc.* **1996**, *118*, 10640.

62. Tholmann, D.; Tonner, D. S.; and McMahon, T. B. *J. Phys. Chem.* **1994**, *98*, 2002.

63. Dunbar, R. C. *J. Phys. Chem.* **1994**, *98*, 8705; Dunbar, R. C. *J. Chem. Phys.* **1991**, *95*, 2537.

64. Price, W. D.; Schnier, P. D.; Jokusch, R. A.; and Williams, E. R. *J. Phys. Chem. B* **1997**, *101*, 664.

65. For example see Kitova, E. N.; Seo, M.; Roy, P; Klassen, J. S. *J. Am. Chem. Soc.* **2008**, *130*, 1214.

66. Kitova, E. N. Bundle, D. R.; Klassen, J. S. *J. Am. Chem. Soc.* **2002**, *124*, 5902.

67. Wong, R. L.; Williams, E. R. *J. Phys. Chem. A* **2003**, *107*, 10976.

68. Freitas, M. A.; Hendrickson, C. L.; and Marshall, A. G. *J. Am. Chem. Soc.* **2000**, 122, 7768.

69. Freitas, M. A.; Hendrickson, C. L.; Marshall, A. G. *Rapid Commun. Mass Spectrom.* **1999**, *13*, 1639.

70. Levine, I. N., *Quantum Chemistry*, **2000** Prentice Hall.

71. Pivonka, N. L.; Kaposta, C.; Brummer, M.; von Helden, G.; Meijer, G.; Woste, L.; Neumark, D. M.; Asmis, K. R. *J. Chem. Phys.* **2003**, *118*, 5275.

72. Misochko, E. Y.; Akimov, A. V.; Goldschleger, I. U. *Russ. Chem. Rev.* **2003**, *72*, 233.

73. Almond, M. J.; Wiltshire, K. S. *Annu. Rep. Prog. Chem., Sect. C: Phys. Chem.* **2001**, *97*, 3.

74. Apkarian, V. A.; Schwentner, N. *Chem. Rev.* **1999**, *99*, 1481.

75. Dunkin, I. R. **1998**, *Matrix-Isolation Techniques, A Practical Approach*, Oxford University Press, UK.

76. Bertrand, G. **2002**, *Carbene Chemistry: From Fleeting Intermediates to Powerful Reagents*, Marcel Dekker Inc., NY, US.

77. Fausto, R. (Ed.) **1996**, *Low Temperature Molecular Spectroscopy*, Kluwer Inc., Amsterdam, The Netherlands.

78. Whittle, E.; Dows, D. A.; Pimentel, G. C. *J. Chem. Phys.* **1954**, *22,* 1943.

79. Ma, R.; Yuan, D.; Chen, M.; Zhou, M. *J. Phys. Chem. A* **2009**, *113*, 1250.

80. Forney, D.; Jakobi, M.; Maier, J. P. *J. Chem. Phys.* **1989**, *90*, 1.

81. Lisy, J. M. *J. Chem. Phys.* **2006**, *125*, 132302.

82. Piest, H.; von Helden, G.; Meijer, G. *Astrophys J.* **1999**, *520*, L75.

83. Hammer, N. I.; Diken, E.G.; Roscioli, J. R.; Johnson, M. A.; Myashakin, E. M.; Jordan, K. D.; McCoy, A. B. *J. Chem. Phys*. **2005**, *122*, 244301.

84. Bopp, J. C.; Roscioli, J. R.; Johnson, M. A.; Miller, T. M.; Viggiano, A. A.; Villano, S. M.; Wren, S. W.; Lineberger, W. C. *J. Phys. Chem. A* **2007**, *111*, 1214.

85. Fridgen, T. D.; McMahon, T. B. *Encyclopedia of Mass Spectrometry* **2005**, *4*, 327.

86. Mesleh, M. F.; Hunter, J. M.; Shvartsburg, A. A.; Schatz, G. C.; Jarrold, M. F. *J. Phys. Chem.* **1996**, *100*, 16082.

87. Wong, R. L.; Williams, E. R.; Counterman, A. E., Clemmer, D. E. *J. Am. Soc. Mass Spectrom.* **2005**, *16*, 1009.

88. Morton, T. H.; Beauchamp, J. L. *J. Am. Chem. Soc.* **1975**, *97*, 2355.

89. Holmes, J. L.; Lossing, F. P. *J. Am. Chem. Soc.* **1982**, *104*, 2931.

90. Bouma, W. J.; Nobes, R. H.; Radom. L. *J. Am. Chem. Soc.* **1982**, *104*, 2929.

91. Gauld, J. W.; Audier, H.; Fossey, J.; Radom, L. *J. Am. Chem. Soc.* **1996**, *118*, 6299.

92. Gauld, J. W.; Radom, L. *J. Am. Chem. Soc.* **1997**, *119*, 9831.

Chapter 2

Methods

2.1 Experimental Method: Infrared Multiple Photon Dissociation (IRMPD)

Trapping ions inside devices such as radio frequency (RF) traps or ion cyclotron resonance (ICR) cells (section 2.1.3) for a desired length of time allows one to apply a variety of techniques to study these ions. One of these techniques is the irradiation of ions with a laser which is the basis of IRMPD spectroscopy. As mentioned in Chapter 1, the low density of ions prevents the direct use of normal infrared spectroscopy, however, consequence (IRMPD) spectroscopy can be conducted. A tunable and intense infrared photon source can be coupled with the FT-ICR to fragment the trapped gaseous ions. Due to the high sensitivity of mass spectrometry, the fragmentation efficiency of mass-selected ionic clusters as a function of laser wavelength can

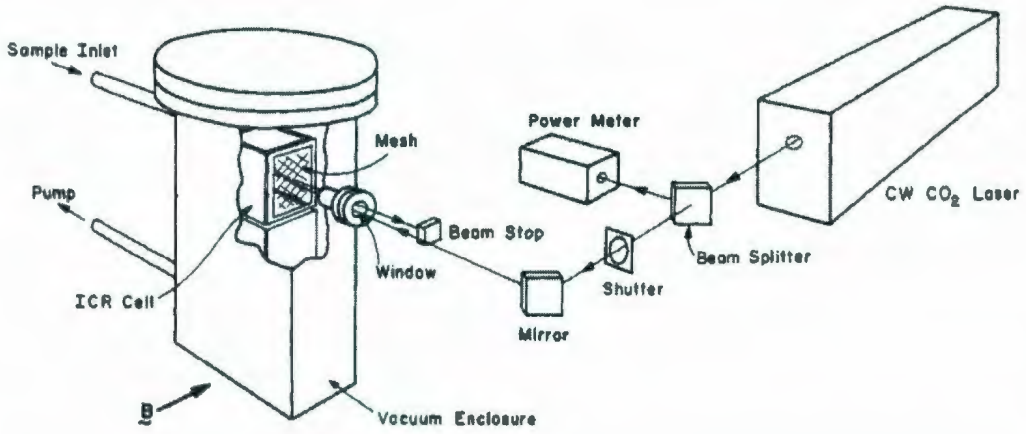

Figure 2.1: Schematic view of the experimental apparatus for low-intensity CW IR laser radiation. Figure reproduced from J. Am. Chem. Soc. 1979, 101, 5503 with permission from American Chemical Society.

be extracted. Plotting the fragmentation yield or efficiency of dissociation against the wavenumber of the IR light produces an IR spectrum of the molecular ion.

The first IRMPD spectrum of mass-selected ions was recorded using a continuous wave CO_2 laser. This was after Isenor[1,2] had pioneered the use of high power CO_2 laser pulses to induce IRMPD of molecules such as SiF_4 in 1971. In an early work by Beauchamp's group,[3] multiphoton dissociation of gas phase diethyl ether proton-bound dimer and its deuterated isomers were reported using a low-intensity infrared CO_2 laser coupled to an ICR spectrometer. A schematic of the instrument is shown in Figure 2.1. The proton-bound dimers were trapped inside the ICR cell for a few seconds and irradiated with the CO_2 laser. The intensity of the laser allows multiple

photon absorptions and because of the low pressure inside the ICR cell, deactivation of the high internal energy ions by collisions is inefficient. Multi-pass experimental conditions were achieved by using several mirrors to increase interaction of the ions with the laser beam.[4] The turning mirror shown in Fig. 2.1 directs the IR beam in an anti-reflection coated ZnSe window and transverses into the ICR cell. Upon irradiation of the diethyl ether proton-bound dimer, loss of one neutral diethyl ether, Equation 2.1, was the only observed decomposition pathway with 31±2 kcal mol^{-1} endothermicity. To dissociate this ion, at least 12 photons (considering that energy of one photon at 1000 cm^{-1} is around 2.8 kcal mol^{-1}) at the laser wavelength were required.

$$[(C_2H_5)_2O]_2H^+ \longrightarrow (C_2H_5)_2OH^+ + (C_2H_5)_2O \tag{2.1}$$

The IRMPD spectra for $(C_2H_5)_2OH^+$, $[(C_2H_5)_2O]_2H^+$, and $(C_2D_5)_2OD^+$ shown in Figure 2.2 display strong absorption bands in the 900-1100 cm^{-1} region. P_D for $(C_2H_5)_2OH^+$, was the fraction of ions dissociated after 1.9 s of irradiation at 48 W cm^{-2} and a $(C_2H_5)_2O$ pressure of 8.8×10^{-8} Torr. P_D for $[(C_2H_5)_2O]_2H^+$ was defined as the fraction of ions dissociated after 2.0 s of irradiation at 10 W cm^{-2} and $(C_2H_5)_2O$ pressure was 4.7×10^{-7} Torr. The experimental conditions for $(C_2D_5)_2OD^+$ were the same as for the photodissociation of $(C_2H_5)_2OH^+$. The dotted line spectra are the gas phase absorption spectra of neutral diethyl ether and $(C_2D_5)_2O$ at high pressures (~20 Torr). By comparing the spectra for the neutral and charged species, C-C and

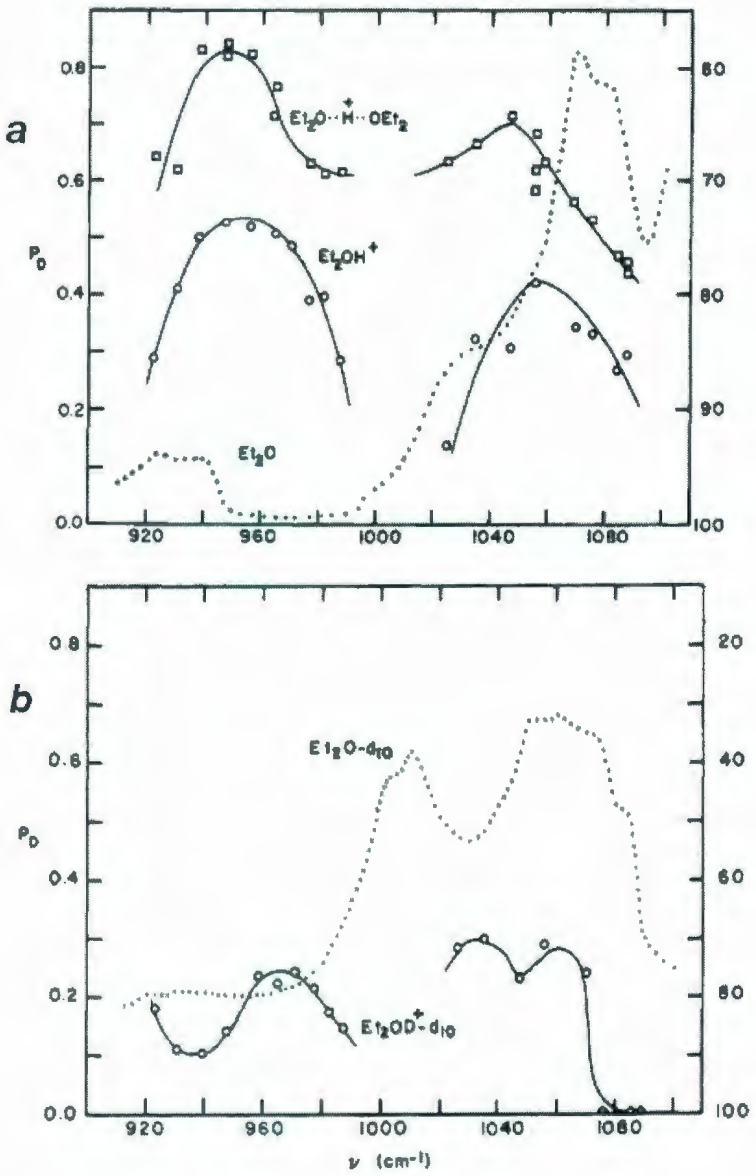

Figure 2.2: (a) Photodissociation spectra of $(C_2H_5)_2OH^+$ and $[(C_2H_5)_2O]_2H^+$ and (b) of $(C_2D_5)_2OD^+$ over the CO_2 laser spectral range. Dotted line is the infrared absorption spectrum of $(C_2D_5)_2O$ at 16 Torr. Figure reproduced from J. Am. Chem. Soc. 1979, 101, 5503 with permission from American Chemical Society.

C-O stretching vibrations as well as methylene waging at nearly the same positions were assigned to the observed bands. reflecting the similarity in their structures. They also studied IRMPD of gas-phase $CH_3CHOC_2H_5^+$, $C_2H_5OH_2^+$, and CH_3CHOH^+ ions trapped in an ICR cell.[5] In addition, a line-tuneable CO laser was used by Odeneye and Stace[6] to investigate the infrared photodissociation of $(NO)_n^+$ cluster ions where $n \leq 5$. The main disadvantage of gas-discharge lasers is that they have a limited and discontinuous tuning range, limiting their practicality for spectroscopic measurements.

The first mid-infrared spectra in the fingerprint region (in the 500 to 1600 cm^{-1} range) on naphthalene, phenanthrene, anthracene, and pyrene gas-phase ions were recorded by Oomens *et al.*[7] using an infrared free electron laser (FEL) in a quadrupole ion trap to conduct multiple photon dissociation spectroscopy of mass-selected bare ions. Fifty to one hundred infrared photons were required to increase the internal energy above the dissociation threshold and fragment these ions. Jones *et al.*[8] also used FEL FT-ICR to record the IRMPD spectrum in the 1100-1600 cm^{-1} for protonated benzene for the first time and experimentally showed that a σ complex species is more stable than either the edge-protonated structure or the face-centered π complex.[9]

One application of IRMPD spectroscopy was to determine the mechanism for water proton-bound dimer formation. Fridgen and coworkers[10] reported the gas-phase IRMPD spectrum for the proton-bound dimer of water. Although their experimental spectrum was not completely similar to the one recorded by Asmis *et al.*[11], it showed a

good agreement with the assignments based on density functional calculation. Marta *et al.*[12] elucidated the mechanism for water proton-bound dimer formation in part using IRMPD spectroscopy. Previously, three mechanisms had been proposed for the formation of water proton-bound dimer inside the ICR cell using $(CF_2H)_2O$. Clair and McMahon[13] developed a method to produce water proton-bound dimers in which $(CF_2H)_2O$ was added directly into the FT-ICR cell in the presence of water vapour. IRMPD spectroscopy revealed that only one of the proposed mechanisms, originally proposed by Clair and McMahon[13] and is shown in Scheme 2.1, is responsible for the formation of proton-bound dimer of water. The experimental IRMPD spectrum

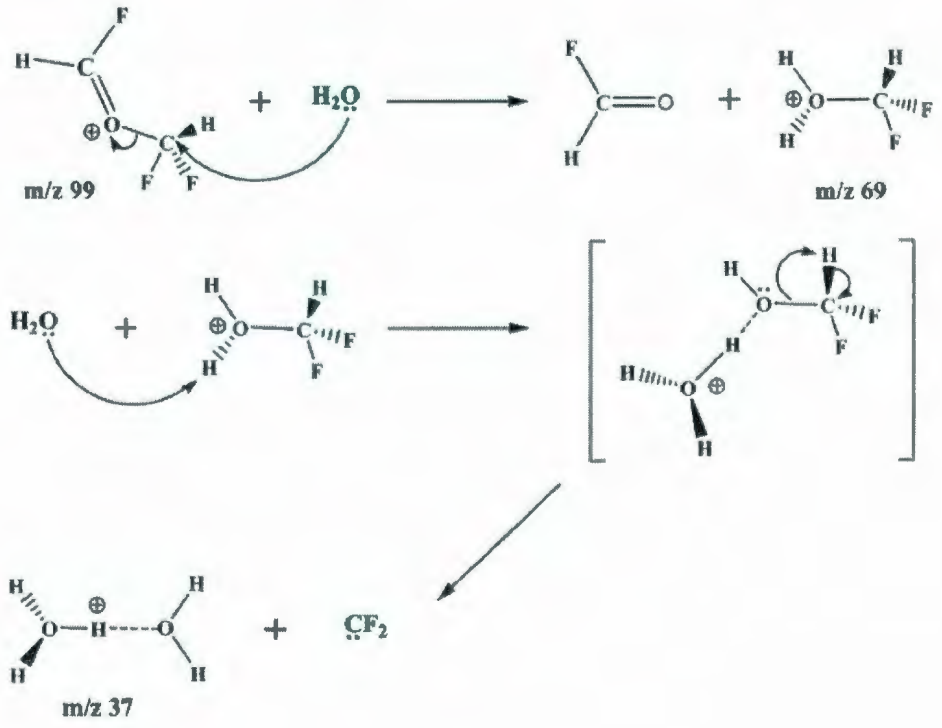

Scheme 2.1

agrees with the intermediate with covalently-bound complexes such as a particular conformer of difluoromethylated formyl fluoride rather than a proton-bound dimer of difluorocarbene and formyl fluoride.[14]

Recent developments in tunable sources of infrared radiation such as the FEL[14] and the optical parametric oscillator/amplifier (OPO/A)[16] (section 2.1.4) have led to an increased ability to record infrared spectra of gaseous ions. The three FEL centers which are equipped with conveniently tunable wavelengths are CLIO (Centre Laser Infrarouge d'Orsay) in Orsay, France, FELIX (FEL for Infrared eXperiments) in Nieuwegein, the Netherlands, and most recently FEL-SUT in Tokyo, Japan. Also, tabletop tunable IR-OPO laser technology has advanced so they can be used to measure IRPMD spectra at a shorter wavelength range (~2.5-4 μm) than those produced by FEL. Okumura *et al.*[17] used an OPO laser in 1985 to record the vibrational spectra of hydrogen cluster ions (H_n^+ where n=5, 7, and 9) between 3800 and 4200 cm^{-1}. Our laboratory for studying gaseous ions at Memorial University has been equipped with an OPO laser, working in the range of 2800-4000 cm^{-1}, which allow us to conduct IRMPD spectroscopy in an FT-ICR mass spectrometer. Structural information can be obtained from a combination of experimental and theoretical approaches. In the following sections, the principles of IRMPD spectroscopy and the experimental set up will be explained in more detail.

2.1.1 Mechanism of IRMPD

The theory of IRMPD and its mechanism have been studied extensively.[18–24] IRMPD is a non-coherent multiple photon absorption process that depends on rapid redistribution of the absorbed photon energy into the semi-coherent background vibrational states. The vibrational energy levels can be categorized by three energy regimes, shown in Figure 2.3b. In the lowest part of the energy diagram, vibrational states are discrete and quantized and, as a result, they can only absorb photons that are resonant with the energy difference between these states. The middle section of the energy diagram is called the quasi-continuum where the anharmonicity in the potential energy surface leads to an increase in the density of states. The coupling is proportional to the density of states at a given energy (ρ(E)) and since ρ(E) is higher at higher energies, highly excited vibrational states will be fully coupled to the background modes. Therefore, complete energy randomization, prior to dissociation occurs and pumping through the quasi-continuum resembles a series of incoherent single photon absorptions. Finally, the upper region is the true continuum state with an infinite number of states.

To observe IRMPD on a mass-selected ion, a vibrational mode must be in resonance with the infrared radiation. Absorption of a photon in resonance with a ν=0 to ν=1 vibrational transition, produces a state which can rapidly be de-excited through distribution of its energy over all vibrational degrees of freedom. The transfer of energy from an excited vibrational mode to the bath of vibrational background states is

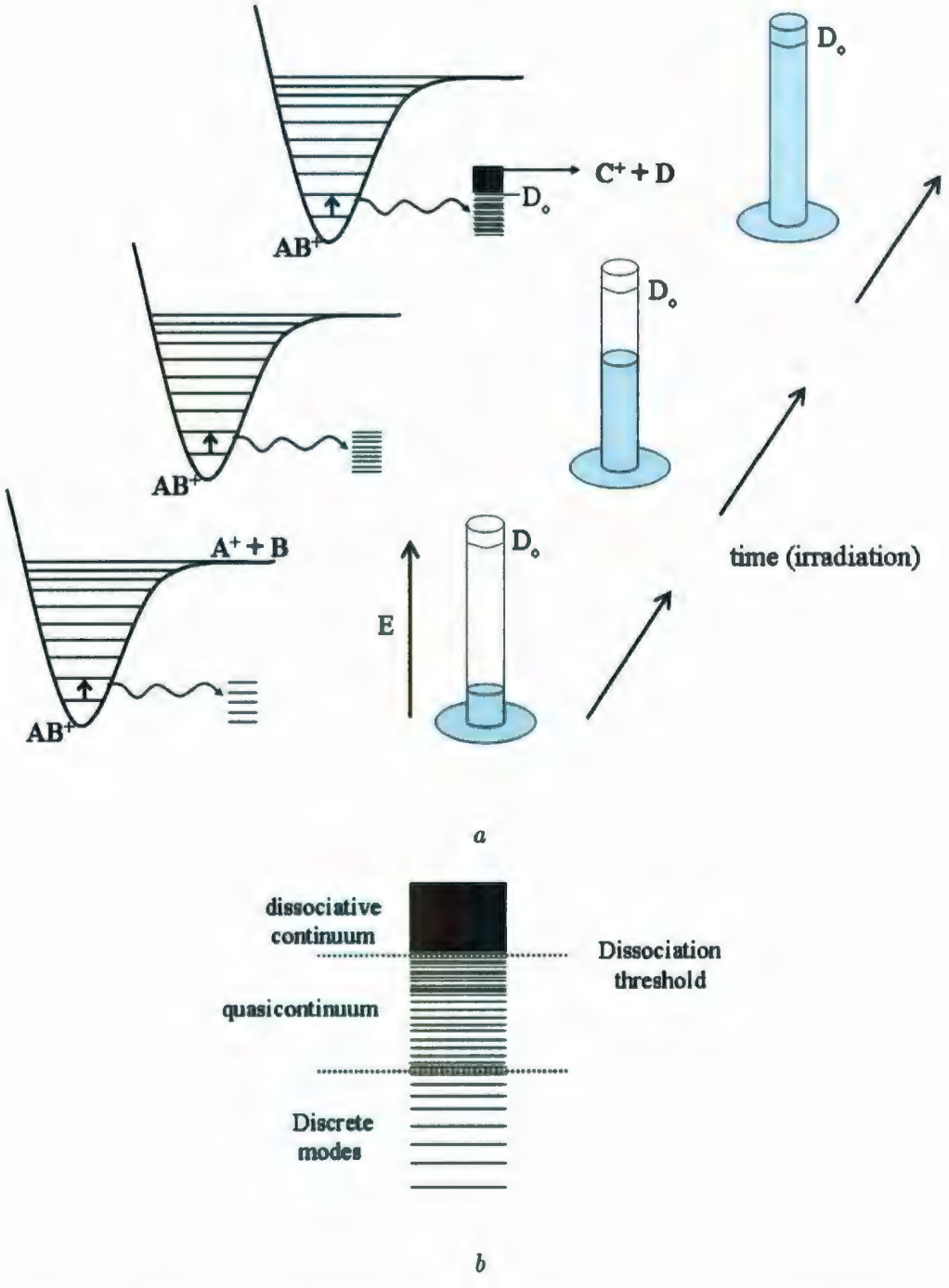

Figure 2.3: (a) Schematic representation of the IRMPD mechanism and (b) vibrational state density in a molecular ion.

called intramolecular vibrational energy redistribution (IVR) (see Figure 2.3a). The efficiency of IVR is a vital key in IRMPD spectroscopy as it transfers the absorbed energy within the molecular ion through the coupling between the other vibrational modes. The IVR process is typically very fast (~1ns) due to anharmonic coupling between the vibrational modes. Following IVR, the next photon is absorbed. The process of photon absorption and IVR repeats itself up to the point where the molecular ion finds itself in the "quasi-continuum" where absorption is less wavelength dependent (see the potential energy diagram in the middle shown in Figure 2.3a). This process repeats itself and as a result, the internal energy of the molecular ion increases and surpasses the threshold to dissociation D_o (in the continuum region). Note that following photon absorption by the molecular ion, the absorbed energy is randomized throughout internal modes of the ion. After increasing the internal energy, a low energy dissociation occurs. It is not necessarily the bond that absorbs the photon which cleaves. For example, if an O-H bond in glycine proton-bound dimer absorbs the laser photon which is resonant with the first fundamental vibrational frequency (ν=0 to ν=1), it will not cause the O-H bond break, instead neutral glycine is lost. The resonant photons absorbed by O-H increases the internal energy of the glycine proton-bound dimer. The increase in the internal energy is enough for the lowest dissociation channel, in this case the loss of neutral glycine. This fact is stressed in the Figure 2.3a by dissociation of molecular ion AB^+ to produce C^+ and D which requires less energy to dissociate than the A^+ and B channel.

An IR spectrum can be constructed by plotting the fragmentation efficiency against laser frequency. The IRMPD efficiency is defined as, Equation 2.2,[25]

$$Efficiency\ (IRMPD) = -\ln[\frac{I_p}{I_p + \sum_i I_{frag,i}}] \tag{2.2}$$

where I_p and $I_{frag,i}$ are the peak hights of the parent ion and all other fragment ions, respectively.

2.1.2 Experiments Set Up

The strategy employed in the IRMPD experiment[26,27] is to accumulate ions and store them for periods of time ranging from ms to 10s of seconds. The trapped ions are irradiated with high intensity and broadly tunable IR lasers. As discussed in section 2.1.1, multiple photons are required to pump a resonant vibrational level of the gaseous ions in order to reach the dissociation energy threshold. The work in the following chapters relied on both the quadrupole ion trap (QIT) and Fourier transform-ion cyclotron resonance (FT-ICR) MS to trap the ions although other types of ion traps such as orbitrap and 22-pole have also been developed for the purpose of trapping ions. These ion traps will be explained in section 2.1.3. Also, IR laser sources such as FELs and OPOs in the mid-IR were both used in our experiments and will be discussed in section 2.1.4. In our experiments, IRMPD spectra were recorded using the combination of a FEL and a Bruker Esquire 3000 quadrupole ion trap and using an OPO mated to a Bruker Apex-Qe 70 FT-ICR.

2.1.3 Ion Traps

2.1.3.1 Quadrupole or RF Ion traps (QIT)

The theory and applications of QIT have been well studied.[28,29] The 1989 Noble Prize was given to physicists Wolfang Paul and Helmut Steinwedel for developing the first quadrupole ion trap mass spectrometer (QITMS) in the 1960's to trap charged particles in two- and three-dimensional quadrupole fields.[30,31] One function of the QIT is to store gaseous ions for a period of time at a pressure of 1 mTorr of helium bath gas. By applying appropriate potentials to the ion trap electrodes, a trapping potential well can be formed which confines the gaseous ions. The QIT can also function as mass spectrometer for detecting ions based on their mass-to-charge ratio.

The QIT consists of three hyperbolic electrodes, two identical end-cap electrodes at the upper and lower parts of the trap and a ring electrode which is located symmetrically between the two end-cap electrodes. The three electrodes of the QIT are shown in Figure 2.4a along with a view of an ion trap cut in half in the axis of cylindrical symmetry in Figure 2.4b. Also, a cross-section of an ideal ion trap is shown in Figure 2.4c where, in theory, the electrodes extend to infinity. The radius of the ring electrode in the central horizontal plane, r_o , and the distance between the two end-cap electrodes along the vertical axis of the ion trap, $2Z_o$, can be seen in this Figure. This geometry of electrodes produces an oscillating parabolic potential well

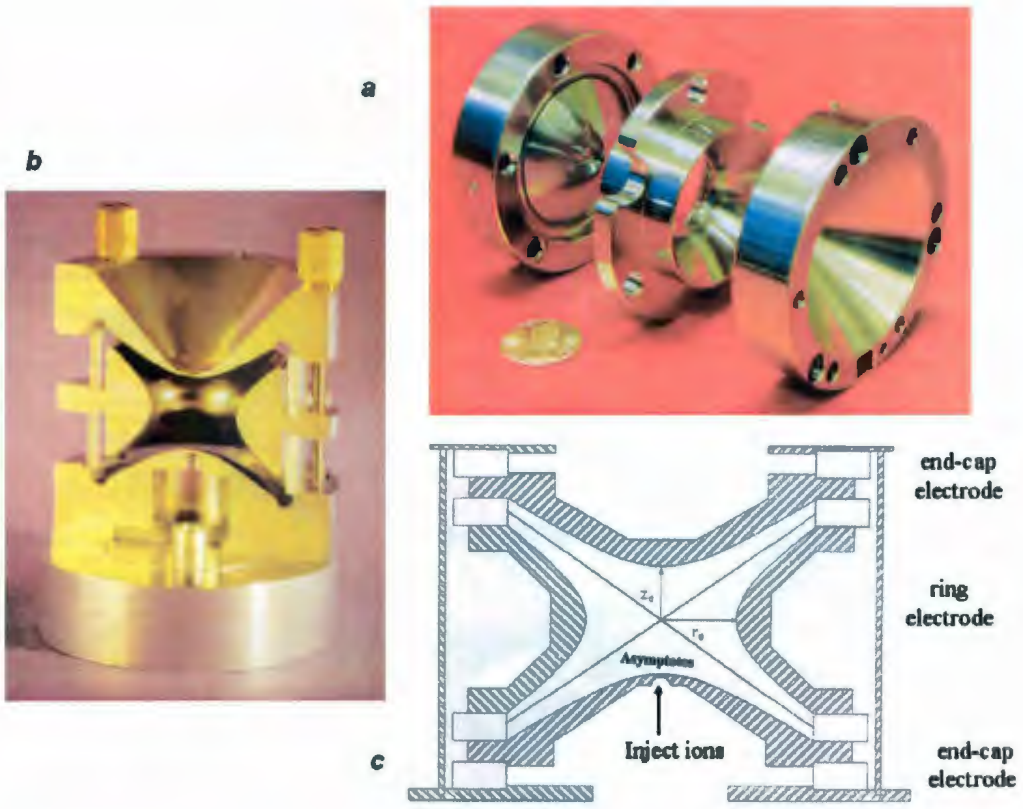

Figure 2.4: Quadrupole ion trap. (a) an open array of the three electrodes. (b) cut in half along the axis of cylindrical symmetry (c) schematic of the 3D ideal ion trap representing the asymptotes, r_0 and z_0. Figure reproduced from J. Mass Spectrom. 1997, 32, 351 with permission from John Wiley and Sons Inc.

by applying an RF potential to the ring electrode and grounded end-cap electrodes which confines ions. A combination of a dc voltage (U) and an RF periodic voltage (V) produces a 3D trajectory of the ions in the trap through which ions of all masses are trapped. An electric potential, Φ_o, is applied to the ring electrode and is of the

form

$$\Phi_0 = U + V\cos\Omega t \tag{2.3}$$

where Ω(2πf, f is the frequency in hertz) is the angular frequency (in rad s^{-1}) of the RF field.

To understand how quadrupole instruments work, one has to first define the motion of a charged particle in the quadrupole field. It has been found that the ion trajectories in a quadrupole field can be defined by the solutions to the second-order linear differential equation described originally by Mathieu.[32] The canonical form of the Mathieu equation is

$$\frac{\partial^2 u}{\partial \zeta^2} + (a_u \quad 2q_u\cos 2\zeta)u = 0 \tag{2.4}$$

$$\zeta \quad \Omega t/2 \tag{2.5}$$

where u is the coordinate axis x, y and z, ζ is a dimensionless parameter defined by Equation 2.5 in which t is time, a_u and q_u are dimensionless trapping parameters that contain information about the mass-to-charge ratio of the confined ions inside the trap. It can be shown that a change of variables from ζ to t results in Equation 2.6,

$$\frac{\partial^2 u}{\partial t^2} - \frac{\Omega^2}{4}\frac{\partial^2 u}{\partial \zeta^2} \tag{2.6}$$

and by substituting Eq. 2.5 and 2.6 in Eq. 2.4 and multiplying the results by mass of an ion, m, one can eventually derive an expression for the force (mass times

acceleration) on an ion, Equation 2.7.

$$m\frac{\partial^2 u}{\partial t^2} = -\frac{m\Omega^2}{4}(a_u - 2q_u \cos\Omega t)u \tag{2.7}$$

The quadrupole potential at any given point within the ion trap device, $\Phi_{x,y,z}$, can be expressed as

$$\Phi_{x,y,z} = \frac{\Phi_0}{r_0^2}(\lambda x^2 + \sigma y^2 + \gamma z^2) \tag{2.8}$$

in which $\Phi_\circ$ is defined in Eq. 2.3 as the applied electric potential, λ, σ and γ are weighting constants for the x, y, and z directions, and $r_\circ$ is a constant and depends on whether the quadrupole acts as an ion trap or mass filter. For the electric field, if the Laplace condition is satisfied, the field in the x, y, and z directions will be linear. Laplace conditions assure that the second differential of the potential at a given point is equal to zero. Therefore,

$$\nabla^2\Phi = \frac{\partial^2\Phi}{\partial x^2} + \frac{\partial^2\Phi}{\partial y^2} + \frac{\partial^2\Phi}{\partial z^2} \tag{2.9}$$

so that,

$$\lambda + \sigma + \gamma = 0 \tag{2.10}$$

The device functions as an ion trap when λ=σ= 1 and γ= -2. Substituting λ= 1 and Φ_0 from Eq. 2.3 in Eq. 2.8 and differentiating Φ with respect to x, the quadrupole field can be obtained,

$$\frac{\partial\Phi}{\partial x} = \frac{2x}{r_0^2}(U + V\cos\Omega t) \tag{2.11}$$

Since the field in the QIT is uncoupled, ion motion can be considered independently in each direction. For example, an ion with a mass of m and charge e feels the force

F_x, Equation 2.12, in the x-direction at any given point within the quadrupole field

$$F_x = ma = m\frac{\partial^2 x}{\partial t^2} = -e\frac{\partial \Phi}{\partial x} \tag{2.12}$$

where a is the ion's acceleration. Therefore, an expression for force on an ion can be obtained by substituting Eq. 2.11 in 2.12,

$$m\frac{\partial^2 x}{\partial t^2} = -\frac{2e}{r_0^2}(U + V\cos\Omega t)x \tag{2.13}$$

Therefore, by obtaining an expression for a force in Mathieu's equation (Eq. 2.7) and comparing that expression with one for the force on an ion in a quadrupole field (Eq. 2.13) through simple mathematical terms in the x-direction (u represents x), the trapping parameters in the x-direction are obtained.

$$a_x = \frac{8eU}{mr_0^2\Omega^2} \tag{2.14}$$

$$q_x = -\frac{4eV}{mr_0^2\Omega^2} \tag{2.15}$$

Applying a similar procedure for trapping parameters in the z-direction and substituting λ=-σ=1 and γ=0 into Eq. 2.8, a_z and q_z for the quadrupole mass filter can be expressed as Equation 2.16 and 2.17.

$$a_z = -\frac{8eU}{mr_0^2\Omega^2} \tag{2.16}$$

$$q_z = \frac{4eV}{mr_0^2\Omega^2} \tag{2.17}$$

Regions of ion trajectory stability can be found based on stable solutions of the Mathieu equation in both z- and r-directions. Once ion trajectories are stable in the

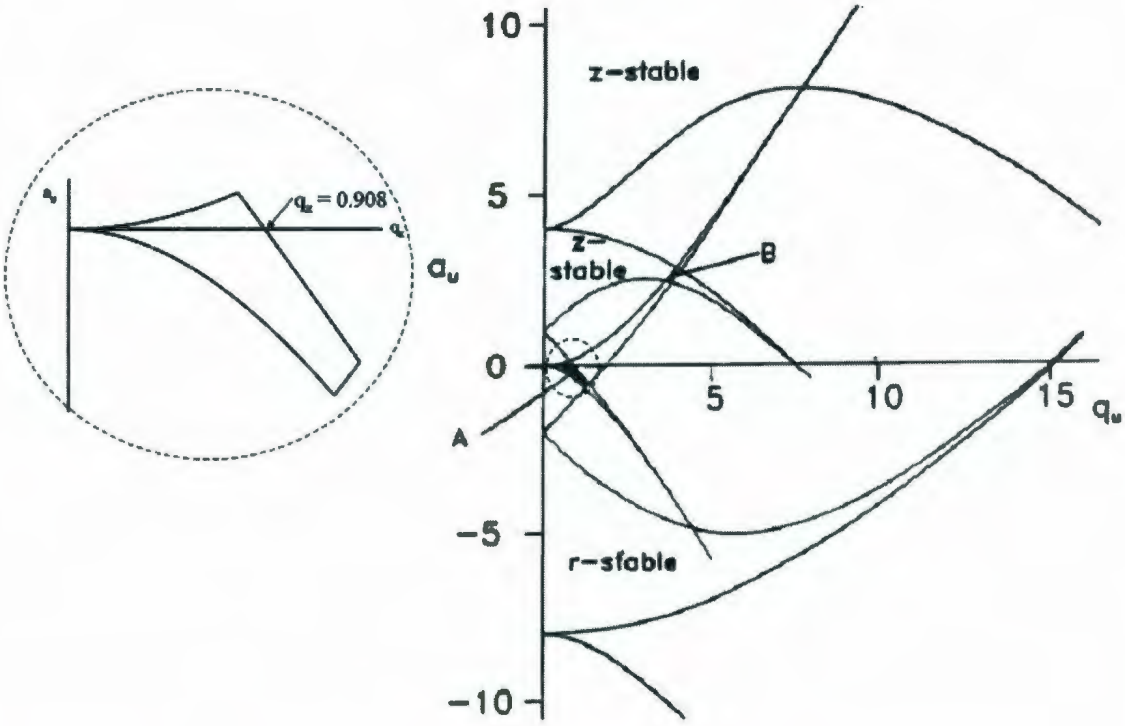

Figure 2.5: Stability diagram. Ions wirh a_u and q_u values that fall in the region A and B will have a stable trajectory and be trapped within the QIT mass spectrometer. Figure reproduced from J. Mass Spectrom. 1997, 32, 351 with permission from John Wiley and Sons Inc.

z- and r-directions simultaneously, ions can be stored in the ion trap. These regions of simultaneous overlap, in which ions move without hitting the electrodes, are shown in a Mathieu stability diagram (a_u vs q_u) in Figure 2.5 and are labeled A and B. The first stability region closest to the origin, A, is used in commercial ion traps.[33] This region is magnified and shown in Figure 2.5. The stability limit, q_z, at the boundary is equal to 0.908.

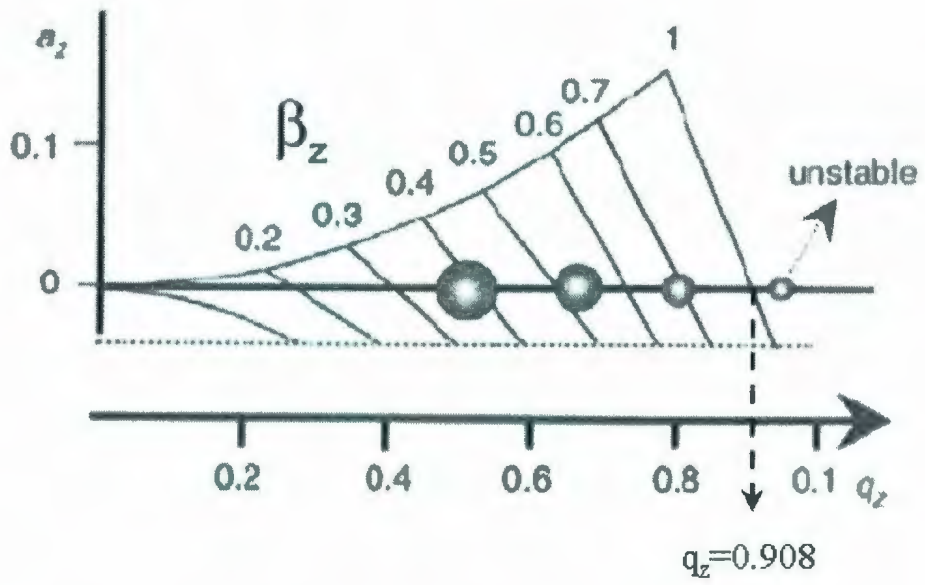

Figure 2.6: Mass analysis by ion ejection at the stability limit.

The expression for a_u and q_u contains the mass-to-charge ratio for a given ion and can also represent the ability of the ion trap to function as a mass spectrometer. Applying a resonant frequency along z expels the ions of a given mass, making the ion trap act as a mass spectrometer. q_z is proportional to V while it has an inverse relationship with mass. Therefore, the smallest ions have the highest q_z values. By raising the RF frequency level, each ion's q_z will increase and shift to higher values corresponding to unstability regions. Once the ions have passed their stability limits, they will be expelled from the trap and reach the detector from the smallest to largest.[34] This function is depicted in Figure 2.6.

In our experiments (Chapter 3), a modified Bruker Esquire 3000 ion trap[35] was

used at CLIO to trap the amino acid proton-bound dimer and allow them to be irradiated with FEL at the center of the ion trap. In order to allow the light enter the center of the ion trap, a conical cavity was built in the ring electrode. A ZnSe entrance window at the Brewster angle was inserted into the hole of the ion trap through which the laser light enters.

2.1.3.2 Fourier Transform Ion Cyclotron Resonance (FT-ICR)

Ion traps such as ICR cells can be used to trap ions as long as desired in low densities. Currently, the ICR is one of the most powerful mass spectrometer in terms of mass range and mass resolving power providing accurate mass measurements. In a uniform magnetic field (B), in the present case a 7.0 Tesla super-conducting magnet, and under high vacuum, ions (with a mass-to-charge ratio of m/q) can be trapped in two dimensions in a periodic cyclotron motion with a cyclotron frequency of f_c and an angular frequency of ω_c (rad/s), defined by Equations 2.18 and 2.19

$$f_c = \frac{\omega_c}{2\pi} \tag{2.18}$$

$$\omega_c = \frac{qB}{m} \tag{2.19}$$

resulting from the balance of Lorentz and centrifugal forces on a stable trajectory. In a fixed magnetic field, Equation 2.19 shows that each mass-to-charge ratio has a unique cyclotron frequency (f_c) which is in the range of a few kHz to a few MHz and is independent of the velocity (kinetic energy) of the ions.

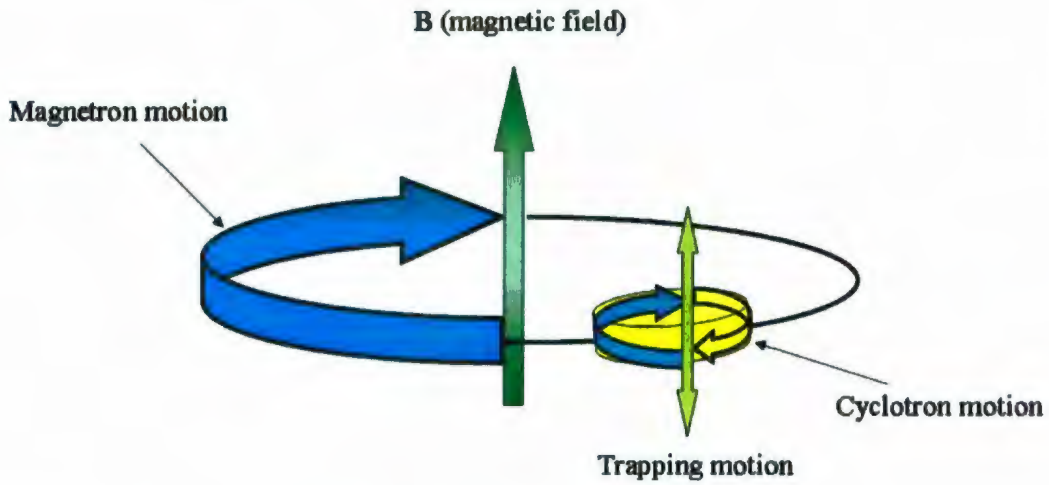

Figure 2.7: Ion motion in the ICR cell.

To trap the ions in the third dimension, an electric field is used which traps the ions along the axis of the magnetic field. In addition to the cyclotron motion of the ions in an ICR cell, a magnetron motion resulting from the combined effect of magnetic and electric fields also exists (see Figure 2.7). This magnetron motion frequency is given by Equation 2.20

$$f_m = \frac{\alpha V}{\pi a^2 B} \tag{2.20}$$

f_m is independent of the mass-to-charge ratio of the ions and typically is less than 100 Hz. In this equation, V is the magnitude of the trapping potential, a is the distance between the trapping plates, and α is a constant related to the analyzer cell geometry. This motion couples with the cyclotron motion and displaces the center of the cyclotron motion. Because numerous reviews and primers on the basic

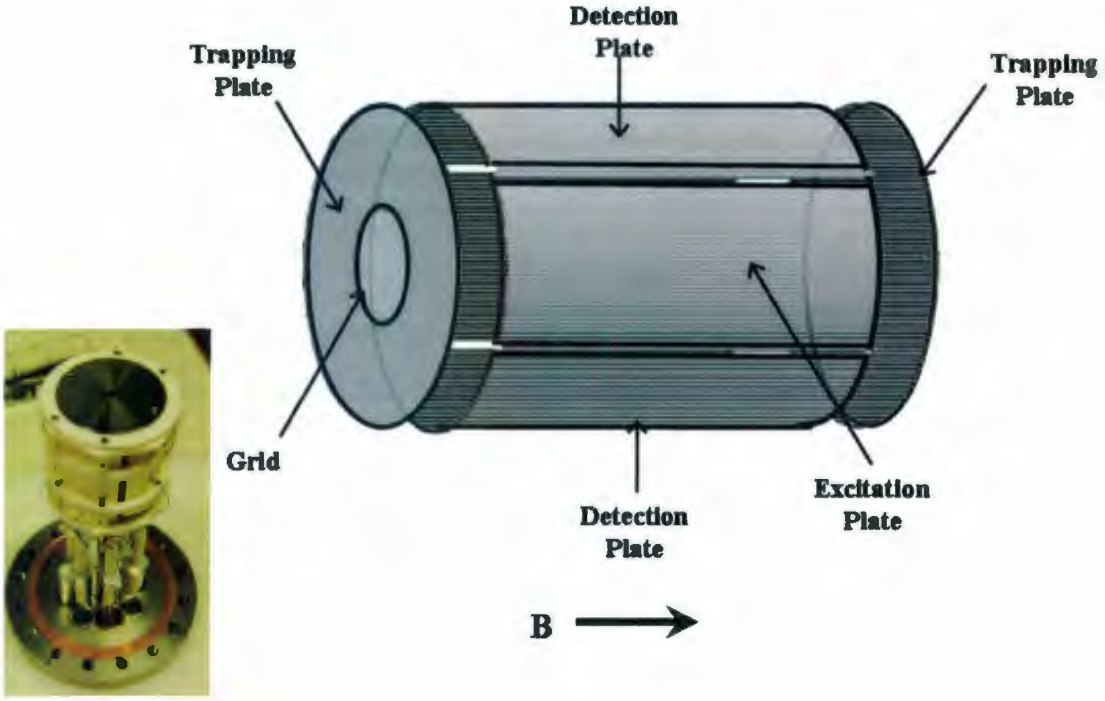

Figure 2.8: Schematic representation of a cylindrical ICR cell.

operation of an FT-ICR MS have been published,[36–40] only the information necessary to understand the experiments in this dissertation will be introduced in this section.

Analyzer cells can have different geometries but the cubic and cylindrical cell geometries are the most common. Figure 2.8 shows a schematic diagram of a cylindrical ICR cell consisting of a pair of end-cap trapping plates, a pair of excitation plates, and a pair of detection plates. The repulsive potentials on the trapping plates cause ion motion along the z axis (in the magnetic field direction). The number of charges confined inside the ICR is limited due to the Coulombic repulsion between ions. If the space charge limit is reached, the possible side effects could be shifts in the cyclotron

frequency, peak broadening, and detecting one peak for ions of similar masses.

The ion source used in our experiments is electrospray ionization (ESI). The mechanism of producing gas-phase ions from a solution of dissolved electrolyte ions can be categorized in the following steps: (a) formation of charged droplets at the ES capillary tip; and (b) evolution of the charged droplets due to solvent evaporation as well as droplet fission caused by Coulombic repulsion of the charges on the droplets, production of the gas-phase ion from very small charged droplets.[41] In ESI, a high voltage (several kV) is applied to the tip of a metal-coated capillary through which the sample solution is running. Small droplets with excess charge are formed. Evaporation of the solvent causes a shrinkage in the droplets. The charge repulsion increases with the smaller size and results in fission into even smaller droplets. Finally, desolvated ions are formed. ESI is an atmospheric pressure technique while the optimum ICR performance is at very low pressures of the order of 10^{-10} Torr. To be able to couple ESI with an ICR, a number of stages of differential pumping is required and this necessitates a distance of at least 1 meter between the source and the ICR cell.[42] A schematic of the instrumentation for ESI-ICR along with the pressure at different stages is shown in Figure 2.9. A gate valve separates the ultra high vacuum region from the rest of the instrument. After producing ions, they have to be injected into the ICR cell. The ions have to penetrate a strong magnetic field and, at the same time, they have to be slow enough to be trapped in the axial direction. The most common method to help the ions traverse the magnetic field is using an RF-only ion

guide. To be able to trap the ions in the cell, the potential on the front trapping plate must be lower that the ions' kinetic energy and to prevent ions from going straight through the cell, the rear potential voltage must be higher. A potential well is created along the axial direction by the dc voltage to hold the ions in this dimension. The magnetic field in the axial direction inhibits ions from hitting the ICR walls through the Lorentz force, causing a cyclotron motion.

The ion detection in ICR is unique among MS techniques in that all ions are detected at the same time. The two steps in the ion detection process are ion excitation and then detection of the induced current on the analyzer cell electrodes which is

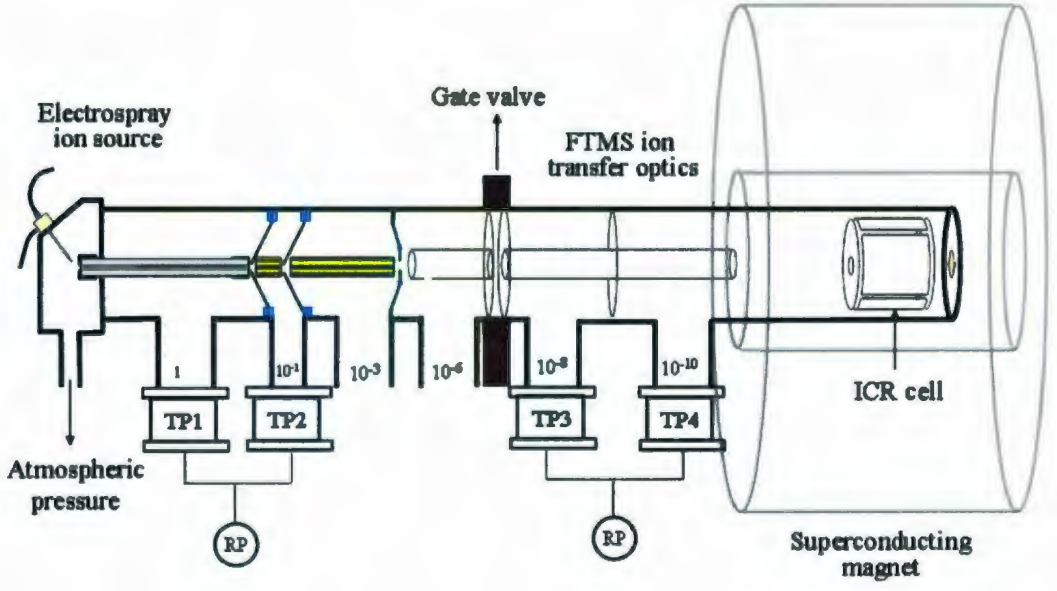

Figure 2.9: A schematic of the instrumentation for ESI-ICR along with pressure at different stages. TP and RP are abbreviations for turbo pump and rough pump, respectively. The pressures shown in each stage are in mbar.

called image current. To excite ions, a sinusoidal RF electric field is applied to the excitation plates for a very short time which has the same frequency as ion cyclotron frequency. The transferred energy increases the ions' kinetic energy. Because the cyclotron frequency remains constant, the ions will excite to a larger orbit and become closer to the detection plates and induce a detectable signal. As a result, the ions with the same mass-to-charge ratio will be excited to the same orbit and rotate around the magnetic field line with their characteristic cyclotron frequency. The ions of a particular mass-to-charge ratio traverse together as a packet. For positively charged ions, when the ions approach a detection plate, electrons are attracted to the plate and when the ion packet approaches the opposite detection plate, electrons are attracted to that plate. This image current, oscillating at the cyclotron frequency of the ions, is detected in an external circuit between the two detection plates. A time domain signal composed of all the image currents of the ions is detected for a period of time on the order of ms. This time domain signal is Fourier transformed to produce a frequency domain signal which is proportional to mass through Equation 2.19. Steps for ion detection in the FT-ICR MS are depicted in Figure 2.10.

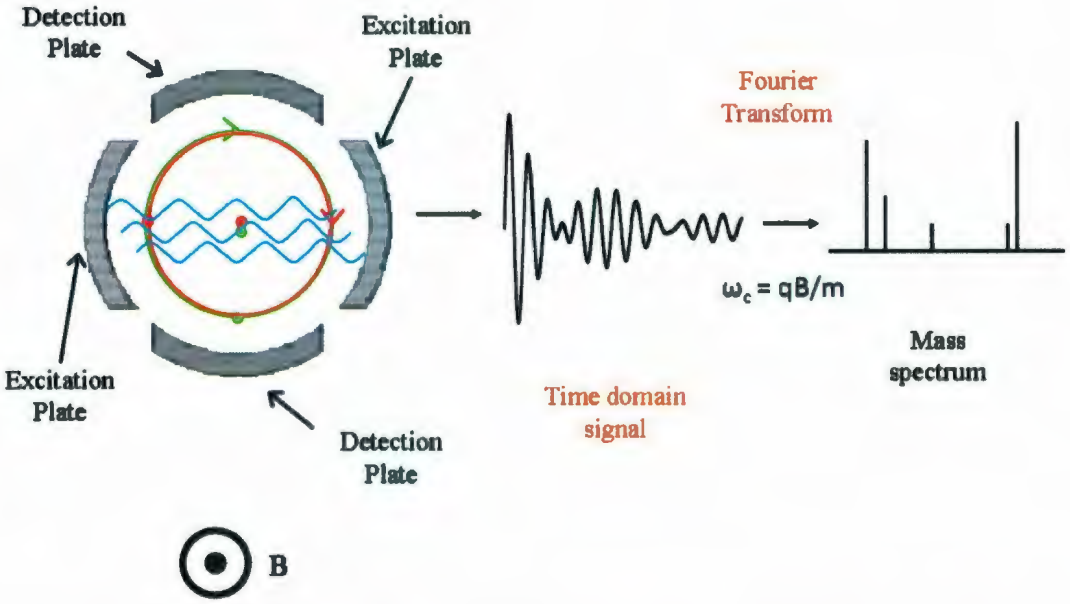

Figure 2.10: Steps in ion detection in a FT-ICR MS. **B** represent the magnetic field.

2.1.4 IR Laser Sources

A laser (light amplification by simulated emission of radiation) is a device to produce coherent, collimated monochromatic light. In the laser emission process, a photon interacts with active excited atoms, resulting in a photon with the same wavelength and phase when depleting the atom to its ground state. The medium in which the laser emission is produced is called the active or amplifying medium. The active medium can be excited by numerous methods such as pumping by absorbing light and collisions with electrons or atoms. In the following sections the two types of lasers used in IRMPD experiments will be explained.

2.1.4.1 IR Free Electron Laser (FEL)

In canonical lasers, the excited atoms or molecules are used to amplify light while in FEL,[18,42] a high-energy electron beam is used as an amplifying medium. The Bremsstrahlung radiation produced by accelerated relativistic electrons is the basis of a free electron laser.[43] The components of a FEL are sketched in Figure 2.11. Groups of electrons (~giga-amperes) are triggered from an electron gun and accelerated to mega electron volts (MeV) with a radio frequency linear accelerator. The high speed electron beam is directed into a set of periodic, transverse magnetic fields called an undulator or a wiggler. According to the Lorentz force, the electrons obtain a wiggling motion. Also, since the light travels faster than electrons, at 3×10^8 m s^{-1}, a lag between the electrons and light is bulit. The alternate change in the magnetic field direction causes a sinusoidal wave pattern for the electron beam. An electron emits radiation in a continuous frequency band when the direction of the magnetic field in the undulator changes. This radiated light travels straight while the electron packet lags behind due to the wiggling movement in the magnetic field. As a result, the radiated light is not coherent. To eliminate the problem, the undulator parameters are set in a way that the lag comes to exactly one or an integer number of wavelengths per undulator period.

Since different electrons emit radiation which is mostly out of phase, the resulting

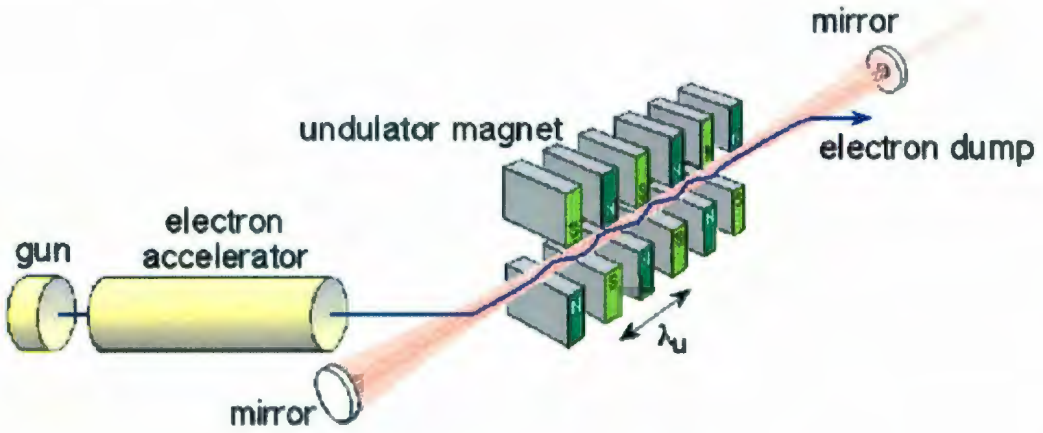

Figure 2.11: A schematic of a FEL.

radiation is weak. The radiation is captured in an optical cavity which is formed by two spherical mirrors in the vicinity of the undulator (see Fig. 2.11) to produce coherent and intense radiation. The length of the cavity is chosen such that a resonance between the fresh electron packets and the light pulses passing in the cavity exists.

Finally, the wavelength, which is the lag amount of the electron bunch and emitted light, is a function of the magnetic field strength through Equation 2.21, making it possible to tune the lasing wavelength.

$$\lambda_n = \frac{\lambda_U(1 + K_{rms}^2)}{2n\gamma^2} \tag{2.21}$$

According to this equation, λ_n the wavelength of the FEL radiation is a function of the electron energy γ , the undulator parameter K_{rms} (rms=root mean square), the undulator period λ_U, and the radiation harmonic number n. The dimensionless undulator parameter K_{rms} is proportional to the magnetic field through Equation

2.22

$$K_{rms} = \frac{eB_U\lambda_U}{2\pi m_e c} \tag{2.22}$$

where e and m_e are the electron charge and mass, respectively, c is the speed of light, and B_U is the rms amplitude of the magnetic field on the undulator axis.[44] By changing the energy of the electrons and/or the magnetic field of the undulator, different wavelengths can be achieved. The magnetic field strength of the undulator can be varied by changing the gap between the two arrays of magnets. The CLIO FEL, which is used in some of our experiments, can generate 8 to 50 MeV electrons as the photon energy depends on the electron kinetic energy as well as the strength and periodicity of the magnetic field. This configuration makes FEL a high intensity laser with a high fluence to produce multiple photons which are efficiently tunable in the 50-2500 cm^{-1} region which is useful for most of the compounds containing active functional groups.

2.1.4.2 Optical Parametric Oscillator (OPO)

OPOs are powerful solid-state coherent laser sources which can be tuned over extensive ranges with high efficiencies.[45–47] An optical parametric oscillator is a nonlinear optical process in which an input pump photon, propagating in a nonlinear optical material, is converted into two lower-energy photons. A schematic of our laser system mated to the FT-ICR is shown in Figure 2.12. In our laboratory at Memorial

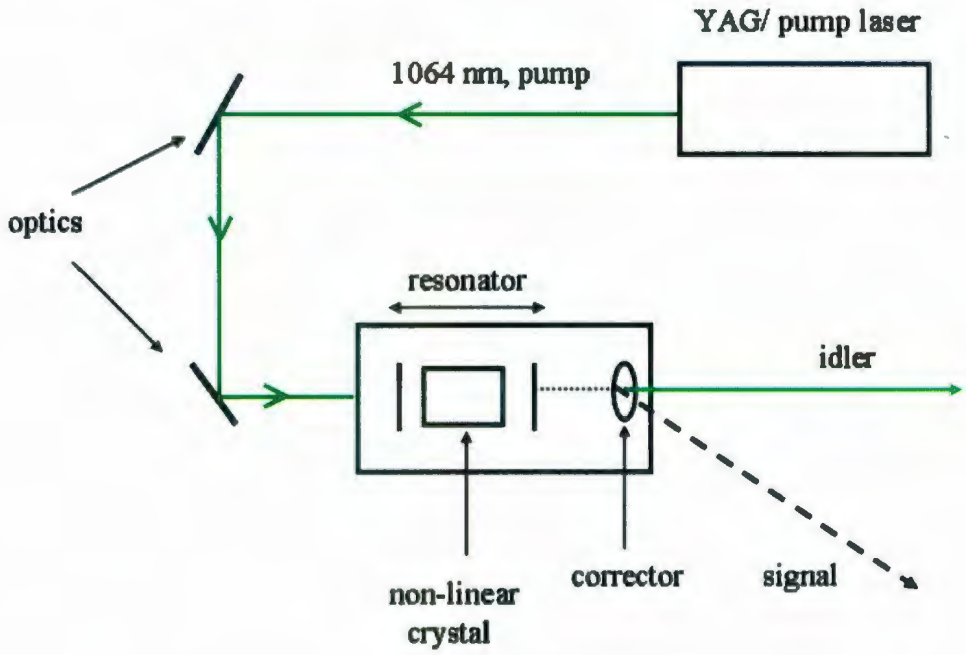

Figure 2.12: A schematic of the YAG:OPO laser.

University, a Brilliant b YAG laser pumps the OPO at the fundamental line of 1064 nm.

The 1064 nm photons pass through a few optics and enter the OPO. The essential parts of the OPO are an optical cavity and a non-linear crystal which is inserted in the cavity. A variety of crystals can be used in the cavity. $LiNbO_3$ and KTP (Potassium titanyl phosphate, $KTiOPO_4$) are two common crystals and are used at CLIO and Memorial University, respectively to produce IR frequencies. By placing the active medium in the optical cavity composed of two or several mirrors, the emitted light is forced to pass through the same active medium numerous times resulting in an increase in amplification. The laser emission is obtained at the output of the cavity

by means of one of the mirrors. Depending on the type of the crystal used in the cavity and rotation of the crystal different output frequencies can be obtained. The incident 1064 line, also called the pump, traverses a variety of optics before entering into the OPO. The OPO splits the input (pump) laser light into two output lights through its non-linear crystal. The two light outputs are called signal and idler and have a lower frequency compared to the input light frequency. The two frequencies are labeled as ω_s and ω_i, representing signal and idler wave frequencies, respectively and the sum of them equals the pumping frequency,

$$\omega_s + \omega_i = \omega_p \tag{2.23}$$

Using the non-linear crystal causes an overlap between the pump and the output waves, resulting in an increase in the amplitude of the signal and idler waves and a decrease in the amplitude of the pump wave. The amplification in the output wave(s) initiates the signal and idler waves to oscillate in the cavity, compensating for any loss of the output waves. A corrector is also used to insure that an intense beam of light is produced since the direction of the output beam changes with a change in crystal's angle. For our experiments, the idler is in the IR energy range and is directed into the ICR cell.

In the neodymium laser, Nd^{3+} (Neodymium) ions are used in yttrium aluminum garnet (YAG), $Y_3Al_5O_{12}$ as a host crystal. The diagram of the atomic transition principle of the active medium used in Nd:YAG solid state lasers is shown in Figure 2.13.

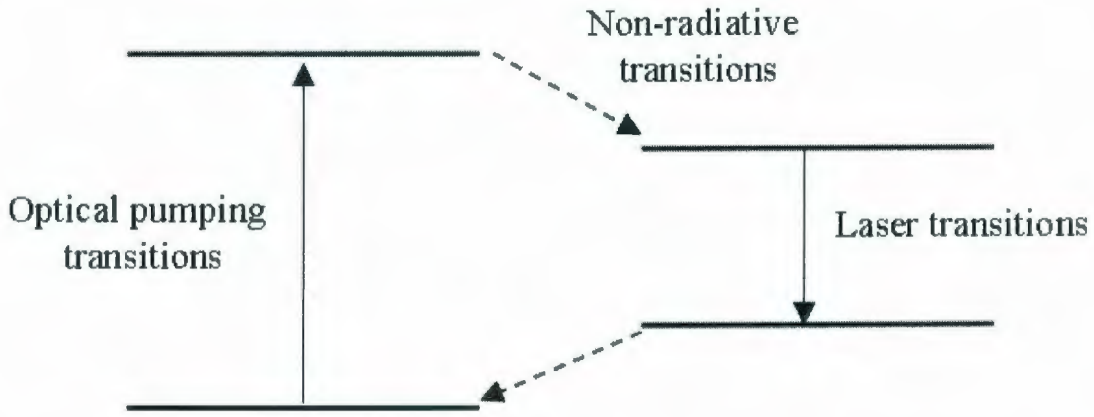

Figure 2.13: The four-level system energy diagram of the Nd:YAG atomic transition principles at 1064 nm.

The laser emission can be continuous or pulsed as energy packets. A Q-switched mode can be used to obtain high-power pulses with a duration of a few nanoseconds. In Figure 2.14, a simplified diagram of a Nd:YAG type Q-switched laser is depicted. This diagram is very similar to that used in the Brilliant in our laboratory at MUN. The cavity consists of the cavity rear mirror with maximum reflectivity and the partially reflecting output mirror. The Nd:YAG rod is the active medium and optically pulse-pumped by a flash lamp. The polarizer, quarter wave plate, and electro-optical modulator are used to block and to Q-switch the laser emission.

The pulsed mid-IR OPOs can be tuned as wide as 1.5-8 μm. Energies of more than 100 mJ per pulse can be produced.

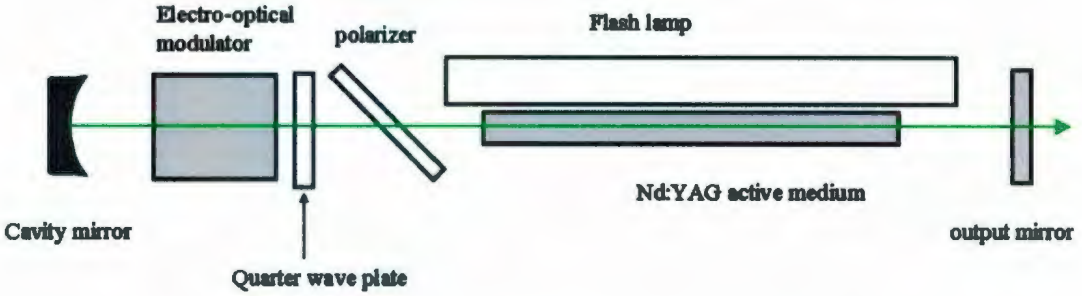

Figure 2.14: Simplified diagram of a Nd:YAG Q-switched laser.

Two experimental set-ups employed in this work to record the IRMPD spectra include a Bruker Apex-Qe 7.0 tesla FT-ICR mass spectrometer coupled to an IR OPO and a Bruker Esquire 3000 QIT mated to a FEL laser located at CLIO. The FT-ICR mass spectrometer consists of three main parts, the ionization source, the superconducting magnet, and the detector. A schematic of a 7.0 Tesla FT-ICR mass spectrometer with an electrospray source is depicted in Figure 2.15. The ions are produced at relatively high pressure (~few mbar); however, the ICR cell requires a very high vacuum (~10^{-10} mbar). As a result, differential vacuum systems are required to achieve the appropriate pressure. A gate valve separates the high-vacuum ICR region from the rest of the instrument. Solutions of investigated species (with a concentration of a few mM) containing alkali metal cations and also acid (HCl) were prepared in 18 Mohm (Millipore) water. All chemicals were purchased from Sigma-Aldrich and used as received. After electrospray ionization of the solutions containing cations/proton (see Fig. 2.15), ions were directed into the ion funnels and

then trapped in a hexapole RF ion trap for a short time (~ms). Packets of ions were extracted through a quadrupole ion guide. Ions in a mass range of interest were conducted and transferred into the accumulation (collision) hexapole cell.

In one set of experiments, solvated cluster ions were produced in the storage hexapole cell of a commercial Bruker Apex-Qe 7.0 T hybrid Q-FTMS.[48] Briefly, in this method of synthesizing solvated ions, the Ar gas in the collision cell was replaced with solvent (water or methanol) selectively adding solvent molecules to the ions, producing gaseous solvated metalated ion clusters. Both solvated and unsolvated metalated ions were selectively transferred into the infinity ICR cell which is located inside a 7.0 T superconducting magnet. The ions were irradiated by an IR laser beam

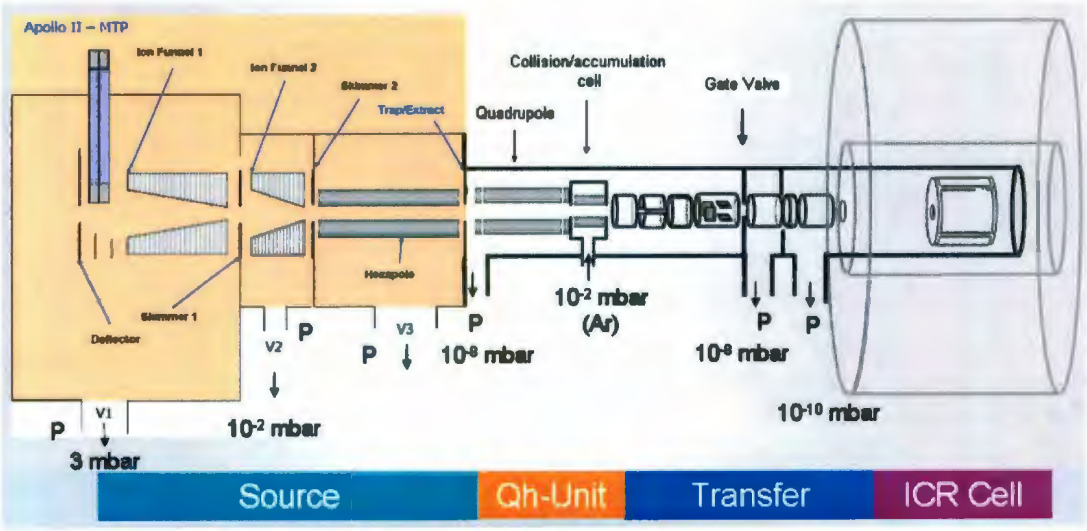

Figure 2.15: Schematic of a Bruker Apex-Qe 7.0 T FT-ICR mass spectrometer, laser photons are shown with an arrow entering the ICR cell.

along the axis of the bore of the magnet. This was done from a tabletop Laser Vision IR OPO system entering through a Brewster window for several seconds to record the IR spectra in 2800-3900 cm^{-1} wave number range. To record the IR spectra in the mid-infrared region, ions were irradiated with CLIO FEL. The scan rate varied between 0.2-0.5 cm^{-1}/s, being 0.2 cm^{-1}/s for most experiments. The pulse length was between 0.2-4.0 s and the bandwidth was <5 cm^{-1}. Exact values for each parameter for individual experiments can be obtained in the following Chapters.

A similar instrument at Memorial University was used to collect data for metalated DNA ions which will be discussed in Chapter 7.

A cartoon of the instrument in which a Bruker Esquire 3000 QIT is mated to the FEL at CLIO and used to record IRMPD spectrum of aliphatic amino acid proton-bound dimers, Chapter 3, is shown in Figure 2.16. In this configuration, the FEL is focused into the center of the QIT through a ZnSe window which is located in the small hole in the ring electrode. Earlier, Simon *et al.*[49] compared the IRMPD spectra of the four simplest protonated methyl esters of amino acids, $GlyMeH^+$, $AlaMeH^+$, $ValMeH^+$, and $LeuMeH^+$ produced by ESI or MALDI obtained in an FT-ICR and an RF quadrupole trap, respectively. They observed a more efficient photodissociation for the ions using the RF quadrupole trap as opposed to the ICR due to the enhanced overlap between the ion cloud and the laser beam. Also, the spectral bands were narrower when a RF quadrupole trap was used. Nonetheless FT-ICR instruments have significant advantages compared to quadrupole ion traps; for instance,

higher mass resolution, more accurate ion manipulation, including mass isolations, and lower pressure, thus limiting collisional damping in the IRMPD process.

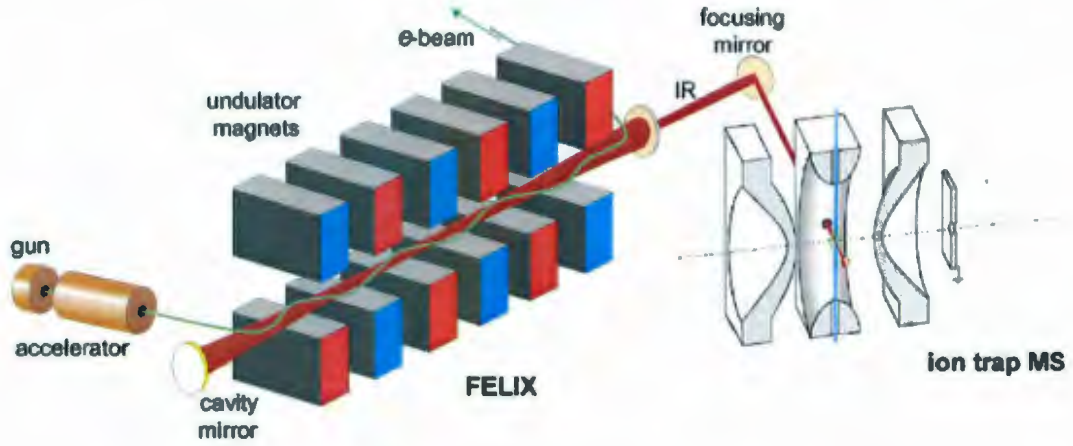

Figure 2.16: A schematic of a Bruker Esquire 3000 QIT mass spectrometer coupled with FEL; laser photons are shown with an arrow entering the QIT. Figure reproduced from Int. J. Mass Spectrom. 2006, 254, 1 with permission from Elsevier.

2.2 Computational Methods

As our main technique is IRMPD, computational methods were applied to simulate the IR spectra for gaseous ions. Subsequently, the simulated IR spectra were compared with experimental IRMPD spectra through this research and will be dis-

cussed here. First of all, a brief description of the computational methods used will be provided. The fundamentals of quantum mechanics and its application to develop computational methods has been widely investigated.[50–54] Any computational method consists of two main parts: a level of theory (method) to correct for a different degree of electron correlation and a basis set to describe the molecular orbitals (MOs). A variety of methods based on first principles, empirical, and/or a combination of the both, and semi-empirical data (obtain some parameters from empirical data) have been developed. The most commonly used methods to theoretically predict structures and IR spectra are based on the first and third categories, *ab initio* and density functional theory (DFT). Since these two methods are employed in our calculations, they will be explained in more detail.

2.2.1 *Ab initio* Method

Ab initio methods are non-empirical and are derived from theoretical principles without any experimental data. In these methods approximations, usually mathematical, are used in order to solve for the wavefunction. The two *ab initio* methods employed in our calculations are Hartree-Fock (HF) and a Post-Hartree-Fock method, MP2. HF is the simplest wavefunction-based *ab initio* method.

Based on quantum mechanics,[55] by solving the Schrödinger equation, Eq. 2.24,

the energy and many properties of a stationary state of a molecule can be obtained,

$$\hat{H}\Psi = E\Psi \tag{2.24}$$

where $\hat{H}$ is a differential operator called Hamiltonian representing the total energy, E is the total energy of the state, and Ψ is the wavefunction. The molecular Hamiltonian $\hat{H}$ is defined as the sum of kinetic and potential energy operators, Eq. 2.25.

$$\hat{H} = \hat{T} + \hat{V} \tag{2.25}$$

in which the kinetic energy ($\hat{T}$) includes the kinetic operators of electron ($\hat{T_e}$) and nuclei (($\hat{T_n}$); and the potential energy operator ($\hat{V}$) is the summation of Coulomb electron-nuclei attraction ($\hat{V_{ne}}$), electron-electron repulsion ($\hat{V_{ee}}$) and nuclear-nuclear repulsion ($\hat{V_{nn}}$). Hence the full molecular Hamiltonian can be written as Eq. 2.26,

$$\hat{H} = \hat{T_e} + \hat{T_n} + \hat{V_{ne}} + \hat{V_{ee}} + \hat{V_{nn}} \tag{2.26}$$

Since nuclei are much heavier than electrons, based on the Born-Oppenheimer approximation one can assume that nuclei are fixed with respect to the motion of electrons. This assumption simplifies the general molecular problem in quantum mechanics and allows factorizing the wave equation:

$$\hat{H} = \hat{H_n} + \hat{H_e} \tag{2.27}$$

and

$$\Psi(R, r) = \Psi_n(R)\Psi_e(r) \tag{2.28}$$

Therefore, the electron motion in the field of fixed nuclei can be solved first to obtain an effective electronic energy (E^{eff}(R)) using the electronic Schrödinger equation,

$$\hat{H^{ele}}\Psi^{ele}(R,r) = E^{eff}(R)\Psi^{ele}(R,r) \tag{2.29}$$

Theoretical studies of electronic structure are aimed to solve the electronic Schrödinger equation, at least approximately, and obtain the effective nuclear potential function (E^{eff}(R)). Hartree-Fock (HF) is the simplest wavefunction-based method and is based on the variational method. In variational calculations the calculated energies are always greater than or equal to the exact energy. Therefore, the HF limit energy (E_{HFL}) itself is always greater than the exact energy value (even using an improved basis set).

By applying the electronic Hamiltonian, the electronic energy is obtained which contains the electron-electron potential energy term, V_{ee} in Eq. 2.26. V_{ee} contains three energy terms including Coulomb repulsion energy, exchange energy, and correlation energy. The correlation energy is sensitive to change in the number of electron pairs and is the only term not accounted for in HF. Correlation energy is always negative and is the single most important problem in quantum chemistry. Correlation energy is the difference between the exact non-relativistic energy (E_{exact}) and the (E_{HFL}), expressed as Eq. 2.30,

$$E_{corr} = E_{exact} - E_{FHL} \tag{2.30}$$

Note that exchange occurs between electrons with the same spin only as shown in Figure 2.17a. Electrons with opposite spins (Figure 2.17b) are not correlated. HF is

useful to obtain an approximate initial optimized geometry and can save a significant amount of time and costs.

Since electron correlation is not taken into account in HF, efforts to develop more accurate post-Hartree-Fock methods have been initiated. Many methods to compute the correlation energy, each with their own strengths and weaknesses, have been developed. Among these modified HF methods is a correlated method in which calculations start with HF and then correct for correlation. Møller-Plesset perturbation theory, MPn, in which n is the order of correction is one type of the correlated method (non-variational). The higher the order of correction, the higher the computational cost ($\sim N^{10}$ time complexity). The correlated method used in our work is MP2 in which the minimal amount of correlation has been added.

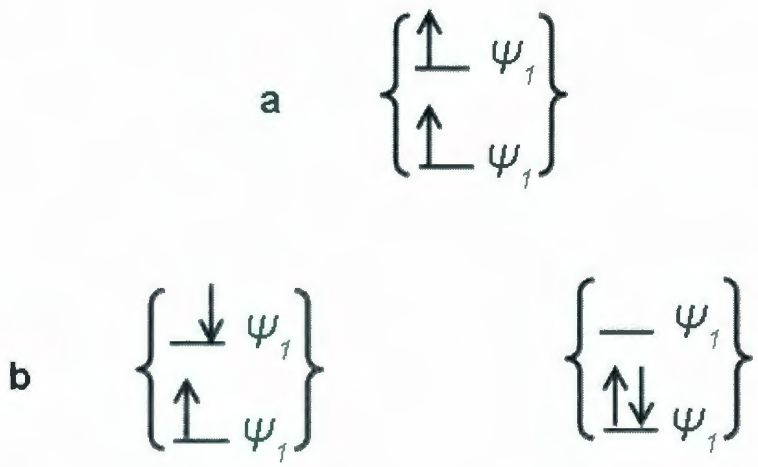

Figure 2.17: electrons with the same spin (a) and electrons with opposite spins (b).

2.2.2 Density Functional Theory (DFT)

DFT, originated by Hohenberg and Kohn,[56] has been a very popular method recently with an acceptable accuracy without extensive computational cost. In DFT, the energy of a system is calculated based on the electron density $\rho(r)$ rather than the wavefunction. Later, Kohn and Sham developed this method for practical applications. DFT methods may contain either empirical data or data from more complex calculations. In this method, the electron density is calculated based on a linear combination of basis functions with a similar mathematical procedure to HF orbitals. A determinant, called Kohn-Sham orbitals, is formed based on these functions that produces the electron density. This electron density is then used to compute the energy. A density functional is hence used to compute the energy from the electron density. A functional is a function of a function, in this case, the electron density and there is a list of different functionals to choose from.

Since Hamiltonian depends on the total number of electrons, electron density is a useful physical observable to work with. A density functional takes the electron density and returns the number of electrons by integrating electron density over all space,

$$N[\rho(r)] = \int \rho(r)dr = n \tag{2.31}$$

in which ρ(r) is a function of three observable (i.e. can be measured through X-ray

diffraction experiments) variables (x,y,z) and ρ(r)dr is the probability of finding an electron in the volume element dr at r. Energy functional can be divided into specific components as shown in Equation 2.32 to facilitate further analysis,

$$E[\rho(r)] = T_{ni}[\rho(r)] + V_{ne}[\rho(r)] + V_{ee}[\rho(r)] + \Delta T[\rho(r)] + \Delta V_{ee}[\rho(r)] \qquad (2.32)$$

where the terms on the right hand side refer, respectively, to the kinetic energy of the non-interacting electrons, the nuclear-electron interaction, the classical electron-electron repulsion, the correction to the kinetic energy deriving from the interacting nature of the electrons, and all non-classical corrections to the electron-electron repulsion energy.

Using ρ, Kohn and Sham could account for exchange-correlation potential. One advantage of DFT is that some portions of electron correlation are considered in the calculation and using appropriate functionals, the results are even similar to MP2 results. DFT calculations are categorized into different classes. One of them is a hybrid method which combines functionals from other methods, producing more accurate results.

Hybrid DFT methods such as B3LYP have been developed in which both exchange and correlation functionals are considered and these are used in this work. The hybrid DFT methods, in particular the B3LYP hybrid density functional, are reliable techniques in terms of both band positions as well as the relative band intensities.[17,25,57–69] The B3LYP functional level of theory could also adequately describe the geometries of small biologically interesting ions. B3LYP has been shown to estimate a good balance

between the electronic exchange and correlation interaction for metal-ligand charged systems by taking into account the charge donation and backdonation. As a result, an accurate geometry optimization can be performed using this functional. Despite the multiphoton character of the IRMPD mechanism, B3LYP has shown reliable results in predicting IR spectra. Because of the incoherent nature of the IRMPD process and the fact that only the few first photons in resonance with the vibrational levels affect the relative intensities of the bands. However, for small ions, a fast energy redistribution may not occur due to a low density of vibrational states and cause significant deviations from the linear absorption spectrum. Also, anharmonic coupling between modes results in a red shift and broadening of the bands.

2.2.3 Basis Sets

The second component of a computational method, the basis set, is a collection of functions to create the molecular orbitals. The larger the basis set, the more complex the calculations will be.

The basis sets used in this research were mainly 6-31+G(d,p) and 6-311++G(d,p). In this notation, 6-31+G(d,p), the first and second sets of numbers (6 and 31, respectively) refer to functions describing core and valence orbitals, respectively. Adding polarization functions (d,p) to the basis set provides more flexibility for the wavefunction to change shape. They often result in more accurate computed geometries

and vibrational frequencies. Although the valence shell of alkali and alkaline-earth metal atoms contains only s-type functions in the electronic ground states, it is suggested to include valence p-type functions in the basis set of these elements. This is due to the fact that in addition to being strong σ-electron donors to electronegative elements, alkali and alkaline-earth metal atoms are also π-electron acceptors. In the absence of the p-type functions, weaker bond strengths are predicted. Longer bond length and larger electric dipole moments are evidence of this phenomenon.[51] Also, including d-type functions in the basis set for molecules containing second-row and heavier main-group elements is essential for the proper description of the equilibrium geometry. Finally, diffuse functions (+) describe the electron far from the nucleus. They are used for describing interactions at long distances, such as van der Waals interactions. For instance, a basis set such as 6-311+G(2d,p) has a triply-split valence representation with two sets of polarization functions and a single set of diffuse functions on heavy atoms, as well as a single set of polarization functions on hydrogen. This basis set represents about as proper a representation as can be applied to small to medium size organic molecules.[51]

2.2.4 Calculation Procedure

The computational procedure throughout this work is as follows. In the first step, geometry optimizations and frequency calculations for numerous structures were

performed at B3LYP/6-31+G(d,p). To examine whether a basis set dependency exists, calculations for some of the species were also carried out using a larger basis set such as 6-311+G(d,p). The results did not show such a dependency, therefore, the smaller basis set was used. All the possible conformers were created manually. Simple HF/6-31+G(d) was initially used to optimize the structures and calculate frequencies in a few cases (such as $(adenine)_2$-M-$(H_2O)_n^+$ where M=H, Li, and K and n=0,1) in order to save time. In addition, for transition metals, Zn cluster ions in Chapter 7, the Gen keyword was used to apply a different basis set to Zn due to its larger size. The Gen keyword allows a user-specified basis set to be used in a Gaussian calculation. Using this keyword at B3LYP, a LANL2DZ basis set was used for Zn while for all other atoms including C, H, N and O a 6-31+G(d,p) was applied to optimize the structures and calculate the vibrational frequencies. Using effective core potential (ECP), the computational costs can be significantly decreased for heavy elements since ECP calculations are restricted to the valence electron system. The core electrons are replaced with an effective potential that eliminates using the core basis functions. This is based on the fact that mainly the valence electrons of an element determine its chemical behavior.[70]

In the next step, thermochemical values were determined using single point calculations at the MP2 method with a 6-311++G(2d,p) basis set. Thermal corrections, the determination of temperature-dependent gas phase conformational population, to enthalpy and free energy values were taken from the B3LYP calculations and added

to the calculated MP2 energies. Enthalpy and free energy values relative to the lowest energy structure were then reported. Equations 2.33 and 2.34 show standard calculations used to obtain the energetics at 298K.

$$H(MP2) = E_e(MP2) + H_{corr}(B3LYP) \tag{2.33}$$

$$G(MP2) = E_e(MP2) + G_{corr}(B3LYP) \tag{2.34}$$

where H_{corr} and G_{corr} are obtained from B3LYP calculations and are defined as

$$H_{corr} = E_{tot} + k_B T \tag{2.35}$$

$$G_{corr} = H_{corr} - TS_{tot} \tag{2.36}$$

and E_{tot} is the summation of translational, rotational, vibrational and electronic energies, Eq. 2.37.

$$E_{tot} = E_t + E_r + E_v + E_e \tag{2.37}$$

2.2.5 Comparison of Experimental IRMPD and Calculated IR Band Intensities and Frequencies

In order to achieve the fragmentation of stronger bonds, multiple photon absorption may be required. This can broaden the observed bands in the IRMPD spectrum because of rotationl bands. Therefore, some information of ionic species in terms

of absorption bands could be buried under a broad peak. Predicted IR absorption spectra can help to uncover the missing bands which are often disregarded.[71]

Choi *et al.*[72] could not observe the O-H asymmetric stretch band for the $NO^+(H_2O)$ ion-molecule complex in the IRMPD spectrum which was predicted to occur at $3671cm^{-1}$ with an intensity 80 percent of that of the symmetric stretch. The detected products from photodissociation of this ion-molecule complex were $NO^+ + H_2O$ which requires at least two photons for dissociation. The possibility of the presence of $N(OH)_2^+$ and $HON(H)O^+$ covalently bound structures was ruled out due to several reasons such as their higher energetics (some 33 kcal mol^{-1})compared to the ion-molecule structure as well as high energy intramolecular hydrogen shifts in order to lead to $NO^+ + H_2O$ products. Therefore, other factors should be responsible for the absence of the O-H asymmetric band. Since the recorded spectra are two-photon dissociation spectra and not absorption spectra, it was hypothesized that ν_3 multiphoton absorption process is not as efficient as ν_1 and also clusters excited in this mode do not efficiently dissociate. This could be explained by a slower relaxation of ν_3 due to its weaker coupling to the intermolecular stretch compared to ν_1, causing variations in predissociation rates. In the two-photon absorption action spectra if IVR from the ν_3 levels takes more time than the laser pulsewidth (10 ns), the second photon would not be absorbed; therefore no dissociation would occur. In fact, this suggests a faster than 10 ns IVR rates for ν_1. For larger clusters, i.e. doubly/ triply hydrated ion complex, the asymmetric stretching vibrations were observed. This can

be explained by a weaker H_2O binding energy which allows the production of more hot ions. Only a single photon would be enough to dissociate these vibrationally excited clusters.

In addition, Pankewitz *et al.*[71] observed a very weakly detectable signal for the strongly infrared active ν_3 (H_2O) mode ($I(\nu_3)$:$I(\nu_1)$=1:9) in their experimental photofragmentation spectrum of $NH_4^+(H_2O)$. This is in contrast with the fact that the asymmetric O-H stretching band in the spectra of gaseous water is stronger than $\nu_1(H_2O)$ by a factor of 14.5-21.9.[73,74] The published action spectra of other singly hydrated cations estimate $I(\nu_3)$ to be twice as $I(\nu_1)$. See Table 2.1 which is taken from Pankewitz *et al.*[71] While the data collected by tagging with weakly binding ligands such as Ar, N_2 and C_6F_6 experiments show an increase in the intensity of the asymmetric O-H stretching band, IRMPD experiments for $NO^+(H_2O)$ and $NH_4^+(H_2O)$ in which the cluster binding is strongest, show extremely weak bands for this mode. It was claimed that the intensity of ν_3 qualitatively anticorrelates with the activation energy for the lowest possible fragmentation pathway so the intensity of ν_3 is stronger when the binding to the water is weaker. Furthermore, the chemical nature of the cationic molecular counterpart in these two clusters affects the ν_1 mode more than ν_3, mainly because in the ν_1 mode, the water's O atom moves parallel to the direction of the two heavy atoms (O and N), whereas in the ν_3 mode it moves perpendicularly.

The calculated frequencies are usually blue shifted from the experimental IRMPD values due to applying the harmonic oscillator approximation. The coupling of vibra-

Cation-water complex	**Exp. I $(\nu_3)/(\nu_1)$**	**Binding energies (kJ mol^{-1}) 300K**
$NO^+(H_2O)$	~0	75
$NH_4^+(H_2O)$	0.11	72.0, 86.2
$Na^+(H_2O)Ar$	1.57	11.6
$Na^+(H_2O)(C_6F_6)_3$	~1	52 (8)[a]
$K^+(H_2O)Ar$	2.44	7.2
$Cs^+(H_2O)$	~0.5-1	57
$Cs^+(H_2O)$ Ar	2.04	-
$C_6H_6^+(H_2O)$	~0.3	59(12)
$C_6H_6^+(H_2O)N_2$	1	-

Table 2.1: A comparison of the ratio of $\nu_3(H_2O)$: $\nu_1(H_2O)$ intensities from action spectra and the enthalpy change for the lowest dissociation channel for cation water complexes (reference 71 and references herein).

[a]Calculated Value (0K)

tional modes due to anharmonic effects are not taken into account in the harmonic approximation. Using a scaling factor, based on comparing the experimental and calculated frequencies is common. A "dual scaling" has been introduced by Halls *et al.*[75] which applies a smaller scaling factor for the high-frequency modes (larger than 1800cm $^{-1}$) due to their larger anharmonicity effects compared to the low-energy modes. Furthermore, by comparing the experimental and computational data, modified theoretical methods could be derived.

Bibliography

1. Isenor, N. R.; Richardson, M. C. *Appl. Phys. Lett.* **1971**, *18*, 224.
2. Isenor, N. R.; Merchant, V.; Hallsworth, R. S.; Richardson, M. C. *Can. J. Phys.* **1973**, *51*, 1281.
3. Bomse, D. S.; Woodin, R. L.; Beauchamp, J. L. *J. Am. Chem. Soc.* **1979**, *101*, 5503.
4. Peiris, D. M.; Cheeseman, M. A.; Ramanathan, R.; Eyler, J. R. *J. Phys. Chem.* **1993**, *97*, 7839.
5. Woodin, R. L.; Bomse, D. S.; Beauchamp, J. L. *J. Am. Chem. Soc.* **1978**, *100*, 3248.
6. Odeneye M. A., Stace A. *Phys. Chem. Chem. Phys.* **2005**, *7*, 998.
7. Oomens, J.; van Roij, A. J. A.; Meijer, G.; Helden, G. V. *Astrophys J.* **2000**, *542*, 404.
8. Jones, W.; Boissel, P.; Chiavarino, B.; Crestoni, M. E.; Fornarini, S.; Lemaire, J.; Maitre, P. *Angew. Chem. Int.* **2003**, *42*, 2057.
9. Eyler, J. R. *Mass Spectrom. Rev.* **2009**, *28*, 448.
10. Fridgen, T. D.; McMahon, T. B.; MacAleese, L.; Lemaire, J.; Maitre, P. *J. Phys. Chem. A* **2004**, *108*, 9008.
11. Asmis, K. R.; Pivonka, N. L.; Santambrogio, G.; Brummer, M.; Kaposta, C.; Neumark, D. M.; Woste, L. *Science* **2003**, *299*, 1375.
12. Marta, R. A.; McMahon, T. B.; Fridgen, T. D. *J. Phys. Chem. A* **2007**, *111*, 8792.
13. Clair, R, L.; McMahon, T. B. *Can. J. Chem.* **1980**, *58*, 863.
14. Fridgen, T. D. *Mass Spectrom. Rev.* **2009**, *28*, 586.

15. Elias, L. R.; Fairbank, W. M.; Madey, J. M. J.; Schwettman, H. A.; Smith, T. I. *Phys. Rev. Lett.* **1976**, *36*, 717.; Deacon, A.G.; Elias, L.R.; Madey, J.M.J.; Ramian, G.J.; Schwettman, H.A.; Smith, T.I. *Phys. Rev. Lett.* **1977**, *38*, 892.; Colson, W.B.; Sessler, A.M. *Annu. Rev. Nucl. Part. Sci.* **1985**, *35*, 25.; O'Shea, P.G.; Freund, H.P. *Science*, **2001**, *292*, 1853.; Colson, W.B.; Johnson, E.D.; Kelley, M.J.; Schwettman, H.A. *Phys. Today*, **2002**, *55*, 35.

16. Haub, J.G.; Hentschel, R.M.; Johnson, M.J.; Orr, B.J. *J. Opt. Soc. Am. B* **1995**, *12*, 2128.; Strossner, U.; Meyn, J-P.; Wallenstein, R.; Urenski, P.; Arie, A.; Rosenman, G.; Mlynek, J.; Schiller, S.; Peters, A. *J. Opt. Soc. Am. B* **2002**, *19*, 1419.; van Herpen, M.M.J.W.; Bisson, S.E.; Ngai, A.K.Y.; Harren, F.J.M. *Appl. Phys. B Lasers Opt.* **2004**, *78*, 281.

17. Okumura, M.; Yeh, L. I.; Lee, Y. T. *J. Chem. Phys.* **1985**, *83*, 3705.

18. MacAleese, L.; Maitre, P. *Mass spectrom Rev.* **2007**, *26*, 583.

19. Black, J. G.; Yablonovitch, E.; Bloembergen, N.; Mukamel, S. *Phys. Rev. Lett.* **1977**, *38*, 1131.

20. Grant, E. R.; Schulz, P. A.; Sudbo, A. S.; Shen, Y. R.; Lee, Y. T. *Phys. Rev. Lett.* **1978**, *40*, 115.

21. Bagratashvili, V. N.; Letokhov, V. S.; Makarov, A. A.; Ryabov, E. A.; *Multiple Photon Infrared Laser Photophysics and Photochemistry* (Gordon and Breach, New York, **1985**).

22. Nesbitt, D. J.; Field, R. W. *J. Phys. Chem.* **1996**, *100*, 12735.

23. Oomens, J.; Sartakov, B. G.; Meijer, G.; von Helden, G. *Int. J. Mass Spectrom.* **2006**, *254*, 1.

24. Fridgen, T. D.; McMahon, T. B. *Encyclopedia of Mass Spectrometry*, **2005**, vol. *4*, Gross and Caprioli, Ed.

25. Lemaire, J.; Boissel, P.; Heninger, M.; Mauclaire, G.; Bellec, G.; Mestdagh, H.; Simon, A.; Le Caer, S.; Ortega, J. M.; Glotin, F.; Maitre, P. *Phys. Rev. Lett.* **2002**, *89*, 273002.

26. Rajabi, K.; Fridgen, T. D. *J. Phys. Chem. A* **2008**, *112*, 23.

27. Bakker, J. M.; Thierry, B.; Lemaire, J.; Scuderi, D.; Maitre, P. *J. Phys. Chem. A* **2007**, *111*, 13415.

28. Paul, W. *Rev. Mod. Phys.* **1990**, *62*, 531.

29. de Hoffmann, E.; Stroobant, V. **2007**, *Mass Spectrometry*, Ed Third, John Wiley & Sons, Ltd., Chapter 2, pp 100-116.

30. March, R. E.; Todd, J. F. J. (Eds) *Practical Aspects of Ion Trap Mass Spectrometry*, **1995**, *Vols 1, 2 and 3*, CRC Press, Boca Raton, FL.

31. Todd, J. F. *Practical Aspects of Ion Trap Mass Spectrometry*, **1995**, *3*, 3.

32. Mathieu, E. *J. Math. Pure Appl. (J. Liouville)*, **1868**, *13*, 137.

33. March, R. E. *J. Mass Spectrom.* **1997**, *32*, 351.

34. Payne, A. H.; Glish, G. L. *Methods in Enzymology*, **2005**, *402*, 109.

35. Aleese, L. M.; Simon, A.; McMahon, T. B.; Ortega, J-M.; Scuderi, D.; Lemaire, J.; Maitre, P. *Int. J. Mass Spectrom.* **2006**, *249*, 14.

36. Marshall, A. G.; Hendrickson, C. L.; Jackson, G. S. *Mass Spectrom. Rev.* **1998**, *17*, 1.

37. Feng, X.; Siegel, M. M. *Anal. Bioanal. Chem.* **2007**, *389*, 1341.

38. Barrow, M. P.; Burkitt, W. I.; Derrick, P. J. *Analyst* **2005**, *130*, 18.

39. McIver, R. T. *Rev. Sci. Instrum.* **1970**, *41*, 555.

40. McIver, R. T.; Hunter, R. L.; Bowers, W. D. *Int. J. Mass Spectrom. Ion Processes* **1985**, *64*, 67.

41. Kebarle, P. *J. Mass Spectrom.* **2000**, *35*, 804.

42. Henry, K. D.; Williams, E. R.; Wang, B. H.; McLafferty, F. W.; Shabanowitz, J.; Hunt, D. F. *Proc. Natl. Acad. Sci. USA* **1989**, *86*, 9075.

43. Mehdian, H.; Jafari, S.; Hasanbeigi, A.; Ebrahimi, F. *Nucl. Instrum. Methods Phys. Res., Sect. A* **2009**, *604*, 471.

44. Polfer, N. C.; Oomens, J. *Mass Spectrom. Rev.* **2009**, *28*, 468.

45. Sorokina, I. T.; Vodopyanov, K. L. *Top. Appl. Phys.: Solid-State Mid-Infrared Laser Sources* **2003**, *89*, 557.

46. *Brilliant/ Brilliant B Instruction Manual*, Quantel, Issue # 5.1.

47. Dmitriev, V. G.; Gurzadyan, G. G.; Nikogosyan, D. N. *Handbook of Nonlinear Optical Crystals* **1991**, *64*, Ed. A E Siegman (New York: Springer) p 81 and references therein.

48. Rajabi, K.; Easterling, M.; Fridgen, T. D. *J. Am. Mass. Spectrom.* **2009**, *20*, 411.

49. Simon, A.; MacAleese, L.; Maitre, P.; Lemaire, J.; McMahon, T. B. *J. Am. Chem.*

Soc. **2007**, *129*, 2829.

50. Hehre, W. J.; Radom, L.; Schleyer, P. V. R.; Pople, J. A. *Ab Initio Molecular Orbital Theory*, **1985**, John Wiley & Sons Ltd.

51. Hehre, W. J. *Practical Strategies for Electronic Structure Calculations*, **1995**, Wavefunction, Irvine, CA.

52. Cramer, C. J. *Essentials of Computational Chemistry: Theories and Models*, **2002**, Wiley.

53. *Encyclopedia of Computational Chemistry*, **1998**, *5 Volumes*, John Wiley & Sons Ltd.

54. Young, D. *Computational Chemistry: A Practical Guide for Applying Techniques to Real World Problems*, **2001**, John Wiley & Sons Ltd.

55. Schrodinger, E. *Ann. Physik.* **1926**, *79*, 361.

56. Hohenberg, P; Kohn, W. *Phy. Rev.* **1964**, *136*, 864.

57. Maitre, P.; Le Caer, S.; Simon, A.; Jones, W.; Lemaire, J.; Mestdagh, H. N.; Heninger, M.; Mauclaire, G.; Boissel, P.; Prazeres, R.; Glotin, F.; Ortega, J. M. *Nucl. Instrum. Methods. Phys. Res. Sect. A* **2003**, *507*, 541.

58. Polfer, N. C.; Paizs, B.; Snoek, L. C.; Compagnon, I.; Suhai, S.; Meijer, G.; von Helden, G.; Oomens, J. *J. Am. Chem. Soc.* **2005**, *127*, 8571.

59. Polfer, N. C.; Oomens, J; Moore, D. T.; von Helden, G.; Meijer, G.; Dunbar, R. C. *J. Am. Chem. Soc.* **2006**, *128*, 517.

60. Stearns, J. A.; Boyarkin, O. V.; Rizzo. T. R. *J. Am. Chem. Soc.* **2007**, *129*, 13821.

61. Bush, M. F.; Oomens, J.; Williams, E. R. *J. Phys. Chem. A* **2009**, *113*, 431.

62. Heaton, A. L.; Bowman, V. N.; Oomens, J.; Steill, J. D.; Armentrout, P. B. *J. Phys. Chem. A* **2009**, *113*, 5519.

63. Moision, R. M.; Armentrout, P. B. *J. Phys. Chem. A* **2002**, *106*, 10350.

64. Moision, R. M.; Armentrout, P. B. *Phys. Chem. Chem. Phys.* **2004**, *6*, 2588.

65. O'Brien, J. T.; Prell, J. S.; Steill, J. D.; Oomens, J.; Williams, E. R. *J. Am. Chem. Soc.* **2009**, *131*, 3905.

66. Rodgers, M. T.; Armentrout, P. B. *J. Am. Chem. Soc.* **2000**, *122*, 8548.

67. Rodgers, M. T.; Armentrout, P. B. *Int. J. Mass Spectrom.* **2007**, *267*, 167.

68. Bauschlicher, C. W.; Langhoff, S. R. *Spectrochimica Acta A* **1997**, *53*, 1225.

69. Hoyau, S.; Norrman, K.; McMahon, T. B.; Ohanessian, G. *J. Am. Chem. Soc.* **1999**, *121*, 8875.

70. Dolg, M. *Modern Methods and Algorithms of Quantum Chemistry, Proceedings*, 2nd Edition, J. Grotendorst (Ed.), John von Neumann Institute for Computing, Julich, NIC Series, **2000**, *3*, pp. 507-540.

71. Pankewitz, T.; Lagutschenkov, A.; Niedner-Schatteburg, G.; Xantheas, S. S.; Lee, Y. *J. Phys. Chem.* **2007**, *126*, 074307.

72. Choi, J.; Kuwata, K. T.; Haas, B.; Cao, Y.; Johnson, M. S.; Okumura, M. *J. Chem Phys.* **1994**, *100*, 7153.

73. Galabov, B.; Yamaguchi, Y.; Remington, R. B.; Schaefer, H. F. *J. Phys. Chem. A* **2002**, *106*, 819.

74. Rothman, L. S.; Gamache, R. R. *et al. J. Quant. Spectrosc. Radiat. Transf.* **1992**, *48*, 469.

75. Halls, M. D.; Velkovski, J.; Schlegel, H. B. *Theor. Chem. Acc.* **2001**, *105*, 413.

Chapter 3

Structures of Aliphatic Amino Acid Proton-Bound Dimers by IRMPD Spectroscopy in the 700 to 2000 cm^{-1} Region

3.1 Introduction*

In recent years there has been an enormous amount of work dedicated to studying the effects of noncovalent interactions such as normal and ionic hydrogen bonding on the structures of molecules which are of biological and pharmacological interest[1]

*This Chapter has been published as K. Rajabi and T. D. Fridgen, *J. Phys. Chem. A* **2008**, 112, 23-30.

as well as supermolecular structures[2–4] in aqueous solutions. The combination of experiment accompanied with ab initio calculations has provided a growing wealth of fundamental knowledge in this area.[5,6]

Of equal importance to knowing the structures of the aqueous phase molecules is understanding the role that solvent has in this structure. To this end, rotational, vibrational and electronic spectra of molecules isolated in the gas phase[7,8] or vibrational spectra of species frozen in cryogenic matrices[9–11] has helped in determining the solvent-free structures. For amino acids such as glycine,[9,12,13] alanine,[10,14] valine,[11,15] and arginine[16] non-zwitterion structures are observed to be the only structures present in the gas phase and islolated in solid argon matrices and theory predicts the non zwitterion structure to be the lowest in energy.

Protonation reactions are fundamental in aqueous solutions containing compounds with heteroatoms such as amino acids. In fact, protonation of biological compounds is of a great interest as it is the initiating step in hydrolysis of amides, peptides and proteins as well as carbohydrates at biological pH.[17] Protonation obviously has an important effect on the electronic and dynamic structure of proteins as well as their conformational structure. Their biological activities are dependent upon three-dimensional structures and therefore protonation plays an important role in the biological activity of proteins. Completely understanding the role of particular conformations in biological activity may be facilitated by studying the solvent-free fundamental building blocks and this is possible because of existing modern ionization methods

in mass spectrometry. Gas phase studies of proteins can be useful to determine the role of protons in stabilizing protein conformation and can also suggest the role of solvent on protein conformation. For example, ion mobility measurements have been used to study helix formation in the gas phase for a series of alanine/glycine-based peptides.[18] In this study, solvent-free peptide ions were produced by electrospray and their conformations determined using ion mobility mass spectrometry. The authors found a reduction in the amount of helix due to interaction of residues with polar side chains for the Ac-$A_3G_{12}KH^+$ peptide, possibly due to hydrogen bonding between the backbone and polar side chains that stabilizes the nonhelical globular conformations.

Numerous studies have been performed on relative proton affinities of amino acids.[19–26] Temperature dependent equilibrium constants and binding energies for amino acid proton-bound dimers such as the glycine proton-bound dimer, have been recently studied using pulsed-ionization high-pressure mass spectrometry (PHPMS).[27] Comparing the experimental thermochemistries with those predicted by ab initio methods can provide information about structural aspects of these fundamental biological species.

Proton bound dimers are also of great interest since they contain a principle intermolecular interaction-the ionic hydrogen bond-noncovalent interactions with strengths of up to about 150 kJ mol^{-1}. They have received much attention in the past mostly from thermochemical and computational studies.[28] Most studies are geared toward understanding the structural aspects of the proton bound dimers as well as their

strengths. Infrared spectroscopy is a sensitive technique for studying the structures of any molecular or ionic species. Proton-bound dimers have been the topic of many recent IRMPD spectroscopic studies.[29–36] Dimers of amino acids which are bound by protons or metal ions are important from a biochemical point of view due to proton and metal ion mobility issues as well as the interest in the strong ionic hydrogen bonding or metal ion binding that exists in these clusters. Small proton-bound dimers are models for larger systems where strong ionic hydrogen bonding exists, such as in proteins. A few IRMPD spectroscopic studies of protonated and solvated amino acids,[37] amino acid proton bound dimers,[38] and complexes of amino acids with sodium ion[39] in the gas-phase have appeared recently. Most recently using IRMPD spectroscopy and computational methods, Bush *et al.*[40] have observed gas-phase zwitterionic arginine when it is bound to metal ions such as Na^+ and K^+. Here we report on the IRMPD spectra of amino acid proton-bound dimers with aliphatic side chains in the 700-2100 cm^{-1} range, as well as the mixed alanine/glycine proton-bound dimer. The spectra are compared to those calculated by DFT methods and discussed in terms of the structures of the proton-bound dimers.

3.2 Methods

3.2.1 Experimental

The combination of a Bruker Esquire 3000 quadrupole ion trap mass spectrometer equipped with an electrospray source coupled to the mid-Infrared FEL at CLIO,[41,42] was used and has been described previously.[43] Solutions containing 0.05 M of glycine, 0.03 M of alanine, 0.030 M valine, and mixture of glycine/alanine with 1:1 ratio were prepared in 18 Mohm (millipore) water. The amino acids were obtained from Aldrich and have been used without further purification. The aqueous amino acid solutions were electrosprayed into a Bruker Esquire 3000 quadrupole ion trap mass spectrometer and accumulation times varied between 150-300 ms. There was no organic phase or acid added to the solution. It was found that by adding acid or an organic layer to the solution, the ion intensity for our proton-bound dimers was depleted and the protonated amino acids were the main species electrosprayed. The ions of interest, proton-bound dimers, were isolated by resonantly ejecting ions of all other masses. The mass spectrometer was modified[43] to include a Brewster-angle window through which passes the monochromatic radiation with a bandwidth of 0.3-0.5 percent of the spectral bandwidth. The FEL was scanned using <5 cm^{-1} increments and the experimental IRMPD spectra in the 700- 2100 cm^{-1} energy range were recorded. Ions were irradiated for between 200-500 ms with the CLIO FEL. If the particular wavelength of the FEL is resonant with a fundamental mode of the trapped ion, dissociation is

observed. On the contrary, if the FEL is tuned such that there is no absorption, no dissociation of the ion is observed. The IRMPD spectra reported are the extent of dissociation plotted against the wavenumber value of the radiation impinging on the ions from the FEL. The resulting IRMPD action spectra were not normalized for the power of the free electron laser.

3.2.2 Computational

The Gaussian 03 suite of programs was used.[44] Geometries were optimized and vibrational spectra were calculated using the B3LYP hybrid density functional method and the 6-31+G(d,p) basis sets. For comparison, the lowest-energy structure of the glycine proton-bound dimer was calculated also using the 6-311++G(d,p) basis set. Many different structures of the proton-bound dimers were considered including zwitterionic structures. Here we show the structures and spectra of the lowest-energy proton-bound dimers. The calculated frequencies were scaled using a scale factor of 0.96.[45] Free energy differences at 298 K relative to the lowest energy isomer are reported for all proton-bound dimers using B3LYP/6-31+G(d,p). For comparison, single-point calculations were computed using the 6-311+G(2df,p) basis set and the thermochemistry and entropies were taken from the B3LYP/6-31+G(d,p) calculations (herein denoted B3LYP/6-311+G(2df,p)//B3LYP/6-31+G(d,p)). These latter calculations were done on the glycine proton-bound dimer and the alanine-glycine

mixed proton-bound dimer.

3.3 Results and Discussion

3.3.1 Electrospray and IRMPD of Protonated Amino Acid Dimers

Electrospraying solutions of glycine, alanine or valine mainly produced the protonated monomers although there was significant intensity for the proton-bound dimer as well as a little trimer in all cases. For the solution containing both glycine and alanine the m/z 165 peak corresponding to the mixed proton-bound dimer was smaller than the m/z 151 and 179 peaks corresponding to the glycine and alanine proton-bound dimer, respectively. The proton-bound dimer intensities were small, $<5\times10^5$ counts for the homogeneous proton-bound dimers and $\sim10^4$ counts for the alanine/glycine proton-bound dimer. Upon irradiation of the isolated proton-bound dimers with the CLIO FEL, the only dissociation observed was the expected loss of neutral amino acid. For the alanine/glycine proton-bound dimer, loss of neutral glycine was the only dissociation observed since glycine has a smaller proton affinity. The results for each amino acid proton-bound dimer are discussed separately.

3.3.2 Glycine Proton-Bound Dimer

The experimental IRMPD spectrum of the glycine proton-bound dimer is shown in Figure 3.1 along with the four lowest energy glycine proton-bound dimer structures and their predicted spectra at the B3LYP/6-31+G(d,p) level and basis set. The difference in free-energies at 298 K are also shown compared to structure A. The first three of these structures are the same as those found by Raspopov and McMahon[27] and are similar in relative energies. They found structures B and C to be 12.8 and 12.7 kJ mol^{-1} higher in free-energy (the DFT hybrid functional MPW1PW91/6-31+G(d)) than structure A. Structure D, in Figure 3.1 was determined to be 23.2 kJ mol^{-1} higher in energy and has not been previously reported. The B3LYP/6-311+G(2df,p)//B3LYP/6-31+G(d,p) calculated free energies also confirm the energetic ordering of the proton-bound dimers (see Figure 3.1). The symmetric double zwitterion structure,[27] by our calculations, is 24 kJ mol^{-1} higher in free energy than A. Also shown in Figure 3.1 is the computed IR spectrum using the 6-311++G(d,p) basis set for structure A, also scaled by 0.96, showing that there is no dependence on the basis set of the computed IR spectrum.

Comparison of the experimental IRMPD spectrum and the calculated IR spectra shows that there is much better agreement between the most stable structure, A, and the experimental IRMPD spectrum. This better agreement between the experimental spectrum and that predicted for structure A in itself does not absolutely confirm the structure of the proton-bound dimer to be that of A. Clearly there is a significant red-

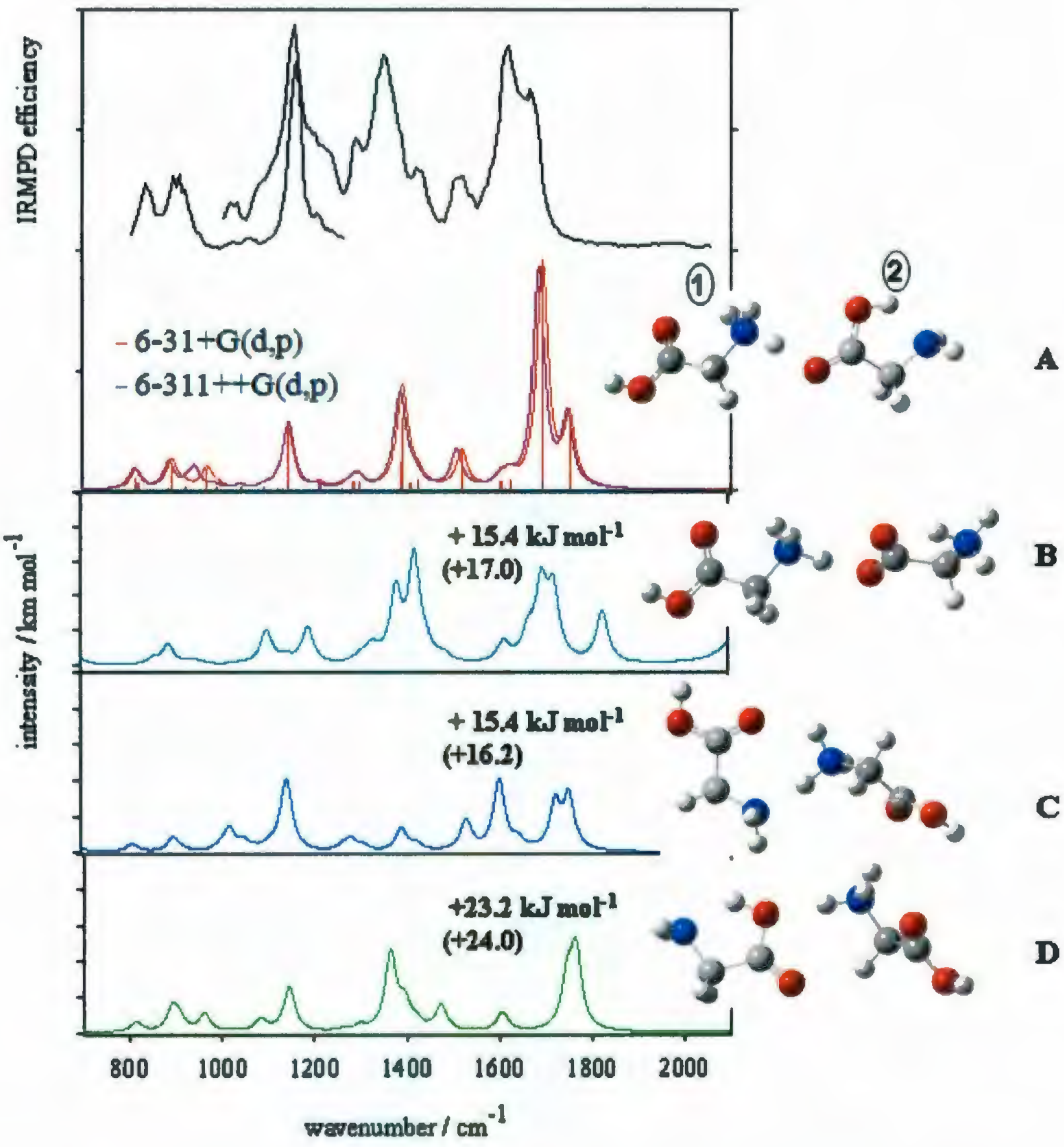

Figure 3.1: IRMPD spectrum of the glycine proton-bound dimer as well as the B3LYP/6-31+G(d,p) predicted spectra for the four lowest-energy structures. B3LYP/6-311+G(2df,p)//B3LYP/6-31+G(d,p) relative free energies compared to A are in parentheses.

shift of the experimental spectrum with respect to the predicted spectrum. However, comparison of the experimental spectrum for the glycine proton bound dimer with the alanine and valine proton bound dimers (section 3.3.6) shows a clear similarity and all of the proton-bound dimers studied here are most likely to have a similar structure about their central part.

It should be noted that, based on our computed value for ΔG between structures A,B and C, both B and C would be expected to contribute only about 0.2 percent to the mixture at 298 K. The C=O stretching bands at 1666 and 1620 cm^{-1} observed in the experimental IRMPD spectrum are in agreement with those calculated for structure A (see Table 3.1 and Figure 3.1). It is expected that the C=O stretch is red shifted from the neutral position since the C=O bond is weakened due to the positive charge. The C=O group involved in the ionic hydrogen bond is expected to be more red-shifted since it is bound strongly to the proton. Other assignments based on comparison to the experimental spectrum, the predicted spectra, and from typical assignments of neutrals are made in Table 3.1. In this table, the frequencies for neutral glycine monomer are also shown from Stepanian and coworkers.[9] In their work, different conformers of neutral glycine were observed based on matrix isolation infrared spectra.

Oh *et al.*[38] have recorded an IRMPD spectrum of electrosprayed glycine proton-bound dimers using an OPO laser in the 3050-3800 cm^{-1} range at 27°C. They assigned the species responsible for the infrared spectrum to structure C in Figure 3.1. In the

Vibrational modes	Experimental IRMPD (cm^{-1})	Predicted Spectrum (A)	Neutral glycine[11]
CO stretch (g1)	1666 sh	1751	1779
CO stretch (g2)	1620	1692	-
NH_3 d-deform (g1)	1521	1624	1630
NH_2 bend (g2)		1604	
NH_3 s-deform	1435 sh	1517	-
COH bending/CH_2 bend (g2)	1356	1391	-
COH bend/C-C stretch (g1)		1388	-
CH_2 s-deform (g2)	1290 sh	1299	-
CH_2 s-deform (g1)		1284	-
C-O str/COH bend (g1)	1158	1190	-
COH oop bend (g2)	1032	967	-
NH_2 wag/CH_2 d-deform (g2)	908	892	-
NH_2 wag/C-C str (g2)	832	811	-

Table 3.1: The experimental and calculated IR absorption wavenumbers in cm^{-1} for glycine proton-bound dimers. sh=shoulder, g1=glycine labelled 1 in Figure 3.1, g2=glycine labelled 2 in Figure 3.1.

inset of Figure 3.2 is a comparison of the computed spectra for structures A, B, and C as well as the experimental spectrum of Oh *et al.*[38] Price *et al.*[46] also determined that structure C was the lowest energy structure using MP2/3-21G(d,p). However, neither group had considered structure A for the proton-bound dimer of glycine. We repeated the calculation on structure A using MP2/3-21G(d)[46] and found that it is lower by a similar amount, 14.1 kJ mol^{-1}. It is apparent by inspecting the inset of Figure 3.2 that their experimental IRMPD[38] spectrum is at least comparable to that predicted for structure A. In their spectrum, the two observed features are the OH stretch (of g1) at about 3580 cm^{-1} and the NH stretch (of g2) at 3370 cm^{-1}. Also predicted to occur in this experimental region are strong bands at 3180 cm^{-1} (NH str of g1) and at 3040 cm^{-1} (OH str of g2) which are probably not observed due to the weakened power from the OPO laser at the limits of its range. Note that this OH stretch predicted to occur at 3040 cm^{-1} is red-shifted from a normal OH stretch due to hydrogen bonding with the amino nitrogen. Based on the additional computational data, our infrared spectrum in the 800 to 2000 cm^{-1} range and the recent equilibrium studies,[27] it is clear that the structure of the glycine proton bound dimer is most likely that of structure A.

Also shown in Figure 3.2 is the computed complete IR spectrum from 400 to 3800 cm^{-1}. It would be beneficial to have data in the 2000 to 3200 cm^{-1} range as this is probably the best region to be able to differentiate between the possible structures of the amino acids. The asymmetric stretching vibration of the central, binding, proton

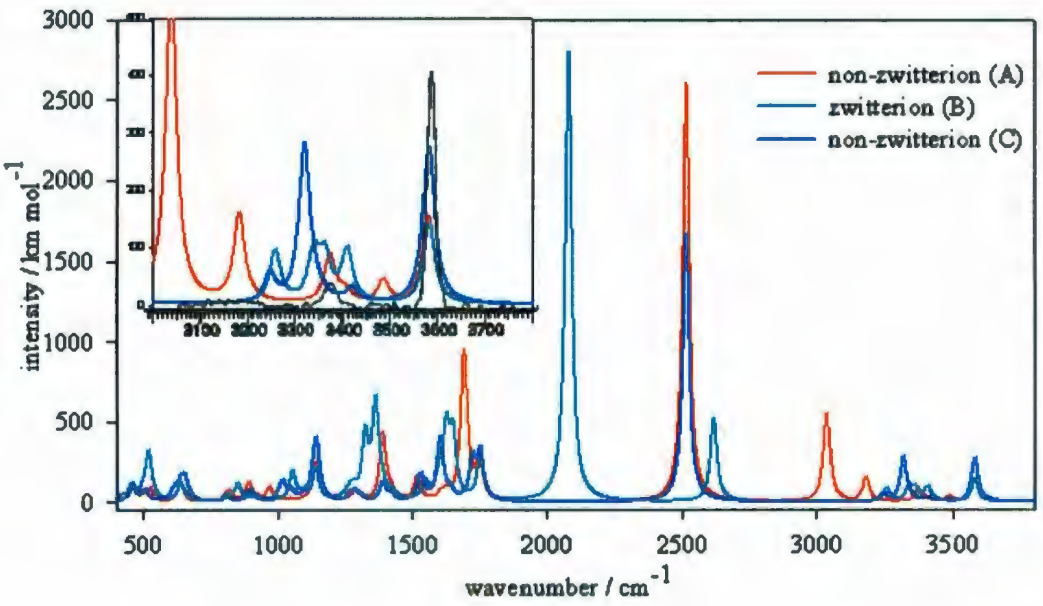

Figure 3.2: Calculated infrared spectra for the three lowest-energy structures for the glycine proton-bound dimer at B3LYP/6-31+G(d,p) also showing the 2000-3800 cm^{-1} region where it may be more likely to be able to distinguish between isomeric structures. In the inset the experimental IRMPD spectrum (in black) from Oh *et al.*[38] is compared with the computed spectra.

between the two amino acids is expected to occur in this region based on calculations.

3.3.3 Alanine Proton-Bound Dimer

In Figure 3.3 are presented the four lowest energy structures for the alanine proton-bound dimer which were predicted using B3LYP/6-31+G(d,p) as well as the difference

in free-energies at 298 K compared to structure A. The structures are similar to those of the glycine proton-bound dimer where structure A is calculated to be the most stable. The predicted IR spectrum for structure A shows good agreement with the

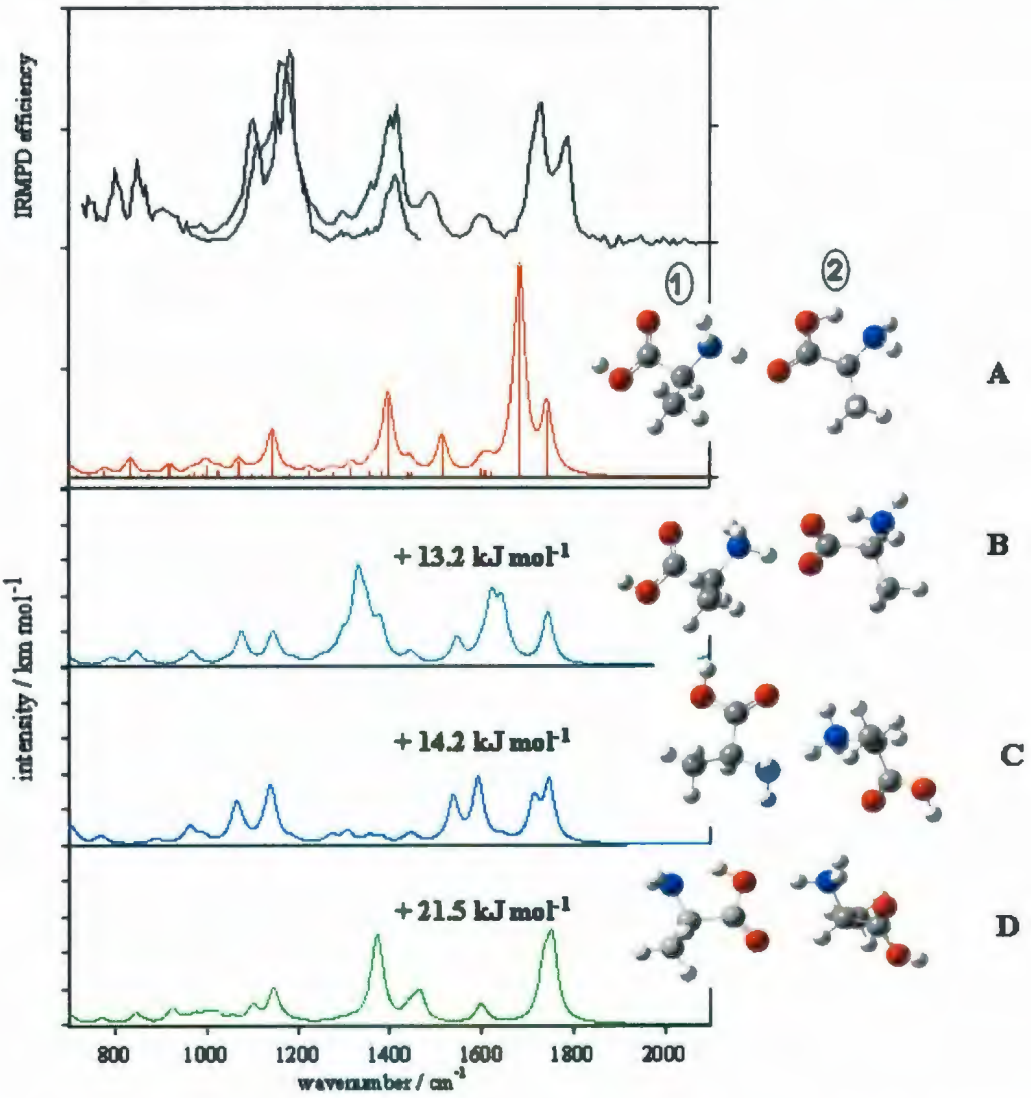

Figure 3.3: IRMPD spectrum of the alanine proton-bound dimer as well as the B3LYP/6-31+G(d,p) predicted spectra for the four lowest-energy structures.

experimental IRMPD spectrum in the 700-2000 cm^{-1} region (see Figure 3.3). Similar to the glycine proton-bound dimer, the C=O stretching absorptions in the alanine proton-bound dimer are slightly red-shifted compared to that of the neutral amino acid[10] (see Table 3.2).

Vibrational modes	**Experimental IRMPD (cm $^{-1}$)**	**Predicted Spectrum (A)**	**Neutral alanine[10]**
CO stretch (a1)	1787	1742	1787
CO stretch (a2)	1730	1683	-
NH_3 d-deform (a1)	1593	1609/1621	-
NH_2 bend (a1)	-	1598	-
NH_3 s-deform	1489	1515	1642
COH bend (a2)	1416sh	1397	-
C-O str/COH bend (a1)	1182	1141	-
NH_3 rock (a1)	1113sh	1120/1098	1117/1153
C-N str (a2)	-	1098	-
NH_2 wag (a2)	850/756/743	832	852

Table 3.2: The experimental and calculated IR wavenumber positions in cm^{-1} for alanine proton-bound dimers. sh=shoulder, a1=alanine labelled 1 in Figure 3.3, a2=alanine labelled 2 in Figure 3.3.

It is puzzling that in the 1000-1300 cm^{-1} range the experimental intensities are

consistently larger than predicted. The problem could be that the normal mode approximation neglects or underestimates coupling between the modes in this region and, perhaps, the stretching motion associated with the proton. This larger than estimated intensity was also observed for the glycine proton-bound dimer (Figure 3.1) and the valine proton-bound dimer (Figure 3.4).

3.3.4 Valine Proton-Bound Dimer

The experimental IRMPD spectrum and calculated IR spectra for the lowest energy structures of the valine proton-bound dimers are shown in Figure 3.4. The calculated most stable structure (structure A) is similar to the glycine and alanine proton-bound dimers discussed above. Absorptions for the C=O stretching at 1792 and 1721 cm^{-1} are observed at experimental IRMPD spectrum which are in agreement with the calculated IR spectra at 1740 and 1679 cm^{-1}. For neutral valine, the C=O stretching absorption is reported[11] to occur at 1762 cm^{-1}. In Table 3.3, a comparison of our calculated and experimental frequencies for the valine proton-bound dimer as well as experimental frequencies for neutral valine monomers are listed.

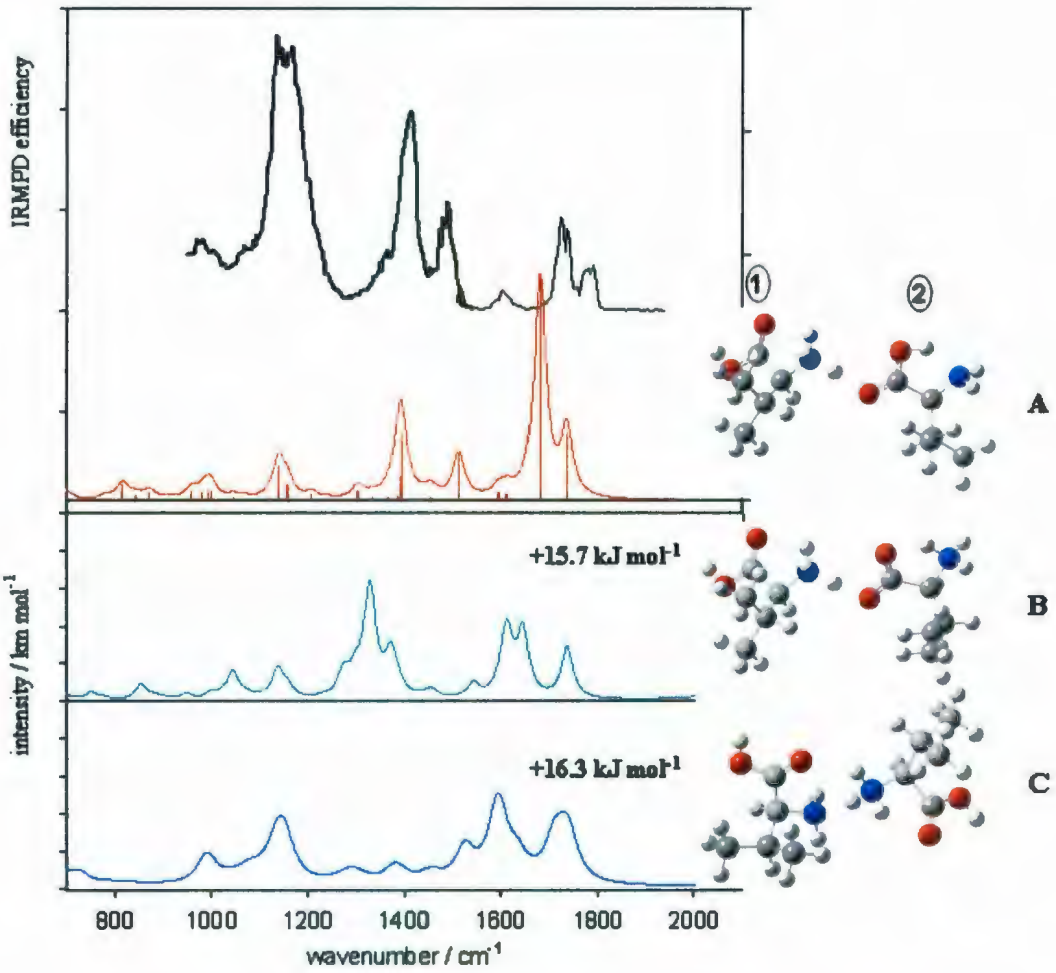

Figure 3.4: IRMPD spectrum of the valine proton-bound dimer as well as the B3LYP/6-31+G(d,p) predicted spectra for the three lowest-energy structures.

Vibrational modes	Experimental IRMPD (cm^{-1})	Predicted Spectrum (A)	Neutral valine[11]
CO stretch (v1)	1792	1735	1762
CO stretch (v2)	1721	1679	-
NH_3 d-deform (v1)	1602	1637	-
NH_2 bend (v2)	-	1594	-
NH_3 s-deform	1488	1512	-
COH bend (v2)	1414	1392	-
COH bend/$CH_{2/3}$ deform (v1)	1166	1157	-
COH bend/NH_3 rock (v1)	-	1138	-
OH oop (v2)	981	999/993	-
C-N str (v1)	-	980	-

Table 3.3: The experimental and calculated IR absorption frequencies in cm^{-1} for valine proton-bound dimers. v1=valine labelled 1 in Figure 3.4, v2=valine labelled 2 in Figure 3.4.

3.3.5 Alanine/glycine mixed proton-bound dimer

For the mixed alanine/glycine protonated dimer, the IRMPD spectrum is only recorded in the 950- 1600 cm^{-1} range due to time constraints on the FEL. The experimental IRMPD spectrum and the two lowest-energy structures, based on structure A in the homogeneous glycine and alanine proton-bound dimers above are shown in Figure 3.6. In all, ten alanine/glycine proton-bound dimer structures were optimized and these two were found to be the lowest in energy and are similar to the lowest-energy structures for the homogeneous proton-bound dimers. It can be seen that the calculated IR spectra for both structures shown in Figure 3.5 are very similar and based on this IRMPD spectrum it is obviously impossible to differentiate between the two. In fact based on the predicted spectra, even if the experimental IRMPD spectrum in the full 700 to 2000 cm^{-1} range were available, it would not likely be possible to differentiate between these two species. From the calculated free energy difference, 3.5 kJ mol^{-1}, the ratio of these two species is predicted to be about 4:1 so structure A1 would need to be considered in a mixture of the proton-bound dimers. By comparing the observed and predicted spectra as well as the experimental spectra for the homogenous proton-bound dimers, the band observed at 1173 cm^{-1} is assigned to the C-O stretch/COH bend of amino acid 1 which is predicted to occur at 1144 cm^{-1} for both A and A1. The shoulder to the red at 1100 cm^{-1} is most likely due to the C-N str/CH_3 rock which is predicted to occur at about 1070 cm^{-1} for both isomers. The C-O stretch/COH bend for amino acid 2 in the proton-bound dimer is

observed in the 1400 cm^{-1} region and is also predicted to occur at about 1400 cm^{-1} for both isomers.

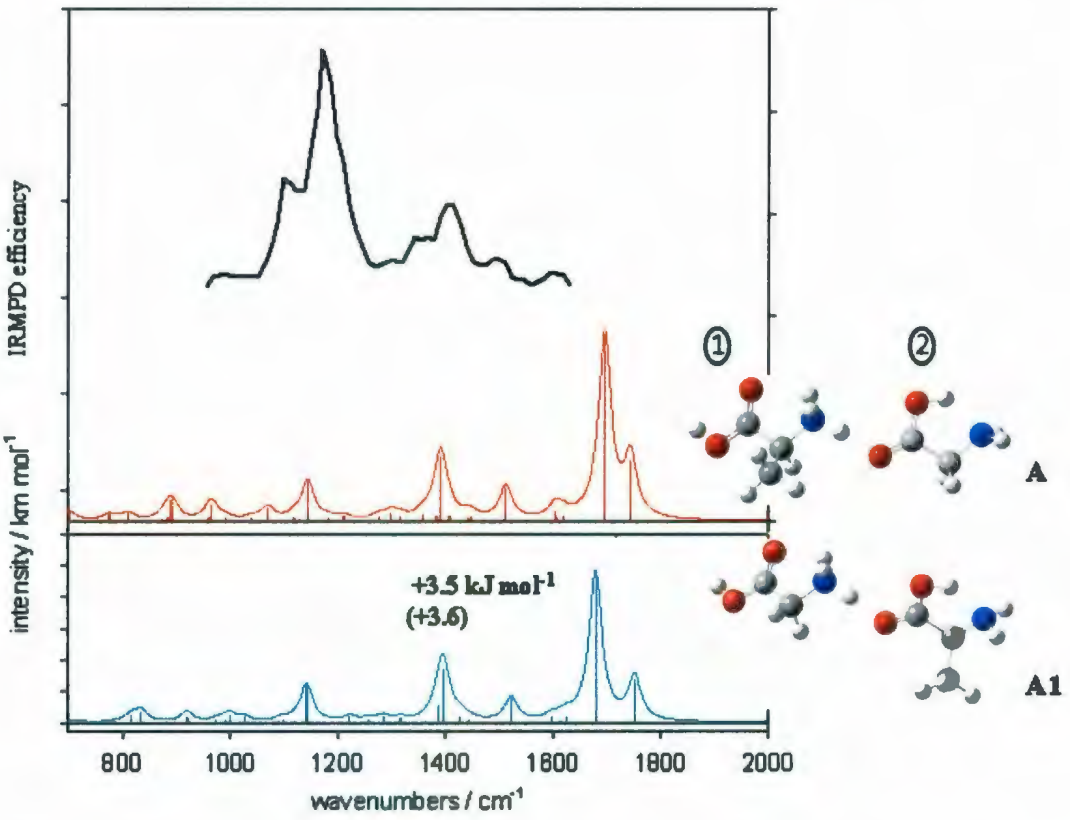

Figure 3.5: IRMPD spectrum of the heterogeneous alanine/glycine proton-bound dimer and the B3LYP/6-31+G(d,p) predicted spectra for the two lowest-energy structures. B3LYP/6-311+G(2df,p)//B3LYP/6-31+G(d,p) relative free energy compared to A is in parentheses.

As with the systems discussed above, the best region of the infrared to differentiate between these two species is in the 2000 to 3100 cm^{-1} region. This is shown clearly in

Figure 3.6 where the predicted spectra for these two isomeric structures are compared in the 2250 to 3750 cm^{-1} range. The asymmetric stretching vibration for the central proton is predicted to occur at 2595 and 2466 cm^{-1} for A and A1, respectively, and the hydrogen bonded O-H stretch is predicted to occur at 3052 and 2965 cm^{-1} for A and A1, respectively. Similarly, the N-H stretch is separated by some 50 cm^{-1}. Clearly in this region of the spectrum, the two structures could be easily distinguished.

The lowest energy structures of the proton-bound dimers presented here require some discussion. It is clear that the amino group is the most basic site of the amino acid and based on this fact that it might be expected that the proton-bound dimers of type C are the lowest in energy. Based on the experimental and computed spectra presented here, the preferred structure of the proton-bound dimers is the A-type where the N-protonated amino acid is bound to the carbonyl oxygen of the second monomer. This can be explained qualitatively on the basis of strong electrostatic bonding. Simply, the strong ionic hydrogen bond binding structure C is not as strong as the ion-dipole interaction when the protonated amino acid interacts with the large dipole of the neutral amino acid which is about 4.5D[47] and 5.0D[48] for glycine and alanine, respectively. Computational studies of mixed protonated dimers have shown that ion-dipole complexes are preferred over "normal" ionic hydrogen bonded proton-bound dimers.[49] The mixed proton-bound dimer is an especially interesting example since the proton affinity of glycine is lower than that of alanine by 15 kJ mol^{-1}. The ion-dipole interaction between protonated glycine and alanine is stronger than that

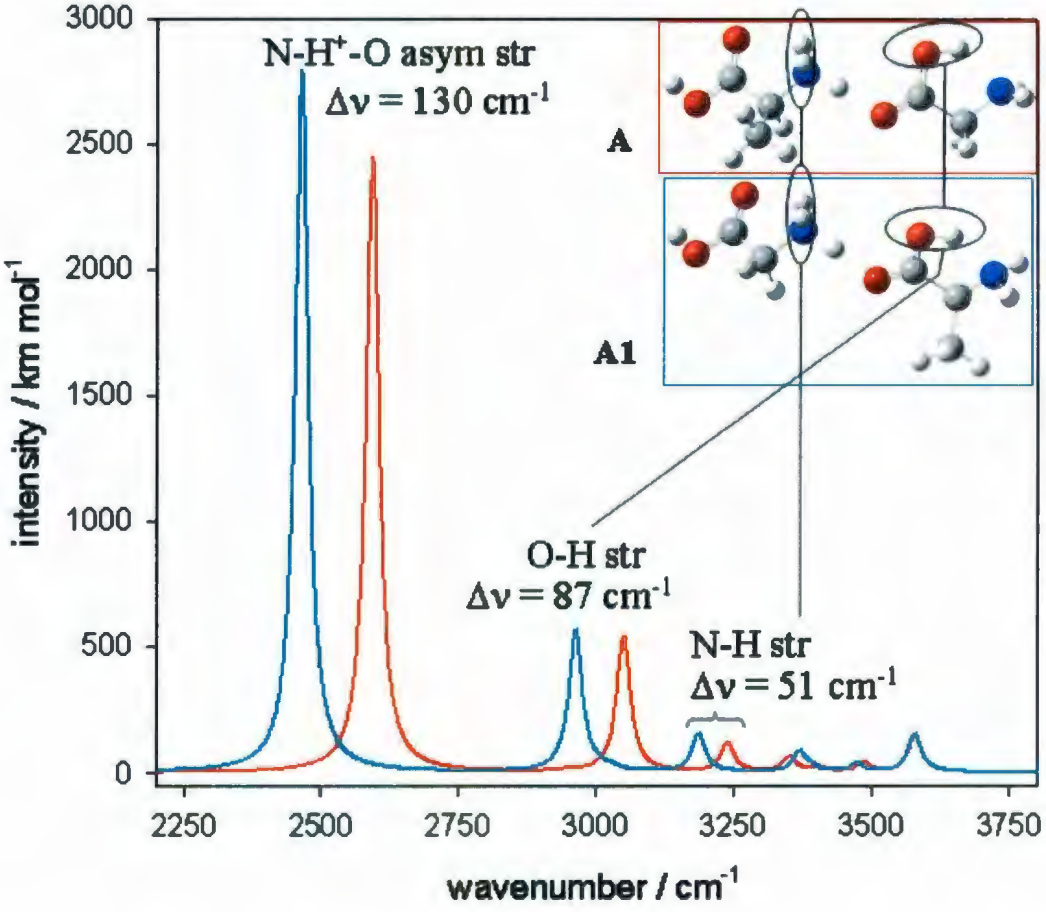

Figure 3.6: B3LYP/6-31+G(d,p) calculated infrared spectra for the two lowest-energy structures of the heterogeneous alanine/glycine proton-bound dimer in the 2200-3800 cm^{-1} region.

between protonated alanine and glycine such that A1 is calculated to be only 3.5 kJ mol^{-1} less stable than A for the mixed proton-bound dimer.

In studies which use the kinetic method to determine relative proton affinities of amino acids (ie. ref. 26) that the lowest energy structure is that of structure

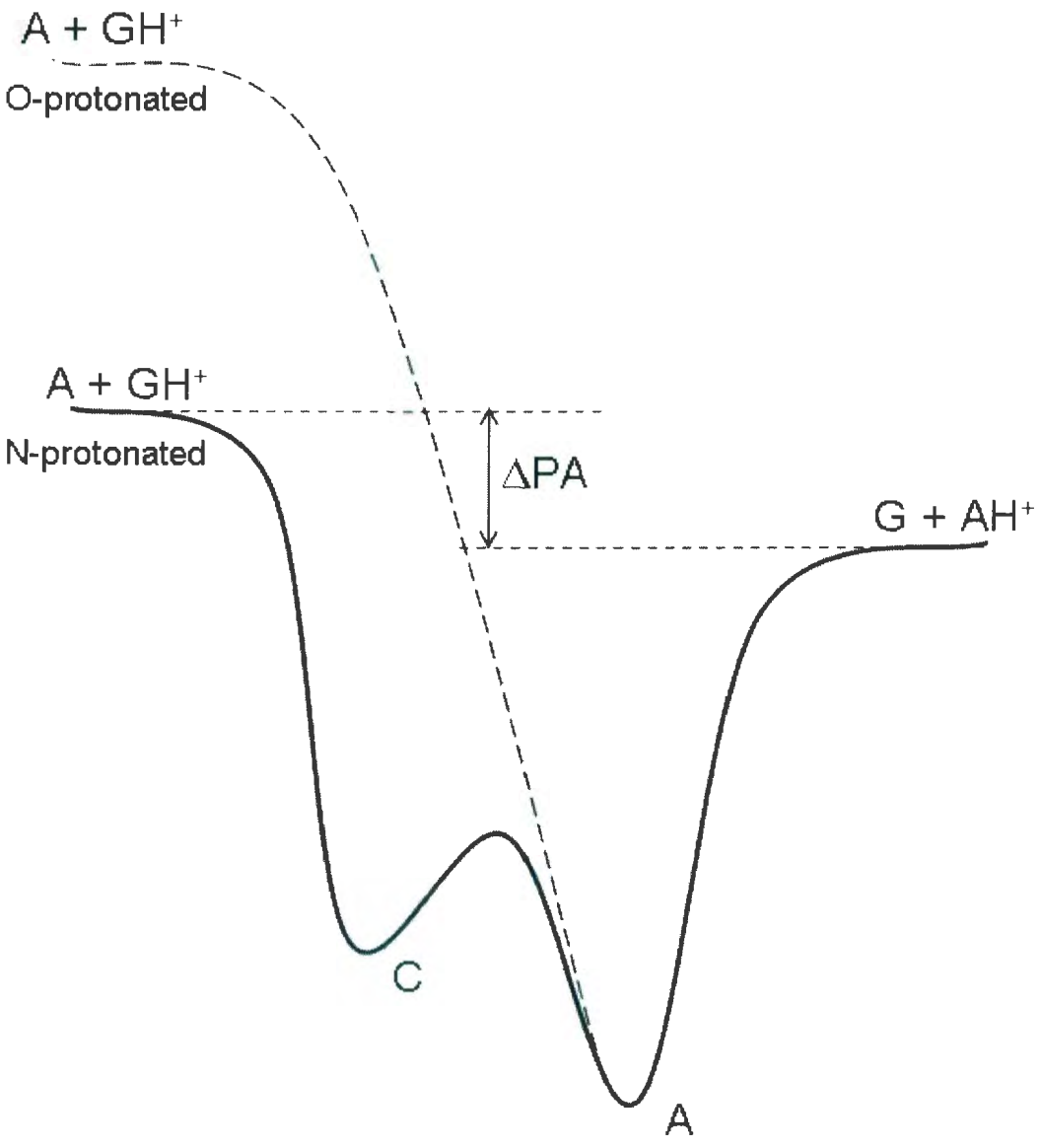

Scheme 3.1

A should not affect these measurements for reasons discussed now. The mixed alanine/glycine proton-bound dimer, for example, will form N-protonated alanine and neutral glycine as its lowest-energy dissociation pathway. One might be tempted to think that structure A will dissociate to an O-protonated glycine and neutral alanine but these products would be much higher in energy than N-protonated glycine and neutral alanine. When this proton-bound dimer begins to dissociate to protonated glycine and alanine, it would most likely isomerize to the C-type ions prior to dissociation as summarized in Scheme 3.1. This isomerization prior to dissociation has been predicted previously for dimethyl ether proton-bound dimers.[50] As long as the energy barrier for interconversion between A and C is low compared to the dissociation energies, the kinetics for dissociation producing N-protonated glycine and N-protonated alanine will be governed by this dissociation enthalpy and the measurements can be used to determine the relative proton affinities. While a complete computation of the potential energy surface of dissociating amino acid proton-bound dimers is beyond the scope of this paper, it is the subject of a future study.

3.3.6 Comparison of the Aliphatic Amino Acid Proton-Bound Dimer Spectra

In Figure 3.7, the IRMPD spectra for glycine, alanine, and valine homogenous proton-bound dimers as well as the mixed alanine/glycine proton bound-dimer are

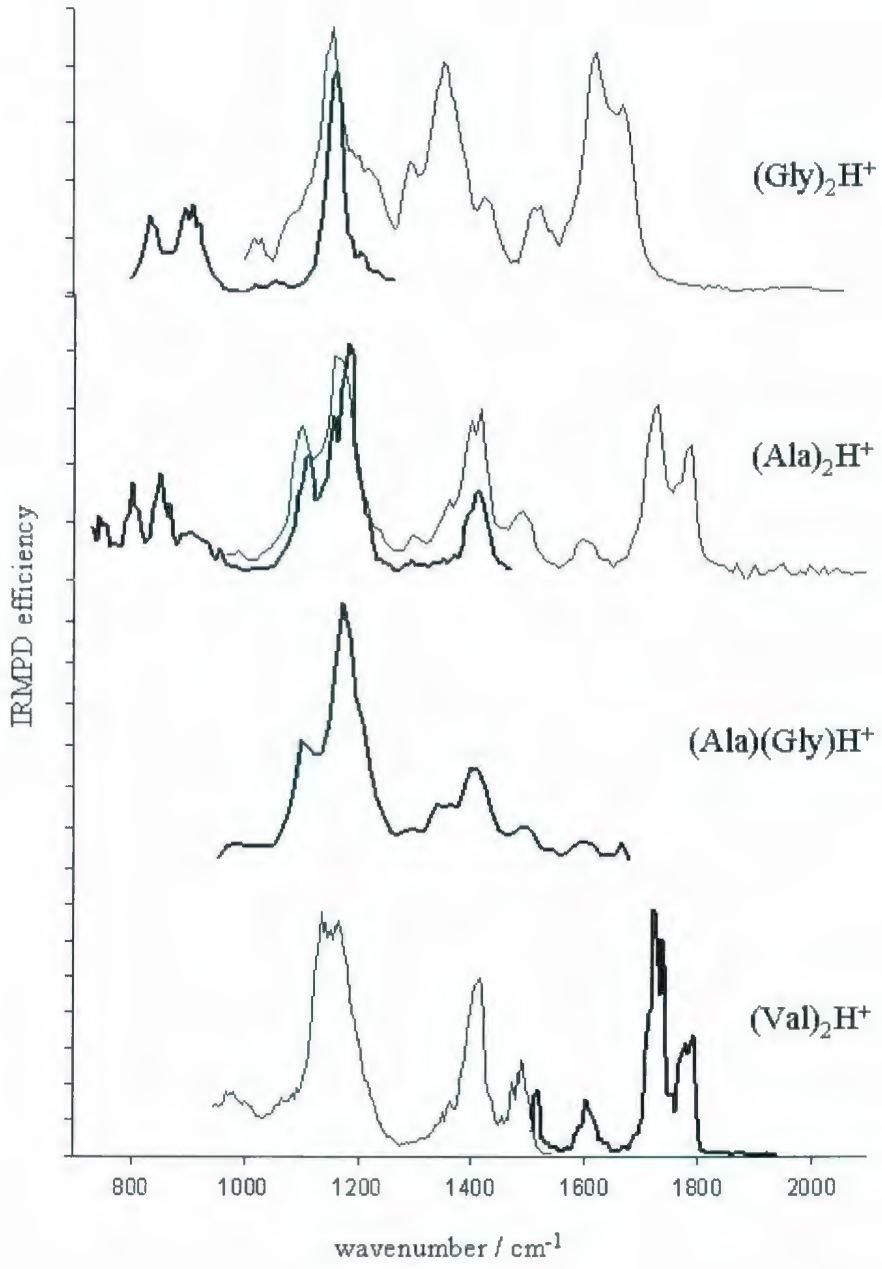

Figure 3.7: IRMPD spectra of all four proton-bound dimers in the 700-2000 cm^{-1} region which shows the similarity of the spectra in this region.

compared. These proton-bound dimers clearly have very similar spectra in this region which might make it difficult to distinguish between the different proton-bound dimers. The similarity in spectra probably reflects the similarity in structure about the central shared proton. The only real distinguishing feature is that, in the 1100 cm^{-1} region, the most intense feature for glycine is one band whereas for all the other proton-bound dimers there is a splitting of this feature due to the CH_3 rock/CN stretch which occurs in this region as well. This difficulty in distinguishing between amino acid proton-bound dimers is in fact predicted by the calculations as seen in Figure 3.8a. However, distinguishing between the proton-bound dimers composed of amino acids with different aliphatic side chains may be possible at higher frequencies as shown in Figure 3.8b due to the differing asymmetric stretching frequencies in 2400-2600 cm^{-1} range which is most likely due to the difference in proton affinities between the ends of the amino acids which are bound by the proton. Also, in the 2900-3100 cm^{-1} region, it may be possible to distinguish between the proton-bound dimers due to the differing positions for the hydrogen bonded N-H and O-H stretching absorptions.

3.4 Conclusions

The IRMPD spectra of amino acid proton-bound dimers with aliphatic side chains in the 700-2100 cm^{-1} range have been recorded. The dominant absorptions in this

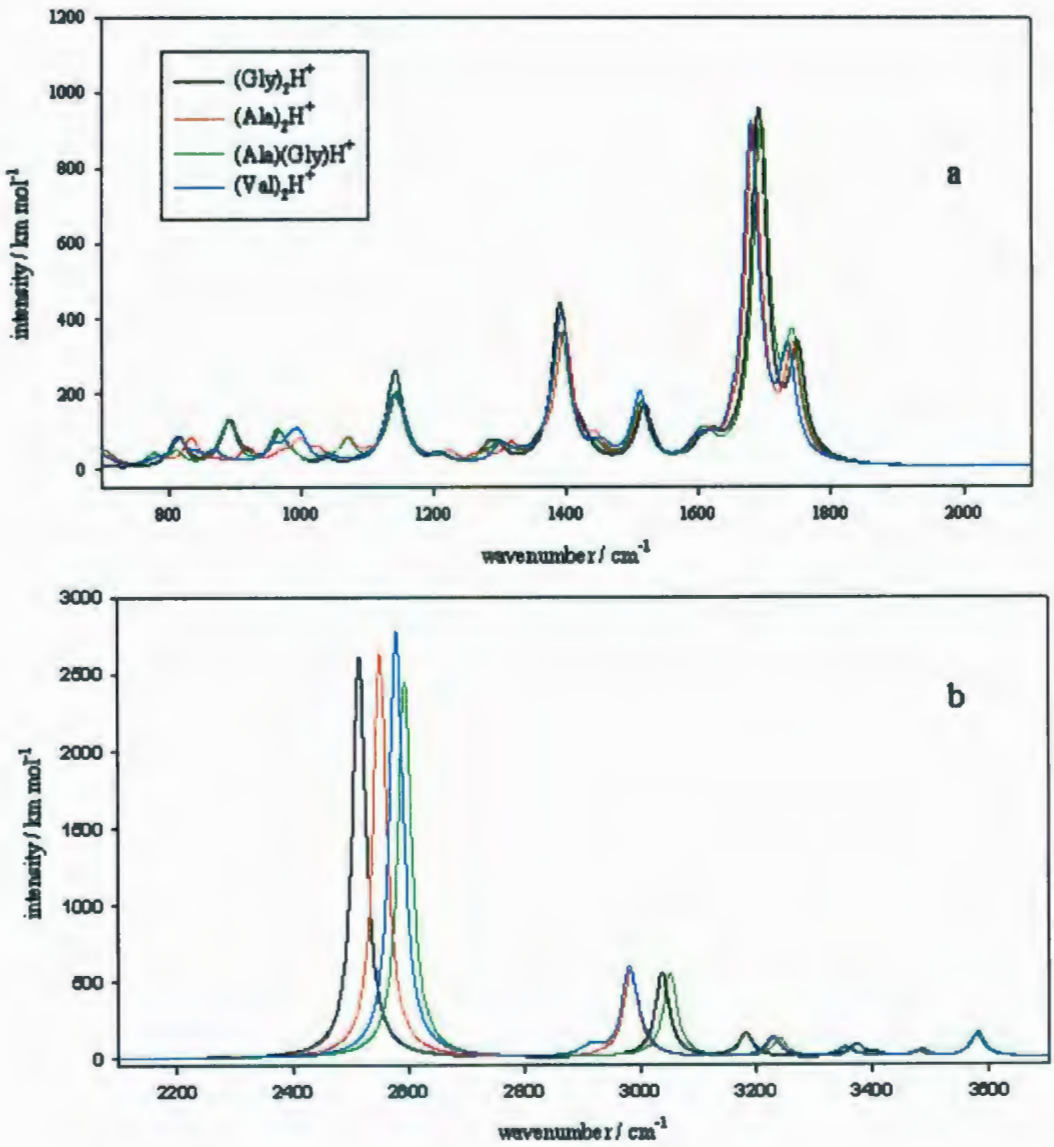

Figure 3.8: Calculated IR spectra for glycine, alanine, alanine/glycine, and valine proton-bound dimers at B3LYP/6-31+G(d,p) showing that they are predicted to have very similar spectra in the 700-2000 cm^{-1} region (a) but that they might be discernible in the higher-energy region (b).

range are C=O stretching and NH_2 bending as well as COH bending. Based on computed IR spectra and the difference in computed free energies, the most stable structures are determined for each of the glycine, alanine, and valine proton-bound dimers as well as the mixed alanine/glycine proton-bound dimer and these proton-bound dimers are concluded to be very similar in structure.

For the glycine proton-bound dimer, structure A (Figure 3.1) is assigned to be the most dominant structure according to our IRMPD spectrum in the 700-2100 cm^{-1} range and by re-analysing the spectrum of Oh *et al.*[38] in the 3050-3800 cm^{-1} range. Although, in their paper,[38] the structure for the proton-bound dimer was assigned to structure C, the calculated IR spectra for structure A shows a much better agreement with their spectrum as well as the one presented in this study. Furthermore, the computed thermochemistry favours structure A in agreement with previous equilibrium studies.[27]

Comparing the experimental IRMPD spectrum and the calculated IR spectra for both the alanine and valine proton-bound dimers show that structure A is also the most probable structure in agreement with the calculated energies. For the alanine/glycine proton-bound dimer, the IRMPD spectrum is only recorded in the 950-1600 cm^{-1} region. However, the predicted lowest-energy structures are very similar to the homogenous proton-bound dimers (ie. glycine proton-bound dimer and alanine proton-bound dimer), and the portion of the spectrum recorded is also comparable to the experimental spectra for the homogenous proton-bound dimers such that a

full spectrum in this region would not likely be very helpful. However, based on the calculated thermochemistry, 3.5 kJ mol $^{-1}$ difference in free energy, two very similar isomers would be expected to exist in a sample. The only region for differentiating the two structures is the asymmetric stretching vibration for the central proton which occurs at 2595 and 2466 cm $^{-1}$ for A and A1, respectively, as well as hydrogen bonded O-H stretching at around 3000 cm $^{-1}$. It is also determined that distinguishing the proton-bound dimers composed of different aliphatic amino acids should be possible in the 2000 to 3200 cm $^{-1}$ range.

Bibliography

1. Yamaguchi, K.; *J. Mass spectrom.* **2003**, *38*, 473.
2. Surewicz, W. K.; Mantsch, H. H.; Chapman, D. *Biochemistry* **1993**, *32*, 389.
3. Wetzel, R.; Shivaprasad, S.; Williams, A. D. *Bichemistry* **2007**, *46*, 1.
4. South, C. R.; Burd, C.; Weck, M. *Acc. Chem. Res.* **2007**, *40*, 63.
5. Gogonea, V.; Merz, K. M. *J. Phys. Chem. A* **1999**, *103*, 5171.
6. Deng, H.; Cahill, S. M.; Abad, J. L.; Lewandowicz, A.; Callender, R. H.; Schramm, V. L.; Jones, R. A. *Biochemistry* **2004**, *43*, 15966.
7. Weinkauf, R.; Schermann, J. P.; deVries, M. S.; Kleinermans, K. *Eur. Phys. J. D.* **2002**, *20*, 309.
8. Robertson, E. G.; Simons, J. P. *Phys. Chem. Chem. Phys.* **2001**, *3*, 1.
9. Stepanian, S. G.; Reva, I. D.; Radchenko, E. D.; Rosado, M. T. S.; Duarte, M.; Fausto, R.; Adamowicz, L. *J. Phys. Chem. A* **1998,** *102*, 1041.
10. Stepanian, S. G.; Reva, I. D.; Radchenko, E. D.; Adamowicz, L. *J. Phys. Chem. A* **1998**, *102*, 4623.
11. Stepanian, S. G.; Reva, I. D.; Radchenko, E. D.; Adamonwicz, L. *J. Phys. Chem. A* **1999**, **103**, 4404.
12. Iijima, K.; Tanaka, K.; Onuma, S. *J. Mol. Struct.* **1991**, *246*, 257.
13. Jensen, J. H.; Gordon, M. S. *J. Am. Chem. Soc.* **1991,** *113*, 7917.
14. Blanco, S.; Lesarri, A.; Lopez, J. C.; Alonso, J. L. *J. Am. Chem. Soc.* **2004**, *126,* 11675.

15. Lesarri, A.; Cocinero, E. J.; Lopez, J.C; Alonso, J. L. *Angew. Chem. Int. Ed.* **2004**, *43*, 605.

16. Rak, J.; Skurski, P.; Simons, J.; Gutowski, M. *J. Am. Chem. Soc.* **2001**, *123*, 11695.

17. Lowry, T. H.; Richardson, K. S.; Mechanism and Theory in Organic Chemistry, 3rd, Harper & Row: New York, **1987**.

18. Sudha, R.; Kohtani, M.; Breaux, G. A.; Jarrold, M. F. *J. Am. Chem. Soc.* **2004**, *126*, 2777.

19. Gorman, J. S.; Spier, J. P.; Turner, C. A.; Amester, I. J. *J. Am. Chem. Soc.* **1992**, *114*, 3986.

20. Bojesen, G. *J. Am. Chem. Soc.* **1987**, *109*, 5557.

21. Bojesen, G.; Breindahl, T. *J. Chem. Soc. Perkins Trans. 2* **1994**, *2*, 1029.

22. Li, X.; Harrison, A. G. *Org. Mass Spectrom.* **1993**, *28*, 366.

23. Harrison, A. G. *Mass Spectrom. Rev.* **1997**, *16*, 201.

24. Mirza, S. P.; Prabhakar, S.; Vairamani, M. *Rapid Comm. Mass Spectrom.* **2001**, *15*, 957.

25. Afonso, C.; Modeste, F.; Breton, P.; Fournier, F.; Tabet, J. C. *Eur. J. Mass Spectrom.* **2000**, *6*, 443.

26. Andriole, E. J.; Colyer, K. E.; Cornell, E.; Poutsma, J. C. *J. Phys. Chem. A* **2006**, *110*, 11501.

27. Raspopov, S. A.; McMahon, T. B. *J. Mass Spectrom.* **2005**, *40*, 1536.

28. Meot-Ner, M. *Chem. Rev.* **2005**, *105*, 213.

29. Fridgen, T. D.; McMahon, T. B.; MacAleese, L.; Lemaire, J.; and Maitre, P. *J. Phys. Chem. A* **2004**, *108*, 9008.

30. Asmis, K. R.; Pivonka, N. L.; Santambrogio, G.; Brummer, M.; Kaposta, C.; Neumark, D. M.; Woste, L. *Science* **2003**, *299*, 1375.

31. Headrick, J. M.; Bopp, J. C.; Johnson, M. A. *J. Chem. Phys.* **2004**, *121*, 11523.

32. Pivonka, N. L.; Kaposta, C.; Brummer, M.; Helden, G. V.; Meijer, G.; Woste, L.; Neumark, D. M.; Asmis, K. R. *J. Chem. Phys.* **2003**, *118*, 5275.

33. Fridgen, T.D.; McMahon, T.B.; Maitre, P.; Lemaire, J. *Phys. Chem. Chem. Phys.* **2006**, *8,* 2483.

34. Fridgen, T. D.; MacAleese, L.; Maitre, P.; McMahon, T. B.; Boissel, P.; Lemaire, J. *Phys. Chem. Chem. Phys.* **2005**, *7*, 2747.

35. Moore, D. T.; Oomens, J.; van der Meer, L.; von Helden, G.; Meijer, G.; Valle, J.; Marshall, A. G.; Eyler, J. R. *Chem. Phys. Chem* **2004**, *5*, 740.

36. Solca, N.; Dopfer, O. *J. Am. Chem. Soc.* **2004**, *126*, 9520.

37. Kamariotis, A.; Boyarkin, O. V.; Mercier, S. R.; Beck, R. D; Bush, M. F.; Williams, E. R.; Rizzo, T. R. *J. Am. Chem. Soc.* 2006, *128*, 905.

38. Oh, H.; Lin, C.; Hwang, H. Y.; Zhai, H.; Breuker, K.; Zabrouskov, V.; Carpenter, B. K.; McLafferty, F. W. *J. Am. Chem. Soc.* **2005**, *127*, 4076.

39. Kapota, C.; Lemaire, J.; Maitre, P.; Ohanessian, G. *J. Am. Chem. Soc.* **2004**, *126*, 1836.

40. Bush, M. F.; O'Brien, J. T.; Prell, J. S.; Saykally, R. J.; Williams, E. R. *J. Am. Chem. Soc.* **2007**, 129, 1612.

41. Prazeres, R.; Glotin, F.; Insa, C.; Jaroszynski, D. A.; Ortega, J. M. *Eur. Phys. J. D.* **1998,** *3*, 87.

42. Paul, W. *Rev. Mod. Phys.* **1990**, *62*, 531.

43. Mac Aleese, L.; Simon, A.; McMahon, T. B.; Ortega, J. M.; Scuderi, D.; Lemaire, J.; Maitre, P. *Int. J. Mass. Spec.* **2006**, *249-250*, 14.

44. Frisch, M. J.; Trucks, G. W.; Schlegel, H. B.; Scuseria, G. E.; Robb, M. A.; Cheeseman, J. R.; Montgomery, J. A., Jr.; Vreven, T.; Kudin, K. N.; Burant, J. C.; Millam, J. M.; Iyengar, S. S.; Tomasi, J.; Barone, V.; Mennucci, B.; Cossi, M.; Scalmani, G.; Rega, N.; Petersson, G. A.; Nakatsuji, H.; Hada, M.; Ehara, M.; Toyota, K.; Fukuda, R.; Hasegawa, J.; Ishida, M.; Nakajima, T.; Honda, Y.; Kitao, O.; Nakai, H.; Klene, M.; Li, X.; Knox, J. E.; Hratchian, H. P.; Cross, J. B.; Adamo, C.; Jaramillo, J.; Gomperts, R.; Stratmann, R. E.; Yazyev, O.; Austin, A. J.; Cammi, R.; Pomelli, C.; Ochterski, J. W.; Ayala, P. Y.; Morokuma, K.; Voth, G. A.; Salvador, P.; Dannenberg, J. J.; Zakrzewski, V. G.; Dapprich, S.; Daniels, A. D.; Strain, M. C.; Farkas, O.; Malick, D. K.; Rabuck, A. D.; Raghavachari, K.; Foresman, J. B.; Ortiz, J. V.; Cui, Q.; Baboul, A. G.; Clifford, S.; Cioslowski, J.; Stefanov, B. B.; Liu, G.; Liashenko, A.; Piskorz, P.; Komaromi, I.; Martin, R. L.; Fox, D. J.; Keith, T.; Al-Laham, M. A.; Peng, C. Y.; Nanayakkara, A.; Challacombe, M.; Gill, P. M. W.; Johnson, B.; Chen, W.; Wong, M. W.;

Gonzalez, C.; Pople, J. A. *Gaussian 03*, Revision B.04; Gaussian, Inc.: Pittsburgh, PA, 2003.

45. Andersson, M. P.; Uvdal, P. *J. phys. Chem. A* **2005**, *109*, 2937.

46. Price, W. D.; Schnier, P. D.; Williams, E. R. *J. Phys. Chem. B* **1997**, *101*, 664.

47. Brown, R. D.; Godfrey, P. D.; Storey, J. W. W.; Bassez, M.-P. *J. Chem. Soc. Chem. Comm.* **1978**, 547.

48. Csaszar, A. G. *J. Phys. Chem.* **1996**, *100*, 3541.

49. a) Burt, M. B.; Fridgen, T. D. *J. Phys. Chem. A*, **2007**, 111, 10738. b) Fridgen, T. D. *J. Phys. Chem. A.* **2006**, *110*, 6122.

50. a) Fridgen, T. D.; McMahon, T. B. *J. Phys. Chem. A.* **2001**, *105*, 1011. b) Fridgen, T. D. McMahon, T. B. *J. Am. Chem. Soc.* **2001**, *123*, 3980.

51. C.G. Atkins, K. Rajabi, E.A.L. Gillis, and T.D. Fridgen, *J. Phys. Chem. A* **2008**, *112*, 10220.

52. Oh, H.; Lin, C.; Hwang, H.Y.; Zhai, H.; Breuker, K.; Zabrouskov, V.; Carpenter, B.K.; McLafferty, F.W. *J. Am. Chem. Soc.* **2005**, *127*, 4076.

53. Stepanian, S. G.; Reva, I. D.; Radchenko, E. D.; Rosado, M. T. S.; Duarte, M. L. T. S.; Fausto, R.; Adamowicz, L. *J. Phys. Chem. A* **1998**, *102*, 1041.

54. Stepanian, S. G.; Reva, I. D.; Radchenko, E. D.; Adamowicz, L. *J. Phys. Chem. A* **1999**, *103*, 4404.

Chapter 4

The Structure of the Protonated Adenine Dimer by IRMPD Spectroscopy and Electronic Structure Calculations

4.1 Introduction*

Adenine (6-aminopurine, $C_5H_5N_5$) plays a crucial role in biochemistry. For example, it is a main component of adenosine triphosphate (ATP), NAD^+, and nucleic acids to name a few. Nucleic acids have been used in constructing materials[1] such

*This Chapter has been published as K. Rajabi, K. Theel, E.A. L. Gillis, G. Beran and T. D. Fridgen, *J. Phys. Chem. A* **2009**, *113*, 8099-8107.

as nanomachines, nanoscaffolds, and DNA computers.[2] DNA bases themselves have gained interest as components of self-assembling structures. For example, 2D sheet-like nano structures containing doubly-protonated adenine have self assembled from low-pH aqueous solutions containing adenine, hydrogen halide and iodide. These structures have been isolated and characterized by X-ray crystallography.[3]

Adenine itself has been the topic of numerous quantum mechanical molecular structure studies to explore geometries, proton affinities, protonation, polyhydration, tautomerism, the structure of the amino group in terms of planarity, and the mechanism of double proton transfer in adenine-containing complexes.[4–14] The presence of "rare" or non-canonical tautomeric forms of DNA bases is closely related to mispairing of purines and pyrimidines, causing spontaneous point mutations.[15–17] Therefore, there is an increasing interest to investigate the structure and tautomerism of the DNA bases. The N9H tautomer of adenine was calculated to be the most stable (Scheme 4.1) in the gas phase by some 30-35 kJ mol^{-1}.[18,19] Protonation of the N9H tautomer at N1 is found to be thermodynamically preferred in the gas phase.[20] Gu *et al.*[4] explored the water-assisted intramolecular proton transfer in the tautomers of adenine using DFT (B3LYP/6-311G(d,p)) calculations and found that the high energy imino form of the tautomers of adenine is stabilized by about 8-12 kJ mol^{-1} in the presence of water due to enhancement of the conjugated π electron system found in the imino form of adenine. Because of its larger dipole moment, the N7H tautomer of adenine was found to be preferentially stabilized in the presence of water, where it

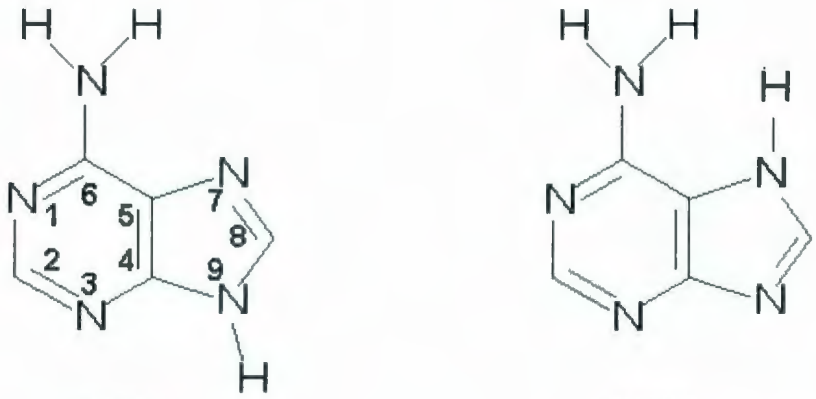

Scheme 4.1

lies only about 16 kJ mol^{-1} above the N9H tautomer.[4] A larger concentration of the N7H tautomer would then be expected in aqueous solutions and in biological systems than is indicated by gas-phase calculations. A water molecule was also found to reduce the energy barrier to the tautomerization by acting as both a proton donor and acceptor, thereby assisting the proton transfer isomerization.[4] The tunneling effect in the intramolecular proton transfer in adenine was investigated using the parabolic barrier approximation and one-dimensional model.[21,22] The tunneling rates were calculated to be 10^{10} times larger than the classical one for the gas phase and $10^3 \sim 10^4$ times larger for the water-assisted process. In addition, the assignment of the bands in the infrared spectra of argon- and nitrogen-matrix-isolated adenine and its ^{15}N isotopomers (substituted at N9 or N7 positions) indicated that only the N9H tautomer of adenine was identified.[23] The results of these studies represent the solid phase since

the source of matrix-isolated adenine is from heating solid adenine in vacuum and entraining the vapor in matrix gas prior to being condensed on a cryogenic substrate.

Proton-transfer reactions are important in biological systems since they can lead to mutations.[16] It is therefore important to investigate the changes in chemical properties of bases due to protonation. Many experimental and theoretical studies have been conducted on protonated nucleic acid bases and related compounds[24–29] due to the remarkable effect protonation has on conformational structure.[30] For example, base protonation has been implicated in the transformation of the B to Z structures of DNA.[31,32] Knowledge of the protonation site is also essential for the design of some drugs which regulate the activity of a selected gene by stabilizing the triple helix formed between the target base sequence and an oligonucleotide.[33] The triple helix structure inhibits transcription resulting in its therapeutic effect.[34] Russo *et al.*[25] have performed gradient-corrected density functional computations with triple-zeta-type basis sets to determine the preferred protonation site and the absolute gas-phase proton affinities of the most stable tautomers of the DNA bases and for the first time predicted the gas phase basicity order among four DNA nucleic acid bases to be: guanine > cytosine > adenine > thymine

A better redistribution of electron density was found in the most favourable protonated species. The nature of the HOMO, molecular electrostatic potential, and charge distribution together can explain the effects that stabilize the most stable protonated structures. Proton affinity values of 873.6 (T), 958.6 (C), 944.7 (A), and 963.6 (G) kJ

mol^{-1} at 298K were obtained, in a fair agreement with available experimental data.

The small energy differences between the adenine tautomers and among their conjugate acids make the identification of the most stable tautomers theoretically challenging. Relative tautomer stabilities are highly sensitive to changes in the treatment of electron-electron correlation and/or the one particle basis.[12,25] Therefore, experimental techniques that target alternative properties are potentially very useful. IR spectroscopy is obviously a powerful technique to study adenine cluster systems. However, other spectroscopic techniques (such as photoexcitation) have been widely used to elucidate changes in the electronic structure and dynamics of adenine due to the presence of a proton. For instance, Marian *et al.*[35] produced protonated adenine ions by electrospray, stored and cooled them in a Paul trap, and dissociated them using resonant photoexcitation with ns UV laser pulses. By comparing their photofragmentation spectra with computed vertical excitation spectra, it was determined that protonation mainly occurs at the N1 position of an N9H tautomer of adenine, with a possible contribution from the N3 protonated N7H tautomer, which lies only 1.9 kJ mol^{-1} higher in energy.

IRMPD spectroscopy[36–38] provides more direct evidence of cation structure. For instance, Atkins *et al.*[39] have used IRMPD spectroscopy in the N-H/O-H stretching region along with electronic structure calculations to determine that the lowest energy structure of sodium-bound glycine dimers consists of two symmetric bidentate ligands. Similarly, for the aliphatic amino acid proton-bound homodimers composed of glycine,

alanine and valine as well as the heterogeneous alanine/glycine mixture, an ion-dipole complex in which the N-protonated amino acid bound to the carbonyl oxygen of the second monomer was found to be the dominant structure.[39,40] In another recent study, the oxazalone structure was confirmed for the b_2^+ ion produced from CID of the protonated AGG peptide while the protonated cyclic dipeptide is a diketopiperazene.[41] Much less work has been done on DNA bases and related compounds. Salpin *et al.*[42] identified the lowest energy structures of the protonated pyrimidic bases using IRMPD spectroscopy in the 900 to 2000 cm^{-1} region.[43] Lithium cationized complexes of thymine and uracil have also been studied in the gas phase by IRMPD spectroscopy in the N-H/O-H stretching region.[44] Based on a combination of experimental and theoretical data, it was found that the lithium cation in both thymine and uracil complexes was most likely bound to O4 to form linear Li^+-bound dimers. Hydration of these Li^+ bound dimers resulted in significant structural changes to enable strong interbase hydrogen bonding, similar to that in the Watson-Crick model of DNA.

In recent theoretical work by Liu *et al.*[9], nine stable proton-bound adenine dimers, $(C_5H_5N_5)_2H^+$, formed from the N9H tautomer of adenine and the N1 protonated N9H tautomer were found. In some of the proton-bound dimers, the proton is partially or completely transferred from the protonated adenine to the neutral. While one might expect the proton-bound dimer to consist of the most stable neutral and protonated monomer forms, Hud and Morton[45] demonstrated that the four proton-bound dimers composed of the N9H tautomer protonated at N1 and the N7H tautomer of adenine

are by far the lowest energy proton-bound dimers, and that the four isomers have fairly similar binding energies. In the present work, the structure of the adenine proton-bound dimer is explored using a combination of theoretical and IRMPD techniques. By comparing the experimental IRMPD spectra with theoretical predictions of the vibrational spectra for various isomers, we hypothesize that only one or two isomers are observed experimentally. While our predicted gas-phase thermochemistry data cannot explain this observation, we performed calculations that suggest that the experimentally observed isomers are thermodynamically favoured in solution. Therefore, we propose that only two of the most stable gas-phase dimers are prevalent in solution, and that these solution-stable dimers are predominantly the ones that are electrosprayed and observed in these gas-phase experiments.

4.2 Methods

4.2.1 Experimental

The details of coupling the ApexQe Bruker FT-ICR mass spectrometer with a 25 Hz Nd:YAG pumped Laservision OPO/A laser have been presented previously.[46] Adenine proton-bound dimers were electrosprayed from ~5 mM solutions of adenine in 18 MΩ Millipore water which had been slightly acidified with a few drops of 1 mM HCl solution (total volume of 10 ml). Protonated adenine dimer (m/z 271) was

isolated in the ICR cell by standard ejection techniques. Absorption of the infrared laser light resulted in dissociation of the proton-bound dimer, which was monitored by a change in mass of the parent ion. The IR laser scan rate was 0.5 cm^{-1} s^{-1} with irradiation times of 2.0 s. This corresponds to a step size of 1 cm^{-1} between points in the IRMPD spectra. IRMPD efficiency is defined as the negative of the natural logarithm of precursor ion intensity divided by the sum of the fragment and precursor ion intensities.

4.2.2 Computational

Optimized structures, dimer interaction energies, harmonic vibrational frequencies, and statistical thermodynamic quantities of the various proton-bound adenine dimer isomers were computed using the B3LYP density functional and the 6-31+G(d,p) basis set in the Gaussian 03 software package.[47] Single point MP2/6-311++G(2d,p) calculations were also done on the B3LYP/6-31+G(d,p) structures. Thermodynamic quantities employing the MP2 electronic energies and the B3LYP thermal corrections are reported as MP2/6-311++G(2d,p) //B3LYP/6-31+G(d,p) energies. In addition, we refine the predicted energies using the recently developed double-hybrid B2P3LYP density functional with the cc-pVTZ basis set.[49] Standard density functionals exhibit known deficiencies in treating van der Waals interactions,[50] and double-hybrid functionals[51] attempt to correct for this deficiency by mixing in Møller-Plesset (MP2)-

like long-range correlation into the functional. The B2P3LYP functional significantly outperforms B3LYP for systems where noncovalent interactions are important, so we use it here. The cc-pVTZ basis set is the recommended basis set for use with B2P3LYP, since the empirical parameters in the functional were fit using this basis set. To compensate for basis set superposition errors (BSSE), the standard Counterpoise correction[52] was also considered. All B2P3LYP calculations were performed using a developmental version of Q-Chem, version 3.1.[53] Because analytical gradients of the B2P3LYP functional are currently unavailable, we utilize B3LYP/6-31+G(d,p) structures and harmonic frequencies (for computing thermodynamics).

Two additional approximations are invoked to accelerate the B2P3LYP energy calculations. First, just as in the original B2P3LYP paper, we use the resolution-of-the-identity (RI) approximation,[54] and the auxiliary cc-pVTZ fitting basis set[55] to speed up the MP2 portion of the B2P3LYP calculation substantially. Second, we utilize a dual-basis Hartree-Fock (HF)/MP2 calculation.[56] In this approach, the HF/cc-pVTZ solution is approximated by taking the converged HF density matrix from a carefully chosen smaller basis set, projecting the density matrix into the larger cc-pVTZ basis set, and taking a single HF iteration in the larger basis set. Using these approximations, the energy of a 5-water-molecule-solvated adenine dimer structure (1044 basis functions in the cc-pVTZ basis) can be computed in about 6 hours on a single processor on a modern workstation. At the same time, these two approximations introduce negligible additional errors into the relative energies.

Two separate strategies were used to address aqueous solvation effects on the proton-bound dimers. First, polarizable continuum model (PCM) calculations[57] at the B3LYP/6-31+G(d,p) level are performed to address bulk solvation effects. Adenine proton-bound dimer gas-phase structures were re-optimized and frequencies computed in the presence of the polarizable continuum. Second, gas-phase calculations (with no PCM model) employing up to 5 explicit water solvent molecules around the proton-bound dimers were used to investigate specific adenine-solvent interactions.

4.3 Results and Discussion

4.3.1 Computed Structures and Thermochemistry of Adenine Proton-Bound Dimers

The four lowest-energy structures of the adenine proton-bound dimer are A through D in Figure 4.1. These structures were first presented by Hud and Morton.[45] They are planar and best described as N3 or N1 protonated N9H adenine tautomers interacting with the N7H neutral tautomer of adenine. At the B3LYP level, they lie some 20 kJ mol^{-1} lower in enthalpy than the proton-bound dimers stemming from the N9H tautomers (E through L in Fig. 4.2).[45]

To begin, we validate the B2P3LYP functional for these systems by comparing the

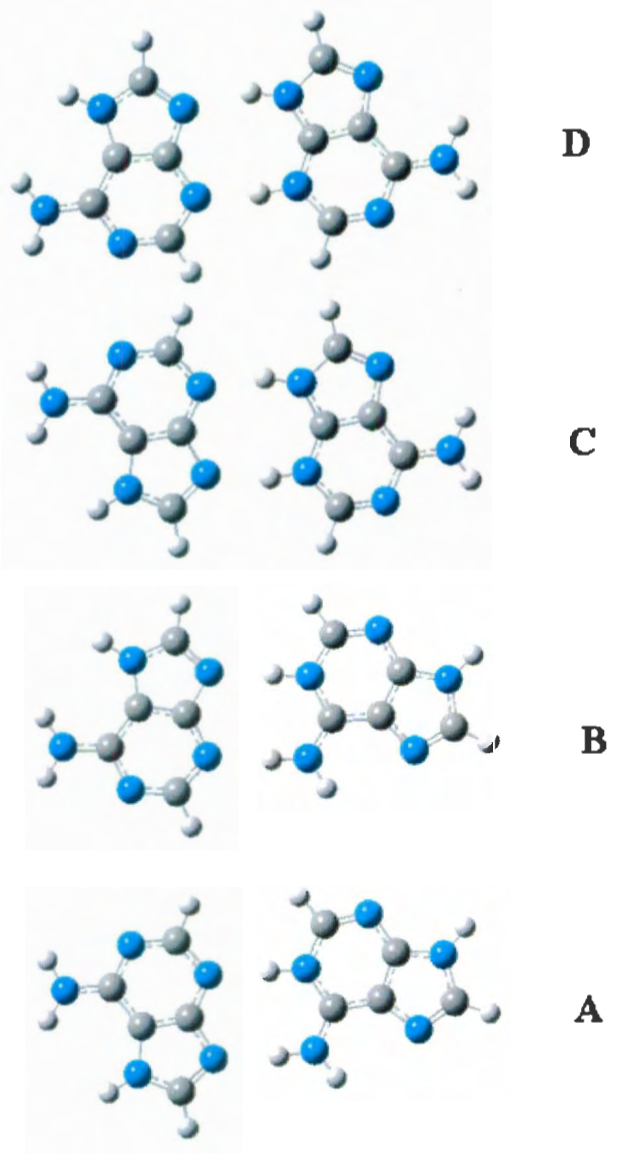

Figure 4.1: B3LYP/6-31+G(d,p) structures of the four lowest-energy proton-bound adenine dimers.

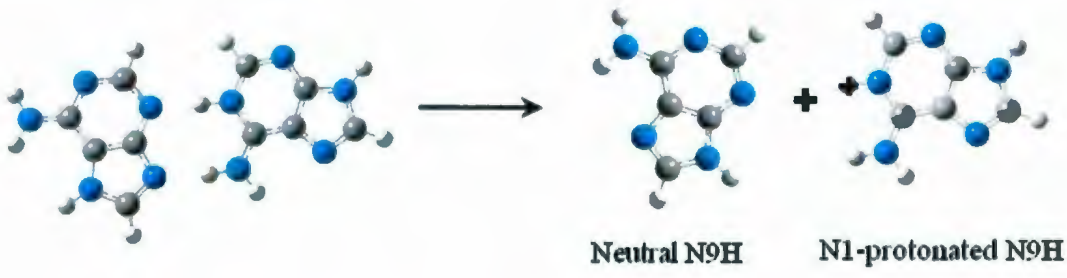

Scheme 4.2

predicted binding energies for the proton-bound adenine dimer with the experimental value of $\Delta H(500\ K) = 127 \pm 4$ kJ mol^{-1} measured by Mautner using high-pressure mass spectrometry experiments.[27] The binding energies are computed relative to the adenine 9H tautomer and the N1-protonated adenine 9H tautomer (see Scheme 4.2).[58] These results are summarized in Table 4.1. As has been noted earlier,[45] B3LYP underestimates the interaction energy for the proton-bound dimer by about 20 kJ mol^{-1}. In contrast, three of the B2P3LYP-predicted isomer interaction energies lie within the experimental uncertainty, and the fourth lies only 1 kJ mol^{-1} outside of that range. Both B3LYP and B2P3LYP suggest that isomer A is the most stable structure since it has the highest binding energy, but the small energy differences between the four structures prevent a definitive prediction of the most stable gas-phase structure. Overall, these results suggest that the B2P3LYP functional performs better for this system. In the remaining sections, we will use B2P3LYP to confirm the B3LYP predictions.

The relative energies of the four lowest-energy proton-bound dimers computed

	B3LYP/6-31+G(d,p)		**B2P3LYP/cc-pVTZ**[a]	
isomer	$\Delta E_{elec}{}^{CP,b}$	**ΔH(500K)**[c]	$\Delta E_{elec}{}^{CP,b}$	**ΔH(500K)**[c]
A	113.8	106.8	132.4	125.4
B	111.3	104.1	129.5	122.3
C	111.0	104.7	131.1	124.8
D	109.4	102.9	129.5	123.1

Table 4.1: Binding energies (kJ mol^{-1}) of the four lowest-energy isomers of the proton-bound adenine dimer relative to N9H adenine and N1-protonated-N9H adenine. The experimental value from reference 58 is ΔH(500 K) = 127±4 kJ mol ^{1}.

[a]Using B3LYP/6-31+G(d,p) optimized geometries.

[b]Counterpoise-corrected electronic interaction energies.

[c]Enthalpies computed using B3LYP/6-31+G(d,p) structures and frequencies.

here and energies for these and other structures published previously[9] are summarized in Table 4.2. MP2/6-311++G(2d,p)//B3LYP/6-31+G(d,p) energies agree with the relative energetic ordering from Hud and Morton[45] and Liu *et al.*[9] The relative energies of these species suggest that the higher energy structures, E through L, are unlikely to be present in significant quantities experimentally.

4.3.2 IRMPD Spectroscopy

Upon absorption of infrared radiation from the OPO laser, the adenine proton-bound dimer (m/z 271) dissociates to produce protonated adenine (m/z 136). No other products were observed.

The IRMPD efficiency spectrum in the 3250-3650 cm^{-1} region is shown as the black trace at the bottom of Figure 4.3. The computed spectra in Figure 4.3 will be discussed below. There are three strong features at 3435, 3481, and 3498 cm^{-1} as well as a much weaker absorption at 3545 cm^{-1}. The two flanking bands can be assigned to the NH_2 symmetric stretching (3435 cm^{-1}) and the NH_2 antisymmetric stretching (3545 cm^{-1}) vibrations based on comparison with experiments conducted on neutral adenine in the gas phase (see Figure 4.4) and isolated in cryogenic matrices.[23,59,60] There have been some major differences reported between the experimental and theoretical frequencies of the NH_2 symmetric and antisymmetric stretching bands for the DNA bases. This is important to justify when comparing the experimental and

Structure	B3LYP/ 6-31++G(d) //B3LYP/ 6-31G(d,p)[b,c]	B3LYP/ 6-311+G(d)[a]	MP2/6-311 ++G(2d,p) B3LYP/ 6-31G+(d,p)[c]	B2P3LYP/ cc-pVTZ// B3LYP/ 6-31G+(d,p)[c]
A	0		0.0 (0.0)	0.0 (0.0)
B	2.6		3.1 (1.9)	3.1 (1.9)
C	2.5		0.7 (1.3)	0.5 (1.1)
D	4		2.3 (2.4)	2.2 (2.3)
E	24.3	0	17.7 (21.1)	
F	27.8	3.8	23.1 (26.6)	
G	31.5	13.1	25.5 (30.0)	
H		15.1	24.5(28.6)	
I		14.1	23.0 (26.1)	
J		15.9	36.2 (35.8)	
K			37.4 (34.5)	
L			46.2 (39.7)	

Table 4.2: Computed relative enthalpies for various adenine proton-bound dimer structures.

[a] from reference 9 and relative to structure E.

[b] from reference 45.

[c] 298 K enthalpies and (free energies in parentheses), relative to structure A.

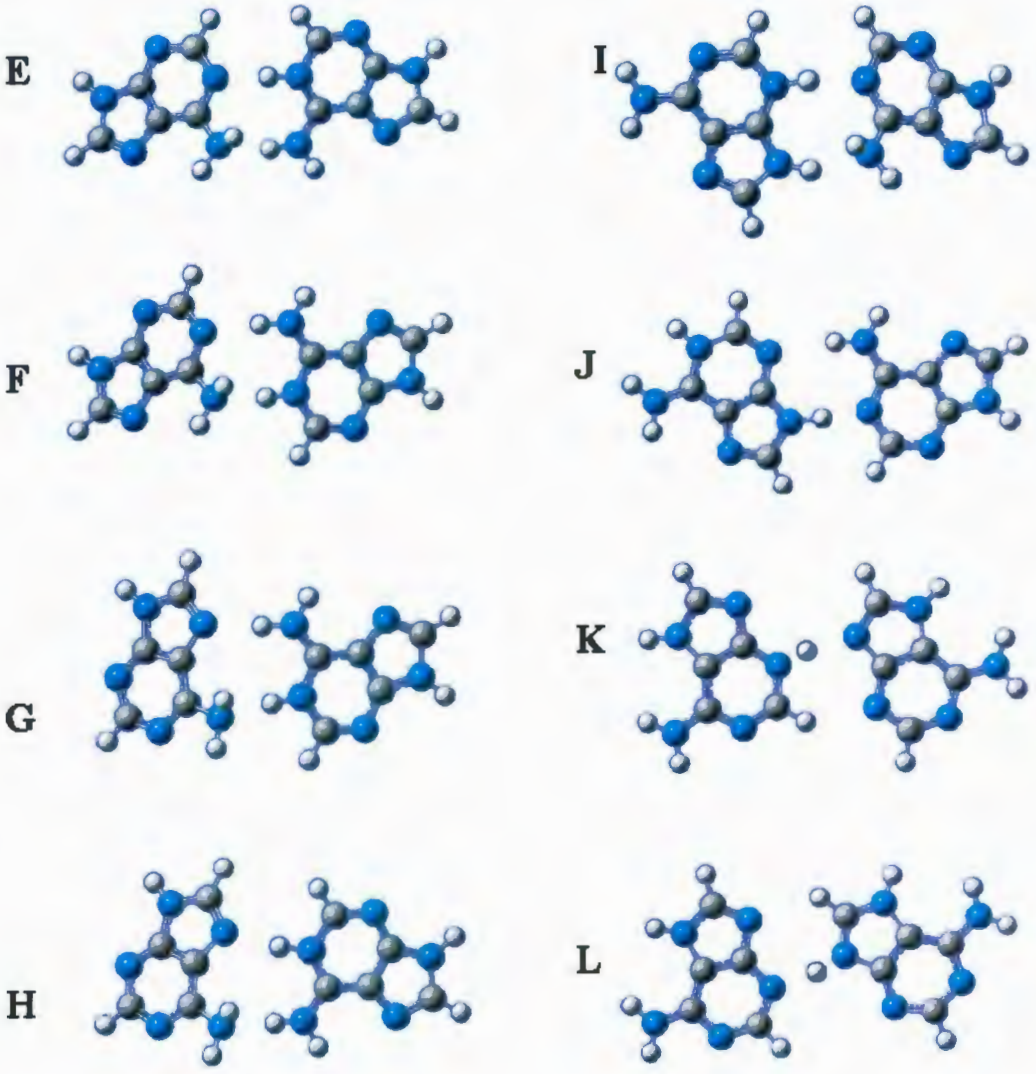

Figure 4.2: B3LYP/6-31+G(d,p) structures of eight high-energy proton-bound adenine dimers.

computed spectra and will be discussed now.

In Figure 4.4, we compare the experimental IRMPD spectrum of the adenine proton-bound dimer and the IR spectrum of neutral adenine in the gas phase[60] which

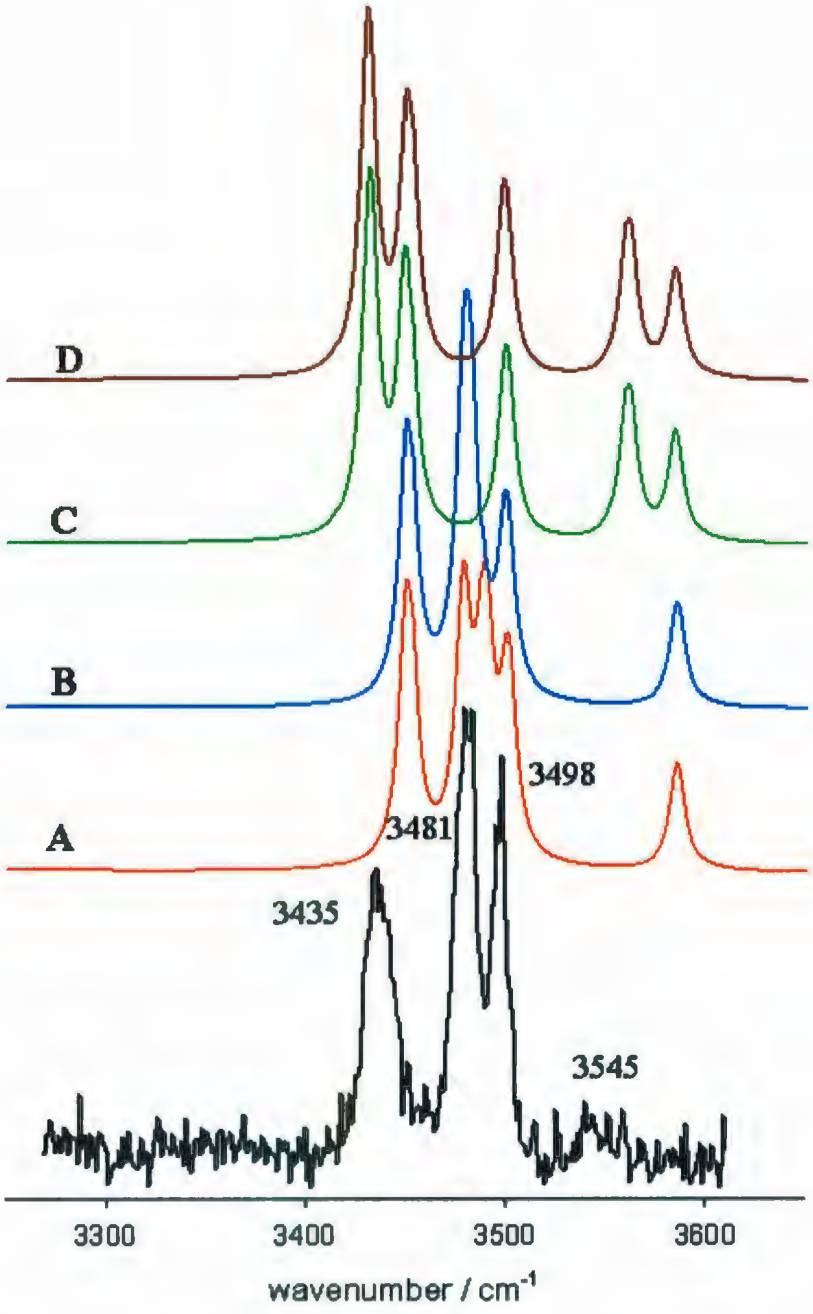

Figure 4.3: Comparison of the experimental IRMPD spectrum of the adenine proton-bound dimers with the B3LYP/6-31+G(d,p) predicted IR spectra for structures A-D (structures in Figure 4.1).

agrees very well with the IR spectrum of matrix isolated adenine[23] and the spectrum determined from hole-burning experiments.[59] It is clear from Fig. 4.4 that the NH_2 antisymmetric stretch and symmetric stretches are in very similar positions for the two species. Also in this figure are the spectra predicted by both B3LYP/6-31+G(d,p) and B3LYP/6-311+G(d,p) scaled by 0.957 and 0.9595, respectively. The scaling factor for the B3LYP/6-311+G(d,p) calculations was chosen to match the position of the N-H stretch predicted by the B3LYP/6-31+G(d,p) calculations and as can be seen from this Figure results did not show any basis set dependencies. This scaling factor is a standard one used by our group.[39,44] It can be seen that the observed NH_2 symmetric and antisymmetric stretching bands are significantly shifted to the red of the predicted band positions in both cases. The same "disagreement" in the positions of these particular modes, NH_2 symmetric and antisymmetric stretching, has also been observed with B3LYP/6-31G(d,p) calculations of adenine[2] and cytosine.[12] The reason for the disagreement between experiment and theory is beyond the scope of this paper but it is important to point out that this disagreement exists and that it must be considered when comparing the experimental and observed spectra of DNA bases and complexes containing an -NH_2 group. We are confident in assigning the 3435 and 3545 cm^{-1} features to the symmetric and antisymmetric stretching vibrations of the proton-bound dimer. Finally, very recent anharmonic calculations on neutral adenine predict the asymmetric and symmetric stretching vibrations at 3539 and 3432 cm^{-1}, respectively, in excellent agreement with experimental values.[61]

The N-H stretching vibrations predicted by the scaled harmonic calculations and the anharmonic calculations are virtually identical.

The two bands in the experimental proton-bound dimer spectrum observed at 3481 and 3498 cm^{-1} (Figure 4.3) may be assigned to free N-H stretching bands based on their positions. Throughout this paper, "free N-H" denotes an N-H group that is not involved in hydrogen bonding, which would strongly red-shift the N-H stretch out of the observable IR region. The band observed at 3501 cm^{-1} (Figure 4.4) for neutral adenine is the N9-H stretch. In the proton-bound dimer the band at 3498 cm^{-1} is in agreement with the theoretically-predicted N7-H stretch of the neutral adenine moiety, for all four lowest energy structures, A to D (see Figure 4.1). In the proton-bound dimer spectrum, the band centered at 3481 cm^{-1} is not observed in the neutral adenine spectrum and is not predicted for structures C and D. In structures C and D as well as neutral adenine, there is only one free N-H moiety. However, in proton-bound dimers A and B there are two free N-H groups. This closely resembles the positions of the predicted absorptions for the N9-H stretch of the protonated adenine moiety for proton-bound dimer structures A and B (see Table 4.3). At almost the same frequency is the free N-H stretch of the amino group involved in hydrogen bonding. This feature observed in the experimental spectrum does not rule out structures C and D from being present in the gas phase, but it does show that structures A and B are present and are perhaps even the dominant species based upon the relative intensities.

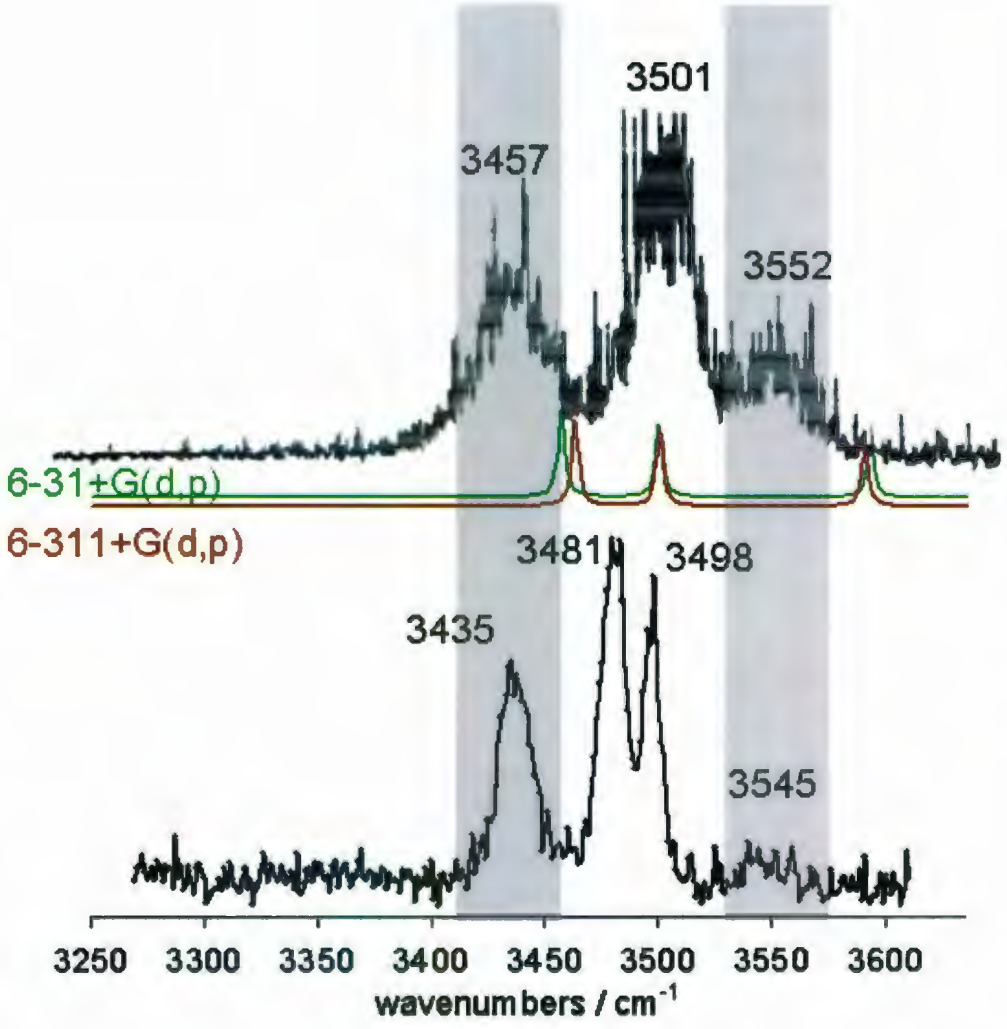

Figure 4.4: Comparison of the experimental IRMPD spectrum of the adenine proton-bound dimer (the black in the bottom) with the gas-phase spectrum of neutral adenine (the black on the top). Also shown are predicted spectra for the N9H tautomer of neutral adenine.

Also in Figure 4.3 are the B3LYP/6-31+G(d,p) predicted IR spectra for the four lowest energy proton-bound dimers, A to D. As discussed above, C and D alone cannot account for the experimental spectrum since the second N-H stretches at 3481 cm^{-1} is not predicted for them. Either of the structures A or B could account for the experimental spectrum since all of the features are accounted for in the predicted spectra. According to the predicted gas-phase thermochemistries, all four isomers are essentially isoenergetic, at least to within the computational error bars. However, if structures C and D are prevalent contributors to the experimental spectrum, the predicted spectra suggest that there would be two each of the NH_2 symmetric and antisymmetric stretching bands or that the experimental bands might be significantly broader than observed. While it is difficult to ascertain whether the weak band at 3545 cm^{-1} is split, the strong band centered at 3435 cm^{-1} does not resemble two bands nor is it significantly broadened. Calculations predict a difference of about 20 cm^{-1} between the two NH_2 symmetric stretching vibrations of C and D (see Table 4.3). Experimentally, the two bands at 3481 and 3498 cm^{-1} in the experimental are well-resolved so we would expect, if C and D are present, there would be two bands around 3435 cm^{-1}.

Observed	assignement	B3LYP/6-31+G(d,p)			
/cm^{-1}		A	B	C	D
3435	NH_2 symmetric stretch	3448	3448	3429[a]/ 3447[b]	3428[a]/ 3447[b]
3481	A(9)-H stretch, free N-H stretch of H-bonded NH_2 group	3479, 3490	3480, 3483		
3498	A(7)-H stretch	3497	3497	3497	3496
3545	NH_2 asymmetric stretch	3582	3583	3558[a]/ 3581[b]	3557[a]/ 3582[b]

Table 4.3: Table of assignments for experimental IRMPD bands for the adenine proton-bound dimer and predicted bands for structures A through D.

[a]of protonated adenine moiety

[b]of neutral adenine moiety

4.3.3 Aqueous Solvation Effects on Dimer Stabilities

Working under the hypothesis that structures A and B are mainly responsible for the experimental infrared spectrum of the adenine proton-bound dimer, an explanation for why structures C and D can be ruled out even though the gas-phase thermochemistries predict virtually equal amounts of all four (Table 4.1) is needed. Because these proton-bound dimers are electrosprayed from solution and desolvated, we explore the effects of solvation on the relative stabilities of the different isomers. Solvent effects remain challenging to address quantum mechanically, so two different approaches are used to investigate them. As we will demonstrate, both solvent models predict qualitatively similar results, suggesting that the models are capturing important physical effects.

First, a polarizable continuum model is used to approximate bulk solvation effects. The geometries of all four structures were therefore re-optimized using the PCM with water (dielectric=78.39) as the solvent at the B3LYP/6-31+G(d,p) level. Frequency calculations were also performed in the presence of the PCM. The thermochemical results of the PCM calculation are shown in Table 4.4. According to the PCM calculations, water preferentially stabilizes structures A and B significantly with respect to C and D.

In order to look at specific localized solvent interaction, explicit microsolvation using a handful of water molecules was examined. Using five water molecules, all hydrogen-bond donors and acceptors on the proton-bound dimers can be saturated

Structure[a]	Unsolvated	PCM	5 waters	5 waters
		B3LYP/6-31+G(d,p)		+ PCM
A	0.0 (0.0)	0.0 (0.0)	0.0 (0.0)	0.0 (0.0)
B	3.1 (1.9)	-0.1 (-0.1)	3.5 (4.2)	-0.2 (0.6)
C	0.5 (1.1)	9.5 (10.4)	21.8 (20.7)	10.6 (11.2)
D	2.2 (2.3)	9.3 (10.5)	22.8 (22.9)	10.2 (11.7)

Table 4.4: Relative enthalpies (relative free energies in parentheses) of solvated and unsolvated adenine proton-bound dimers A, B, C, D.

[a]Unless otherwise stated, all energies are B2P3LYP/cc-pVTZ//B3LYP/6-31+G(d,p), 298 K values.

with water molecules. These structures, which could be reasonably expected to correspond to the inner-most solvent coordination layer in bulk water, are presented in Figure 4.5, and their relative B2P3LYP/cc-pVTZ energies are listed in Table 4.4. In contrast to the gas-phase results, and in good agreement with the PCM ones, the A/B micro-solvated structures are substantially more stable than the C/D ones. Similarly, calculations employing both the explicit solvent molecules and the PCM model provide energies consistent with the explicit-only and PCM calculations (Table 4.4). Simple equilibrium constant calculations based on either the microsolvated or PCM relative free energies suggest that mixtures of isomers A-D in solution will contain less than than 1 percent each of C and D at 298 K. The ratio of A to B

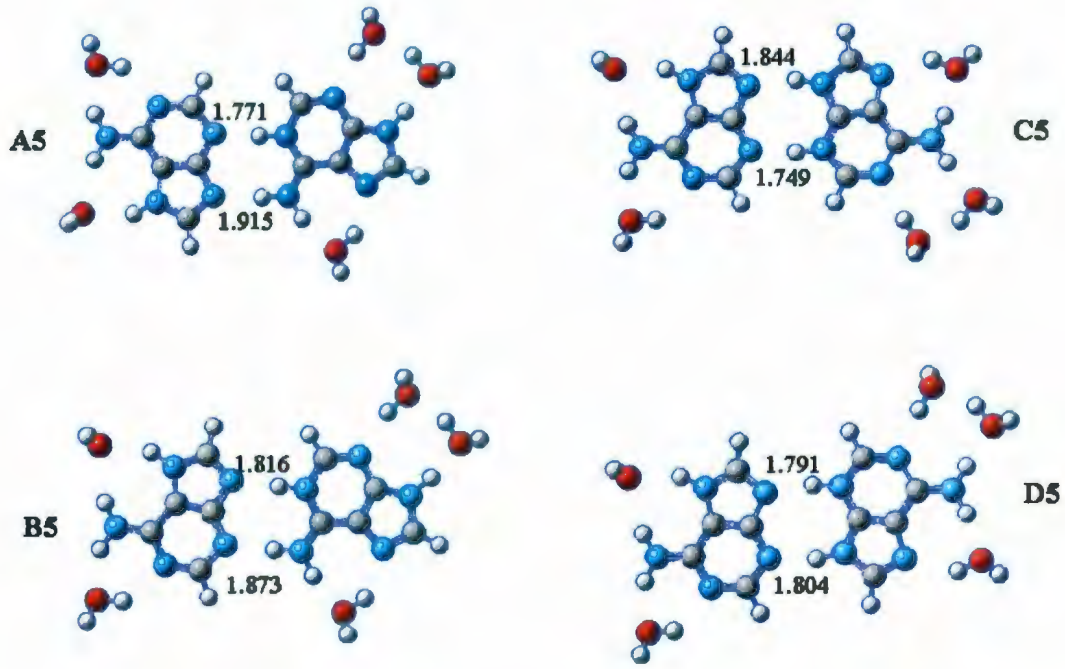

Figure 4.5: B3LYP/6-31+G(d,p) structures of the four lowest-energy adenine proton-bound dimers microsolvated with five water molecules.

depends on the exact free energies used, but it ranges from almost a 50:50 mixture (PCM) to 84 percent A (5-water microsolvated). These results are consistent with the interpretation of the IRMPD spectra discussed above.

Examining these results in more detail, Table 4.5 lists the relative stabilities of the singly-solvated A and C dimer structures presented in Figure 4.6. (Solvated structures for B and D are in Figure S1 in the Appendix 1.) The four single water molecule solvation sites are the most acidic available sites on each of the proton-bound dimers. Each solvation site donates a proton from the adenine to the water, and two of these sites also have an adjacent proton-acceptor site, which accepts a hydrogen

bond from the water molecule. The key difference between the A/B and the C/D dimers is the orientation of the NH_2 group on the right adenine molecule. In A/B, this group is directly involved in the proton-bound dimer formation, while in C/D it is completely accessible to the solvent. A water-adenine hydrogen bond at this site on the side opposite the 5-membered ring is the least favoured position, as is clear from the relative energies of structures A1iv, C1iii, and C1iv (23.8, 24.4, and 28.6 kJ mol^{-1}, respectively). Because C/D have two such solvent-accessible sites, they are stabilized less in water than the A/B proton-bound dimers.

Neither the PCM model nor the explicitly microsolvated model truly describes the bulk water solvation effects. However, both models provide the same results: structures C and D are significantly less stable in water than are A and B. Because the dimers exist in solution prior to electrospray or are borne in aqueous solution during the electrospray process, we propose that the relative stability of these dimers in solution determines which isomers are observed in the IRMPD spectra. This hypothesis assumes that the dimers A and/or B do not isomerize to C and/or D in the gas phase. This assumption seems reasonable, given that the binding energies of these proton-bound dimers are approximately 120-130 kJ mol^{-1} and that substantial disruption of the hydrogen bonding and tautomerization would be required, resulting in a substantial energy barrier for isomerization of A or B to C or D. In other words, isomerization seem quite unlikely on the timescale of the electrospray/desolvation process. This hypothesis is also consistent with the apparent absence of strong sig-

Structure	Relative H (G)[a] B2P3LYP/cc-pVTZ// B3LYP/6-31+G(d,p)
A1i	0.0 (0.0)
A1ii	12.4 (8.3)
A1iii	17.0 (4.5)
A1iv	23.8 (20.8)
B1i	3.0 (3.1)
B1ii	15.7 (13.4)
B1iii	21.5 (10.5)
B1iv	26.3 (24.2)
C1i	-0.3 (-0.8)
C1ii	14.2 (11.9)
C1iii	24.4 (21.2)
C1iv	28.6 (14.3)
D1i	1.4 (0.9)
D1ii	15.0 (12.9)
D1iii	25.8 (22.9)
D1iv	30.3 (15.9)

Table 4.5: 298 K relative enthalpies (and free energies) for singly solvated adenine proton-bound dimers. See Figure 4.6 for structures.

[a]298 K

nals for isomers C and D in the spectra. In contrast, the gas-phase energies which find all four structures nearly degenerate. cannot explain this observation.

4.3.4 Comparison of IRMPD Spectrum With Higher-Energy Isomers

In Figure 4.7, the IRMPD spectrum is compared to the computed spectra for structures E through L. Structures I and J have multiple strong bands in the lower-energy portion of the spectrum and therefore can be ruled out on spectroscopic grounds. However, structures E, F, G, H, K, and L cannot be equivocally ruled out based solely by comparison of the experimental and computed spectra. These structures alone cannot account for the spectrum, but the absence of predicted bands does not rule them out. Structures E through L can, though, be ruled out based on their computed energies. Even PCM calculations with these structures do not lower their energies with respect to A and B.

4.4 Conclusions

Gas-phase calculations predict four isoenergetic isomers of the proton-bound adenine dimer. In contrast, the IRMPD spectrum of electrosprayed adenine proton-

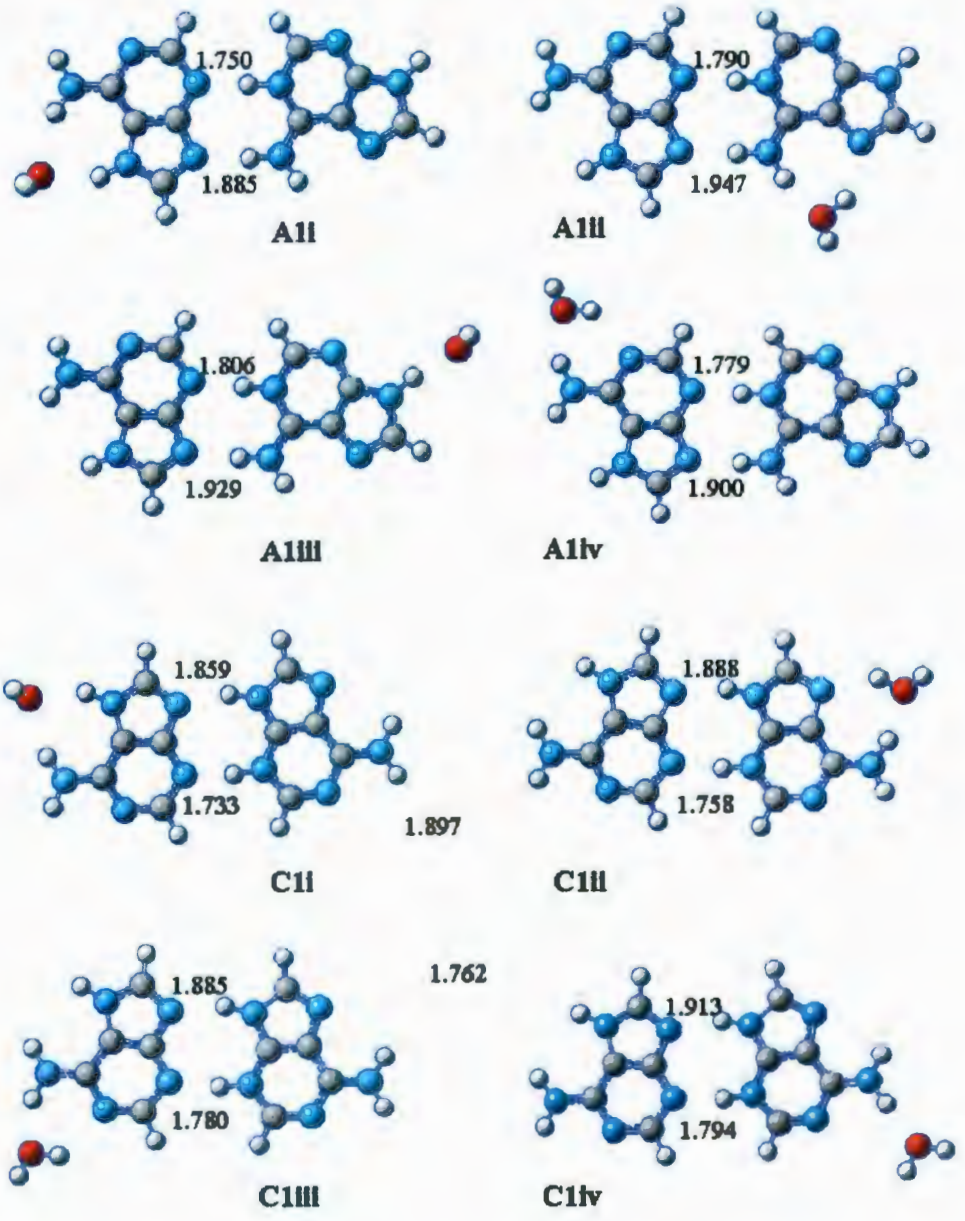

Figure 4.6: The four B3LYP/6-31+G(d,p) singly microsolvated structures each for A and C. Microsolvated structures for B and D are in Appendix 1.

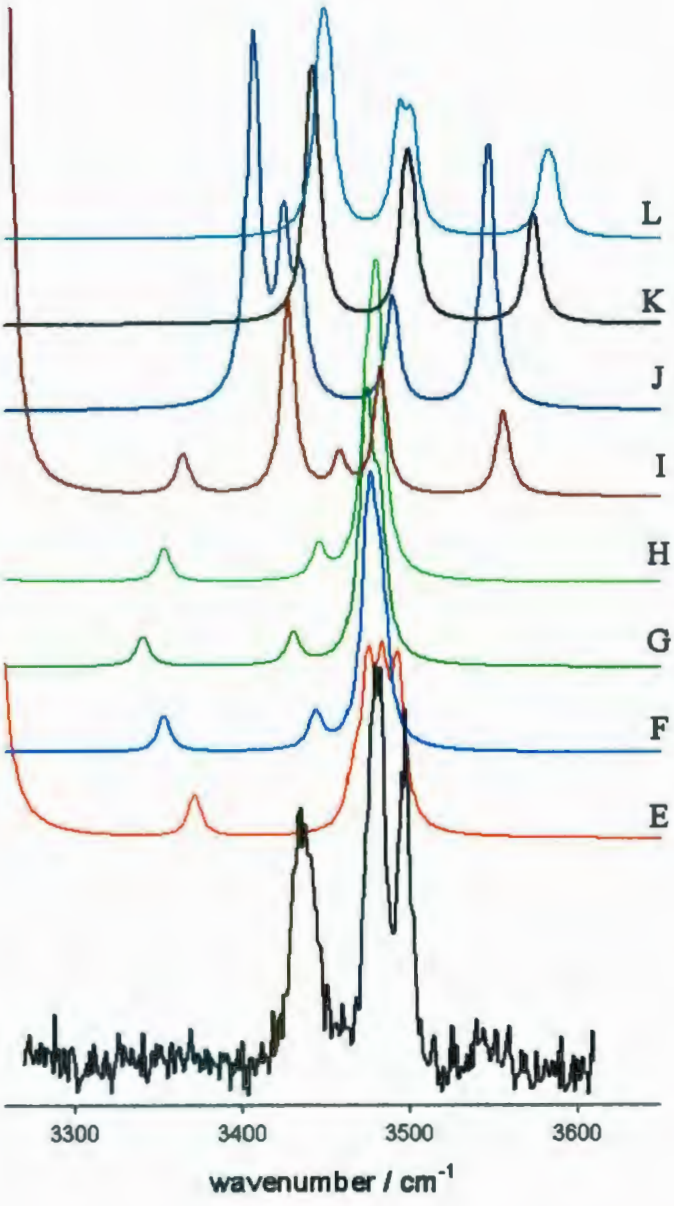

Figure 4.7: Comparison of the experimental IRMPD spectrum of the adenine proton-bound dimers with the B3LYP/6-31+G(d,p) predicted IR spectra for structures E-L (structures in Figure 4.2).

bound dimers with the predicted IR spectra reveal that only two of the isomers are present. PCM model calculations and microsolvation calculations with five explicit water molecules qualitatively agree that solvation significantly stabilized two of the four isomers. These two solvent-stabilized isomers are consistent with the interpretation of the IRMPD spectra. This work demonstrates that, in some cases, using gas-phase calculations to predict the structures of ions born in solution and transferred to the gas-phase via electrospray ionization can give misleading results.

4.5 Supporting Information

This information is available free of charge via the Internet at http://pubs.acs.org as well as Appendix 1.

Bibliography

1. Seeman, N. C. *Nature* **2003**, *421*, 427.
2. Mao, C.; LaBean, T.; Reif, J. H.; Seeman, N. C. *Nature* **2000**, *407*, 493.
3. Cheng, Y.T., Wang, Z. M.; Liao, C. S.; Yan, C. H. *New. J. Chem.* **2002**, *26*, 1360.
4. Gu, J.; Leszezynski, J. *J. Phys. Chem. A* **1999**, *103*, 2744.
5. Sukhanov, O. S.; Shishkin, O. V.; Gorb, L.; Podolyan, Y.; Leszczynski, J.; *J. Phys. Chem. B* **2003**, *107*, 2846.
6. Del Bene, J. E. *J. Phys. Chem.* **1983**, *87*,367.
7. Chandra, A. K.; Nguyen, M. T.; Uchimaru, T.; Zeegers–Huyskens, T. *J. Phys. Chem. A* **1999**, *103*, 8853.
8. Mennucci, B.; Toniolo, A.; Tomasi, J. *J. Phys. Chem. A* **2001**, *105*, 4749.
9. Liu, B. P.; Ding, Y. J.; Yuan, X. A. *J. Mol. Struct. THEOCHEM,* **2008**, *848*, 47.
10. Park, H. S.; Nam, S. H.; Song, J. K.; Park, S. M.; Ryu, S. *J. Phys. Chem. A* **2008**, *112*, 9023.
11. Delchev, V. B.; Shterev, I. G.; Mikosch, H.; Kochev, N. T. *J. Mol. Model* **2007**, *13*, 1001.
12. Wang, F.; Downton, M. T.; Kidwani, N. *J. Theo. Comput. Chem.* **2005**, *4*, 247.
13. Zierkiewicz, W.; Komorowski, L.; Michalska, D.; Cerny, J.; Hobza, P. *J. Phys. Chem. B* **2008**, *112*, 16734.
14. Herrera, B.; Toro-Labbe, A. *J. Phys. Chem. A* **2007**, *111*, 5921.
15. Florian, J.; Leszczynski, J. *J. Am. Chem. Soc.* **1996**, *118*, 3017.

16. Lowdin, P. O. *Adv. Quantum Chem.* **1965**, *2*, 213.

17. Topal, M. D.; Fresco, J. R. *Nature* **1976**, *263*, 285.

18. Hanus, M.; Kabalac, M.; Rejnek, J.; Ryjacek, F.; Hobza, P. *J. Phys. Chem. B* **2004**, *108*, 2087.

19. Guerra, C. F.; Bickelhaupt, F.; Saha, S.; Wang, F. *J. Phys. Chem. A* **2006**, *110*, 4012.

20. Turecek, F.; Chen, X. *J. Am. Soc. Mass Spectrom.* **2005**, *16*, 1713.

21. Bell, R. L. *The tunnel effect in Chemistry,* Chapman and Hall: New York, **1980**.

22. Curtiss, L. A.; Drapcho, D. L.; Pople, Y. A. *Chem. Phys. Lett.* **1984**, *103*, 437.

23. Nowak, M. J.; Lapinski, L.; Kwiatkowski, J. S.; Leszezynski, J. *J. Phys. Chem.* **1996**, *100*, 3527.

24. Bonaccorsi, B.; Pullman, A.; Scrocco, E.; Tomasi, J. *Theor. Chim. Acta* **1972**, *24*, 51.

25. Russo, N.; Toscana, M.; Grand, A.; Jolibois, F. *J. Comput. Chem.* **1998**, *19*, 989.

26. Podolyan, Y.; Gorb, L.; Leszczynski, J. *J. Phys. Chem. A* **2000**, *104*, 7346.

27. Meot-Ner, M. *J. Am. Chem. Soc.* **1979**, *101*, 2396.

28. Wolken, J. K.; Turecek, F. *J. Am. Soc. Mass Spectrom.* **2000**, *11*, 1065.

29. Greco, F.; Liguori, A.; Sindona, G.; Uccelle, N. *J. Am. Chem. Soc.* **1990**, *112*, 9092.

30. Kumar, G. S.; Das, S.; Bhadra, K.; Maiti, M. *Bioorg. Med. Chem.* **2003**, *11*, 4861.

31. Chen, F. M. *Biochemistry* **1984**, *23*, 6159.

32. Volker, J.; Klump, H. H. *Biochemistry* **1994**, *33*, 13502.

33. Wilson, W. D.; Tanious, F. A.; Mizan, S.; Yao, S.; Kiselyov, A. S.; Zon, G; Strekowski, L. *Biochemistry* **1993**, *32*, 10614.

34. Cooney, M.; Czernusszewicz, G.; Postel, E. H.; Flint, S. J.; Hogan, M. E. *Science* **1988**, *241*, 456.

35. Marian, C.; Nolting, D.; Weinkauf, R. *Phys. Chem. Chem. Phys.* **2005**, *7*, 3306.

36. Fridgen, T. D. *Mass Spectrom. Rev.* **2009**, *28*, 586.

37. Polfer, N. C.; Oomens, J. *Mass Spectrom. Rev.* **2009**, *28*, 468.

38. Eyler, J. R. *Mass Spectrom. Rev.* **2009**, *28*, 448.

39. Atkins, C. G.; Rajabi, K.; Gillis, E. A. L.; Fridgen, T. D. *J. Phys. Chem. A* **2008**, *112*, 10220.

40. Rajabi, K.; Fridgen, T. D. *J. Phys. Chem. A* **2008**, *112*, 23.

41. Yoon, S. H.; Chamot-Rooke, J.; Perkins, B.; Hilderbrand A. E.; Poutsma, J. C.; Wysocki, V. H. *J. Am. Chem. Soc.* **2008**, *130*, 17644.

42. Salpin, J. Y.; Guillaumont, S.; Tortajada, J.; MacAleese, L.; Lemaire, J. Maitre, P. *Chem. Phys. Chem.* **2007**, *8*, 2235.

43. Rajabi, K.; Easterling, M. L.; Fridgen, T. D. *J. Am. Soc. Mass Spectrom.* **2009**, *20*, 411.

44. Gillis, E. A. L.; Rajabi, K.; Fridgen, T. D. *J. Phys. Chem. A* **2009**, *113*, 824.

45. Hud, N. V.; Morton, T. H. *J. Phys. Chem. A* **2007**, *111*, 3369.

46. Bakker, J. M.; Besson, T.; Lemaire, J.; Scuderi, D.; Maitre, P. *J. Phys. Chem. A* **2007**, *111*, 13415.

47. Gaussian 03, Revision B.04, M. J. Frisch, G. W. Trucks, H. B. Schlegel, G. E. Scuseria, M. A. Robb, J. R. Cheeseman, J. A. Montgomery, Jr., T. Vreven, K. N.

Kudin, J. C. Burant, J. M. Millam, S. S. Iyengar, J. Tomasi, V. Barone, B. Mennucci, M. Cossi, G. Scalmani, N. Rega, G. A. Petersson, H. Nakatsuji, M. Hada, M. Ehara, K. Toyota, R. Fukuda, J. Hasegawa, M. Ishida, T. Nakajima, Y. Honda, O. Kitao, H. Nakai, M. Klene, X. Li, J. E. Knox, H. P. Hratchian, J. B. Cross, C. Adamo, J. Jaramillo, R. Gomperts, R. E. Stratmann, O. Yazyev, A. J. Austin, R. Cammi, C. Pomelli, J. W. Ochterski, P. Y. Ayala, K. Morokuma, G. A. Voth, P. Salvador, J. J. Dannenberg, V. G. Zakrzewski, S. Dapprich, A. D. Daniels, M. C. Strain, O. Farkas, D. K. Malick, A. D. Rabuck, K. Raghavachari, J. B. Foresman, J. V. Ortiz, Q. Cui, A. G. Baboul, S. Clifford, J. Cioslowski, B. B. Stefanov, G. Liu, A. Liashenko, P. Piskorz, I. Komaromi, R. L. Martin, D. J. Fox, T. Keith, M. A. Al-Laham, C. Y. Peng, A. Nanayakkara, M. Challacombe, P. M. W. Gill, B. Johnson, W. Chen, M. W. Wong, C. Gonzalez, and J. A. Pople, Gaussian, Inc., Pittsburgh PA, **2003**.

48. Benighaus, T.; Distasio, R. A. Jr.; Lochan, R. C.; Chai, J.; Head-Gordon, M. *J. Phys. Chem. A* **2008**, *112*, 2702.

49. Dunning, T. H. *J. Chem. Phys.* **1989**, *90*, 1007.

50. Kristyan, S.;Pulay, P. *Chem. Phys. Lett.* **1994**, *229*, 175.

51. a) Grimme, S. *J. Chem. Phys.* **2006**, *124*, 034108. b) Schwabe, T.; Grimme, S. *Phys. Chem. Chem. Phys.* **2007**, *9*, 3397.

52. Boys, S.F.; Bernardi, F. *Mol. Phys.* **1970**, *19*, 553-566.

53. Y. Shao, L. F. Molnar, Y. Jung, J. Kussmann, C. Ochsenfeld, S. T. Brown, A. T. B. Gilbert, L. V. Slipchenko, S. V. Levchenko, D. P. O'Neill, R. A. DiStasio, Jr., R. C.

Lochan, T. Wang, G. J. O. Beran, N. A. Besley, J. M. Herbert, C. Y. Lin, T. Van Voorhis, S. H. Chien, A. Sodt, R. P. Steele, V. A. Rassolov, P. E. Maslen, P. P. Korambath, R. D. Adamson, B. Austin, J. Baker, E. F. C. Byrd, H. Dachsel, R. J. Doerksen, A. Dreuw, B. D. Dunietz, A. D. Dutoi, T. R. Furlani, S. R. Gwaltney, A. Heyden, S. Hirata, C.-P. Hsu, G. Kedziora, R. Z. Khalliulin, P. Klunzinger, A. M. Lee, M. S. Lee, W. Z. Liang, I. Lotan, N. Nair, B. Peters, E. I. Proynov, P. A. Pieniazek, Y. M. Rhee, J. Ritchie, E. Rosta, C. D. Sherrill, A. C. Simmonett, J. E. Subotnik, H. L. Woodcock, III, W. Zhang, A. T. Bell, A. K. Chakraborty, D. M. Chipman, F. J. Keil, A. Warshel, W. J. Hehre, H. F. Schaefer, III, J. Kong, A. I. Krylov, P. M. W. Gill, and M. Head-Gordon, *Phys. Chem. Chem. Phys.* **2006**, *8*, 3172.

54. a) Dunlap, B. I. *J. Chem. Phys.* **1983**, *78*, 3140. b) Feyereisen, M.; Fitzgerald, G.; Komornicki, A. *Chem. Phys. Lett.* **1993**, *208*, 359. c) Eichkorn, K.; Treutler, O.; Öhm, H.; Häser, M; Ahlrichs, R. *Chem. Phys. Lett.* **1995**, *240*, 283.

55. Weigend, F.; Köhn, A.; Hättig, C. *J. Chem. Phys.* **2002**, *116*, 3175.

56. Steele, R. P.; Distasio, R. A. Jr.; Shao, Y.; Kong, J.; Head-Gordon, M. *J. Chem. Phys.* **2006**, *125*, 074108.

57. Cossi, M.; Rega, N.; Scalmani, G.; Barone, V. *J. Comp. Chem.* **2003**, *24*, 669.

58. The stability of the N3-protonated adenine 7H tautomer is computed to be nearly the same as the N1-protonated adenine 9H tautomer, as they differ by only a fraction of a kJ mol^{-1}. Which species is more stable depends on exactly which functional and

basis set is used, but for B2P3LYP/cc-pVTZ, the N1H/9H species is 0.4 kJ mol^{-1} more stable. These relative stabilities of the two tautomers agree well with the experimental results from reference 35.

59. Plutzer C.; Kleinermanns, K. *Phys. Chem. Chem. Phys.* **2002**, *4*, 4877.

60. Colarusso, P.; Zhang, K.; Guo, B.; Bernath, P. *Chem. Phys. Lett.* **1997**, *269*, 39.

61. Zierkiewicz, W.; Komorowski, L.; Michalaska, D.; Cerny, J.; Hobza, P. *J. Phys. Chem. B* **2008**, *112*, 16734.

Chapter 5

Solvation of Electrosprayed Ions in the Accumulation/ Collision Hexapole of a Hybrid Q-FTMS

5.1 Introduction*

Studies of solvated ions in the gas-phase provide information about the preferred coordination of ions by solvent molecules, their conformational geometries, and changes of geometry upon solvation.[1] The structural properties are typically deduced from fundamental studies of their thermochemistries, reactivities, and more recently, the vibrational spectroscopy of gaseous ions.[2] The ultimate purpose and challenge for

*This Chapter has been published as K. Rajabi, M. L. Easterling and T. D. Fridgen, *J. Am. Soc. Mass Spectrom.* **2009**, *20*, 411-418.

studying the physical properties of sequentially solvated ions is to extrapolate to, or contrast these properties with those in the solution phase, especially for biologically interesting ions. Mass spectrometry has become a powerful technique for investigating biomolecules following the development of electrospray ionization (ESI)[3] and matrix-assisted laser desorption/ionization (MALDI).[4–6] Noncovalently bound biological complexes can be transferred from aqueous solutions to the gas phase by ESI for further study of the completely desolvated complex. In some instances, a small amount of solvated ions has been reported from electrospray, allowing the structure, reactivity and thermochemistry of the hydrated ions to be studied.[7] Lee *et al.*[8] studied extensively hydrated peptides from an electrospray source by operating the capillary at room temperature, with no nebulizer or drying gas, and optimizing the potentials in the electrospray source. These ions were found to be cooled to between 130 and 150 K by evaporation of water without drying gas, effectively freezing the biomolecules. Rodriguez-Cruz *et al.*[9] studied doubly protonated gramicidin S ions with up to 50 water molecules attached in a modified instrument with a home-built electrospray source equipped with a heated capillary inlet. They formed the ions under "gentle" electrospray conditions and later described two possible mechanisms for formation of hydrated ions by ESI,[10] condensation of solvent onto ions due to expansion inside the ESI interface and/or solvent evaporation of more extensively hydrated ions or electrospray droplets. The extent of hydration of gas-phase gramicidin S $(M+2H)^{2+}$ ions was observed to decrease with an increase in the temperature of the capillary.

Rodriguez-Cruz and Williams[11] also studied solvent exchange reactions of hydrated divalent alkaline earth metals with benzene by ESI Fourier-Transform mass spectrometry (FTMS) at room temperature. Aqueous solutions of metal chloride salts were introduced to the mass spectrometer by nanoelectrospray. Metal ions with 4-7 water molecules were selected and thermalised in the accumulation process by introducing N_2 gas. After isolating the ions of interest, they were exposed to benzene at constant pressure. They showed that the rate constant of ligand exchange increases with the size of the metal due to the stronger cation-π interaction between the metal ion and benzene. In addition, for the heptahydrated metal ions, the seventh water molecule was shown to be in an outer solvation shell, bound much more weakly, by observing the rates of unimolecular dissociation reactions losing subsequent water molecules. Recently, the structures of hydrated Ca^{2+} ions directly from an electrospray source have been studied by consequence spectroscopy[12] and thermochemically by collision-induced dissociation in a guided ion beam tandem mass spectrometer.[13] These studies show conclusively that the Ca^{2+} ion has six water molecules in the first solvent shell bound directly to the metal ion. While electrospray has been useful in the study of solvated ions, other methods of generating solvated gaseous ions typically involve a high pressure source of ions[14–19] or by injecting ions[20] or electrons[21,22] into a molecular expansion.

Electrospray, under normal circumstances, is usually a very efficient method of forming completely desolvated gaseous ions. At Memorial, we are interested in study-

ing the structures and chemistry of ion-molecule complexes, such as protonated or metal ion-bound species which are also solvated, using techniques such as IRMPD spectroscopy, BIRD,[23] and by ion-molecule reactions.[24] As a means to achieve this, a Bruker apex Qe 70 FTMS has been obtained. As in any FTMS, due to the very low operating pressure of the ion cyclotron resonance (ICR) cell, solvated species must be prepared outside the ICR cell. The purpose of this paper is to explain the method of solvating ions in the storage hexapole cell of a commercial hybrid Q-FTMS. We also present results of some preliminary studies of various solvated ions.

5.2 Experimental

For this work, three different Bruker apex-Qe 70 FTMS instruments were used. The first is at the Bruker showroom in Billerica, MA, one is at the University of Paris 11 in Orsay, France, and the third is at Memorial University in St. John's, NL. The instrument in Orsay currently is mated to both a free electron laser and a Laser Vision OPO/A laser. Details of IRMPD experiments with both lasers have been published previously.[25] The IRMPD spectrum reported here was recorded using the OPO/A laser operating in the 2500-4000 cm^{-1} region covering the N-H and O-H stretching vibrations. If the laser is resonant with an infrared absorption then dissociation of the ion is observed. The spectral width of the laser was estimated to be 5 cm^{-1}.

A schematic of the source, quadrupole/hexapole, ion transfer optics and ICR cell

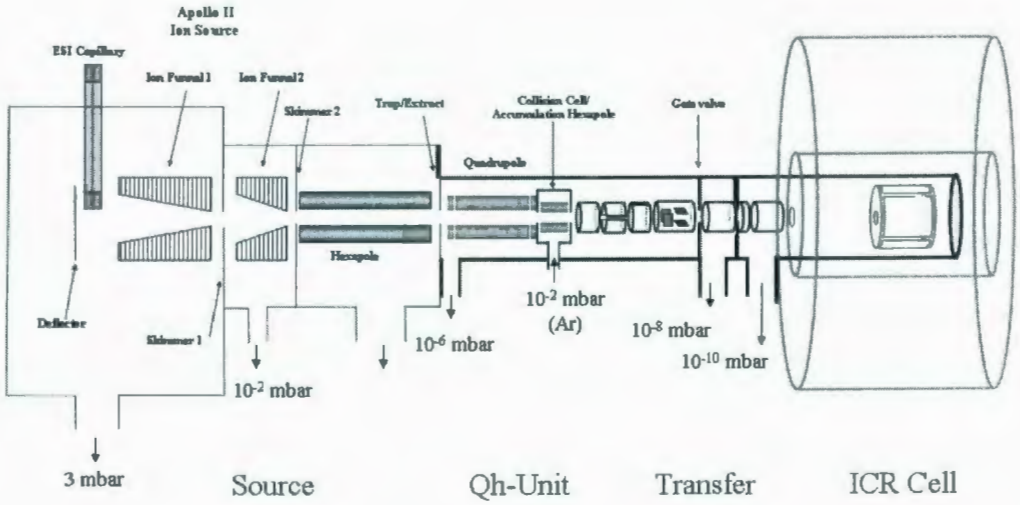

Figure 5.1: Schematic showing the source, Qh region, ion transfer optics, and ICR cell for the Bruker Apex Qe 70 FTMS.

region is shown in Figure 5.1. In normal electrospray ionization mode, a small amount of Ar gas (0.1-0.2 L min^{-1}) flows into the collision hexapole to aid in trapping of ions and can be used to affect collision induced dissociation (CID). The pressure in the vacuum chamber around the collision cell is $\sim 10^{-5}$ mbar when Ar or solvent is flowing into the collision hexapole where the pressure is estimated to be $\sim 10^{-3}$ to 10^{-2} mbar. Ions are typically accumulated in the collision cell hexapole for a brief period of time, 100-500 ms, but to prepare solvated species, higher accumulation times are desirable to increase the signal intensity. Following accumulation, the ions are transferred from this hexapole through a series of ion optics to the ICR cell. The instrument at Memorial University has been modified to include a second leak valve to introduce solvent into the quadrupole and hexapole region. While this adds

flexibility and ease of use. experiments on the Billerica and Orsay instruments were conducted by simply replacing the Ar collision gas with a solvent, methanol or water in the present experiments, in a glass vial. However, as noted below, if one prefers less solvation, the addition of a small pressure of solvent and some Ar to increase trapping efficiency makes at least two gas inlets necessary. The solvents. were freeze-pump- thawed to expel dissolved air.

Precursor ions were electrosprayed from aqueous solutions containing 0.1 mM adenine or thymine, and a few drops of 1 mM LiCl, KCl or $CuSO_4$ in 18 MOhm Millipore water. The DNA bases and salts were obtained from Aldrich and were used without further purification. The water used to provide vapour for solvating was 18 MΩ. The methanol used was 99.8 percent and was purchased from ACP Chemicals in Montreal.

5.3 Results and Discussion

The conditions in the accumulation cell play a crucial role in successful addition of solvent. Ion kinetic energy is expected to and does play a fairly important role in whether solvation occurs. In this instrumental configuration (Figure 5.1), the ion kinetic energy at the point of entry to the collision cell is programmed by how the collision cell is biased to the second stage of the ion funnel. Lowering the relative DC bias of the collision cell increases the kinetic energy over what is necessary to efficiently deliver the ions into the hexapole trap, effectively the 'zero volt' collision

energy. For these experiments, the effect of kinetic energy on solvation was explored by modulation of the collision cell DC bias. Zero to a few tenths of volts of collision energy has very little effect on solvation but more than a few volts results in inefficient solvation. As well, high collision voltages typically result in less cluster ions making it to the ICR cell. In Figure 5.2a, the effect of collision voltage is shown on the fraction of solvated $(Thy)_2Li^+$, defined as the intensity of $(Thy)_2Li^+(H_2O)$ divided by the sum of $(Thy)_2Li^+(H_2O)$ and $(Thy)_2Li^+$ intensities. After a few tenths of a volt collision energy, the fraction of solvated ions drops off fairly linearly. The total ion intensity (only $(Thy)_2Li^+$ and its solvated analogue) is also plotted. The total ion intensity increases slightly from 0 to $\sim$2 V then drops off markedly. Typically we use 0 or very close to it, but not more than 1 V collision energy for IRMPD experiments.

The trapping time in the accumulation cell is also an important parameter. Shorter times typically result in a larger degree of solvation but also less total ion signal. There are instances however, when total ion signal remains high, but a shorter time results in a stronger signal for solvated ions, and this parameter must be optimized for each system. For experiments such as IRMPD spectroscopy where hundreds of steps in wavelength are required with four to eight scans per wavelength, shorter times are beneficial. For solvation of $(Thy)_2Li^+$, Figure 5.2b shows the effect of accumulation time on both the fraction of solvation and the total ion intensity. Typically $\sim$2 s is a good balance between a decent degree of solvation, good ion intensity and total experiment time. The loss of solvated ion signal at longer times is most likely due to heating

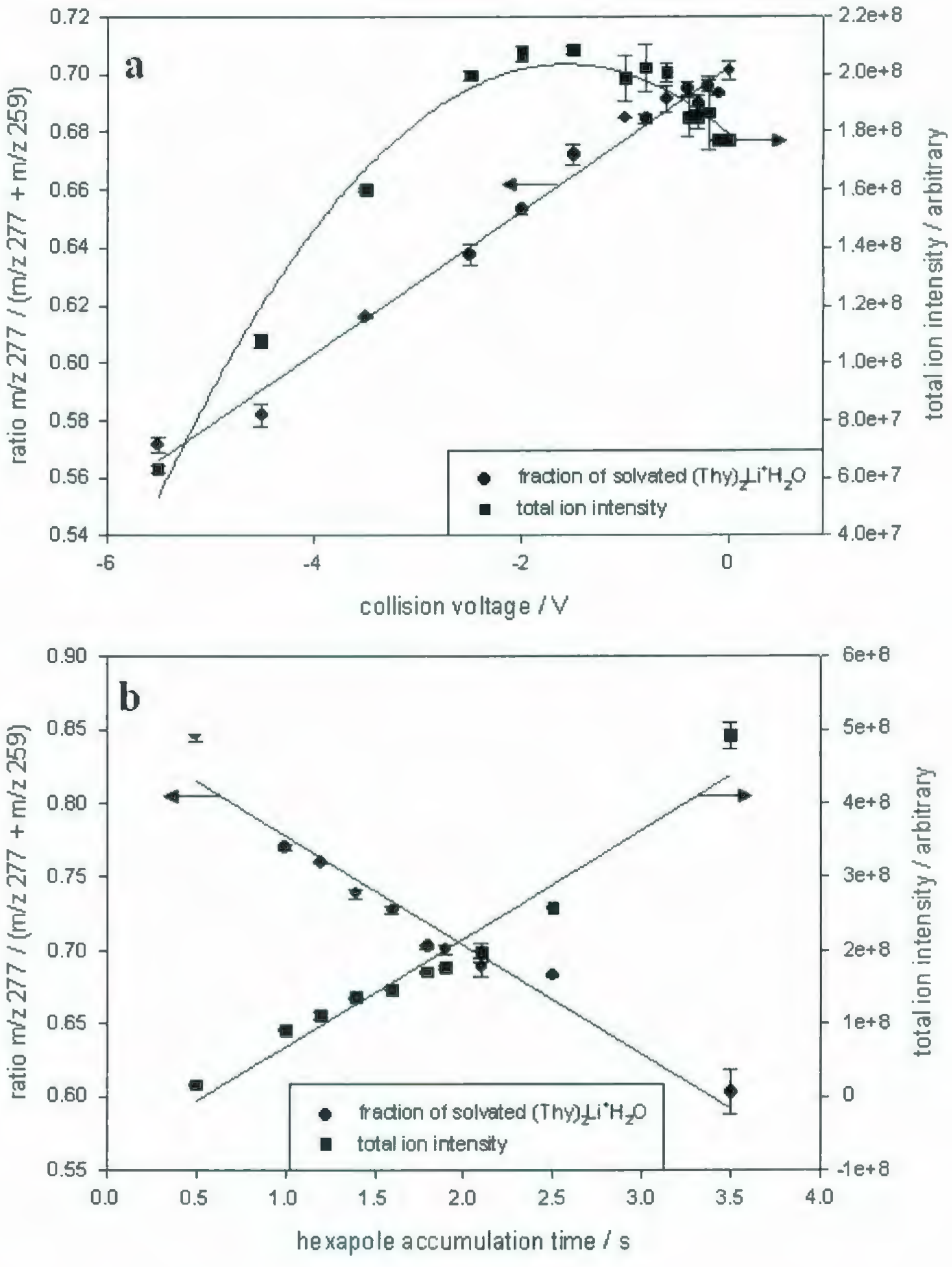

Figure 5.2: The fraction of solvated Thy_2Li^+ and total ion intensity versus (a) collision voltage and (b) hexapole accumulation time. The "fitted" lines are merely to guide the eye. Arrows indicate the ordinate to which the data belong.

of ions in the hexapole trap. Sannes-Lowery *et al.*[26,27] have reported that excessive storage times, more than a few seconds, can cause dissociation in biomolecules with low dissociation thresholds, termed multipole storage assisted dissociation (MSAD).

The pressure of solvent also must be optimized. If the solvent pressure is too high, the signal starts to fall off because the accumulation cell is filled with the solvent vapour, presumably resulting in loss of ions from the accumulation cell due to collisions. Typically the pressure reading on the ion gauge is $5\text{-}6\times10^{-5}$ mbar.

In addition, the chemical characteristic of the species is also important. For example, the basicity of the DNA bases can influence the ease and extent of solvation. For example, it was found that it was easier to solvate ions containing uracil and thymine than adenine. Presumably this is because uracil and thymine are less basic than adenine.[28] The charge in cationized adenine is more diffuse which may impede solvation. Furthermore, in our experience, solvation occurs at the "ionic centre" or the metal cation. As such, steric considerations and the size of the metal ion can affect solvation. While it is possible to attach many solvent molecules to potasiated bases, lithiated bases are difficult to multiply solvate. Furthermore, while it was possible to attach two water molecules to $(Thy)Li^+$, we were only able to add one water to $(Thy)_2Li^+$. Due to the different chemical nature of each ionic species, one set of conditions to prepare a particular ion with a given degree of solvation may not work for another ion. However, limited solvation in the accumulation cell seems to be efficient and highly reproducible once the right conditions are found.

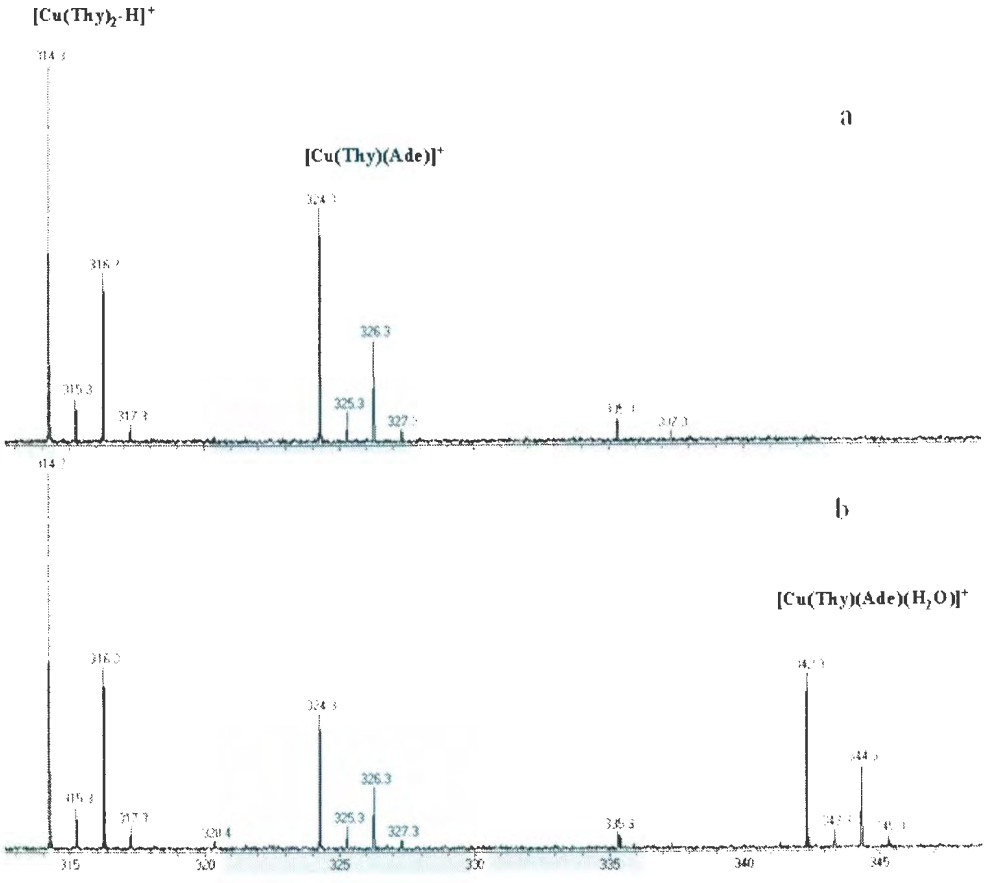

Figure 5.3: (a) ESI mass spectra of a 0.1 mM $CuCl_2$ solution containing ~0.1 mM thymine and a few drops of 0.1 mM adenine in 18 MΩ water. (b) same experiment except with water vapor in the hexapole accumulation cell.

One example which illustrates how the chemical nature or structure of the precursor ion can affect solvation is displayed in Figure 5.3. A small amount of adenine solution was also added to the thymine/$CuSO_4$ solution and it was possible to observe two ions containing copper. The first, whose main isotopic mass is at m/z 314 is $[Cu(Thy)_2\text{-}H]^+$ and the second at m/z 324 is $[Cu(Thy)(Ade)]^+$. At this point, it is uncertain as to why the former loses H^+ to remain singly charged, while the ion containing adenine is reduced by an electron. However, what is also interesting is that under no conditions was it possible to solvate the m/z 314 ion while the m/z 324 ion adds one molecule of water to form m/z 342. The $[Cu(Thy)(Ade)]^+$ ion also seemed to be maximized by spending 1.5 s time in the accumulation cell. The mass spectrum shown in Figure 5.3b is after 1.5 s in the accumulation cell while longer storage times resulted in less m/z 342 and more m/z 324 but overall less ion intensity. The ability of m/z 324 to add water and the inability of m/z 314 to add water could be due to the difference in binding energy of water to these ions and/or major structural differences. For example the structure of m/z 314 ion could limit access of solvent to the "central" copper ion. This is a question for further study using spectroscopic, thermochemical and computational techniques.

In Figure 5.4 BIRD plots are presented for solvated potassium cation bound dimers of adenine, $(Ade)_2K^+$, with up to three solvent molecules of either water (Fig. 5.3a) or methanol (Fig. 5.3b). While it was possible to add three water molecules to $(Ade)_2K^+$, it was not possible to obtain much more than 15 percent of the total ion

abundance of $(Ade)_2(H_2O)_nK^+$. Based on its instability in the ICR cell this is likely due to a small binding energy for the third water molecule. For methanol, a good abundance of triply solvated ion, ~70 percent of the total solvated ion intensity was obtained. BIRD rate constants were derived from this data by modelling the intensity vs time data assuming a sequential loss of solvent dissociation mechanism, (X= H_2O, CH_3OH)

$$(Ade)_2(X)_3K^+ \xrightarrow{k_{3\to2}} (Ade)_2(X)_2K^+ + X \tag{5.1}$$

$$(Ade)_2(X)_2K^+ \xrightarrow{k_{2\to1}} (Ade)_2(X)K^+ + X \tag{5.2}$$

$$(Ade)_2(X)K^+ \xrightarrow{k_{1\to0}} (Ade)_2K^+ + X \tag{5.3}$$

which, based on the fits to the data, is a good assumption.

In all cases, BIRD rate constants for the loss of water are significantly larger than for the loss of methanol (see Table 5.1). A temperature study is required to obtain binding energies[29] for sequential solvent loss; however, it is safe to make a few qualitative remarks. BIRD rates are mainly dependent upon the binding energy of the complex, but the rate of photon absorption is also important. Therefore, to compare methanol and water binding energies, one has to take into account the difference in absorption properties of water and methanol. The strongly absorbing O-H symmetric stretch at higher energy are replaced by relatively weak C-H stretching. The HOH bend is replaced by a strongly absorbing CO stretch and HOC bend (among other torsional modes). Based on the positions of these bands and the blackbody radiation curve which is at a maximum at about 1000 cm^{-1}, it is safe to say the methanol ligand

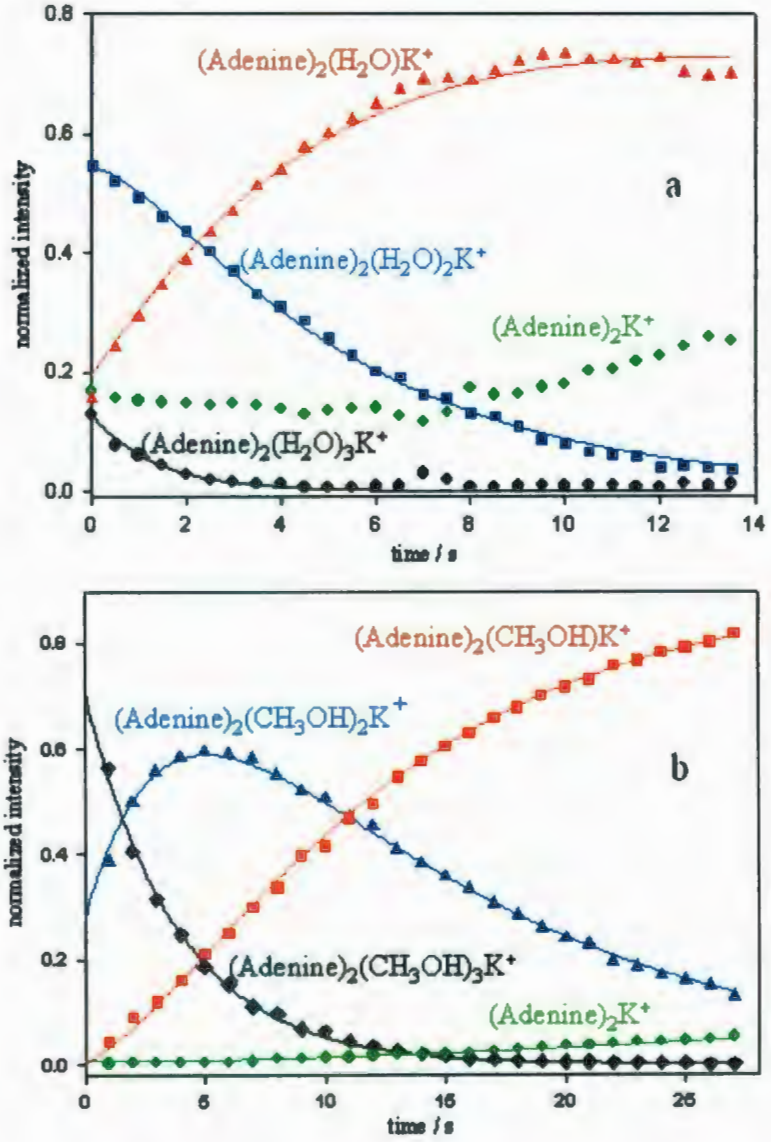

Figure 5.4: (a) BIRD plots for sequential loss of solvent from $(Ade)_2(X)_3K^+$, ((a) X=H_2O, (b) X=CH_3OH). Rate constants for sequential solvent loss are in Table 5.1.

	$(Ade)_2(H_2O)_nK^+$			$(Ade)_2(CH_3OH)_nK^+$
	k(no isol)	k(isol n=3)	k(isol n=2)	k(no isol)
	s^{-1}	s^{-1}	s^{-1}	s^{-1}
n=3→n=2	.737±.065	.733±.010	–	.261±.004
n=2→n=1	.212±.002	–	.300±.008	.084±.001
n=1→n=0	.012±.001	–	.019±.001	.003±.000

Table 5.1: Summary of BIRD rate constants for solvent loss for $(Ade)_2(H_2O)_nK^+$ and $(Ade)_2(CH_3OH)_nK^+$ clusters at 298 K.

is at least as strongly absorbing of blackbody radiation as a water ligand. Based on absorbing properties alone, the complexes solvated with methanol would probably be expected to have a larger BIRD rate constant than those solvated with water. That it has a smaller rate constant can only be attributed to a stronger binding energy for methanol to the central $(Ade)_2K^+$.

Also, in Table 5.1 are the BIRD rate constants obtained when $(Ade)_2(H_2O)_3K^+$ or $(Ade)_2(H_2O)_2K^+$ were isolated in the ICR cell using correlated harmonic excitation fields (CHEF).[30,31] It is not expected that the BIRD rate constants are affected by the isolation process. The BIRD rate constants for the $(Ade)_2(H_2O)_{2\rightarrow1}K^+$ reaction are found to be 0.212 and 0.300 s^{-1} when n=3 or n=2 are isolated, respectively. These values are different due to the errors in modelling the multiple rate constants. When n=3 is isolated, it is expected that the n=2 to n=1 rate constant is in greater error

due to its dependence upon the n=3 to n=2 rate constant, which typically has at most a 10 percent error associated with it from the modelling. In order to obtain reliable rate constants it is necessary to isolate the ion of interest. The 0.300 s^{-1} rate constant for dissociation of $(Adc)_2(H_2O)_2K^+$ is expected to be more reliable.

The mass spectrum obtained by electrospraying a 0.1 mM adenine and a few drops of 1.0 mM LiCl solution followed by 2 s of accumulation of the lithium ion bound adenine dimer in the accumulation hexapole with approximately 10^{-2} mbar background pressure of water is shown in Figure 5.5a. Both m/z 277 ($(Adc)_2Li^+$) and m/z 295 ($(Adc)_2Li^+(H_2O)$) are detected. Following absorption of the tunable OPO laser tuned to 3350 cm^{-1} and focussed into the ICR cell for 0.5 s, loss of water is detected (Figure 5.5b).

These results have shown that solvating cluster ions is possible in the accumulation hexapole of a hybrid Q-FTMS. In Figure 5.6, the IRMPD spectra of both $(Adc)_2Li^+$ and $(Adc)_2Li^+(H_2O)$ are displayed along with the lowest energy computed structures and B3LYP/6-31+G(d,p) predicted IR spectra. The details of the combination of the Bruker Apex Qe 7T FT-ICR MS with the Laser Vision infrared OPO/A in Orsay, France has been described previously. Briefly, the tunable OPO/A laser is scanned in frequency from about 2 to 4 μm (or in the reverse direction). When the laser radiation is resonant with a vibrational mode, the ion absorbs a few photons until it is able to dissociate. Absorption is detected by a decrease in the precursor ion intensity concurrently with an increase in fragment ion intensity. The IRMPD efficiency is

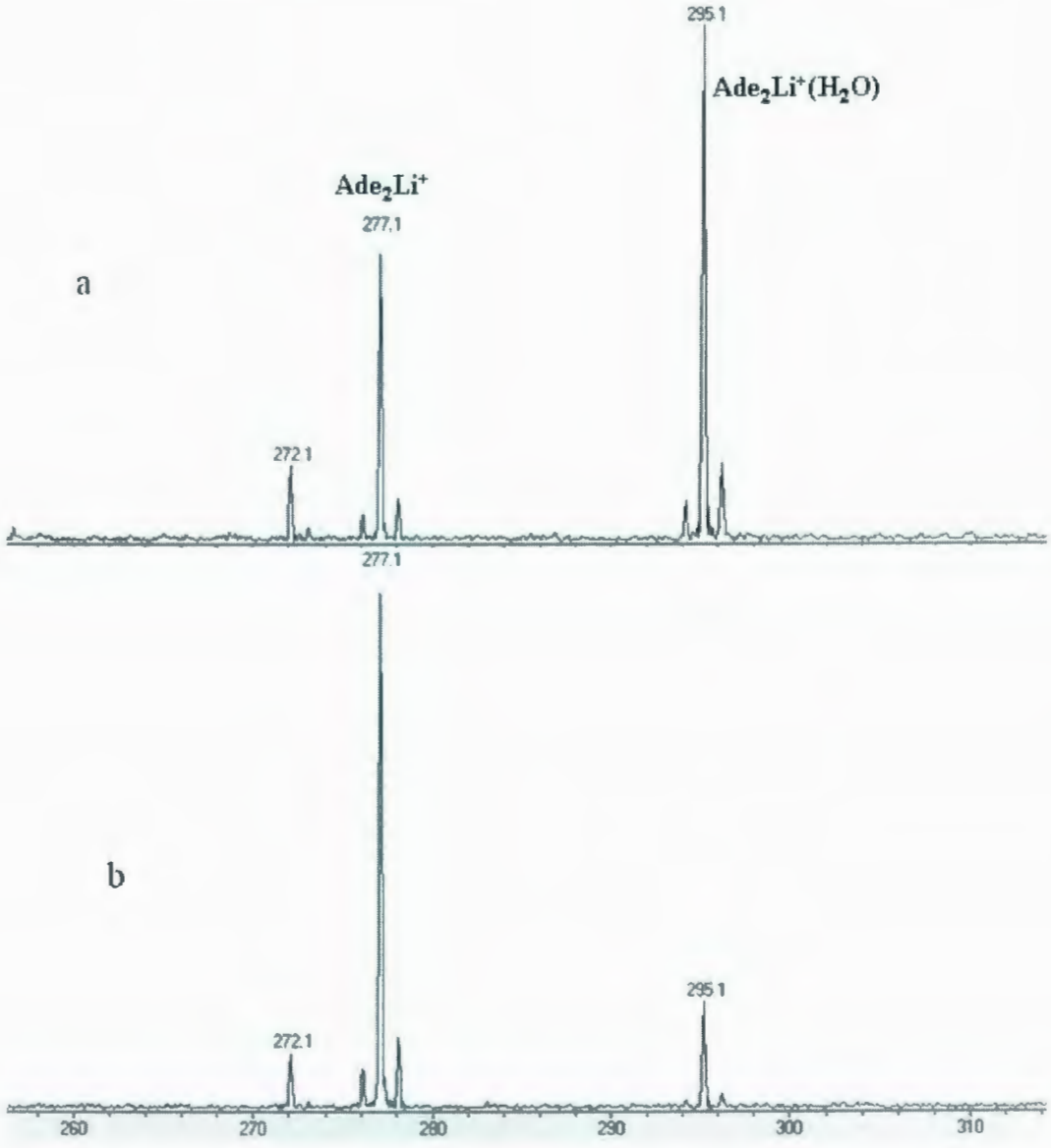

Figure 5.5: (a) ESI mass spectra showing the formation of $(Ade)_2Li^+(H_2O)$ by reacting $(Ade)_2Li^+$ with water vapor in the accumulation hexapole. (b) Mass spectrum showing the effect of absorption of the OPO laser tuned to 3350 cm^{-1} for 0.5 s.

defined as the negative of the natural logarithm of the ratio of fragment ion intensities to the sum of the fragment and precursor ion intensities. While these spectra will be fully discussed along with those of other species in a forthcoming article, a brief discussion of the spectra will be given here. The IRMPD spectrum of $(Ade)_2Li^+$ (bottom of Figure 5.6) is fairly simple with the two main features at 3435 and 3490 cm^{-1} assigned to the NH_2 symmetric stretching vibrations and the N-H stretch, respectively. There is also a weak feature centred at 3550 cm^{-1} corresponding to the NH_2 asymmetric stretching modes. These band positions are clearly well reproduced by the B3LYP/6-31+G(d,p) theoretical predictions (scaled by 0.958). The addition of one water molecule to this structure provides a richer IRMPD spectrum (top spectrum in Figure 5.6). The NH_2 symmetric stretching vibrations and the N-H stretch at 3446 and 3504 cm^{-1}, respectively, and the NH_2 asymmetric stretch at 3557 cm^{-1} are observed, in very similar positions as for the bare Li^+-bound dimer of adenine discussed above. The new feature at 3724 cm^{-1} is assigned to water asymmetric OH stretching. The absence of a symmetric OH stretch for water, typically observed around 3650 cm^{-1}, indicates that one of the O-H bonds is involved in hydrogen bonding. The two broad bands centred at 3180 and 3360 cm^{-1} are typical of strongly hydrogen bonded, and therefore red-shifted, O-H stretching vibrations. While there are many possible structures for the $(Ade)_2Li^+(H_2O)$ ion, two which are the lowest in free-energy and differ by less than 1 kJ mol^{-1} (B3LYP/6-31+G(d,p)) that have been discovered are shown along with their predicted infrared spectra. The exper-

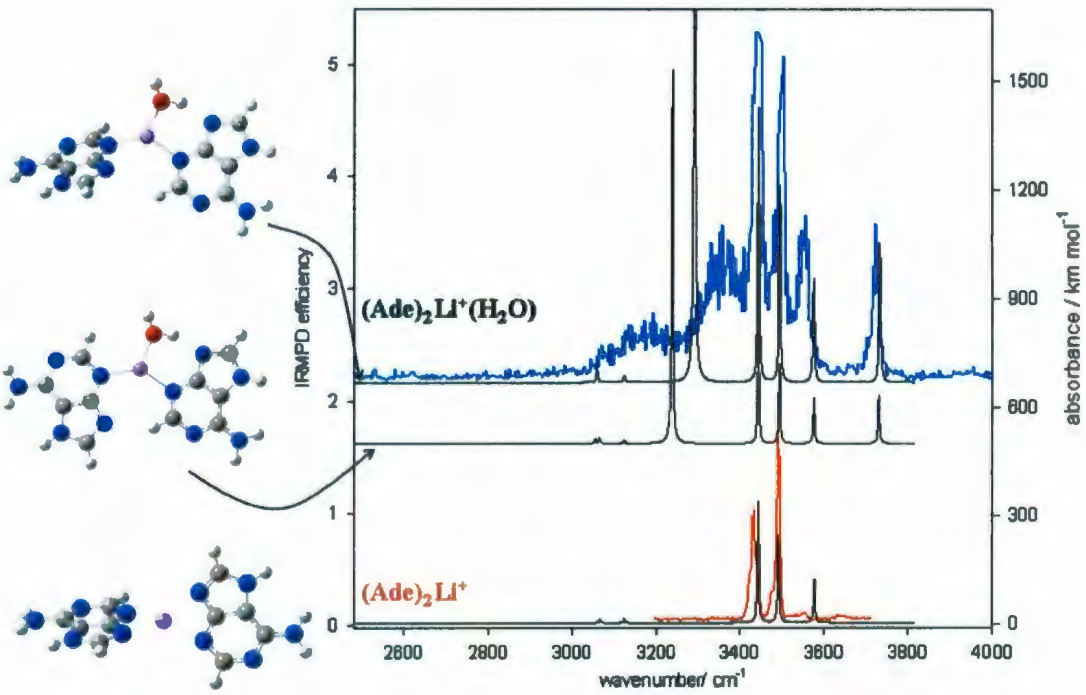

Figure 5.6: IRMPD spectra of $(Ade)_2Li^+$ and $(Ade)_2Li^+(H_2O)$ in 2500-4000 cm^{-1} region. Also shown are B3LYP/6-31+G(d,p) computed structures and infrared spectra of the lowest energy structure for $(Ade)_2Li^+$ and two lowest energy structures for $(Ade)_2Li^+(H_2O)$.

imental and computed infrared spectra agree very well above 3400 cm^{-1}. There is some disagreement between the experimental and predicted spectra for the two lower energy features, but this is to be expected for strongly anharmonic vibrations such as hydrogen bonded O-H stretches. The important point with regard to the spectra is that the experimental spectra are consistent with structures such as those shown in Figure 5.6. Furthermore, when water is added to the adenine Li^+-bound dimer in the

hexapole, it adds to the Li^+ ion, which is the most thermodynamically stable position.

5.4 Conclusions

Evidence is provided for the efficient solvation of cations in the hexapole accumulation cell of a hybrid Q-FTMS. While the number of parameters to modify are numerous, our experience shows that the most sensitive parameters are the collision energy in the hexapole, pressure of both argon and solvent in the hexapole, accumulation time, and the chemical nature of the species. By solvating ions in the hexapole, it is possible to obtain very interesting physical data such as BIRD kinetics as well as IRMPD spectra, both of which can be used to determine structural information for the species under investigation.

Bibliography

1. Desfrancois, C.; Carles, S.; Schermann, J. P. *Chem. Rev.* **2000**, *100*, 3943.
2. MacAleese, L.; Philippe, M. *Mass Spectrom. Rev.* **2007**, *26*, 583.
3. Fenn, J. B.; Mann, M.; Meng, C. K.; Wong, S. F.; Whitehouse, C. M. *Science* **1989**, *246* , 64.
4. Karas, M.; Hillenkamp, F. *Anal. Chem.* **1988**, *60*, 2299.
5. Tanaka, K.; Ido, Y.; Yoshida, Y.; Yoshida, T. *Proceedings of the second Japan-China Joint Symposium on Mass Spectrometry*; Osaka, Japan, September **1987**.
6. Tanaka, K.; Waki, H.; Ido, Y.; Akita, S.; Yoshida, T. *Rapid Commun. Mass Spectrom.* **1988**, *2*, 151.
7. Klassen, J. S.; Blades, A.T.; Kebarle, P. *J. Phys. Chem.* **1995**, *99*, 15509.
8. Lee, S. W.; Freivogel, P.; Schindler, T.; Beauchamp, J. L. *J. Am. Chem. Soc.* **1998**, *120*, 11758.
9. Rodriguez-Cruz, S. E.; Klassen, J. S.; Williams, E. R. *J. Am. Soc. Mass. Spectrom.* **1997**, *8*, 565.
10. Rodriguez-Cruz, S. E.; Klassen, J. S.; Williams, E. R. *J. Am. Soc. Mass. Spectrom.* **1999**, *10*, 958.
11. Rodriguez-Cruz, S. E.; Williams, E. R. *J. Am. Soc. Mass. Spectrom.* **2001**, *12*, 250.
12. Bush, M. F.; Saykally, R. J.; Williams, E. R. *Chem. Phys. Chem.* **2007**, *8*, 2245.
13. Carl, D. R.; Moision, R. M.; Armentrout, P. B. *Int. J. Mass Spectrom.* **2007**, *265*, 308.

14. Bogdanov, B.; McMahon, T.B. *Int. J. Mass Spectrom.* **2005**, *241*, 205.

15. Bogdanov, B.; Peschke, M.; Tonner, D. S; Szulejko, J. E.; McMahon, T. B. *Int. J. Mass Spectrom.* **1999**, *185-187*, 707.

16. Chowdhury, S.; Grimsrud, E. P.; Kebarle, P. *J. Phys. Chem.* **1987**, *91*, 2551.

17. Zhan, D.; Rosell, J.; Fenn, J. B. *J. Am. Soc. Mass Spectrom.* **1998**, *9*, 1241.

18. Hiraoka, K.; Mizuse, S.; Yamabe S. *J. Phys. Chem.* **1988**, *92*, 3943.

19. Yang, X.; Castleman, A. W. *J. Phys. Chem.* **1990**, *94*, 8500.

20. Cabarcos, O. M.; Weinheimer, C. J.; Martinez, T. J.; Lisy, J. M. *J. Chem. Phys.* **1999**, *110*, 9516.

21. Asmis, K. R.; Santambogio, G.; Zhou, J.; Garand, E.; Headrick, J.; Goebbert, D.; Johnson, M. A.; Neumark, D. M. *J. Chem. Phys.* **2007**, *126*, 191105-1.

22. Roscioli, J. R.; Hammer, N.I.; Johnson, M. A.; Diri, K.; Jordan, K. D..*J. Chem. Phys.* **2008**, *128*, 104314.

23. Dunbar, R. C. *Mass Spectrom. Rev.* **2004**, *23*, 127.

24. Brodbelt, J. S. *Mass Spectrom. Rev.* **1997**, *16*, 91.

25. Bakker, J. M.; Besson, T.; Lemaire, J.; Scuderi, D.; Maitre, P. *J. Phys. Chem. A* **2007**, *111*, 13415.

26. Sannes-Lowery, K. A.; Hofstadler, S. A. *J. Am. Soc. Mass Spectrom.* **2008**, *11*, 1.

27. Sannes-Lowery, K. A. Griffey, R. H.; Kruppa, G. H.; Speir, J. P.; Hofstadler, S. A. *Rapid Commun. Mass Spectrom.* **1998**, *12*, 1957.

28. Hunter, E. P.; Lias, S. G. *J. Phys. Chem. Ref. Data* **1998**, *27*, 413.

29. For example, Schnier, P. D.; Price, W. D.; Jockusch, R. A; Williams, E. R. *J. Am. Chem. Soc.* **1996**, *118*, 7178.

30. Heck, A. J. R.; Koning, L. J.; Pinkse, F. A.; Nibbering, N. M. M. *Rapid Commun. Mass Spectrom.* **1991**, *5*, 406.

31. de Koning, L. J.; Nibbering, N. M. M.; van Orden, S. L.; Laukien, F. H. *Int. J. Mass Spectrom. Ion Processes* **1997**, *165-166*, 209.

Chapter 6

Structures of Alkali Metal Ion-Adenine Complexes and Hydrated Complexes by IRMPD Spectroscopy and Electronic Structure Calculations

6.1 Introduction*

A balance of a variety of interactions between individual building blocks in DNA

*This Chapter has been accepted to be published as K. Rajabi, E.A.L. Gillis, and T.D. Fridgen, *J. Phys. Chem. A* **2010**, Manuscript ID jp-2009-098683.

and the chemical entities in its environment play a crucial role in the secondary structure of DNA. These interactions include hydrogen bonding between nucleic acid bases, between the nucleic acid bases and solvent,[1] as well as electrostatic interactions between nucleic acid bases and metal ions.[2,3] Non-specific dispersion forces between the DNA bases and metal ions, forming stacked structures, are also very important.

Many studies have been conducted on the protonation of nucleic acid bases using both experimental and theoretical techniques[4–9] due to the remarkable effects on conformational structure.[10] For example, base protonation has been implicated in the transformation of the B to Z structures of DNA.[11,12] Gas-phase studies of proton affinities have been conducted[8,9] as have ab initio calculations.[6] Knowledge of the protonation site is essential for the design of some drugs which regulate the activity of a selected gene by stabilizing the triple helix formed between the target base sequence and an oligonucleotide.[13] The triple helix structure inhibits transcription resulting in its therapeutic effect.[14] Aminopurine homodimers and their conjugate acid ions were investigated by DFT calculations[15] and the four lowest-energy proton bound dimers are found to be composed of one A9 and one A7 tautomer of adenine; two dimers protonated at N1 and two protonated at N3. Our recent IRMPD spectroscopy and computational study on the electrosprayed proton-bound adenine dimers[16] concluded that only two of these structures are observed. The two observed proton-bound dimers are greatly stabilized by solvent and are the only two which exist to any great extent in solution before/during being transmitted to the gas-phase by the electrospray source.

Metal ions also have a fundamental effect on biological processes[17] as the conformational behaviour and function of DNA are influenced by their presence.[2,3,18-22] Alkali metal ions affect synthesis, replication and cleavage of DNA and RNA, as well as their structural integrity. In addition, different metal ions can influence structural changes in DNA with the nature of the metal ion affecting genetic information transfer. For example, alkali metal ions stabilize the B form of DNA and prevent it from undergoing transitions.[23,24] The relative bond strength between the metal ion and the donor groups of the nucleic acid chain affects the nature of the interaction. Knowledge about the fundamental modes of binding can help determine the interaction of metal ions with more complex nucleic acid structures.[25] Direct functions such as redox capabilities, as well as indirect functions including conformational changes, are affected by metal ions.[26] Shack *et al.*[22] first discovered metal ion stabilization effects on the DNA double helix. A linear relationship between the melting temperature (T_m) of DNA and the logarithm of ionic strength was discovered.[23] Furthermore, a lower concentration of divalent ions (Mg^{2+} and Co^{2+}) was required to have the same effect on T_m compared to univalent ions. Metal ions stabilize the double helix by neutralizing the negative charges on the phosphate backbone and decrease its ability to uncoil. However, at higher concentrations, metal ions such as Cu^{2+} destabilize the DNA double helix because they also bind to the base and compete with the hydrogen-bonding of the DNA double helix, decreasing T_m. The ability of transition metal ions to bind with the phosphate backbone has the order Co(II) > Ni (II) > Mn(II) >

Zn(II) > Cd(II) > Cu(II) > Ag(II) > Hg(II). Generally, more significant changes occur on binding metal ions to the nucleobases than those upon binding to the phosphate backbone.[27] Thus, fundamental biological and pharmacological information can be deduced from the study of the interaction of metal ions with the nucleobases.[28]

The DNA double helix is unzipped and new strands are formed during DNA replication and protein synthesis. These processes involve the breaking of hydrogen bonds between the base pairs and solvent molecules play a major role in this step.[29] Also, since the helical form of DNA is not stable in the gas phase or in non-polar solvents, the presence of water is essential to its stabilization.[30,31] Water molecules can also influence mispairing[32,33] as well as DNA-protein and DNA-ligand[34] interactions by forming water bridges between the hydrophilic atoms of each molecule. Understanding the interactions between nucleic acids and solvent will aid in defining the solution-phase behaviour of DNA.[35] Step-wise solvation studies, therefore, are required. The effect of solvents such as acetic acid,[36] alcohols[37] and ammonia[38] on isolated nucleic acid bases have been studied.

The important aspect of gas-phase studies is that changes in ion structure can be investigated upon solvation without interference by the rest of the solvent. Water molecules have been shown to induce major changes in the structure and energetics of the ionized nucleic acid base complexes. For example, using IRMPD spectroscopy in the gas phase, hydration of Li^+-bound homodimers of uracil and thymine was found to promote hydrogen bonding between the nucleic acid bases.[39]

In this paper, we investigate the structures of the complexes formed between one or two adenine molecules and alkali metal ions such as Li^+, Na^+, K^+, and Cs^+ in the gas-phase along with singly-solvated ions by IRMPD spectroscopy and electronic structure calculations.

6.2 Methods

6.2.1 Experimental

As described previously[40] a coupling of the FT-ICR mass spectrometer and a 25 Hz Nd:YAG pumped Laservision IR OPO/A laser at CLIO was employed to record the IRMPD spectra. Solutions of 5 mM $C_5H_5N_5$ (adenine) were prepared in 18 MΩ Millipore water with 10 mM solutions of the alkali metal cation chlorides (LiCl, NaCl, KCl, and CsCl) added dropwise to 10 mL of the adenine solution. All chemicals were purchased from Sigma-Aldrich and used as received. Following electrospray of the solutions, ions were mass selected and transferred to the hexapole accumulation (collision) cell of the Apex Qe70 FT-ICR. Ions could be hydrated in the accumulation hexapole as described previously.[41] Briefly, this method of rehydrating the ions involved replacing the Ar gas in the collision cell with water vapour. Finally, the ions were transferred into the ICR cell and isolated by standard ion ejection/isolation techniques. The ions were irradiated for between 0.2 and 4.0 seconds using the benchtop

IR OPO/A system of Laservision. Normally 2-4 scans were accumulated. The laser was typically scanned at about 0.25 cm^{-1}/s, resulting in data points collected between 1 and 3 cm^{-1} apart. The IRMPD efficiency is defined as the negative logarithm of the parent ion signal divided by the sum of the parent and fragment ion signal.

6.2.2 Computational

Hybrid density functional methods (DFT) have proven to be successful in describing nucleic base dimers[42] and DNA triplex.[43] Also, the B3LYP hybrid functional has been found to be trustworthy for geometry optimizations.[44] Structures, vibrational frequencies, and thermal contributions to the enthalpy for the cluster ions were computed using the B3LYP hybrid density functional method and the 6-31+G(d,p) basis set using the Gaussian 03[45] suite of programs. All possible planar complexes of the cation with acceptor atoms were investigated with respect to A7 and A9 tautomers of adenine. For hydrated clusters, both direct attachment of water to the metal ions and to adenine were considered. The computed vibrational frequencies were scaled by a factor of 0.956. In addition, the absence of imaginary frequencies in the vibrational frequency analysis confirmed that the optimized structures are local minima on the potential energy surface. Since comparisons are made for clusters containing differing degrees of hydrogen bonding, single point energy calculations were done at MP2/6-311++G(2d, p) on the B3LYP/6-31+G(d, p) optimized structures to

obtain more trustworthy relative thermochemistries. These energies employing the MP2 electronic energies and the B3LYP thermal corrections are reported as MP2/6-311++G(2d,p)//B3LYP/6-31+G(d, p) Gibbs energies. All Gibbs energies reported here were calculated at 298 K which should be a good estimate of the temperature of the ions under study.

6.3 Results and Discussion

In all, four categories of adenine cluster ions in the gas-phase were examined. The first is a single adenine bound to metal ions, $(C_5H_5N_5)M^+$, where M=K, Cs and the second is the metal ion-bound dimer, $(C_5H_5N_5)_2M^+$, where M=Li, Na, and K. The sole dissociation routes for both $(C_5H_5N_5)M^+$ and $(C_5H_5N_5)_2M^+$ were found to be loss of neutral base. Mass spectra for some of these ions in the presence and absence of a resonant laser absorption are shown in Appendices 4-9 and represent loss of a neutral adenine. While it was possible to make $(C_5H_5N_5)Li^+$ and $(C_5H_5N_5)Na^+$, IRMPD products would be Li^+ and Na^+ which are below the mass detection limit of the FT-ICR. Due to the low signal intensity and instability of the ion signal with these systems, it was not possible to use ion depletion as the sole detection method to produce an IRMPD spectrum. The ion signal for $(C_5H_5N_5)_2Cs^+$ was too weak to conduct these experiments. The hydrated monomers ,$(C_5H_5N_5)M^+(H_2O)$ (M=Li, Na and K), and dimer, $(C_5H_5N_5)_2Li^+(H_2O)$, were also studied, however, attempts

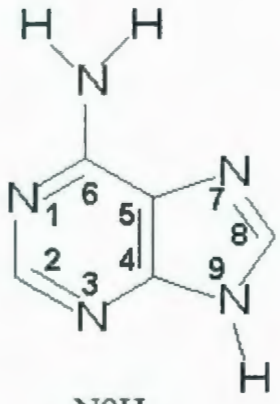

N9H

Scheme 6.1

to hydrate $(C_5H_5N_5)Cs^+$ were not successful. The results for the four categories are compared and discussed separately below. They are also compared with predicted IR spectra.

The standard numbering of atoms in adenine is used as shown in Scheme 6.1.

6.3.1 A Comparison of the Experimental IRMPD Spectra of $(C_5H_5N_5)_2Li^+$, $(C_5H_5N_5)Li^+(H_2O)$ and $(C_5H_5N_5)_2Li^+(H_2O)$

The IRMPD spectra of $(C_5H_5N_5)_2Li^+$, $(C_5H_5N_5)Li^+(H_2O)$ and $(C_5H_5N_5)_2Li^+(H_2O)$ are compared in Figure 6.1. For $(C_5H_5N_5)_2Li^+$, the band centred at 3434 cm^{-1} and the weak absorption at 3555 cm^{-1} can be assigned to the symmetric and asymmetric NH_2 stretching vibrations, respectively. The band centred at 3491 cm^{-1} is the N-H stretch of the dimer. These bands are similar in position to those observed in neutral

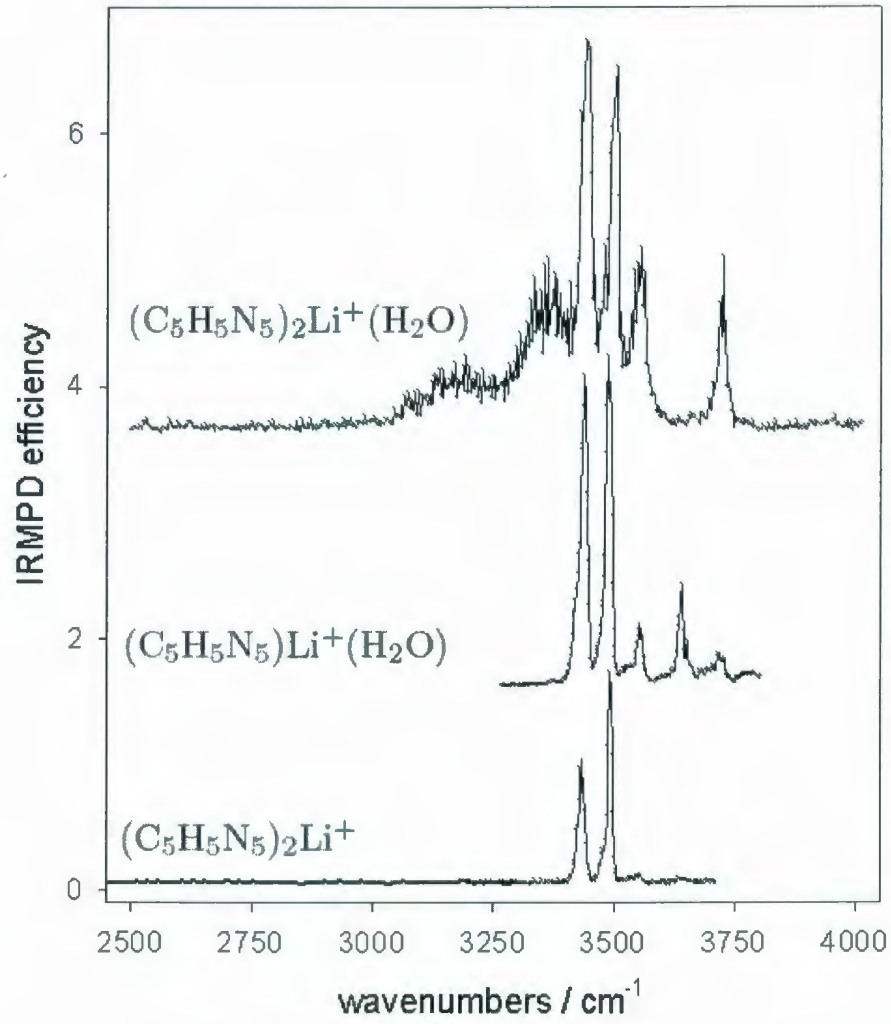

Figure 6.1: Comparison of the experimental IRMPD spectra of $(C_5H_5N_5)_2Li^+$, $(C_5H_5N_5)Li^+(H_2O)$ and $(C_5H_5N_5)_2Li^+(H_2O)$.

gas-phase adenine[46] (3457, 3552, and 3501 cm^{-1} for the symmetric stretch, asymmetric stretch and the N-H stretch respectively) and those for the protonated dimer of adenine (3435 and 3545 cm^{-1} for the symmetric and asymmetric stretches and 3481 and 3498 cm^{-1} for the N-H stretches).[19] The simplicity of the IRMPD spectrum for

$(C_5H_5N_5)_2Li^+$ may indicate a fairly symmetric structure.

The spectrum of $(C_5H_5N_5)Li^+(H_2O)$ has two more bands observed at 3642 and 3728 cm^{-1} and attributable to the symmetric and asymmetric stretching absorptions of the water moeity. The positions of the symmetric and asymmetric NH_2 stretching vibrations and the N-H stretch remain virtually unchanged (see Table 6.2).

The spectrum of $(C_5H_5N_5)_2Li^+(H_2O)$ is only a little more complex. There are still sharp bands centred at 3452 and 3557 cm^{-1} (the symmetric and asymmetric NH_2 stretching bands, respectively) and at 3504 cm^{-1}, the N-H stretch. There are at least two broad bands centred at 3190 and 3350 cm^{-1} which are similar in nature to hydrogen bonded N-H stretching vibrations observed in hydrated uracil and thymine Li^+ bound dimers.[39] The "asymmetric stretch" of the water moiety is also present at 3724 cm^{-1}, however, the symmetric stretch is absent indicating that water is not symmetric; one of the O-H bonds is involved in a hydrogen bond.

A comparison between the IRMPD spectra for each of these complexes with predicted spectra as well as spectra for species composed of different alkali metal cations and is discussed below. The observed IRMPD band positions for $(C_5H_5N_5)_2Li^+$, $(C_5H_5N_5)Li^+(H_2O)$, and $(C_5H_5N_5)_2Li^+(H_2O)$ are compared in Table 6.2 with the band positions for $(C_5H_5N_5)_2H^+$ and neutral adenine.

6.3.2 $(C_5H_5N_5)M^+$ and $(C_5H_5N_5)_2M^+$

Kabelac and Hobza[47] performed a thorough study on the interactions of all 14 amino and imino tautomers of adenine with Na^+, Mg^{+2} and Zn^{+2} cations using MP2(RI-MP2)/TZVPP method and basis set. Their results show that these ions prefer binding to adenine in a bidentate fashion rather than forming a single interaction. Furthermore, the lowest-energy structure for the Na^+-adenine complex was found to be the A7 adenine tautomer with a bidentate binding of Na^+ to N3 and N9, similar to structure 1 in Figure 6.2. The second lowest-energy Na^+-adenine structure ($\sim$10 kJ mol^{-1} higher in energy)[47] was determined to be the A9 imino tautomer where the hydrogen from N6 is on N1 and Na^+ is bound to N7 and N6, similar to structure 2 in Figure 6.2. The next lowest energy structures, some 30 kJ mol^{-1} higher in energy[47] were found to be similar to the A1 tautomer with Na^+ bound to N3 and N9 (similar to structure 3 in Figure 6.2) and the A9 tautomers with Na^+ bound to N6 and N1 or N6 and N7, (similar to structures 4 and 5, respectively, in Figure 6.2). Our own calculations agree very well with these, for example for $(C_5H_5N_5)Na^+$ structure 2 is found to be 12.5 kJ mol^{-1} higher in Gibbs energy than structure 1.

The IRMPD spectrum for $(C_5H_5N_5)Cs^+$ (Figure 6.2) reveals a band centred at 3536 cm^{-1} and a much weaker one at 3427 cm^{-1} which can be ascribed to the symmetric and antisymmetric stretch of the NH_2 group and one at 3488 cm^{-1} which is the N-H stretch. The spectrum of $(C_5H_5N_5)K^+$ (Figure 6.2) is quite similar. Both spectra are consistent with the lowest energy structure being the A7 tautomer with

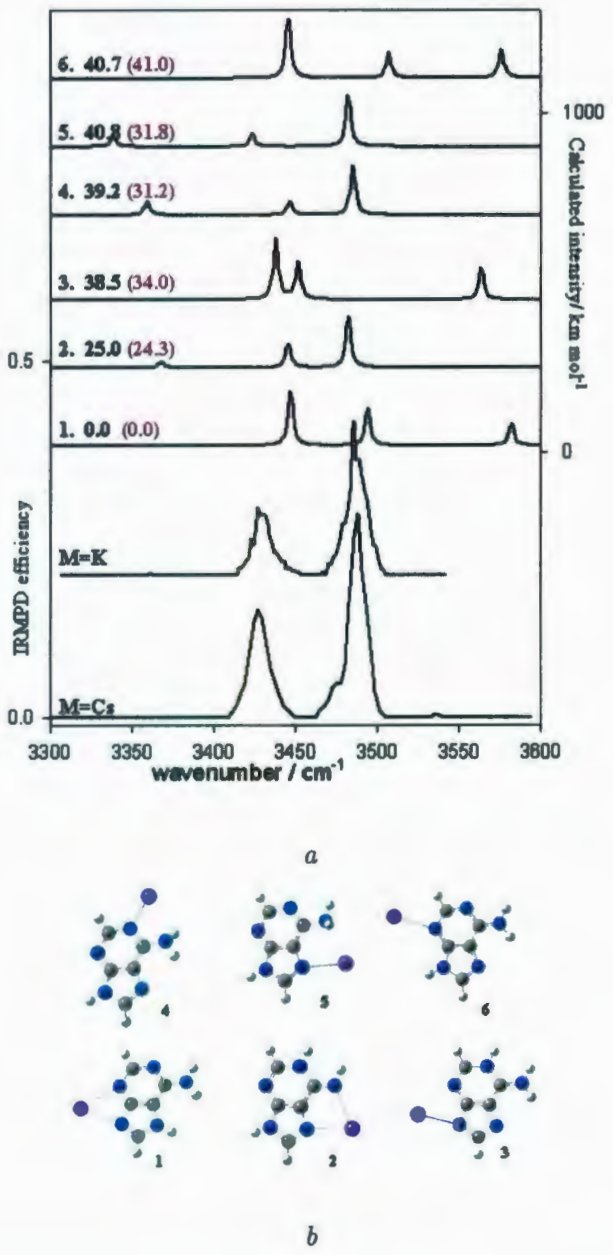

Figure 6.2: Experimental IRMPD spectra of $(C_5H_5N_5)M^+$ (where M=K,Cs) as well as B3LYP/6-31+G(d,p)-computed IR spectra (a) for the six-lowest energy structures (b). The 298 K B3LYP/6-31+G(d,p) as well as MP2/6-311++G(2d,p)//B3LYP/6-31+G(d,p) (in parentheses) relative Gibbs energies (kJ mol^{-1}) are provided for each K^+-bound structure.

the alkali metal ion bound to N3 and N9. Our calculations also predict this structure to be the most stable for $(C_5H_5N_5)Cs^+$ and the energetic orderings are in line with those predicted by Kabelac and Hobza for M=Na.[47]

That the A7 tautomer is lower in energy when binding alkali metal ions than the A9 tautomer is reasonable considering the difference in dipole moments; the dipole moment of the A7 tautomer is calculated to be 7.49 D compared to 2.44 for the A9 tautomer.[48] Rodgers and Armentrout[26] experimentally observed the A9 tautomer of adenine with Li^+, Na^+, and K^+ attached in to the N7 position (5 in Figure 6.2), different from the complex concluded to be observed in this work. We believe that the results are dependent on the method of producing the ion-molecule complexes. In their method, metal ions were added to the neutral nucleobase in the gas phase. Since the most stable tautomer of adenine is the A9 form and due to a (likely) significant barrier to tautomerization, their conclusions are not surprising. However, in the present study, ions are produced by electrospray and there is plenty of time in solution and bimolecular mechanisms for tautomerization so that the lowest energy structure is the one produced.

Russo, Toscano and Grand[49] performed calculations on $(C_5H_5N_5)Li^+$ and determined that the A9 imino tautomer where the hydrogen from N6 is on N1 and Li^+ is bound to N7 and N6 (similar to structure 2 in Figure 6.2) is lower in energy by about 2 kJ mol^{-1} compared to the A7 amino tautomer bound to Li^+ through N3 and N9 (structure 1 in Figure 6.2). Our MP2/6-311++G(2d,p)//B3LYP/6-31+G(d, p)

	Li	Na	K
$(C_5H_5N_5)M^+$			
Structure 1	5.2	0.0	0.0
Structure 2	0.0	12.8	24.3
$(C_5H_5N_5)M^+(H_2O)$			
Structure a	0.0	0.0	0.0
Structure b	3.6	17.5	31.2
PCM-$(C_5H_5N_5)M^+$			
Structure 1a	0.0	-	-
Structure 2	35.1	-	-

Table 6.1: Comparison of 298 K MP2/6-311++G(2d,p)//B3LYP/6-31+G(d,p) relative Gibbs energies (in kJ mol^{-1}) for the lowest-energy amino[a] and imino[b] structures of $(C_5H_5N_5)M^+$ and $(C_5H_5N_5)M^+(H_2O)$.

calculations place structure 2 lower in Gibbs energy by 5.2 kJ mol^{-1} over structure 1 for $(C_5H_5N_5)Li^+$. The relative energies for structures 1 and 2 for $(C_5H_5N_5)Li^+$ are summarized in Table 6.1. Clearly, the binding of the metal ion to the imine nitrogen overcomes the tautomerization energy of adenine for Li^+, but as the size (and therefore hardness) of the metal cation increases, the less it stabilizes the imine tautomer. While we do not have a spectrum of $(C_5H_5N_5)Li^+$, more will be said about this structure pertaining to $(C_5H_5N_5)Li^+(H_2O)$ below.

A comparison of the experimental IRMPD spectrum for Li^+ bound adenine dimer in the 3050-3700 cm^{-1} region along with the simulated IR spectra for seven isomers of $(C_5H_5N_5)_2Li^+$ is shown in Figure 6.3. The structures responsible for the calculated spectra are provided in Figure 6.4. The lowest-energy structure calculated for the Li^+ bound dimer is structure A composed of two A7 tautomers, each bound to Li^+ through N3 and N9, with the two adenine planes perpendicular to each other. While it is not possible to rule out structures B and C based solely on the spectra presented here, their computed Gibbs energies relative to A make them unlikely contributors to the spectrum. Structures D through G, however, can be ruled out based on comparison of their calculated spectra with the experimental IRMPD spectrum especially in the region below 3400 cm^{-1} where the hydrogen-bonded N-H stretching vibrations are predicted to occur but are absent in the experimental spectrum.

Calculations for the Na^+ and K^+ bound dimers were conducted with similar results for the lowest-energy structure, whose predicted spectrum is consistent with the experimental IRMPD spectra as can be seen in Figure 6.5 (for all calculated structures see Figure S2 and S3 in Appendices 2 and 3). It is worth noting, at this point, the disagreement between the experimental and predicted IR band positions for the symmetric and antisymmetric stretch. Clearly, from Figure 6.5, the observed IRMPD bands are significantly to the red, in energy, of the computed and scaled bands. This has been explained previously for the proton-bound dimer and neutral adenine.[16] The same disagreement in the positions of the NH_2 symmetric and antisymmetric

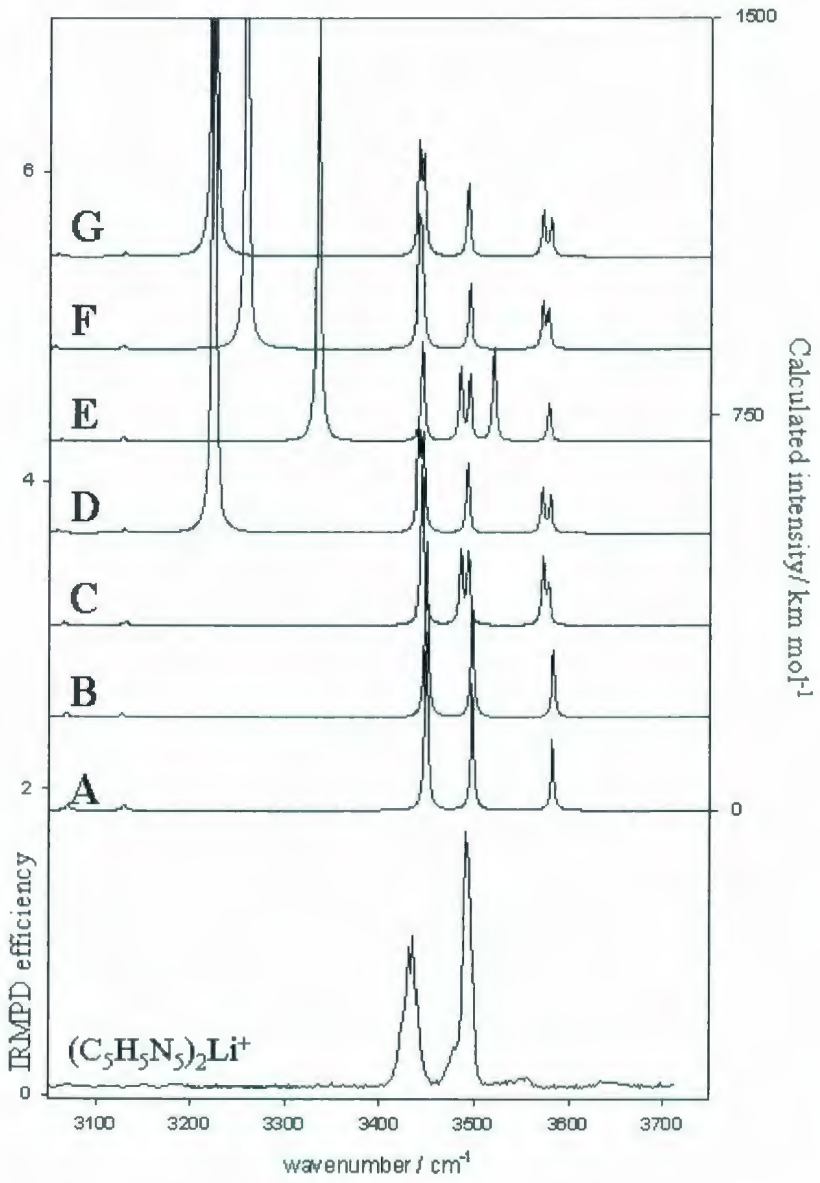

Figure 6.3: Comparison of the experimental IRMPD spectrum of $(C_5H_5N_5)_2Li^+$, with B3LYP/6-31+G(d,p) calculated spectra. Letter designations correspond to structures in Figure 6.4.

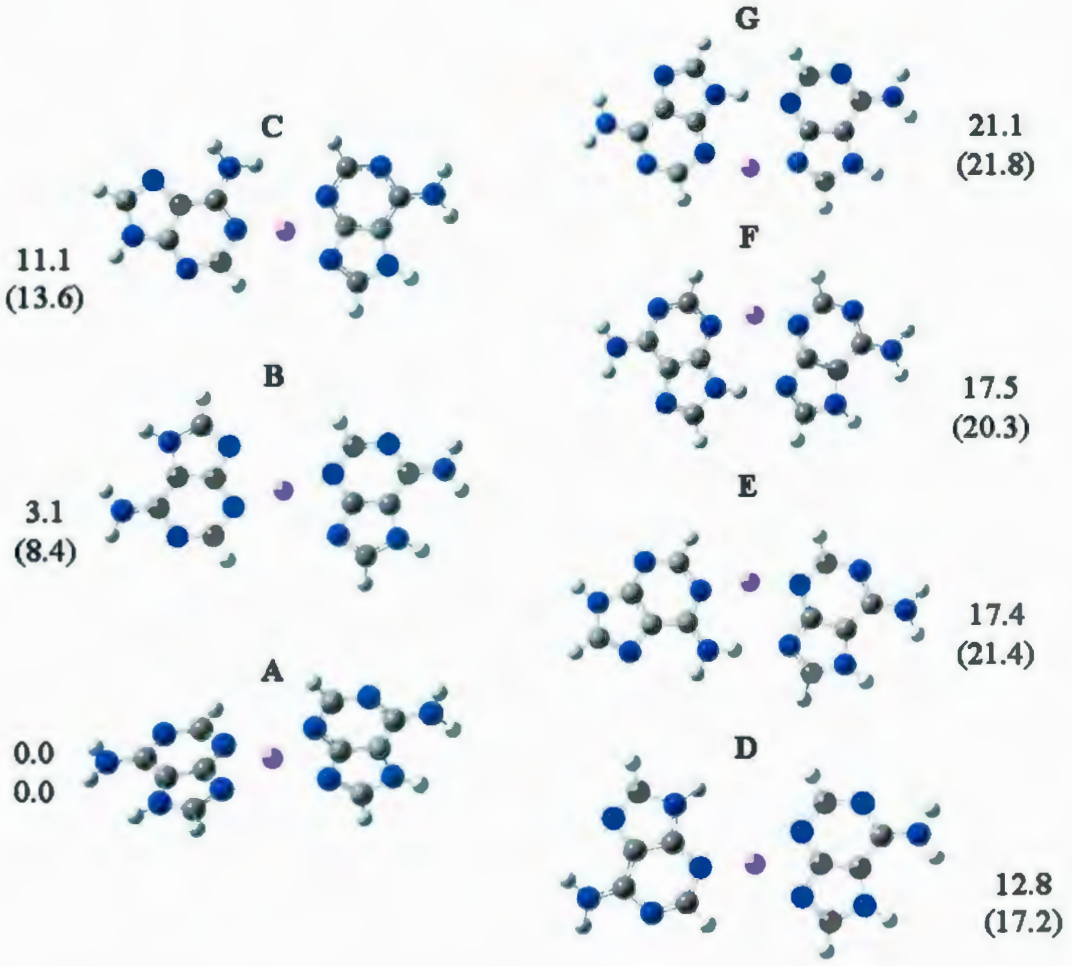

Figure 6.4: B3LYP/6-31+G(d,p) calculated structures for $(C_5H_5N_5)_2Li^+$. B3LYP/6-31+G(d,p) and MP2/6-311++G(2d,p)//B3LYP/6-31+G(d,p) (in parentheses) Gibbs energies (kJ mol^{-1}) are also provided.

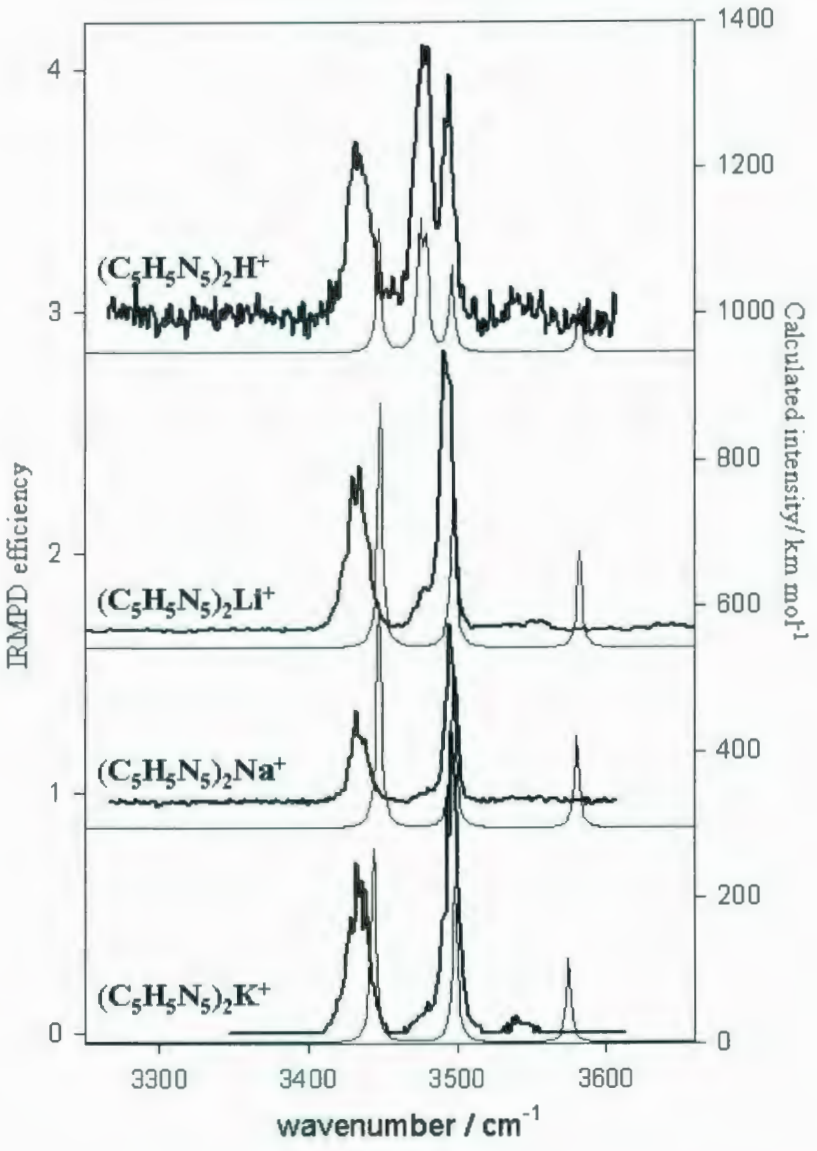

Figure 6.5: IRMPD spectra of $(C_5H_5N_5)_2M^+$, M=H, Li, Na, and K. Also shown are the B3LYP/6-31+G(d,p) predicted spectra for the lowest-energy structure for each dimer.

stretching was also observed with B3LYP/6-31G(d,p) calculations of adenine[50] and cytosine.[51] Recent anharmonic calculations on neutral adenine predict the asymmetric and symmetric stretching vibrations at 3539 and 3432 cm^{-1}, respectively, in excellent agreement with experimental values[52] while leaving the N-H stretch virtually unchanged.

6.3.3 $(C_5H_5N_5)M^+(H_2O)$

In Figure 6.6, the computed spectra for various isomers of $(C_5H_5N_5)Li^+(H_2O)$ are compared with the experimental IRMPD spectrum. The IRMPD spectrum is in very good agreement with the lowest-energy structure which is the A7 tautomer of adenine with Li^+ bound to N3 and N9 with a water molecule attached to the metal ion, Li^+ in this case. The lowest-energy structure composed of the A9 tautomer (e) is too high in energy to be present in any significant amount as are structures c and d. For structures c and e, the bands predicted to occur below 3400 cm^{-1} are not present in the experimental spectrum. Structure d, composed of the A1 tautomer cannot be completely ruled out spectroscopically but the bands predicted ~3400 cm^{-1} are less consistent with the experimental spectra. Structure b, which is composed of the imine form of adenine with Li^+ bound at the imine nitrogen (N6) and N7, is predicted to be 3.6 kJ mol^{-1} higher in Gibbs energy than a, so one might expect it to be present in a small amount (~20 percent).

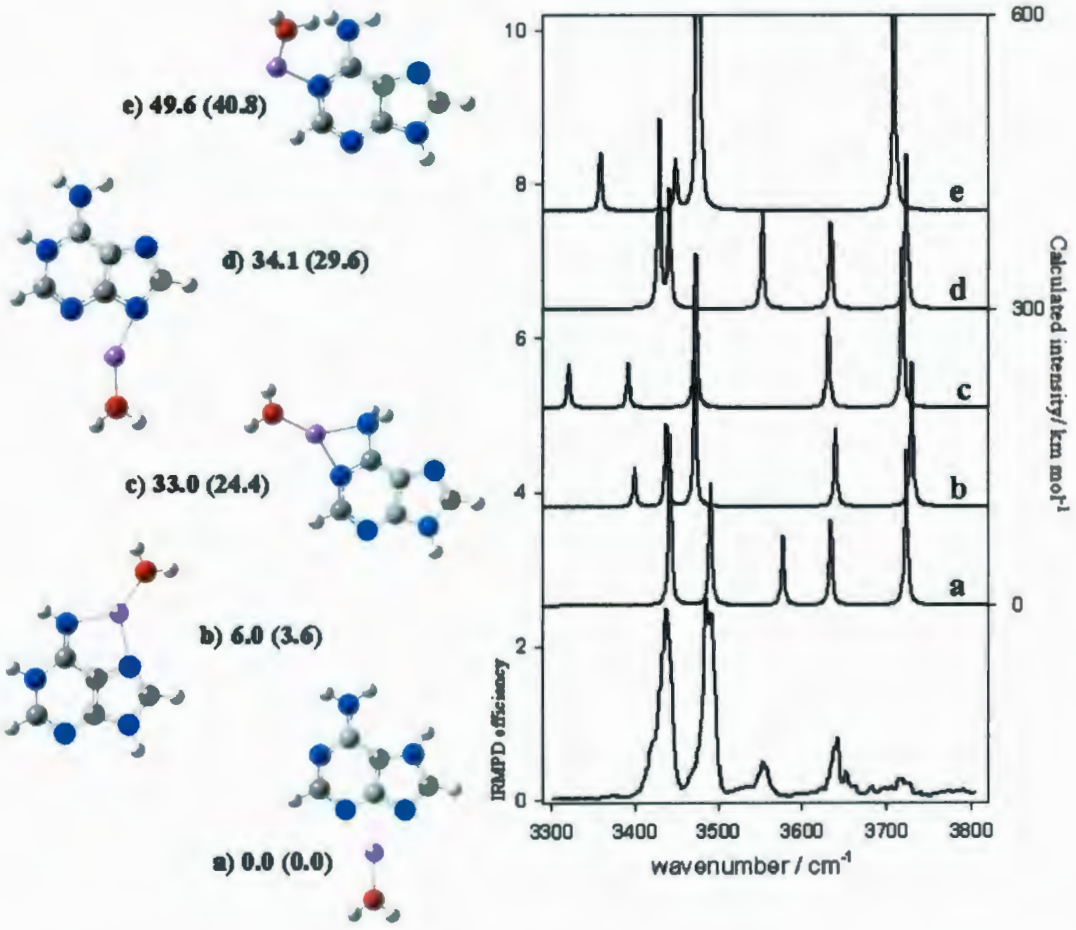

Figure 6.6: The experimental IRMPD spectrum for $(C_5H_5N_5)Li^+(H_2O)$ in the 3300-3800 cm^{-1} range along with the five lowest-energy structures and their computed IR spectra. The 298 K B3LYP/6-31+G(d,p) as well as MP2/6-311++G(2d,p)//B3LYP/6-31+G(d,p) (in parentheses) relative Gibbs energies (kJ mol^{-1}) are provided for each structure.

It is interesting to note that the MP2/6-311++G(2d,p)//B3-LYP/6-31+G(d,p) calculations predict the imine form of $(C_5H_5N_5)Li^+$ (structure 2 in Fig. 6.2) to be lower in Gibbs energy by 5.2 kJ mol^{-1}. If the imine form of $(C_5H_5N_5)Li^+$ is electrosprayed then the re-solvation process should produce ion b for $(C_5H_5N_5)Li^+(H_2O)$ and the observed spectrum should better resemble that predicted for ion b. However, the band predicted to occur just below 3400 cm^{-1} is not observed in the experimental IRMPD spectrum and therefore there is no evidence for ion b. We conclude, based on the spectral data, that structure 1 is formed in the electrospray source and then re-solvated so that it is structure a that is responsible for the experimental IRMPD spectrum. In an attempt to model the ions in solution, structures 1 and 2 for the lithium cation (Fig. 6.2) were re-optimized using the polarizable continuum model (PCM) in Gaussian with a dielectric equal to that of bulk water. The structure changed slightly in that the lithium cation was no longer bidentate in solution, see structure 1a in Scheme 6.2. Single point calculations were also done in the PCM using MP2/6-311++G(2d,p). In Table 6.1, the results of the energy calculations are summarized. The imine form of $(C_5H_5N_5)Li^+$ in bulk water is substantially higher in Gibbs energy (by 35 kJ mol^{-1}) than structure 1 and does not likely exist in solution. These calcuations are in agreement with the conclusions drawn from the IRMPD experiments, that structure 1 is the structure that is electrosprayed from solution and is re-solvated in the gas-phase to give structure a which is observed by IRMPD spectroscopy (see Scheme 6.2).

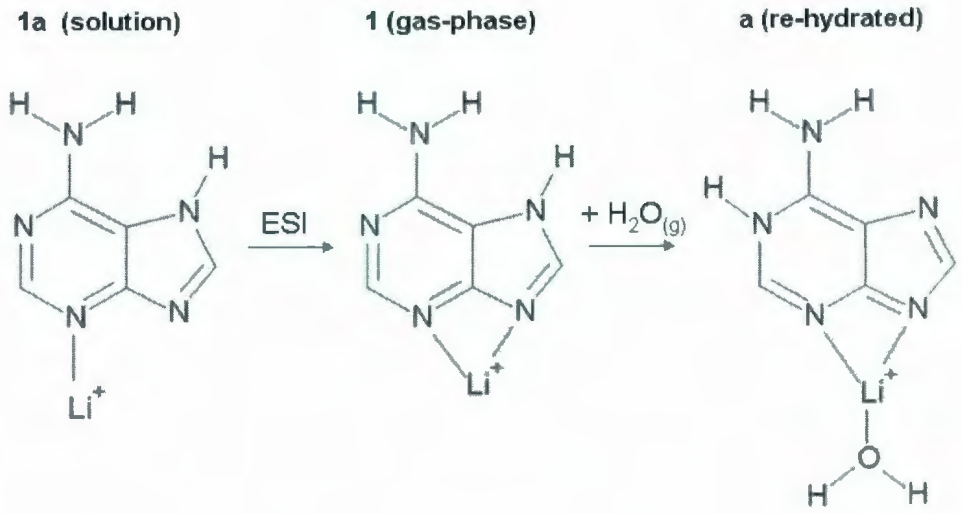

Scheme 6.2

The low intensity of the experimental asymmetric H_2O stretch compared to that predicted has been described previously.[39,53] There is poor coupling between the asymmetric stretch and other modes within the molecule so that intramolecular vibrational energy redistribution is slow making subsequent photon absorption during a laser pulse inefficient. This results in lower intensities than expected for the asymmetric H_2O stretch.

In Figure 6.7, the IRMPD spectra of $(C_5H_5N_5)Li^+(H_2O)$, $(C_5H_5N_5)Na^+(H_2O)$, and $(C_5H_5N_5)K^+(H_2O)$ are compared as are the computed spectra for each of their lowest energy structures. It can be concluded from the similarity of the IRMPD spectra that the three hydrated alkali metal-cation/adenine complexes are similar in structure. Due to the agreement of these experimental spectra with the predicted spectra

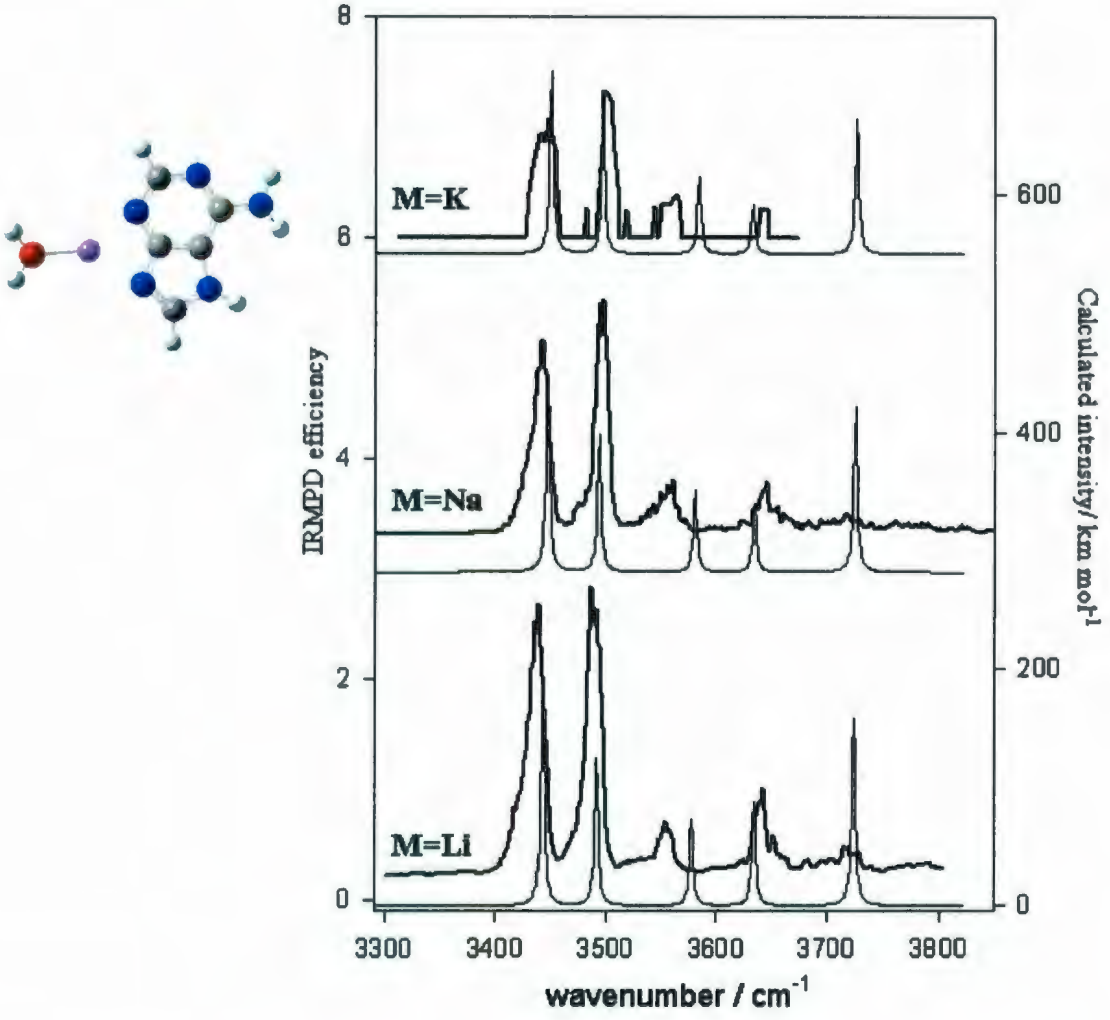

Figure 6.7: Comparison of the experimental IRMPD spectra and the predicted IR spectra for the B3LYP/6-31+G(d,p) lowest-energy structures IR spectra for $(C_5H_5N_5)M^+(H_2O)$ where M=Li, Na, and K.

for the lowest energy structures together with the computed thermochemistries, it is concluded that $(C_5H_5N_5)M^+(H_2O)$ ions are the M^+-hydrated A7 adenine tautomers with M^+ bound to adenine at the N3 and N9 positions.

6.3.4 $(C_5H_5N_5)_2Li^+(H_2O)$

In Figure 6.8, the experimental IRMPD spectrum for the hydrated Li^+-bound dimer of adenine is compared to computed spectra for several isomeric structures. Similar to the non-hydrated Li^+-bound dimer, two A7 tautomers form the lowest energy structures (Figure 6.9), and as expected, water tends to attach to the lithium ion rather than to adenine as was the case for Li^+-bound uracil and thymine dimers.[39] As mentioned previously, an interesting feature (or lack thereof) of the IRMPD spectrum is that the symmetric stretch of water is not present, indicating that water is participating in hydrogen bonding as a hydrogen bond donor. Therefore, structures where water is solely bound to Li^+ are ruled out as there would be a symmetric stretch at about 3642 cm^{-1} similar to $(C_5H_5N_5)Li^+(H_2O)$. None of the structures with non-hydrogen bonded H_2O were lower in energy. The lowest-energy structure with water bound to Li^+ where water is not hydrogen bonded is calculated to be 15 kJ mol^{-1} higher in Gibbs energy and is composed of an A9 and A7 adenine both bound to Li^+ through N3. The lowest-energy structure in which H_2O was not bound to Li^+ was predicted to be some 32 kJ mol^{-1} higher in Gibbs energy. As such, the only structures that are presented are those for which water is bound to Li^+ and is participating, as a donor, in hydrogen bonding with one (or two) of the adenine moieties. Similarly, based on the results of the $(C_5H_5N_5)M^+$ and $(C_5H_5N_5)_2M^+$ calculations

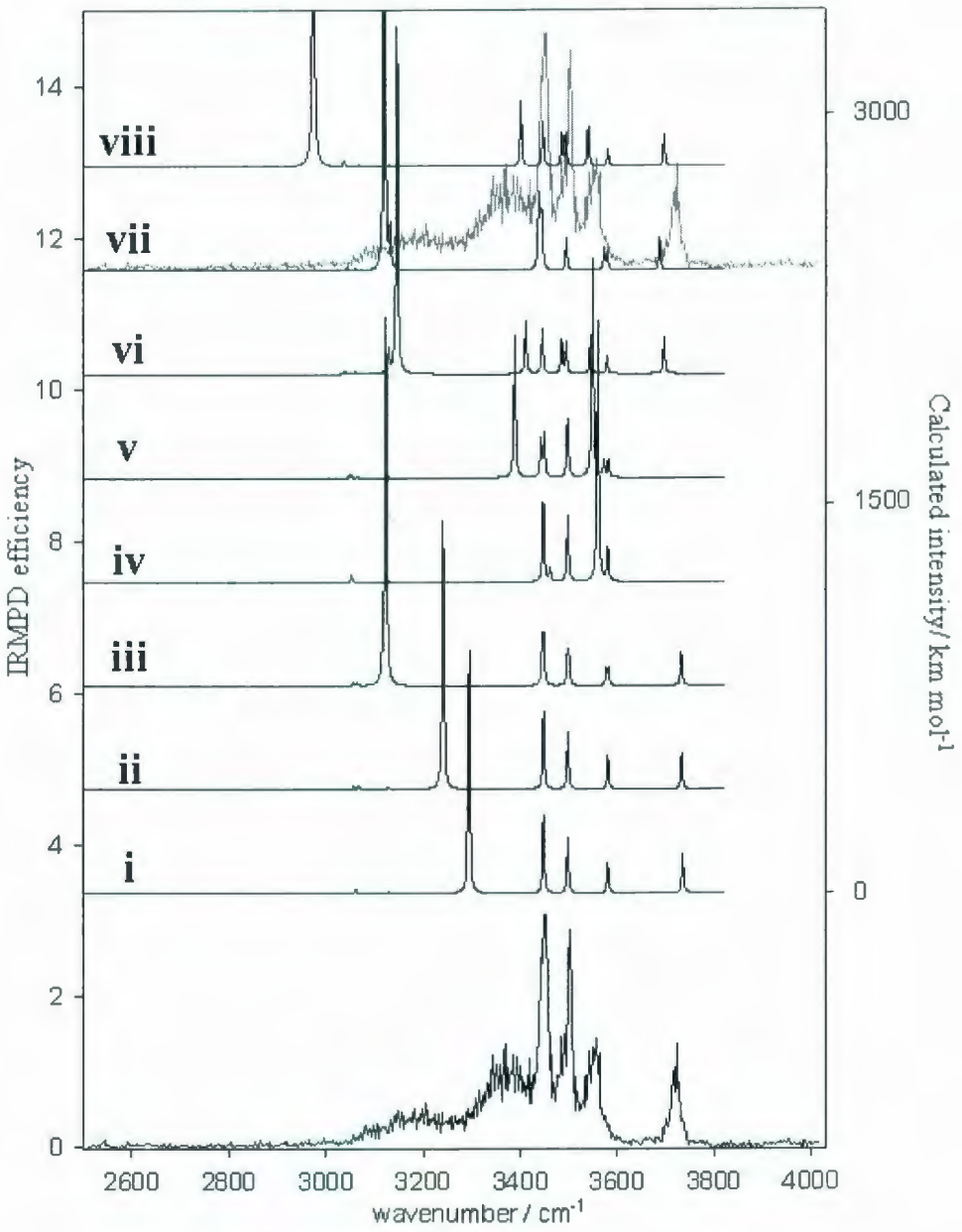

Figure 6.8: The IRMPD spectrum for $(C_5H_5N_5)_2Li^+(H_2O)$ in the 2500-4000 cm^{-1} region along with the predicted IR spectra for the eight lowest-energy structures composed of A7A7 and A7A9 adenine tautomers (for structures and energies see Figure 6.9)

presented here and in Kabelac and Hobza,[47] as well as the experimental results for $(C_5H_5N_5)M^+$, $(C_5H_5N_5)_2M^+$ and $(C_5H_5N_5)M^+(H_2O)$, we only considered structures composed of two A7 adenine tautomers or one A7 and one A9 tautomer. As seen in Figure 6.8, the lowest-energy structure composed of A7 and A9 tautomers is some 12 kJ mol^{-1} higher in Gibbs energy.

The lowest energy structures found are both labelled as i and are very similar except for a rotation around the Li^+-N bond. They are isoenergetic and have identical predicted infrared spectra. Structure ii is also very similar in energy and structure except that the two adenine molecules are coplanar, unlike structures i. These three structures have Li^+ bound to N3 of both adenine molecules. Structure iii is slightly different in that one of the adenine molecules is bound to Li^+ through N9. This change in Li^+ binding is only slightly destabilizing. The computed spectra for these four lowest-energy structures are perfectly consistent with the experimental IRMPD spectrum. In fact, only one of these structures could not account for the observation of the two broad bands at 3190 and 3350 cm^{-1}, which are assigned to hydrogen-bonded O-H stretching modes. It is very likely that all four contribute to the observed IRMPD spectrum.

In next two lowest energy structures (iv and v in Figure 6.9), water is bound through two hydrogen bonds. As such, the two hydrogen bonds are slightly weaker, as evidenced by the significantly smaller predicted red-shifts of the O-H stretching vibrations. Also due to both O-H bonds being involved in hydrogen bonding, both

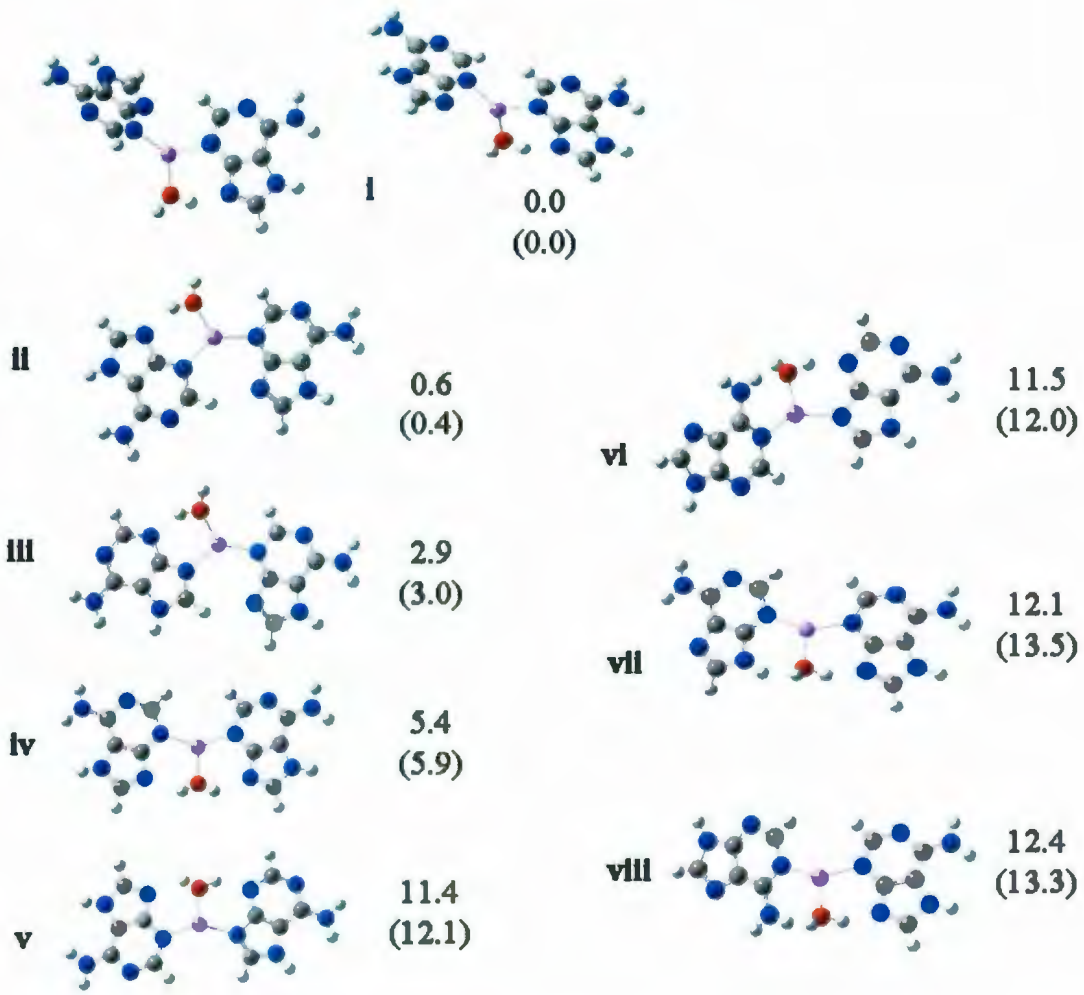

Figure 6.9: The lowest-energy calculated structures for $(C_5H_5N_5)_2Li^+(H_2O)$. The 298 K B3LYP/6-31+G(d,p) and MP2/6-311++G(2d,p)//B3LYP/6-31+G(d,p) (in parentheses) relative Gibbs energies (kJ mol^{-1}) are provided for each structure.

stretching modes are red-shifted. These species are at most minor contributors based on their calculated Gibbs energies, but cannot be "completely" ruled out as minor contributors by spectroscopic means.

The next three lowest energy structures are composed of one A7 and one A9 tautomer. While their computed relative Gibbs energies rule them out as significant contributors to the mixture, this may also be done on spectroscopic grounds. The non-hydrogen bonded O-H stretch for these three isomers does not agree nearly as well, being slightly to the red of the observed band and those predicted for structures i, ii, and iii. As well, for structures vi and viii, there are two bands predicted around 3550 cm^{-1}, but only one band can be identified experimentally.

6.4 Conclusions

We have investigated complexes between adenine and the alkali metal ions Li^+, Na^+, K^+, and Cs^+ by IRMPD spectroscopy and electronic structure calculations. Some singly-solvated complexes were also investigated. By comparing the experimental and the simulated spectra, it is possible to rule out various structures and to assign structures to the species probed in these experiments. Single point calculations on the B3LYP/6-31+G(d,p) geometries have been performed at MP2/6-311++G(2d, p) to obtain good estimates of the relative thermochemistries for the different structures and, in all cases, the computed IR spectrum for the lowest energy structure is

mode	$(C_5H_5N_5)_2Li^+$	$(C_5H_5N_5)Li^+$-(H_2O)	$(C_5H_5N_5)_2Li^+$-(H_2O)	$(C_5H_5N_5)_2H^+$[a]	Neutral $(C_5H_5N_5)$[b]
H-bonded OH str			3190/3350 broad		
NH_2 sym str	3434	3438	3452	3435	3457
N-H str	3491	3486	3504	3481/3498	3501
NH_2 asym str	3555	3554	3557	3545	3552
H_2O sym str		3642			
H_2O asym str		3728	3724		

Table 6.2: Bands (in cm^{-1}) observed for $(C_5H_5N_5)_2Li^+$, $(C_5H_5N_5)Li^+(H_2O)$ and $(C_5H_5N_5)_2Li^+(H_2O)$ compared with neutral adenine and the adenine proton-bound dimer.

[a]from reference 19

[b]from reference 52

consistent with the experimental IRMPD spectrum.

Based on the IRMPD spectra and the energy calculations, it is concluded that all adenine-M^+ and adenine-M^+-H_2O ions are composed of the A7 tautomer of adenine which is attached to the cations in a bidentate fashion through N3 and N9 and for the hydrated ion water binds directly to the metal ion through oxygen. The calculations predict the imine tautomer of Li^+-adenine to be the lowest energy structure in the gas phase. However, when singly hydrated, the imino form of adenine-Li^+ is computed to be higher in energy than the A7 tautomer with Li^+ bound to N3 and N9. Furthermore, solution-phase calculations predict the imine form to be higher in energy than the A7 tautomer. Since our experiments show no evidence for the imine tautomer suggests that we are probing the solution phase structure of this ion in the gas-phase.

For the hydrated lithium cation-bound adenine dimer, the water molecule is concluded to be bound to the metal ion as well as hydrogen bonded to a free basic site of one of the adenine monomers. It is also concluded that several conformers are responsible for the observed IRMPD spectrum.

6.5 Supporting Information

This information is available free of charge via the Internet at http://pubs.acs.org as well as Appendices 2 and 3.

Bibliography

1. Kabelac, M.; Hobza, P. *Phys. Chem. Chem. Phys.* **2007**, *9*, 903.
2. McFail-Isom, L.; Sines, C. C.; Williams, L. D. *Curr. Opin. Struct. Bio.* **1999**, *9*, 298.
3. Shui, X.; Sines, C. C.; McFail-Isom, L.; VanDerveer, D.; Williams, L. D. *Biochemistry.* **1998**, *37*, 16877.
4. Bonaccorsi, B.; Pullman, A.; Scrocco, E.; Tomasi, J. *Theor. Chim. Acta* **1972**, *24*, 51.
5. Russo, N.; Toscana, M.; Grand, A.; Jolibois, F. *J. Comput. Chem.* **1998**, *19*, 989.
6. Podolyan, Y.; Gorb, L.; Leszczynski, J. *J. Phys. Chem. A* **2000**, *104*, 7346.
7. Wolken, J. K.; Turecek, F. *J. Am. Soc. Mass Spectrom.* **2000**, *11*, 1065.
8. Greco, F.; Liguori, A.; Sindona, G.; Uccelle, N. *J. Am. Chem. Soc.* **1990**, *112*, 9092.
9. Meot-Ner, M. *J. Am. Chem. Soc.* **1979**, *101*, 2396.
10. Kumar, G. S.; Das, S.; Bhadra, K.; Maiti, M. *Bioorganic & Medicinal Chemistry 11,* **2003**, 4861.
11. Chen, F. M. *Biochemistry* **1984**, *23*, 6159.
12. Volker, J.; Klump, H. H. *Biochemistry* **1994**, *33*, 13502.
13. Wilson, W. D.; Tanious, F. A.; Mizan, S.; Yao, S.; Kiselyov, A. S.; Zon, G; Strekowski, L. *Biochemistry* **1993**, *32*, 10614.
14. Cooney, M.; Czernusszewicz, G.; Postel, E. H.; Flint, S. J.; Hogan, M. E. *Science* **1988**, *241*, 456.
15. Hud, N. V.; Morton, T. H. *J. Phys. Chem. A* **2007**, *111*, 3369.
16. Rajabi, K.; Theel, K.; Gillis, E. AL.; Beran, G.; Fridgen, T. D. *J. Phys. Chem. A*

2009, *113*, 8099..

17. Eichhorn, G. L. In *Inorganic Biochemistry*, Eichhorn, G. L., Ed.; Elsevier: New York, **1973**; p 1191.
18. Eichhorn, G. L. *Adv. Inorg. Biochem.* **1981**, *3*,1.
19. Shack. J.; Jenkins, R. J.; Thompsett, J. M. *J. Biol. Chem.* **1953**, *203*, 373.
20. Dove, W. F.; Davidson, N. *J. Mol. Biol.* **1962**, *5*, 467.
21. Eichhorn, G. L. *Nature* **1962**, *194*, 474.
22. Eichhorn, G. L.; Shin, Y. A. *J. Am. Chem. Soc.* **1968**, *90*, 7323.
23. Eichhorn, G. L. In *Inorganic Biochemistry*, Eichhorn, G. L., Ed.; Elsevier: New York, **1973**; p 1210.
24. Eichhorn, G. L.; *Coord. Chem. Rev.* **1993**, *128*, 167.
25. Cerda, B. A.; Wesdemiotis, C. *J. Am. Chem. Soc.* **1996**, *118*, 11884.
26. Rodgers, M. T.; Armentrout, P. B. *J. Am. Chem. Soc.* **2000**, *122*, 8548.
27. Shin, Y. A.; Eichhorn, G. L. *Biopolymers* **1977**, *16*, 225.
28. Yang, Z.; Rodgers, M. T. *J. Am. Chem. Soc.* **2004**, *126*, 16217.
29. Casaes, R. N.; Paul, J. B.; McLaughlin, R. P.; Saykally, R. J.; Mourik, T. V. *J. Phys. Chem. A* **2004**, *108*, 10989.
30. Rueda, M.; Kalko, S. G.; Luque, F. J.; Orozco, M. *J. Am. Chem. Soc.* **2003**, *125*, 8007.
31. Rueda, M.; Kalko, S. G.; Luque, F. J.; Orozco, M. *J. Am. Chem. Soc.* **2006**, *128*, 3608.

32. Kennard, O. *J. Biomol. Struct. Dyn.* **1985**, *3*, 205.

33. Cruse, W. B. T.; Saludjian, P.; Biala, E.; Strazewski, P.; Prange, T.; Kennard, O. *Proc. Natl. Acad. Sci. U. S. A.* **1994**, *91*, 4160.

34. Morávek, Z.; Neidle, S.; Schneider, B. *Nucleic Acids Res.* **2002**, *30*, 1182.

35. Gueron, M.; Kochoyan, M.; Leroy, J. L. *Nature* **1987**, *328*, 89-92.

36. Janke, E. M. B.; Limbach, H. H.; Weisz, K. *J. Am. Chem. Soc.* **2004**, *126*, 2135.

37. Haranezyk, M.; Rak, J.; Gutowski, M.; Radisic, D.; Stokes, S. T.; Bowen, K. H. *J. Phys. Chem. B* **2005**, *109*, 13383.

38. Wu, R.; McMahon, T. B. *J. Am. Chem. Soc.* **2007**, *129*, 569.

39. Gillis, E. A. L.; Rajabi, K.; Fridgen, T. D. *J. Phys. Chem. A* **2009**, *113*, 824.

40. Mac Aleese, L.; Simon, A.; McMahon, T. B.; Ortega, J. M.; Scuderi, D.; Lemaire, J.; Maître, P. *Int. J. Mass. Spectrom.* **2006**, *249-250*, 14.

41. Rajabi, K.; Easterling, M. L.; Fridgen, T. D. *J. Am. Chem. Mass Spectrom.* **2009**, *20*, 411.

42. Nir, E.; Janzen, C.; Imhof, P.; Kleinermanns, K.; de Vries, M. S. *Phys. Chem. Chem. Phys.* **2002**, *4*, 740.

43. Peters, M.; Rozas, I.; Alkorta, I.; Elguero, J. *J. Phys. Chem. B* **2003**, *107*, 323.

44. Liu, B. P.; Ding, Y. J.; Yuan, X. A. *J. Mol. Struct. THEOCHEM* **2008**, *848*, 47.

45. Frisch, M. J.; Trucks, G. W.; Schlegel, H. B.; Scuseria, G. E.; Robb, M. A.; Cheeseman, J. R.; Montgomery, J. A., Jr.; Vreven, T.; Kudin, K. N.; Burant, J. C.; Millam, J. M.; Iyengar, S. S.; Tomasi, J.; Barone, V.; Mennucci, B.; Cossi, M.;

Scalmani, G.; Rega, N.; Petersson, G. A.; Nakatsuji, H.; Hada, M.; Ehara, M.; Toyota, K.; Fukuda, R.; Hasegawa, J.; Ishida, M.; Nakajima, T.; Honda, Y.; Kitao, O.; Nakai, H.; Klene, M.; Li, X.; Knox, J. E.; Hratchian, H. P.; Cross, J. B.; Adamo, C.; Jaramillo, J.; Gomperts, R.; Stratmann, R. E.; Yazyev, O.; Austin, A. J.; Cammi, R.; Pomelli, C.; Ochterski, J. W.; Ayala, P. Y.; Morokuma, K.; Voth, G. A.; Salvador, P.; Dannenberg, J. J.; Zakrzewski, V. G.; Dapprich, S.; Daniels, A. D.; Strain, M. C.; Farkas, O.; Malick, D. K.; Rabuck, A. D.; Raghavachari, K.; Foresman, J. B.; Ortiz, J. V.; Cui, Q.; Baboul, A. G.; Clifford, S.; Cioslowski, J.; Stefanov, B. B.; Liu, G.; Liashenko, A.; Piskorz, P.; Komaromi, I.; Martin, R. L.; Fox, D. J.; Keith, T.; Al-Laham, M. A.; Peng, C. Y.; Nanayakkara, A.; Challacombe, M.; Gill, P. M. W.; Johnson, B.; Chen, W.; Wong, M. W.; Gonzalez, C.; Pople, J. A. *Gaussian 03*, Revision B.04; Gaussian, Inc.: Pittsburgh, PA, **2003**.

46. Colarusso, P.; Zhang, K.; Guo, B.; Bernath, P. *Chem. Phys. Lett.* **1997**, *269*, 39.

47. Kabelac, M.; Hobza, P. *J. Phys. Chem. B* **2006**, *110*, 14515.

48. Wang, F.; Downton, M. T.; Kidwani, N. *J. Theo and Comp. Chem.* **2005**, *4*, 247.

49. Russo, N.; Toscano, M.; Grand, A. *J. Phys. Chem. B.* **2001**, *105*, 4735.

50. Nowak, M. J.; Lapinski, L.; Kwiatkowski, J. S.; Leszczynski, J. *J. Phys. Chem.* **1996**, *100*, 3527.

51. Kwiatkowski, J.S. ; Leszczynski, J. *J. Phys. Chem.* **1996**, *100*, 941.

52. Zierkiewicz, W.; Komorowski, L.; Michalaska, D.; Cerny, J.; Hobza, P. *J. Phys. Chem. B.* **2008**, *112*, 16734.

53. Pankewitz, T.; Lautschenkov, A.; Niedner-Schatteburg, G.; Xantheas, S. S.; Lee, Y.-T. *J. Chem. Phys.* **2007**, *126*, 074307.

Chapter 7

Metalated Thymine

7.1 Introduction

Since the discovery of the double helix structure of poly-deoxyribonucleic acid (DNA) in 1953 by Watson and Crick,[1] countless research has been conducted on DNA.[2–5] Divalent transition metal ions have major effects on the structure and stability of triple-helical DNA. In many cases, their behavior is found to be different than the divalent alkaline earth metal ions, perhaps due to their increased affinities for nucleobases.[6] Zinc is one of the most abundant transition metals in the cytoplasm and its role in the gene regulatory Zn finger proteins is well indicated.[7–9] In addition, Zn^{2+} may be involved in stabilization of the triplex DNA conformation.[10] This was concluded from studies of numerous divalent metal ions, which showed that only zinc, cadmium, and magnesium ions were active in DNA triplex formation with an

efficiency in the order of $Zn^{2+} > Cd^{2+} > Mg^{2+}$.

The zinc ion is involved in numerous cellular processes such as reproduction, immunofunction, and defense against free radicals.[11–13] It was demonstrated that the zinc ion can influence DNA replication, transcription, repair, and DNA unwinding and rewinding.[14,15] Also, conformational changes that occur within the DNA structure can induce distortion of the Watson-Crick guanine-cytosine base pair and are controlled by zinc ion.[16,17] Zn(II) ions are also involved in DNA B→Z transitions.

Because of the exceptional ability of DNA in self-assembly, it has gained major attention in nanotechnology for use as nano-wires and nano-architecture.[18,19] As such, its physical properties, such as electrical and magnetic properties have been extensively investigated.[20–24] Inserting divalent metal ions such as Zn^{2+}, Co^{2+} and Ni^{2+} between the bases of a base pair, DNA becomes conducting and this is important in nanotechnological applications.[19,25] A possible charge injection mechanism to DNA for the metal ions of Ca, Mg, and Zn doped DNA was proposed based on DFT calculations.[26] It was realized that the hydrated metal ions located near the anionic phosphate groups of the DNA backbone are in the form of M^{2+} while these cations have only a single charge in the absence of water.

Zn^{2+} in protein catalytic sites facilitates the deprotonation of a bound water molecule.[27] Experimental observations also support this fact. For example, Polfer and coworkers[28] used IRMPD spectroscopy to study clusters composed of the aromatic amino acid phenylalanine and $ZnCl_2$. To transfer the cluster ions to the gas phase,

they electrosprayed the solution and found that a deprotonated Zn phenylalanine dimer $[(Phe\text{-}H)\ Zn\ (Phe)]^+$ at m/z 393 (for ^{64}Zn) was produced. Two dissociation channels were observed for the singly-charged cation; a major loss of water and a minor loss of neutral phenylalanine. Therefore, the total IRMPD spectrum was produced based on both dissociation channels. Based on the comparison between the experimental IRMPD and calculated IR spectra for a variety of structures in the 700-1800 cm^{-1} region, a tetrahedral Zn^{2+} conformer in which Zn^{2+} attaches to the N and O sites of each amino acid was proposed to exist under these experimental conditions. This conformer, along with the calculated and IRMPD spectra are shown in Figure 7.1. This structure confirms the natural form of Zn^{2+} in a biological environment since in proteins Zn^{2+} tends to form conformers with tetrahedral geometry.[9,29]

Matrix-assisted laser desorption/ionization Fourier transform ion cyclotron resonance (MALDI FT-ICR) mass spectrometry experiments revealed that divalent metal ions, including Zn^{2+}, interact mostly with the nucleobase rather than the phosphate group.[30] Also, using MALDI FT-ICR, Hettich[31] investigated the effect of Zn^{2+} among other transition metal ions on oligonucleotides such as dACGT tetranucleotide. In this experiment, an aqueous $ZnCl_2$ solution and the matrix solution of compound 2,5-dihydroxybenzoic acid (DHB) in acetonitrile/water were mixed. An aqueous oligonucleotide solution was then added to the mixture. The sample was placed onto a stainless steel probe tip and inserted into the vacuum chamber of the mass spectrometer where it was irradiated with the laser to produce ions. The negative ion

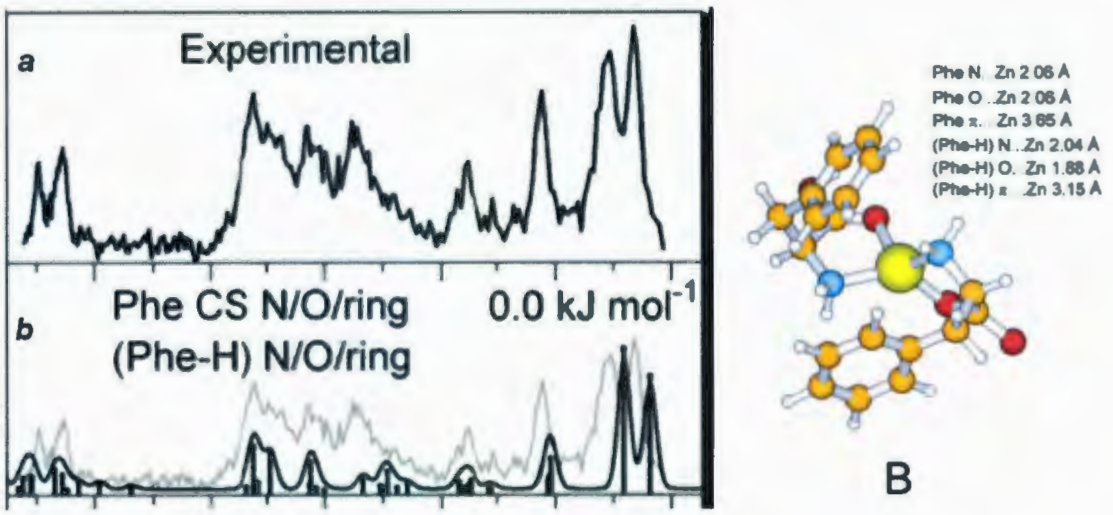

Figure 7.1: Comparing the experimental (a) and calculated (b) IR spectra for structure B of [(Phe-H) Zn (Phe)]$^+$. Figure reproduced from J. Am. Chem. Soc. 2006, 128, 517 with permission from American Chemical Society.

mass spectrum showed that dACGT can accept up to three Zn^{2+}. A possible structure for this cluster ion was proposed in which two of the phosphate groups and the nucleobases are interacting with Zn^{2+} (see Figure 7.2). One piece of evidence to support the proposed location of Zn^{2+} comes from the fragmentation of the parent ion which loses thymine and water, suggesting that Zn^{2+} most probably is not directly interacting with the thymine moiety.

Zn (II) has also been found to be important in the stabilization of the non-canonical forms of nucleobases.[31–33] Canonical N9 adenine offers three possible binding sites (N1, N3, and N7) at physiological pH, with the N1 position being the most favourable metal-binding site. However, using a Zn (II) salt and 9-ethyladenine,

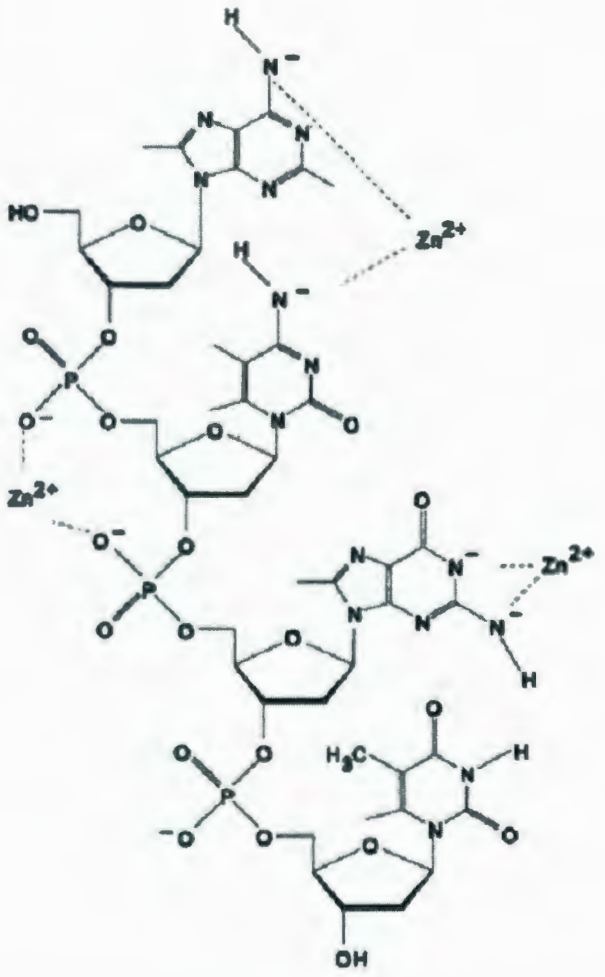

Figure 7.2: The proposed structure for dACGT and three Zn^{2+} species. Figure reproduced from Int. J. Mass Spectrom. 2001, 204, 55 with permission from Elsevier.

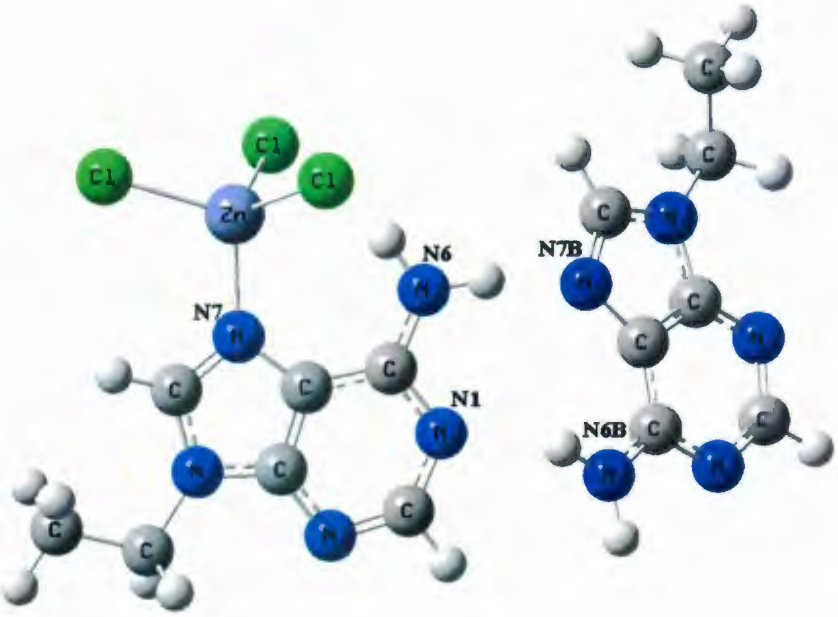

Figure 7.3: Proposed structure of [Zn(9-EtA-N7)Cl3](9-EtAH).

Zn(II) can attach to the N7 of the adenine in a dimer of adenine-adeninium base pair stabilizing the non-canonical structure shown in Figure 7.3.[34] This compound has been successfully synthesized and the X-ray crystallographic structure consisting of a Zn(II) anionic complex and 9-ethyladeninium resembles the ab initio calculated structure. In this complex, the Zn(II) is ligated to three chloride and the N7 position of an 9-ethyladenine with a distorted tetrahedral geometry. An intramolecular H-bond interaction between the N6H and Cl also stabilizes this conformer. In addition, intermolecular hydrogen bonding of N6H...N7 and N1...N6H is responsible for self-assembly of the adenine-adeninium complex in a polymeric ribbon-like 1D supramolecular structure. At physiological conditions, the divalent cationic form of

Figure 7.4: The three lowest-energy structures of thymine Zn(II) calculated at B3LYP/6-311+G(2df,2p). See text for the relative energetics.

zinc, Zn^{2+}, exists which has a filled d electronic shell. Therefore, it has limited catalytic activity in proteins due to its inertness to redox reactions. As a soft Lewis acid with a vacant s orbital, Zn^{2+} has strong interactions with the heteroatoms of numerous ligands.[28] Investigating the interaction of bare zinc ion with nucleobases in the presence of solvent, water in particular, can provide information regarding the electronic and structural properties of the complexes, leading to elucidation of the role of Zn^{2+} in the biophysics of DNA and RNA molecules. Marino et al.[35] studied the interaction of zinc ion with purine and pyrimidine DNA and RNA bases in the gas phase by DFT calculations at the B3LYP/6-311+G(2df,2p) level. They found that the zinc ion preferably coordinates to the nucleobases, except for cytosine, in a bi-dentate fashion rather than a mono-coordinated fashion. In the case of thymine-Zn^{2+}, the global minimum (T3-Zn^{2+} in Fig 7.4) is a structure in which Zn^{2+} coordinates to N3 and O4 and is 66.5 kJ mol^{-1} below the lowest energy tautomer of free thymine with

Zn^{2+}. The three lowest energy structures for thymine-Zn^{2+} (T1-Zn^{2+}, T2-Zn^{2+}, and T3-Zn^{2+}) are shown in Figure 7.4. The relative minimum T2-Zn^{2+} is calculated to be only 1.7 kJ mol^{-1} higher in energy relative to the global minimum (T3-Zn^{2+}) while a significant energy difference between the free tautomers of thymine was reported.[36–38] This reflects the metal ion stabilization effects on the higher energy tautomers producing almost isoenergetic isomers. Also, zinc ion was found to be closer to oxygen than to nitrogen in the bi-coordinated complexes. In addition, absolute Zn^{2+} metal ion affinity (MIA) values at 298 K, for these tautomers were calculated to be 777.8, 918.4, and 925.1 kJ mol^{-1} for the T1, T2, ans T3 zinc ion tautomers, respectively. As expected, the global energy minimum has been calculated to have the largest MIA value since it has the strongest interaction with Zn^{2+}. The authors further argued that since the formation of adducts from the high-energy free thymine tautomers demands enormous amount of energy, the most probable MIA must be 777.8 kJ mol^{-1} corresponding to the highest energy isomer (T1-Zn^{2+}). Although this study revealed some information about the effect of zinc ion on thymine and other nucleobases, the presence of solvent was not considered which is of a particular importance as it may change the metal ion binding properties drastically. Investigating the interaction of bare zinc ion with nucleobases in the presence of solvent, water in particular, can provide information regarding the electronic and structural properties of the complexes, leading to elucidation of the role of Zn^{2+} in the biophysics of DNA and RNA molecules. To this end, we decided to investigate the effect of a water molecule on the

thymine-Zn(II) system. In this research, using the experimental IRMPD approach combined with computational techniques, the structures of singly hydrated thymine zinc ion-bound dimers were studied.

7.2 Methods

7.2.1 Experimental

All the experiments for this chapter were performed at Memorial University. Within the last two years, we have set up our FT-ICR MS laboratory equipped with an OPO laser which allows us to apply a variety of techniques including IRMPD to study gaseous ions. The instrumental set up is very similar to the one explained in the previous Chapters and is depicted in Figure 7.5. An ApexQe Bruker FT-ICR mass spectrometer is coupled to a Brilliant B Nd:YAG pumped OPO laser. Desolvated thymine zinc ion-bound dimers were produced by electrospraying a mixture of 1 mM solutions of thymine in 18 MΩ Millipore water and a few drops of 0.01 M $Zn(NO_3)_2$ solution. All chemicals were purchased from Aldrich and used as received. Thymine zinc ion dimer (m/z 315) was isolated in the accumulation cell for 2.1 s, where water vapor was introduced at $\sim 10^{-2}$ mbar which resulted in singly solvated $[(Thy_2\text{-}H)\text{-}Zn\text{-}(H_2O)]^+$. The singly hydrated ions were transferred to the ICR cell where the isolated $[(Thy_2\text{-}H)\text{-}Zn\text{-}(H_2O)]^+$ at m/z 333 were irradiated with the tunable OPO

Figure 7.5: FT-ICR MS instrument coupled with an OPO/A laser at Memorial University.

laser. Absorption of a resonant infrared laser photon resulted in dissociation of the precursor ion through loss of water and was monitored by a change in mass of the parent ion producing m/z 315. The IR irradiation time was 2.0 s with a step size of 1.4 cm^{-1} between points in the IRMPD spectrum. The IRMPD efficiency is defined as the negative of the natural logarithm of precursor ion intensity divided by the sum of the fragment and precursor ion intensities.

7.2.2 Computational

The Gaussian 03 suite of programs was used for all electronic structure calculations.[39] Optimized structures, harmonic vibrational frequencies of the various hydrated zinc ion-bound thymine dimer isomers were computed using the B3LYP density functional. The Gen keyword with 6-31+G(d,p) basis set on C, H, O, and N atoms and LANL2DZ basis set on Zn with ECP was used and will be addressed as B3LYP/ 6-31+G(d,p)//LANL2DZ. To obtain the most stable structure(s) of $[(Thy_2\text{-}H)\text{-}Zn\text{-}(H_2O)]^+$ geometry optimization of numerous structures of thymine-zinc ion were systematically attempted. In the next step another thymine was added to the optimized structures and the thymine zinc ion-bound dimer structures were optimized. Finally, one water molecule at different positions was added to the zinc ion-bound dimer structures and these structures were then optimized and their vibrational frequencies were calculated. Final optimized structures are shown in Figure and will be discussed in section 7.3. All examined structures with Zn^{2+} at different binding sites were converted to these four structures once they optimized. Here we show the structures and spectra of the lowest-energy hydrated zinc ion-bound dimers. The calculated frequencies were scaled using a scale factor of 0.956.[40] 298 K free energy differences relative to the lowest energy isomer are reported for all hydrated zinc ion-bound dimers using MP2 single point energy calculations with a 6-311G(2df,p) basis set on all atoms except Zn and a LANL2DZ basis set on Zn. MP2 calculations were performed on the B3LYP/ 6-31+G(d,p)//LANL2DZ optimized structures. The larger

6-311++G(2df,p) basis set was first chosen for MP2 calculations but the required memory to do single point calculations was not available. Therefore, the smaller 6-311G(2df,p) was used to obtain energetics. The obtained value from MP2 is in line with the values from B3LYP calculations.

7.3 Results and Discussion

The IRMPD spectrum of $[(Thy_2\text{-H})\text{-Zn-}(H_2O)]^+$ in the 3100-3850 cm^{-1} region is shown in Figure 7.6. Three main absorptions are observed at 3710, 3621, and 3448 cm^{-1}. Based on the peak positions, the two peaks at the higher frequency region are expected to be due to the water symmetric and asymmetric stretching vibrations. To confirm this assumption, the IRMPD spectrum for $[(Thy_3\text{-H})\text{-Zn}]^+$ was also recorded and is shown in red dashed line in Figure 7.6. The two peaks assigned to water absorptions are absent in this spectrum and this could be further evidence that 3710 and 3621 cm^{-1} are most probably water asymmetric and symmetric vibrations, respectively.

The structure of thymine along with typical atom-numbering is shown in scheme 7.1. Starting from $[(Thy\text{-H})\text{-Zn}]^+$, all possible bi-dentate positions for Zn^{2+} including N1N3, N1O2, N3C5, N3O2, and N3O4 were investigated. Two types of N3N1 structures were optimized, one deprotonated at N3 and another deprotonated at N1. Upon optimization, both of these structures converged to N3O4 and N1O2 structures,

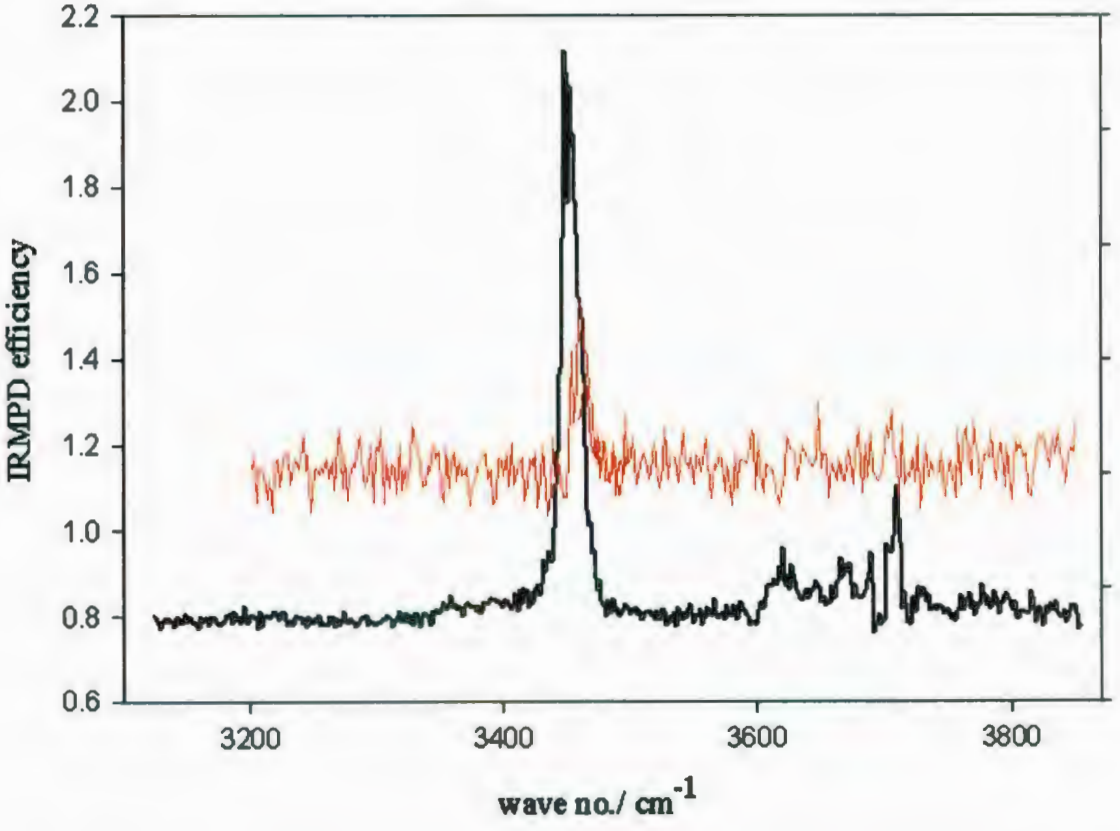

Figure 7.6: IRMPD spectra for $[(Thy_2\text{-}H)\text{-}Zn\text{-}(H_2O)]^+$ (in black) and $[(Thy_3\text{-}H)\text{-}Zn]^+$ (in red) in the 3100-3850 cm^{-1} region.

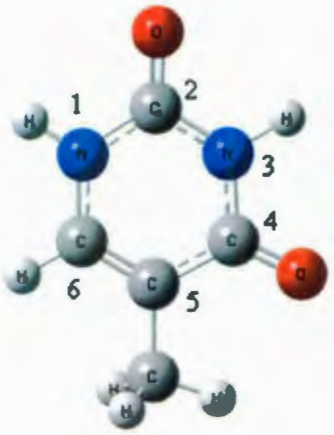

Scheme 7.1

respectively. Among all structures, N3O4 was calculated to have the lowest energy, followed by N3O2, N1O2 and finally N3C5, which are calculated to be 21.9, 32.6, and 239.0 kJ mol^{-1}, respectively, higher in free energy relative to N3O4 structures based on the B3LYP/ 6-31+G(d,p)//LANL2DZ. As expected, carbon serves as the least favoured coordination site for Zn^{2+} and based on our calculations this structure is 239.0 kJ mol^{-1} higher in the 298 K free energy difference relative to the lowest energy isomer (N3O4). A similar structure was found by Marino et al.[38] as the lowest energy conformer for thymine-Zn^{2+}, structure T3-Zn^{2+} in Figure 7.4. Note that this structure is a doubly-charged cation whereas ours is singly charged. Nonetheless, N3 and O4 function as the most favoured coordination sites in the most stable structures in both singly and doubly charged species. In contrast to the doubly-charged ion, for the lowest energy structure of singly-charged species, the Zn-N bond length is calculated to be shorter than Zn-O. This could be explained based on a higher

negative charge on the nitrogen (N3) in the singly-charged species. The presence of hydrogen at the O2 position causes less negative charge on N3 in the doubly-charged ion, probably through a small hydrogen bonding interaction. Therefore, the Zn-N bond length in the singly-charged cluster (without hydrogen on O2) is shorter due to more negative charges on N3 than the doubly-charged T3-Zn^{2+} in Fig. 7.4. In the next step, one thymine was added to the $[(Thy\text{-}H)\text{-}Zn]^+$ lowest energy structure at different positions. The most stable structure for $[(Thy_2\text{-}H)\text{-}Zn]^+$ was calculated to have a C_{2v}-like symmetry in which Zn^{2+} coordinates to N3 and O4 sites of each of thymine moieties. Finally, the attachment of one water molecule at a variety of positions for different structures was inspected. Generally, two types of water molecule attachment to the thymine zinc ion-bound dimers includes direct coordination to the Zn^{2+} and/or interaction with oxygen and hydrogen sites within the thymine moieties. Between the two, the former was found to stabilize the thymine zinc ion-bound dimer the most since a stronger interaction between the positive charge on Zn^{2+} and the oxygen of water exists.

The calculated IR spectra for the lowest energy structures of $[(Thy_2\text{-}II)\text{-}Zn\text{-}(H_2O)]^+$ is shown in Figure 7.7 and will be discussed in more detail. The most stable structure for $[(Thy_2\text{-}H)\text{-}Zn\text{-}(H_2O)]^+$ is similar to the one for $[(Thy_2\text{-}H)\text{-}Zn]^+$ in which water is directly attached to the zinc ion (A in Figure 7.7). Structure B is only 1.8 kJ mol^{-1} higher in the relative 298 K free energy calculated at MP2/6-311g(2df,p)//LANL2DZ //B3LYP/ 6-31+G(d,p)//LANL2DZ. In this structure, the O2/ N3 sites of one

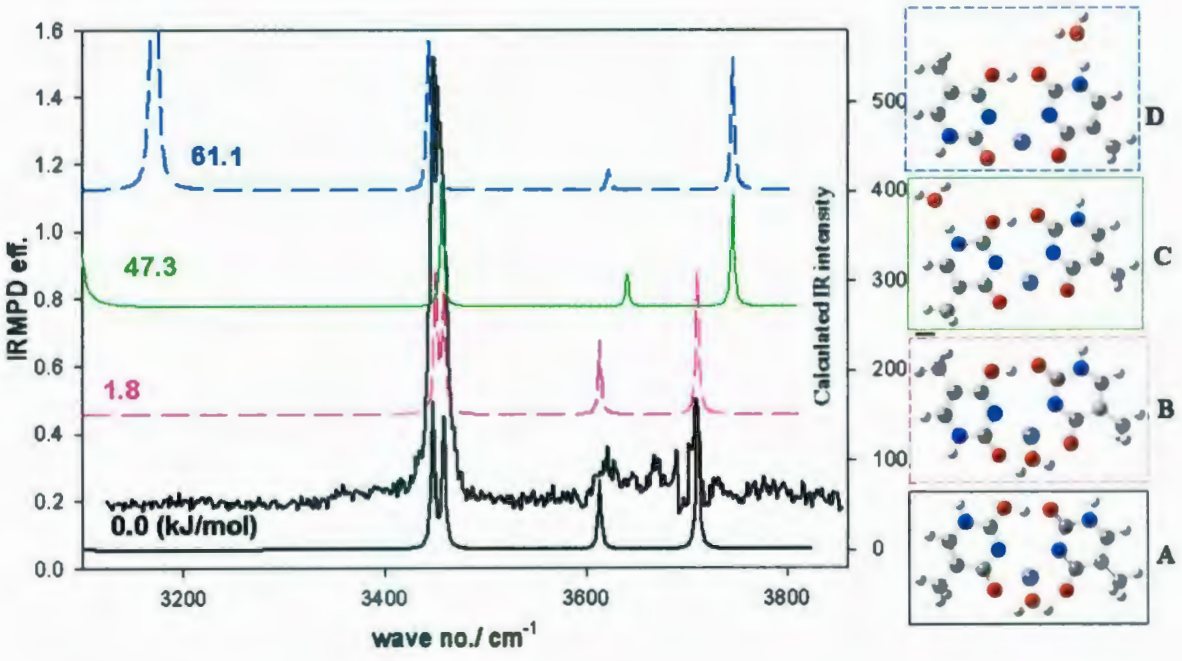

Figure 7.7: A comparison of the experimental IRMPD (in solid black) and calculated IR spectra for the $[(Thy_2\text{-}H)\text{-}Zn\text{-}(H_2O)]^+$ four lowest energy. The relative free energies (kJ mol^{-1}) at 298 K compared to structure A are provided for each structure.

thymine and the N3/O4 of another thymine interact with the zinc ion. As predicted, the calculated IR spectra for structures A and B are very similar and it is impossible to distinguish between the two based on the spectroscopic data. In structures C and D, water interacts with the hydrogen and oxygen sites rather than Zn^{2+}. This configuration is very high in energy, 47.3 kJ mol^{-1} higher in 298 K free energy relative to the lowest energy isomer (A). The observed features in the IRMPD spectrum are reproduced for structures C and D; however, the bands for water are blue-shifted in the calculated spectra. Compared to A and B, in structures C and D, oxygen has more negative charge since it is interacting with a hydrogen of thymine rather than zinc ion. This results in a stronger bond between oxygen and hydrogen atoms in water, shifting the symmetric and asymmetric vibrations to the higher energy range of the IR spectra than when H_2O is bonded to Zn^{2+}. A peak at 3171 cm^{-1} is predicted for structure D, corresponding to the extremely red-shifted N-H vibration involved in the H-bond with water, is not observed in the IRMPD spectrum. Therefore, it seems reasonable to rule this structure out based on both the spectroscopic and thermodynamic data. The fact that structure C is 47.3 kJ mol^{-1} higher in the free energy difference relative to A helps to rule out structure C from being present under experimental conditions. As predicted in Figure 7.8 in the lower energy section of the IR spectrum, i.e. in the 1800-2800 cm^{-1} region, it may be possible to distinguish structure A from structure B and the rest of isomers since the shared hydrogen oscillating between the two O2 of the two thymine moieties is highly red-shifted to 2017 cm^{-1}. Therefore, the future

Observed (cm^{-1})	Assignments	Structure A	Structure B
3710	water asymmetric stretching	3712	3712
3621	water symmetric stretching	3614	3615
3448	N1-H stretching	3459(R)	3460(R)
		3449(L)	3451(L)

Table 7.1: Vibrational frequency assignments for $[(Thy_2\text{-}H)\text{-}Zn\text{-}(H_2O)]^+$. Observed frequencies are obtained form the IRMPD spectrum and the calculated values for structure A and B are extracted from the predicted frequencies at B3LYP/6-31+G(d,p)//LANL2DZ scaled at 0.956.

work is to record the IRMPD spectrum in this region.

Vibrational frequencies were assigned based on both structure A and B and are summarized in Table 7.1. As mentioned, the water asymmetric and symmetric stretching vibrations were observed at 3710 and 3621 cm^{-1} which are in good agreement with the predicted absorptions at 3712 and 3614 cm^{-1}. However, recording the IR spectrum in the 3600-3800 cm^{-1} range is beneficial to clarify if the two observed peaks are resolved. In addition the two free N1-H stretching vibration(s) were recorded at 3448 cm^{-1} and predicted by calculations to occur at 3459 and 3450 cm^{-1} for the right and left thymine moieties, respectively.

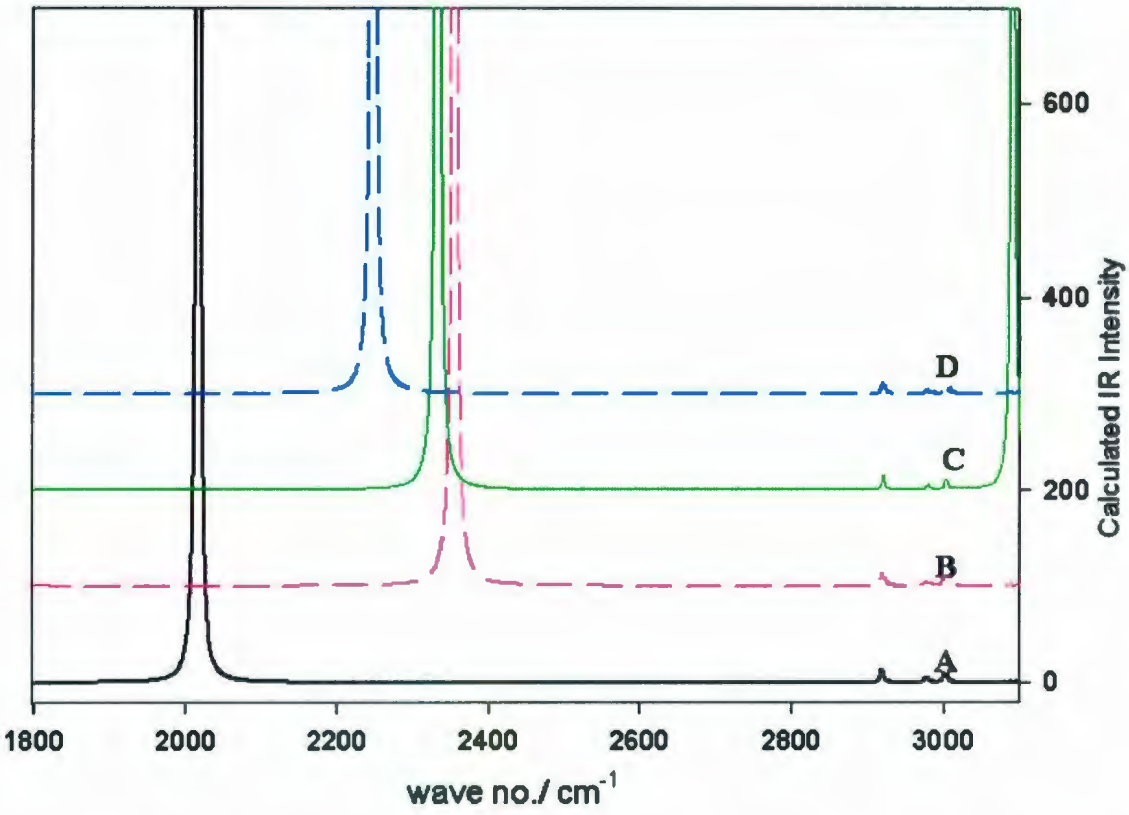

Figure 7.8: The predicted IR spectra for structures A, B, C, and D (as shown in Figure 7.7) in the 1800-3000 cm^{-1} region.

7.4 Conclusions

An attempt at determining the structures of $[(Thy_2\text{-}H)\text{-}Zn\text{-}(H_2O)]^+$ under electrospray conditions was initiated. By comparing the experimental and calculated IR spectra in the 3100-3850 cm^{-1} region, two structures were assigned as possible structures under experimental conditions. These structures are the two lowest energy structures predicted by B3LYP/6-31+G(d,p)//LANL2DZ. The most stable structure

is a zinc ion-bound dimer with the Zn^{2+} shared between the two thymines at N3O1 sites and the water molecule is directly attached to the zinc ion. Recording an IRMPD spectrum in the 1800-2800 cm^{-1} region may be beneficial in distinguishing between the two lowest energy structures, A and B.

Bibliography

1. Watson, J. D.; Crick, F. H. *Nature* **1953**, *171*, 737.
2. Wilkins, M. H. F.; Stokes, A. R.; Wilson, H. R. *Nature* **1953**, *171*, 738.
3. Franklin, R. E.; Gosling, R. G. *Nature* **1953**, *171*, 740.
4. Bowater, R. P. *Nature Encyclopedia of the Human Genome (Ed. Cooper, D. M.), Macmillan* **2003**, 1.
5. For example see Kuper, J.; Kisker, C. *Bioforum.* **2009**, *32*, 26.
6. Sabat, M.; Lippert, B. *Met. Ions in Biol. Syst.* **1996**, *33*, 143.
7. Klug, A.; Rhodes, D. *Trends Biochem. Sci.* **1987**, *12*, 464.
8. Schwabe, J. W. R.; Klug, A. *Nat. Struct. Mol. Biol.* **1994**, *1*, 345.
9. Berg, J. M.; Shi, Y. *Science* **1996**, *271*, 1081.
10. Bernues, J.; Beltran, R.; Casasnovans, J. M.; Azorin, F. *Nucl. Acids. Res.* **1990**, *18*, 4067.
11. Bray, T. M.; Bettger, W. *J. Free Radic. Biol. Med.* **1990**, *8*, 281.
12. Powell, S. R. *J. Nutr.* **2000**, *130*, 1447S.
13. Ho, E. *J. Nutr. Biochem.* **2004**, *15*, 572.
14. Falchuk, K. H. *Mol. Cell Biochem.* **1998**, *188*, 41.
15. Volbeda, A.; Lahm, A.; Sakiyama, F.; Suck, D. *EMBO J.* **1991**, *10*, 1607.
16. Vallee, B. L.; Falchuk, K. H. *Physiol. Rev.* **1993**, *73*, 79.
17. Kang, S.; Wells, R. D. *J. Biol. Chem.* **1994**, *269*, 9528.
18. Shih, W. M.; Quispe, J. D.; Joyce, G. F. *Nature* **2004**, *427*, 618.
19. Wettig, S. D.; Li, C. Z.; Long, Y. T.; Kraatz, H. B. *Anal. Sci.* **2003**, *19*, 23.
20. Mizoguchi, K. *Proc. SPIE* **2008**, *7040*, 70400Q-1.

21. Fink, H. W.; Schenenberger, C. *Nature* **1999**, *398*, 407.

22. de Pablo, P. J.; Moreno-Herrero, F.; Colchero, J.; Gomez Herrero, J.; Herrero, P.; Baro, A. M.; Ordejon, P.; Soler, J. M.; Artacho, E. *Phys. Rev. Lett.* **2000**, *85*, 4992.

23. Mizoguchi, K.; Tanaka, S.; Ogawa, T.; Shiobara, N.; Sakamoto, H. *Phys. Rev. B* **2005**, *72*, 033106 (1-4).

24. Dekker, C.; Ratner, M. A. *Phys. World* **2001**, *14*, 29.

25. Lee, J. S.; Latimer, L. J. P.; Reid, R. S. *Biochem. Cell Biol.* **1993**, *71*, 162.

26. Kino, H.; Tateno, M.; Boero, M.; Torres, J. A.; Ohno, T.; Terakura, K.; Fukuyama, H. *J. Phys. Soc. Jpn.* **2004**, *73*, 2089.

27. Deerfield, D. W.; Carter, C. W., Jr.; Pederson, L. G. *Int. J. Quantum Chem.* **2001**, *83*, 150.

28. Polfer, N. C.; Oomens, J.; Moore, D. T.; von Helden, G.; Meijer, G.; Dunbar, R. C. *J. Am. Chem. Soc.* **2006**, *128*, 517.

29. Venkataraman, D.; Du, Y.; Wilson, S. R.; Hirsch, K. A.; Zhang, P.; Moore, J. S. *J. Chem. Educ.* **1997**, *74*, 915.

30. Hettich, R. L. *Int. J. Mass Spectrom.* **2001**, *204*, 55.

31. Navarro, J. A. R.; Lippert, B. *Coord. Chem. Rev.* **1999**, *186*, 653.

32. Moroni, F.; Famulari, A.; Raimondi, M.; Sabat, M. *J. Phys. Chem. B* **2003**, *107*, 4196.

33. Sponer, J.; Sabat, M.; Gorb, L.; Leszczynski, J.; Lippert, B.; Hobza, P. *J. Phys. Chem. B* **2000**, *104*, 7535.

34. Amo-Ochoa, P.; Alexandre, S. S.; Pastor, C.; Zamora, F. *J. Inorg. Biochem.* **2005**, *99*, 2226.

35. Marino, T.; Mazzuca, D.; Toscano, M.; Russo, N.; Grand, A. *Int. J. Quantum. Chem.* **2007**, *107*, 311.

36. Russo, N.; Sicilia, E.; Toscano, M.; Grand, A. *Int. J. Quantum. Chem.* **2002**, *90*, 903.

37. Marino, T.; Russo, N.; Toscano, M.; Grand, A. *Int. J. Quantum. Chem.* **2004**, *98*, 347.

38. Russo, N.; Toscano, M.; Grand, A. *J. Mass Spectrom.* **2003**, *38*, 265.

39. Frisch, M. J.; Trucks, G. W.; Schlegel, H. B.; Scuseria, G. E.; Robb, M. A.; Cheeseman, J. R.; Montgomery, J. A., Jr.; Vreven, T.; Kudin, K. N.; Burant, J. C.; Millam, J. M.; Iyengar, S. S.; Tomasi, J.; Barone, V.; Mennucci, B.; Cossi, M.; Scalmani, G.; Rega, N.; Petersson, G. A.; Nakatsuji, H.; Hada, M.; Ehara, M.; Toyota, K.; Fukuda, R.; Hasegawa, J.; Ishida, M.; Nakajima, T.; Honda, Y.; Kitao, O.; Nakai, H.; Klene, M.; Li, X.; Knox, J. E.; Hratchian, H. P.; Cross, J. B.; Adamo, C.; Jaramillo, J.; Gomperts, R.; Stratmann, R. E.; Yazyev, O.; Austin, A. J.; Cammi, R.; Pomelli, C.; Ochterski, J. W.; Ayala, P. Y.; Morokuma, K.; Voth, G. A.; Salvador, P.; Dannenberg, J. J.; Zakrzewski, V. G.; Dapprich, S.; Daniels, A. D.; Strain, M. C.; Farkas, O.; Malick, D. K.; Rabuck, A. D.; Raghavachari, K.; Foresman, J. B.; Ortiz, J. V.; Cui, Q.; Baboul, A. G.; Clifford, S.; Cioslowski, J.; Stefanov, B. B.; Liu, G.; Liashenko, A.; Piskorz, P.; Komaromi, I.; Martin, R. L.; Fox, D. J.; Keith, T.; Al-Laham, M. A.; Peng, C. Y.; Nanayakkara, A.; Challacombe, M.; Gill, P. M. W.; Johnson, B.; Chen, W.; Wong, M. W.; Gonzalez, C.; Pople, J. A. *Gaussian 03*, Revision B.04; Gaussian, Inc.: Pittsburgh, PA, **2003**.

40. Andersson, M. P.; Uvdal, P. *J. phys. Chem. A* **2005**, *109*, 2937.

Chapter 8

Conclusions and Future Aspects

Mass spectrometry has played a crucial role in studying noncovalent interactions. Noncovalent interactions have major effects on biological processes by providing the ion more flexibility to vary their structures. With the development of electrospray ionization technique, mass spectrometry has been a very important tool to obtain structural information from gaseous ions. A variety of MS-based techniques have been developed to study the gas-phase ions. The technique of IRMPD has shown its utility to determine the 3D structure of gaseous ions. Using this technique, structures of small biologically relevant ions such as amino acids and nucleic acid bases complexed or bound with a proton or metal cations in the gas-phase were determined. Structures of the simplest aliphatic amino acid proton-bound dimers including glycine, alanine and valine were determined in Chapter 3 based on analyzing both experimental IRMPD spectra in the 700 to 2000 cm^{-1} region as well as computational data.

The experimental IRMPD spectra were consistent with the simulated IR spectra for the lowest energy structures of different amino acids which were slightly different from that assigned by previous spectroscopic studies. An ion-dipole complex between N-protonated amino acid and the carboxyl group of the second amino acid were concluded to be responsible for the IRMPD spectra. In fact the high similarity of the IRMPD spectra for different amino acids reflects the similarity in their structures. These structures were later confirmed by recording the IRMPD spectrum for the glycine proton-bound dimer in the N-H/O-H region.

The importance of employing computational methods to aid in the analysis and interpretation of the experimental data has been demonstrated. However, the computational results must be disentanled with extreme caution to prevent any incorrect conclusions. Among the parameters one has to consider when dealing with the computational results is the experimental method used to obtain the data. For example, in Chapter 4, the simulated IR spectra for only two of the four lowest-energy protonated adenine dimer isomers were similar to the experimental IRMPD while based on MP2/6-311++G(2d,p)//B3LYP/6-31+G(d,p) calculations the four lowest-energy structures were almost isoenergetic. Since the ions were produced by ESI from the solution phase, the effect of water as a solvent was considered in another set of calculations. Two independent computational approaches were used to take solvation effects into account, PCM and microsolvation with five explicit water molecules at the B2P3LYP/cc-pVTZ//B3LYP/6-31+G(d,p) level, showed that water only prefer-

entially stabilizes these two observed isomers, consistent with the interpretation of the IRMPD spectra. The results suggest caution is required when using gas-phase calculations to predict the structures of gaseous ions borne in solution by ESI. Also, another important conclusion in studying these gaseous ions is that they, at least for the small ions studied in this work, preserve their solution phase structures in the gas phase. Therefore, gas phase studies reflect the solution phase behaviour with the advantage of removing solvent interferences.

To investigate the influence of solvent on the ions' structure, a method was developed to produce the solvated ions in the gas phase and explained in Chapter 5. These solvated ions then were investigated by IRMPD spectroscopy and BIRD to obtain kinetic data. The solvation of electrosprayed ions occurs in the accumulation/collision hexapole of a hybrid Q-FTMS by introducing the solvent into the cell. Various parameters control the efficiency of the solvation. The most sensitive parameters based on our experience were the collision energy in the hexapole, the pressure of both collision gas and solvent in the hexapole, the ion accumulation time, and the chemical nature of the species. Applying this method to adenine-K^+ ions, up to three solvent molecules were attached to the metalated adenine. These solvated ions then were studied by BIRD to obtain the dissociation rate constants for loss of solvent from the cluster ions. In addition, the solvation method was successfully applied to adenine (Chapter 6) and thymine (Chapter 7) cluster ions to produce singly hydrated ions and the structures of ions were determined by IRMPD spectroscopy.

In Chapter 6, structures of alkali metal ions such as Li^+, Na^+, K^+, and Cs^+ with adenine were determined by IRMPD spectroscopy and electronic structure calculations. Also, the solvation method (Chapter 5) was applied to these ion complexes to produce singly hydrated cluster ions. The structures of these hydrated ions were also studied in the gas phase to determine their structures. By comparing the experimental and the simulated spectra it was possible to rule out various structures and to assign structures to the species probed in these experiments. In all cases the computed IR spectrum for the lowest energy structure is consistent with the experimental IRMPD spectrum. Based on the IRMPD spectra and the single point energy calculations at the MP2/6-311++G(2d,p)//B3LYP/6-31+G(d,p), it is concluded that all adenine-M^+ and adenine-M^+-H_2O are composed of the A7 rare tautomer of adenine which is attached to the cations in a bidentate fashion through N3 and N9 and for the hydrated ion water binds directly to the metal ion through oxygen. The gas-phase calculations for adenine Li^+ predict the lowest-energy structure to be the imino tautomer. However, the imino form of adenine-Li^+-H_2O is higher in energy. It is extrapolated from this data that the lowest-energy solution-phase structure of adenine Li^+ is in fact the A7 tautomer with Li^+ bound to N3 and N9. For the hydrated lithium cation-bound adenine dimer, the water molecule is concluded to be bound to the metal ion as well as hydrogen bonded to a free basic site of one of the adenine monomers. This structure was initially hypothesized based on the appearance of the IRMPD spectrum of the hydrated lithium cation-bound adenine dimer. Observing only one absorption

band at the higher energy region (~3600-4000 cm^{-1}) of the spectrum instead of two suggests that the water molecule is not symmetrically attached to the adenine metal ion moiety.

Due to the importance of m-DNA, an attempt to investigate the structure of singly hydrated thymine zinc ion-bound dimer was initiated (see Chapter 7). It was found that thymine loses one proton in the presence of zinc. Therefore, the produced solvated $[(Thy\text{-}H)Thy\text{-}Zn\text{-}(H_2O)]^+$ cluster was singly charged. Solely comparing the IRMPD spectrum in the 3100-3850 cm^{-1} region and simulated IR spectra was not sufficient to assign only one structure to the observed spectrum. Based on thermochemical values the two lowest energy structures were assigned as possible structures under the experimental conditions. In the most stable structure, the water is directly attached to the zinc of the zinc ion-bound dimer in which the Zn^{2+} is shared between the two thymines at N3O4 sites. Furthermore, computational data suggested that recording IRMPD spectrum in the 1800-2800 cm^{-1} region might be useful to distinguish between the two lowest energy structures. Therefore, recording the spectrum for $[(Thy\text{-}H)Thy\text{-}Zn\text{-}(H_2O)]^+$ cluster in this lower energy region is part of the future work. Also, trying other transition metals such as copper would be beneficial. In this step, recording the IRMPD spectrum for singly hydrated thymine copper-bound dimer is very helpful. Comparing the IRMPD spectra, for example, for zinc and copper ion clusters with thymine is extremely valuable since it can reveal a significant amount of information regarding to the structures of these cluster ions.

Understanding the key interactions in biological systems, starting from a small biological system such as those discussed in this research is vital. However, in order to extend the applicability of these fundamental studies to the real world, increasing the size of the system under study may be crucial. DNA consists of nucleic acid bases, sugars and backbone phosphates. Adding one or more sugar to nucleic acid bases can help to better mimic DNA structure in biological conditions. Once the interactions of sugar with nucleic acid bases are known, in the next step, phosphate can be added to the system. A stepwise and systematic study of a system containing all three components of DNA reveals key interactions between them, aiding to better understand biological behaviour of DNA.

Studying the ESI mechanism is of great importance to understand the required condition for a particular structure formation. For example, in Chapters 4 and 6, adenine structures with proton and metal cations were found to be stabilized by solvent molecules. Further study is needed to decide whether these stable ions are coming directly from solution or they are formed during the ESI process. By investigating the ESI mechanism it may also be possible to comprehend whether dimers and larger clusters are forming in the solution or in the gas-phase.

Finally, there is still high demands in the instrumentation of IRMPD spectroscopy in order to obtain sharper absorption peaks. Lots of information can be buried under the broad peaks. In order to obtain sharper peaks, the mechanism of IRMPD should be carefully investigated. Examining the steps involved in the IVR process is essential

in order to minimize the peak broadening.

Appendices

Appendix 1

The four B3LYP/6-31+G(d,p) singly microsolvated adenine proton-bound dimers structures each for B and D.

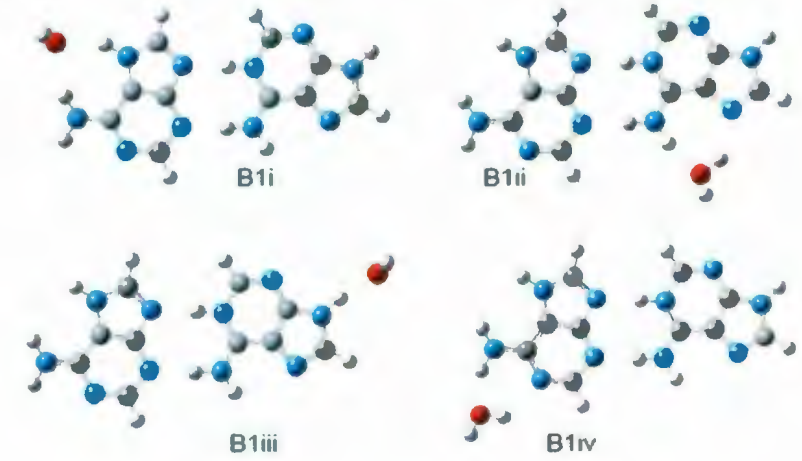

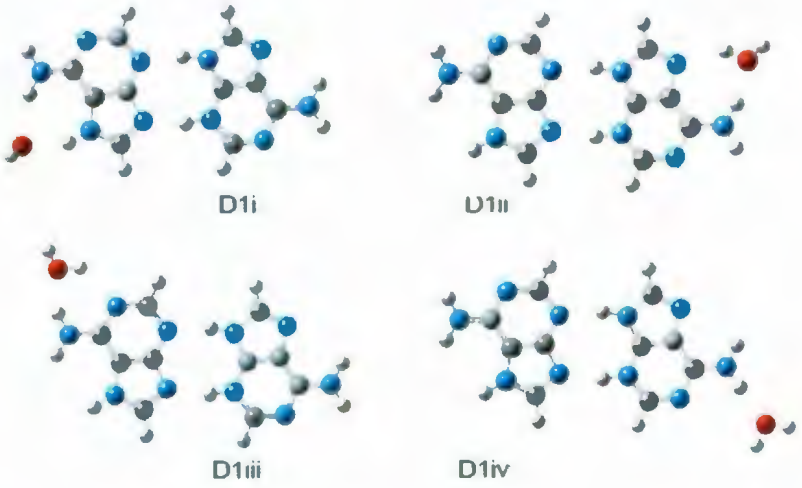

Appendix 2

The lowest-energy calculated structures for $(C_5H_5N_5)_2Na^+$. The 298 K B3LYP/6-31+G(d,p) and MP2/6-311++G(2d,p)//B3LYP/6-31+G(d,p) (in parentheses) relative free energies (kJ mol^{-1}) are provided for each structure.

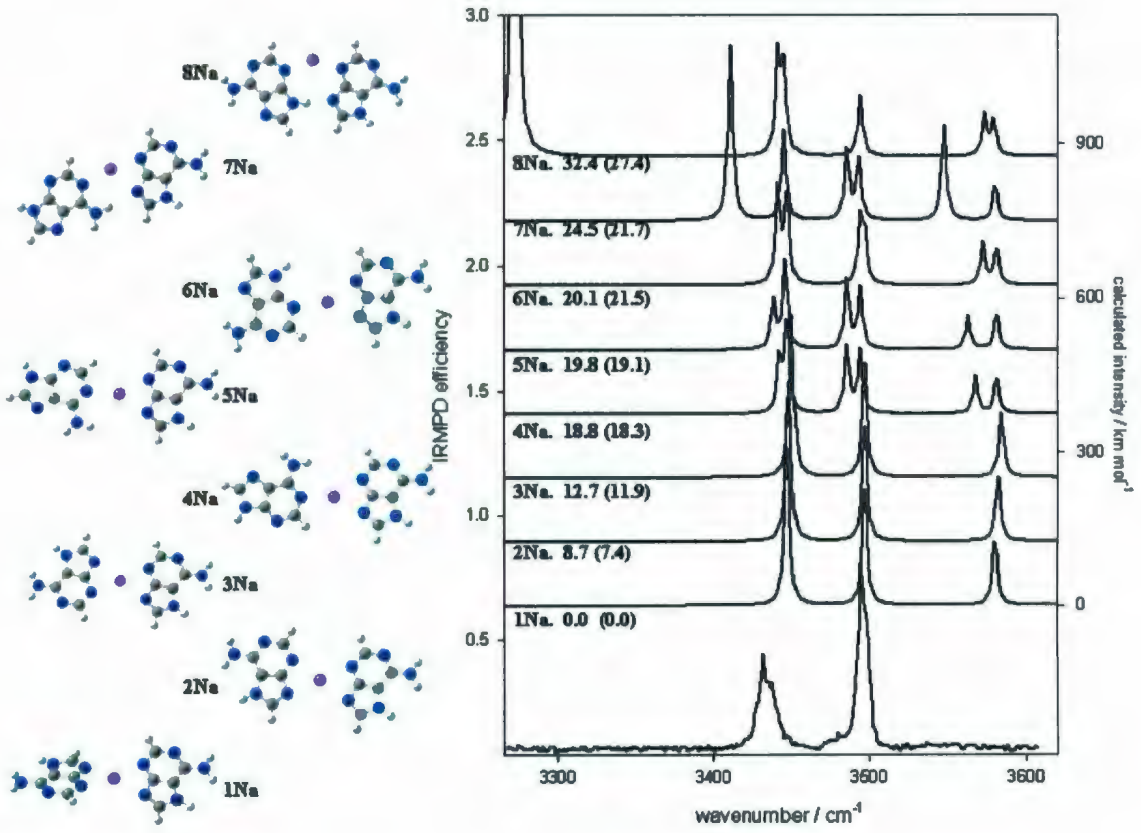

Appendix 3

IRMPD spectra of $(C_5H_5N_5)_2K^+$ as well as B3LYP/6-31+G(d,p) computed IR spectra for various isomers. The 298 K B3LYP/6-31+G(d,p) and MP2/6-311++G(2d,p)//B3LYP/6-31+G(d,p) (in parentheses) relative free energies (kJ mol^{-1}) are provided for each structure.

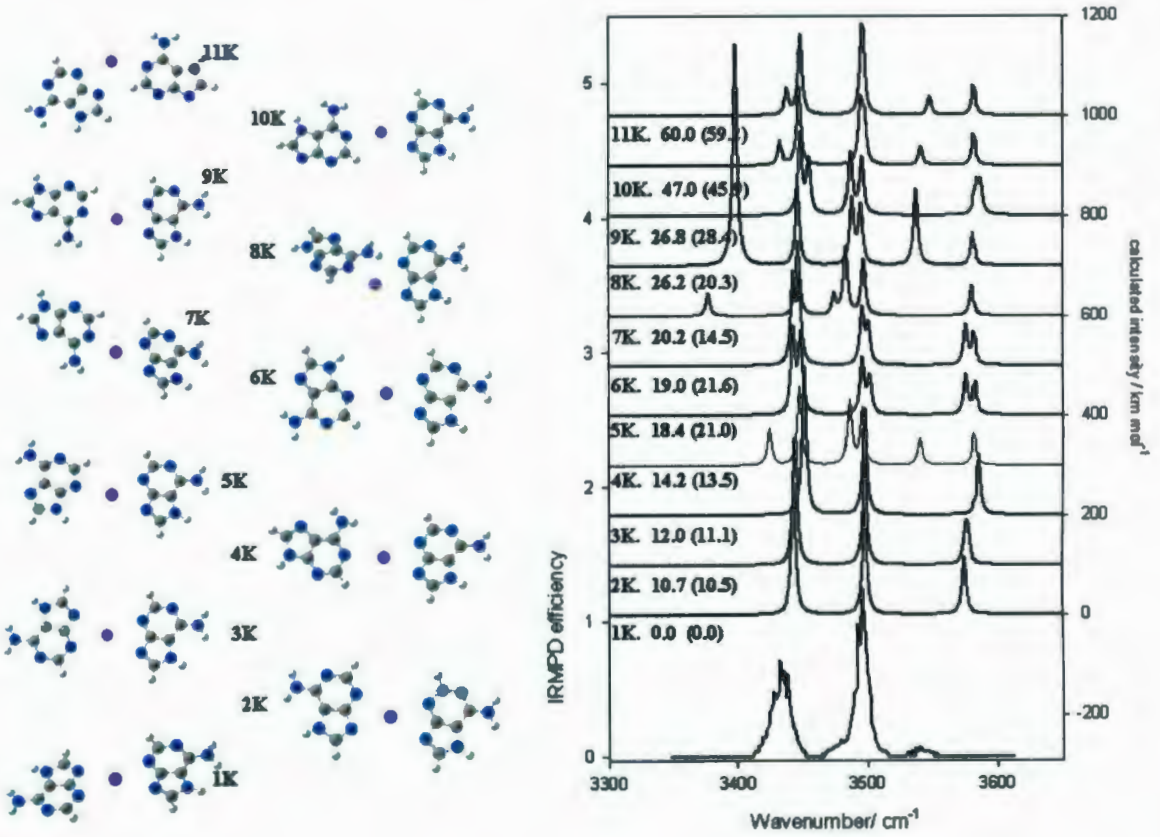

Appendix 4

Mass spectrum showing the effect of non-resonant absorption of the OPO laser by $(C_5H_5N_5)K^+$.

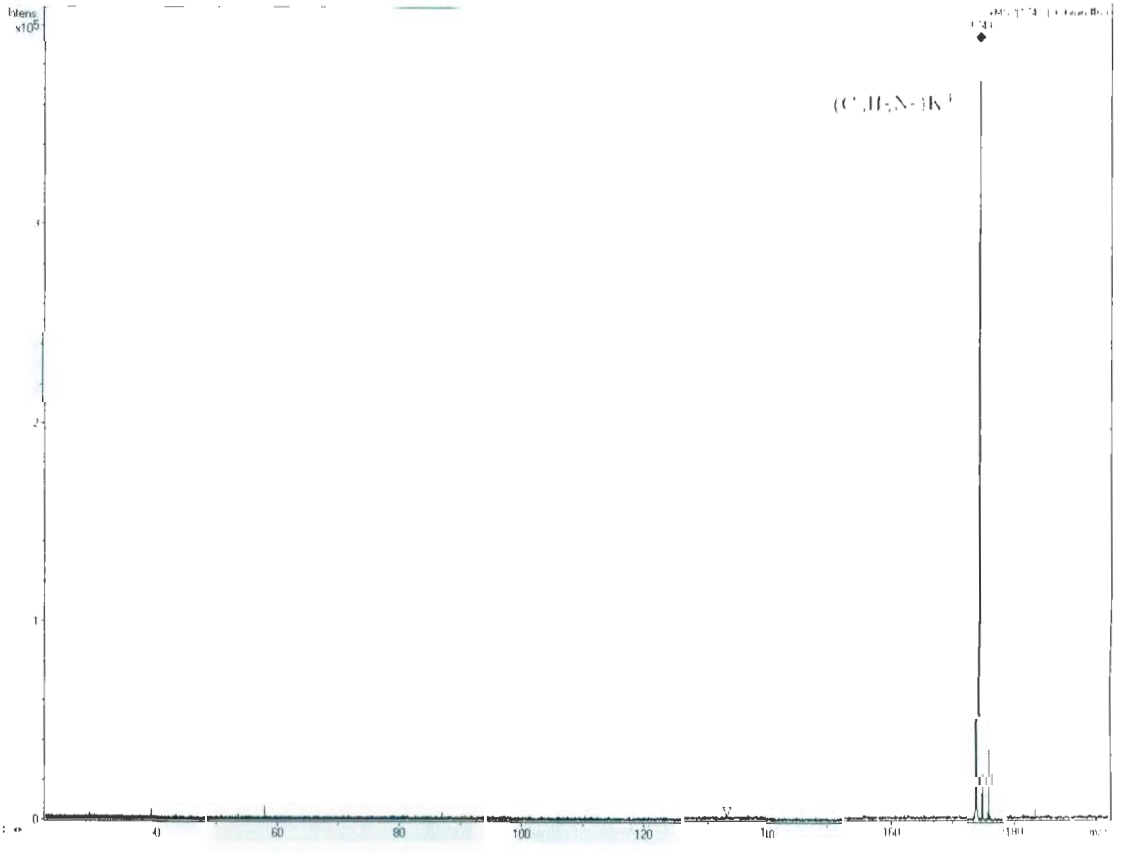

Appendix 5

Mass spectrum showing the effect of resonant absorption of the OPO laser by $(C_5H_5N_5)K^+$ and formation of K^+.

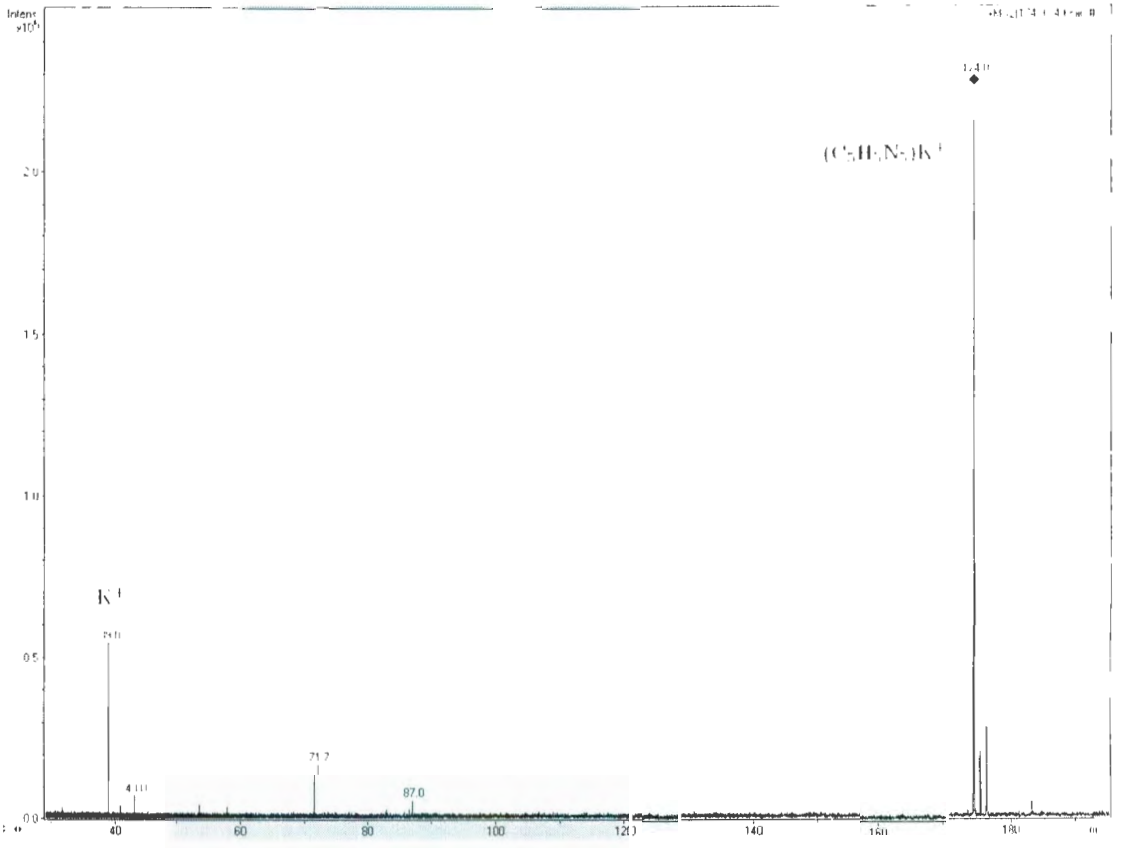

Appendix 6

Mass spectrum showing the effect of non-resonant absorption of the OPO laser by $(C_5H_5N_5)_2Li^+$.

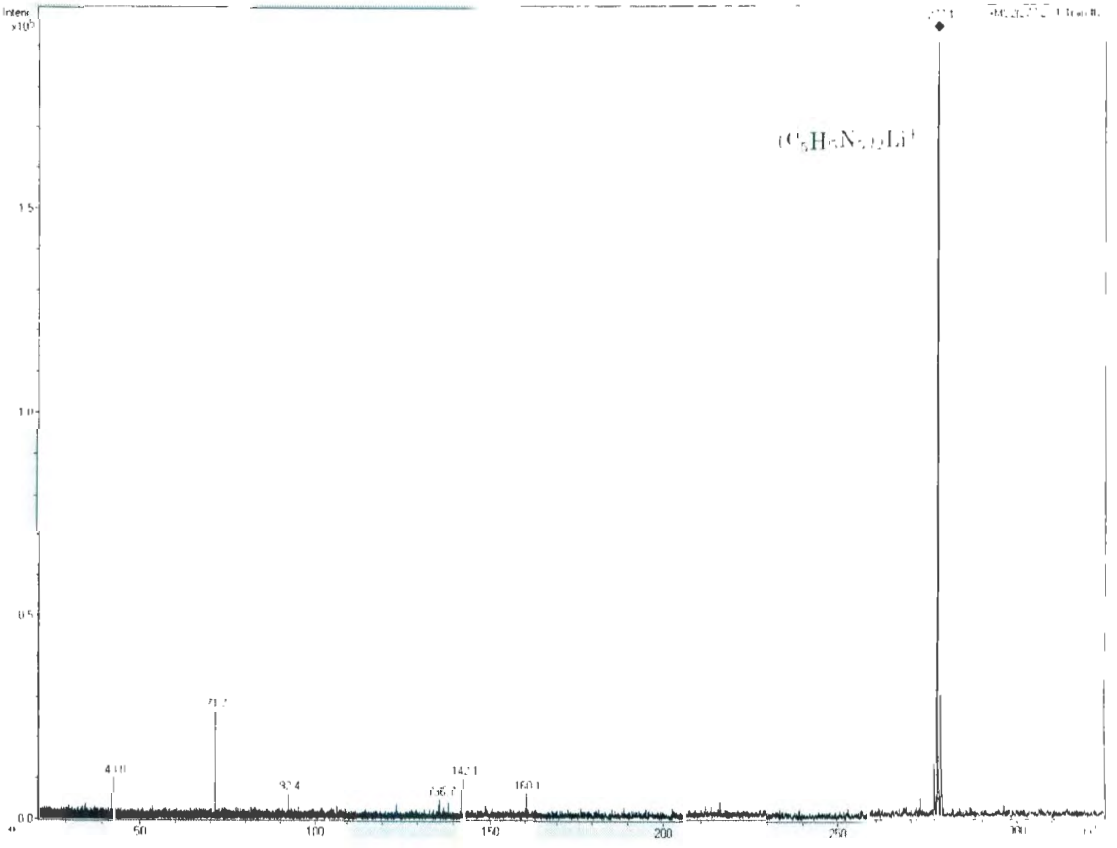

Appendix 7

Mass spectrum showing the effect of resonant absorption of the OPO laser by $(C_5H_5N_5)_2Li^+$ and formation of $(C_5H_5N_5)Li^+$.

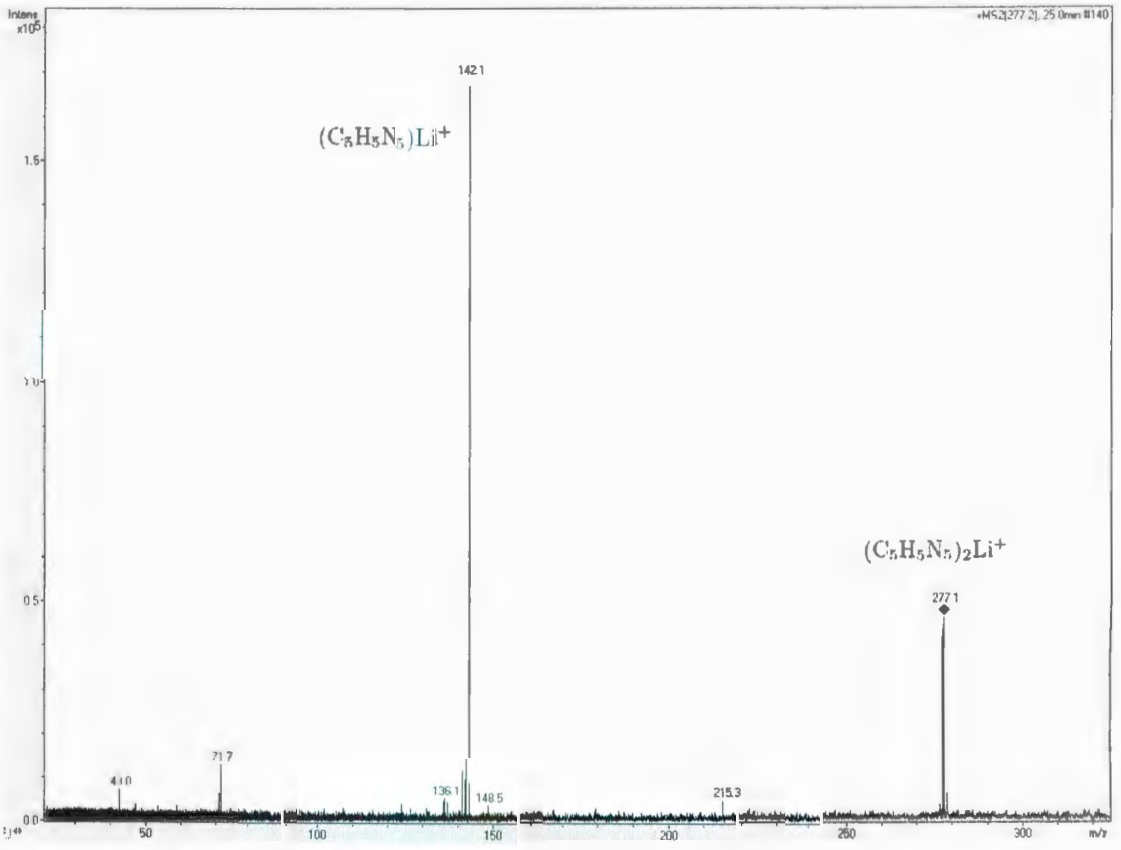

Appendix 8

Mass spectrum showing the effect of non-resonant absorption of the OPO laser by $(C_5H_5N_5)Li^+H_2O$.

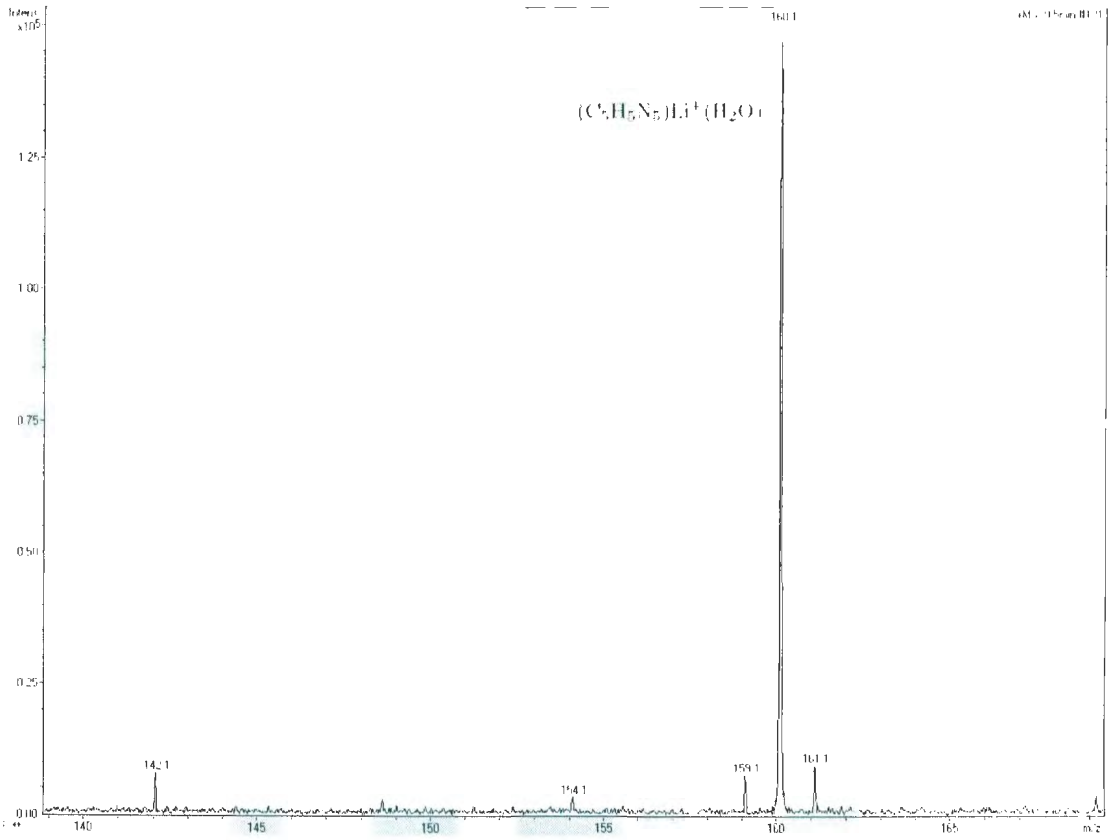

Appendix 9

Mass spectrum showing the effect of resonant absorption of the OPO laser by $(C_5H_5N_5)Li^+H_2O$ and formation of $(C_5H_5N_5)Li^+$.

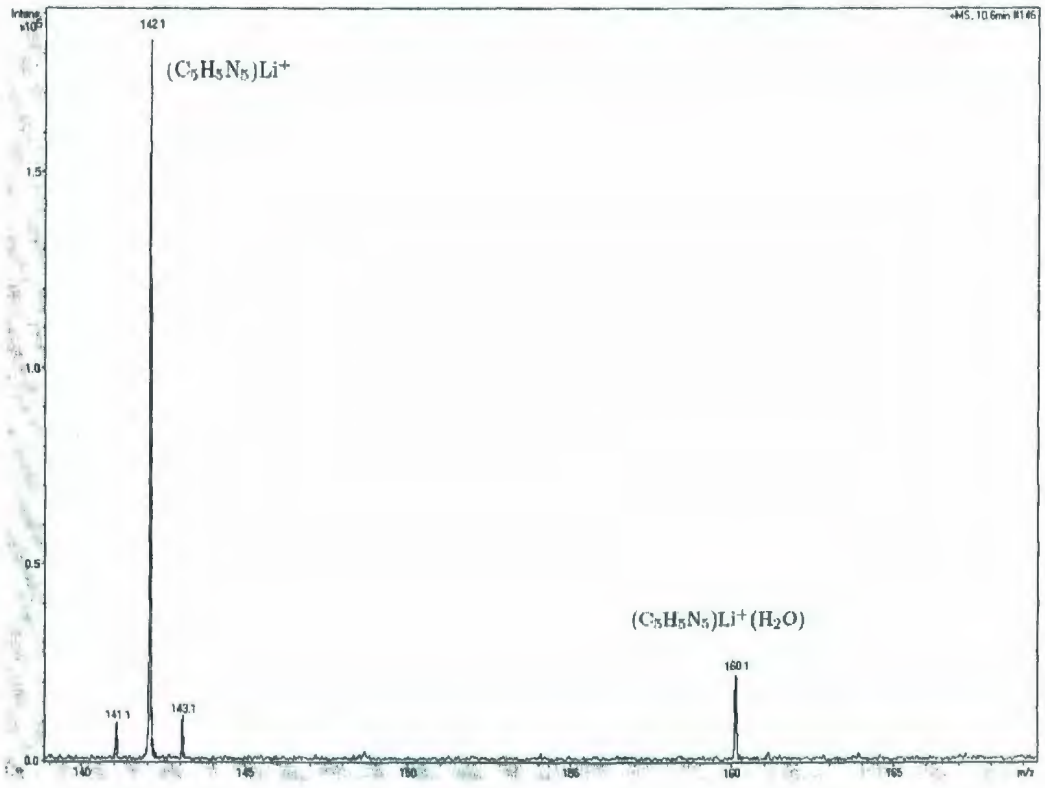

VITA

Name: Khadijeh Rajabi

Education:

- **Ph.D.,** Memorial University of Newfoundland, St. John's, NL, Canada (2006- 2009).
- **M.Sc.**, Sharif University of Technology, Tehran, Iran (2002- 2004).
- **B.Sc.**, Sharif University of Technology, Tehran, Iran (1997- 2001).

Publications

1. **K. Rajabi** , T.D. Fridgen, " Structures of Aliphatic Amino Acid Proton-Bound Dimers by IRMPD Spectroscopy in the 700 to 2000 cm^{-1} Region", *Journal of Physical Chemistry A*, **2008**, *112*,23-30.
2. **K. Rajabi**, M. Easterling, T.D. Fridgen, "Solvation of Electrosprayed Ions in the Accumulation/Collision Hexapole of a Hybrid Q-FTMS", *Journal of American Society for Mass Spectrometry*, **2009**, *20 (3)*, 411-418.
3. **K. Rajabi**, K. Theel, E. AL. Gillis, G. Beran, T.D. Fridgen, "The Structure of the Protonated Adenine Dimer by IRMPD Spectroscopy and Electronic Structure Calculations", *Journal of Physical Chemistry* A, **2009**, *113*, 8099-8107.
4. **K. Rajabi**, E. AL. Gillis, T.D. Fridgen, "Structures of Alkali Metal Ion-Adenine Complexes by IRMPD Spectroscopy and Electronic Structure Calculations," *Journal of Physical Chemistry A*, **2009**, Accepted.

VITA

5. E. AL. Gillis, **K. Rajabi**, T.D. Fridgen, "Structures of Hydrated Li^+-Thymine and Li^+-Uracil Complexes by IRMPD Spectroscopy in the N-H/O-H Stretching Region" *Journal of Physical Chemistry A*, **2009**, 113, 824-832.

6. C. G. Atkins, **K. Rajabi**, E. AL. Gillis, T.D. Fridgen, "IRMPD Spectra of Proton- and Sodium Ion-Bound Glycine Dimers In the N-H and O-H Stretching Region" *Journal of Physical Chemistry A*: **2008**, *112*, 10220-10225.

Conference Proceedings

1. **Oral Presentation:** 57th ASMS conference on Mass Spectrometry, Philadelphia, PA, USA, May 31-June 4, 2009. **K. Rajabi**, E.A.L. Gillis, K. Theel, G. Beran, T.D. Fridgen, *"Structures of Hydrated Metalated and Protonated Adenine by IRMPD Spectroscopy and Electronic Structure Calculations."*

2. **Oral Presentation:** 56th ASMS conference on Mass Spectrometry, Denver, CO, USA, June 1-5, 2008. E.A.L. Gillis, **K. Rajabi,** C. Atkins, T.D.Fridgen, "*Structures of Hydrated Li^+-Thymine and Li^+-Uracil Complexes by IRMPD Spectroscopy in the N-H/O-H Stretching Region.*"

Posters & Conferences

3. Defended M. Sc. Thesis, Sharif University of Technology, Tehran, Iran. (October 2004)

VITA

4. **Oral presentation:** 23rd Annual Trent Conference on Mass Spectroscopy, YMCA Geneva Park, Orillia, ON, Canada. July 31-August 3, 2006. **K. Rajabi**, T.D. Fridgen *"Cation-Bound DNA Bases: Experiments and Calculations Leading to Gas- Phase Infrared Spectroscopic Studies."*

5. **Poster presentation:** 2007 Gordon Research Conference on Gaseous Ions: Structures, Energetics and Reactions, Ventura, CA, USA, February 25- March 2. **K. Rajabi**, T.D. Fridgen *"IRMPD Spectra of Amino Acid Proton-Bound Dimers."*

6. **Poster presentation:** 55th ASMS conference on Mass Spectrometry, Indianapolis, IN, USA, June 3-7, 2007. **K. Rajabi**, T.D. Fridgen *"Solvation of Electrosprayed DNA Base and Amino Acid Clusters in the Accumulation Quadrupole of a Hybrid Q-FTMS."*

7. **Poster presentation:** 2007 Gordon Research Conference on the Chemistry and Physics of Matrix Isolated Species, Lewiston, ME, USA, July 15-20. E. Jewer, K. Rajabi, T.D. Fridgen *"The O-H Stretch of the Enol Form of β-Diketones."*

8. **Poster presentation:** 24th Annual Trent Conference on Mass Spectroscopy, YMCA Geneva Park, Orillia, ON, Canada. July 30-August 2, 2007. **K. Rajabi**, T.D. Fridgen *"Structures of Aliphatic Amino Acid Proton-Bound Dimers by IRMPD Spectroscopy in the 700 to 2000 cm^{-1} Region."*

9. **Poster presentation:** 24th Annual Trent Conference on Mass Spectroscopy, YMCA Geneva Park, Orillia, ON, Canada. July 30-August 2, 2007. **K. Rajabi**, T.D. Fridgen

VITA

"Solvation of Electrosprayed DNA Base and Amino Acid Clusters in the Accumulation Quadrupole of a Hybrid Q-FTMS."

10. **Oral Presentation:** 2007 Atlantic Theoretical Chemistry Symposium, St. John's, NL, Canada. August 2-4. **K. Rajabi**, T.D. Fridgen *"Structures of Aliphatic Amino Acid Proton-Bound Dimers by IRMPD Spectroscopy in the 700 to 2000 cm^{-1} Region."*

11. **Oral Presentation:** 2007 Atlantic Theoretical Chemistry Symposium, St. John's, NL, Canada. August 2-4. E. Jewer, **K. Rajabi**, T.D. Fridgen *"The O-H Stretch of the Enol Form of* β*-Diketones."*

12. **Oral presentation:** 2007 Tandem Mass Spectrometry Workshop, Lake Louise, AB, Canada. November 28-December 1. **K. Rajabi**, T.D. Fridgen *"Infrared Spectra of Ion and Solvated Complexes from IRMPD Spectroscopy."*

13. **Poster Presentation:** 91st Canadian Chemistry Conference and Exhibition, Edmonton, AB, Canada. May 24-28, 2008. **K. Rajabi**, E. AL. Gillis, T.D. Fridgen *"Structures of Hydrated Metalated Adenine by IRMPD Spectroscopy."*

14. **Oral Presentation:** 91st Canadian Chemistry Conference and Exhibition, Edmonton, AB, Canada. May 24-28, 2008. **K. Rajabi**, E. AL. Gillis, C. G. Atkins, T.D. Fridgen *"Structures of $(Thy)_nLi^+(H_2O)_m$, $(Ura)_nLi^+(H_2O)_m$ and $(Gly)_2H^+$ by IRMPD Spectroscopy."*

15. **Poster presentation:** 25th Annual Trent Conference on Mass Spectroscopy, YMCA Geneva Park, Orillia, ON, Canada. July 28-31, 2008. **K. Rajabi**, E. AL. Gillis, T.D. Fridgen *"Structures of Metal Ion-Bound Adenine Complexes by IRMPD and Density Functional Calculations."*

16. **Oral presentation:** 25th Annual Trent Conference on Mass Spectroscopy, YMCA Geneva Park, Orillia, ON, Canada. July 28-31, 2008. C. G. Atkins, **K. Rajabi**, E. AL. Gillis, T.D. Fridgen *"Characterizing Intermolecular Interactions and Structures of Glycine Homodimers using IRMPD Spectroscopy in the N-H/O-H Stretching Region."*

17. **Oral presentation:** 25th Annual Trent Conference on Mass Spectroscopy, YMCA Geneva Park, Orillia, ON, Canada. July 28-31, 2008. E. AL. Gillis, **K. Rajabi**, T.D. Fridgen *"Structures of Hydrated Li^+-Thymine and Li^+-Uracil Complexes by IRMPD Spectroscopy in the N-H/O-H Stretching Region."*

18. **Oral presentation:** Atlantic Theoretical Chemistry Symposium, Sydney, NS, Canada. August 13-15, 2008. E. AL. Gillis, **K. Rajabi**, T.D. Fridgen *"Structures of Hydrated Li^+-Thymine and Li^+-Uracil Complexes by IRMPD Spectroscopy in the N-H/O-H Stretching Region."*

19. **Oral presentation:** Tandem Mass Spectrometry workshop, Lake Louise, Alberta, Canada. December 3-December 6, 2008. E. AL. Gillis, **K. Rajabi**, T.D. Fridgen *"Structures of Hydrated Li^+-Thymine and Li^+-Uracil and the Mixed Li^+-*

Adenine/Thymine Complexes by IRMPD Spectroscopy in the N-H/O-H Stretching Region."

20. **Poster presentation:** 2009 Gordon Research Conference on the Gaseous Ions: Structures, Energetics and Reactions. Galvestion, TX, USA. **K. Rajabi**, E.A.L. Gillis, K. Theel, G. Beran, T.D. Fridgen *"The Solution Phase Structure of the Adenine Proton-Bound Dimer by Gas-Phase IRMPD Spectroscopy and Electronic Structure Calculations."*